Title

Development of Natural and Unnatural Metalloproteins for Abiotic Catalysis

Author

Chen, Rei Chi

Publication Date

2023

Peer reviewed|Thesis/dissertation

Development of Natural and Unnatural Metalloproteins for Abiotic Catalysis

By

Rei Chi Chen

A dissertation submitted in partial satisfaction of the

requirements for the degree of

Doctor of Philosophy

in

Chemistry

in the

Graduate Division

Of the

University of California, Berkeley

Committee in charge:

Professor John Hartwig, Chair

Professor Jonathan Rittle

Professor Richard Kramer

Summer 2023

Abstract

Development of Natural and Unnatural Metalloproteins for Abiotic Catalysis

By

Rei Chi Chen

Doctor of Philosophy in Chemistry

University of California, Berkeley

Professor John F. Hartwig, Chair

The following dissertation presents the development of abiotic catalysis with natural metalloproteins and artificial metalloenzymes (ArMs) by application of directed evolution and the integration of different strategies to develop ArMs.

Chapter 1 provides an overview of the development of abiotic catalysis in metalloenzymes. This section presents the concept of enzymatic promiscuity, by which abiotic reactions – reactions unnatural to the protein or to biosynthetic pathways – were discovered in natural proteins and subsequently enhanced through mutagenesis. It also explores directed evolution and the strategies employed to create enzyme libraries. In addition, the chapter presents assembly strategies for incorporating metal cofactors into protein scaffolds to create artificial metalloenzymes and the abiotic reactions catalyzed by these modified enzymes.

Chapter 2 focuses on the application of an abiotic zinc hydride active site in carbonic anhydrase that catalyzes the reduction of dialkyl ketones. Overcoming the inherent limitations of wild-type carbonic anhydrase, this chapter demonstrates how directed evolution and rational design were employed to generate reactive variants. Computational studies that explain the origins of enantioselectivity and substrate scope is also discussed.

Chapter 3 describes the preparation of artificial metalloenzymes by covalent anchoring and dative anchoring. The first section of the chapter describes an artificial myoglobin created by covalent anchoring of a heme cofactor to the myoglobin backbone. The second section describes an optimized protocol for preparing copper-substituted carbonic anhydrase, which is characterized using various analytical approaches. The Cu-hCAII variant is shown to exhibit carbene transfer reactions that are not observed with the original carbonic anhydrase.

Table of Content

Acknowledgment

First, I would like to express my gratitude to my PhD supervisor Professor John Hartwig who guided me not only in the knowledge of chemistry but also the research skills, problem-solving abilities, communication, and scientific writing. I am truly thankful for his steadfast support throughout these past years. I extend my appreciation to the members of my Ph.D. committee, Professor Jonathan Rittle and Professor Richard Kramer for their valuable insights and suggestions on my research. I would like to thank Professor Douglas Clark for his advice and support across all of my research projects. Moreover, I would like to thank to my undergraduate advisors Professor Chia-Chun Chen and Professor Shang-Cheng Hung. They have been remarkable mentors during my undergraduate studies and have continued to provide consistent support throughout my Ph.D. years I also want to show my deep gratitude to Mr. Rubber Chen from Pioneer Material Precision Tech. for financial support and emotional support during my time in UC Berkeley.

I am truly grateful to my labmates for their talent and insights in chemistry, as well as for fostering a friendly and collaborative working environment. In particular, I would like to acknowledge Dr. Pengfei Ji, Dr. Zhennan Liu, and Dr. Yang Gu for their invaluable support and mentorship in my research studies. I am also thankful to Dr. Jason Ma and Dr. Yehao Qiu for their exceptional talent and insightful suggestions during our daily discussions. I want to express my appreciation to Eli McAmis for his valuable contributions to our shared research projects. I am grateful to Isaac Yu for his helpful discussions and revisions of my writing.

I would like to thank everyone in Latimer 723, including Dr. Martí Garçon, Dr. Akira Tanushi, and Yuanzhe Xie, for engaging conversations on scientific and daily life topics, which have contributed to the positive working environment. I extend my gratitude to the members of our subgroup, Dr. Bloomer, Isaac Joyner, Jenna Manske, Gabe Herrera, and Andrew Quest, for sharing their knowledge in biology and biocatalysis and providing valuable suggestions.

I am also thankful for the support of my friends outside the lab. I express my gratitude to Sarah Chen, my former roommate and dear friend, for her unwavering support in research and emotional well-being. I would also like to thank Yen-Cheng Lin, Chin Lee, Oscar Chen, and Jonathan Chou for their helpful suggestions and support in various aspects. I won't be able to survive without their company. Special thanks to Eunha from VVZ and AZKi from Cover Corp. for their support through their voice and hard work.

Most importantly, I would like to convey my deepest appreciation to my parents. Thank you for being very supportive and granting me the opportunity to explore and pursue my passions throughout my life.

Chapter 1

Overview of Metalloenzymes in Biocatalysis: Current Status and Improvement

1.1 Introduction

Biocatalysis harnesses the power of enzymes, which are natural catalysts derived from living organisms, to catalyze chemical reactions with high selectivity and efficiency. Enzymes lower the activation energy required for reactions, thereby causing reactions to occur with altered specificity and under milder conditions than the uncatalyzed reactions. This sustainable approach offers advantages, such as reduced energy consumption, high regio- and stereoselectivity, and the ability to work with sensitive substrates. Biocatalysis finds applications in fields such as pharmaceuticals, fine chemicals, agriculture, and biofuels.[1] For example, Merck developed a route containing an *in vitro* biocatalytic cascade process for the manufacture of Islatravir, an HIV reverse transcriptase translocation inhibitor. The cascade process avoids the waste generated by the purification of intermediates and involved the utilization of five engineered enzymes that convert non-natural substrates to Islatravir in a streamlined three-step biocatalytic cascade in 76% yield. This innovative process significantly reduces the number of steps required compared to previously reported routes, showcasing the efficiency and potential of biocatalysis for optimized synthesis. [2–4] (Figure 1.)

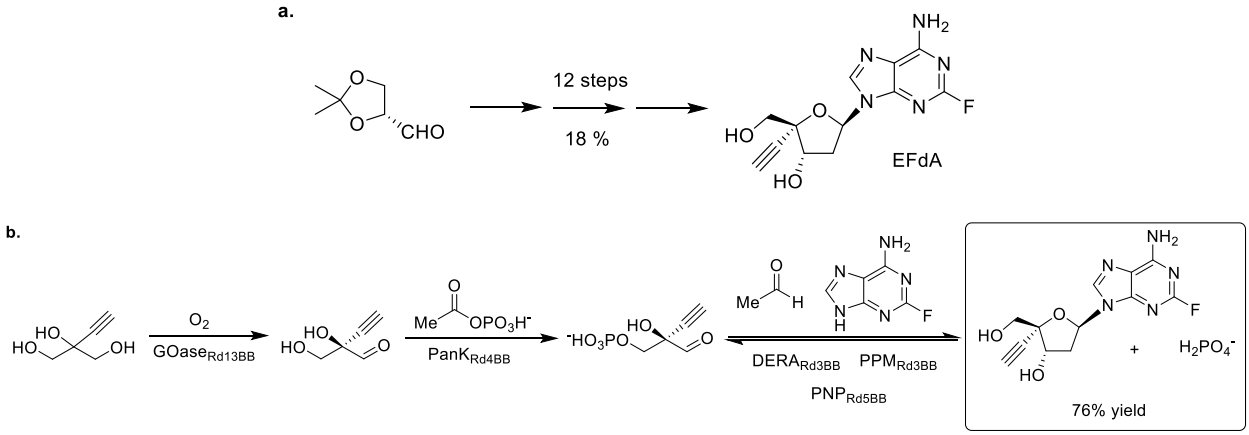

Figure 1. Comparison of two synthetic routes to Islatravir. a. synthetic route achieved with organic synthesis and small molecule catalysts. b. synthetic route incorporating biocatalytic processes.

Scientists often exploit the inherent promiscuity of enzymes, which refers to the ability of an enzyme to catalyze multiple reactions, to repurpose the function of the various enzymes to broaden the reaction scope for biocatalysis. Unlike specific enzymes that have evolved to catalyze a single reaction, promiscuous enzymes have broader substrate specificity, allowing them to participate in diverse chemical transformations.

The scope for the promiscuity of enzymes is further expanded as the development of protein engineering. The field of protein engineering has emerged to push the boundaries of natural enzymes and explore the vast potential of biocatalysis. One prominent approach in this field is directed evolution, a method introduced by Francis Arnold and recognized with the 2019 Nobel Prize in Chemistry. Directed evolution aims to mimic the natural process of evolution within the controlled environment of a laboratory, utilizing molecular biology techniques.[5,6] Directed evolution has widely improved enzymes capabilities not only in the accessibility of unnatural

substrates but also improvement of the function efficiently under conditions such as pH- or solvent tolerance in industrial processes.

In section 1.2, the promiscuity of reactions catalyzed by metalloenzymes will be introduced, emphasizing their capacity to catalyze a wide array of chemical transformations beyond their native function. This section will also present the general methods employed for conducting directed evolution, with a particular focus on strategies aimed at designing proteins capable of undergoing directed evolution to improve reaction reactivity and selectivity.

However, the promiscuous reactivity of enzymes is not sufficient to catalyze all types of reactions in synthetic chemistry. To address this limitation, the concept of artificial metalloenzyme is introduced. Organometallic catalysts are important for organic catalysis by enabling reactions that are not commonly found in nature. Therefore, the idea of incorporating organometallic catalysts into protein scaffolds that provide an enantiomeric environment was introduced. The enzymes prepared through this strategy are referred to as artificial metalloenzymes.[7,8] The first artificial metalloenzyme was introduced by Wilson and Whitesides in the 1970s.[9] However, protein engineering techniques at that time were in their early stages of development, which hindered the progress in the field of artificial metalloenzymes. Nevertheless, with the advancements in protein engineering, the development of artificial metalloenzymes has gained significant attention, due to the remarkable ability of such enzymes to catalyze a wide range of abiotic reactions. In section 1.3, the general design of ArMs, strategies for the preparation of ArMs, and abiotic reactions catalyzed by ArMs will be introduced.

1.2 Natural Enzymes for Abiotic Reactivity

1.2.1 Discovery of Enzyme Promiscuity

Enzyme promiscuity can be defined as the ability of an enzyme to catalyze physiologically irrelevant reactions. It can be further categorized into substrate and functional promiscuity.[10,11] Substrate promiscuity, which originates from the active site plasticity, is defined as the ability of the enzyme to accommodate versatile substrates. For example, CYP3A4, a kind of human cytochrome P450, is one of the most important enzymes for humans because it participates in the metabolism of the majority of pharmaceuticals. The extreme promiscuity in substrate specificity and cooperative substrate binding of CYP3A4 can cause undesired drug-drug interactions and cause side effects. Therefore, the study of the activity of CYP3A4 has become an important topic during drug development and therapy.[12]

Functional promiscuity refers to the ability of a protein to perform functions beyond its natural function, creating opportunities for developing abiotic reactions using enzymes. Despite their original functions in biocatalytic process, many enzymes possess the ability to catalyze diverse synthetic reactions by accepting abiotic reactants. This expansion of their scope allows them to catalyze reactions that are typically associated only with small-molecule catalysts. Cytochromes P450 (CYPs) are a family of hemoproteins that has the native function to catalyze oxidation reactions through a Fe(IV)-oxo intermediate (compound I).[13] Exploiting the versatility of metal porphyrins, which are capable of carbene transfer reactions[14] and nitrene transfer reactions,[15] researchers have successfully introduced Fe-carbene and Fe-nitrene intermediates into P450s,

leveraging their structural resemblance to the Fe-oxene intermediate.[16,17] (Figure 2.) The discovery of these abiotic carbene and nitrene intermediates has paved the way for various biocatalytic transformations, including cyclopropanation of unactivated alkenes,[18] cyclopropanation of alkynes,[19] stereoselective formation of C-N,[20,21] C-S,[22] C-Si,[23] and C-B[24] bonds, as well as enantioselective amination,[25,26] and aziridination.[27]

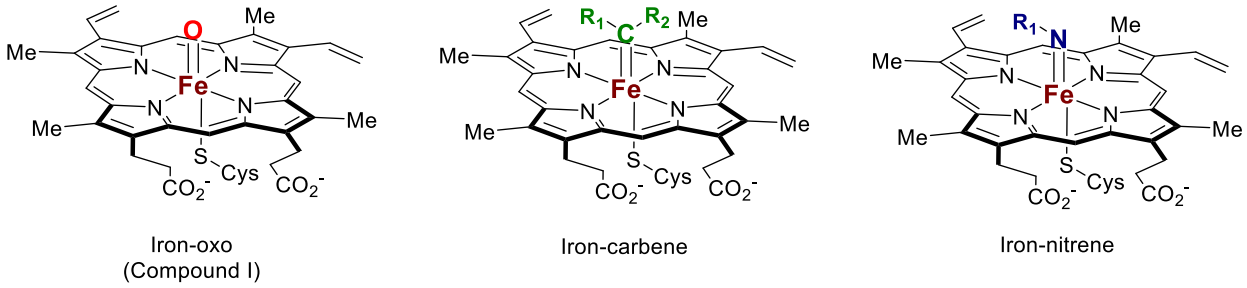

Figure 2. Iron-oxo intermediate and abiotic intermediates within a hemoprotein for carbene and nitrene transfer reactions.

Metalloproteins beyond hemoproteins also have the potential to be repurposed and to exhibit promiscuous reactivity. An example of this is the conversion of a non-heme Fe(II)/α-ketoglutarate (FeII/αKG)-dependent hydroxylase into a chlorinase by enzyme engineering. This transformation involves manipulating the enzyme's active site to enable competition between the rebound of the hydroxyl group and the rebound of the halide group with the substrate. This conversion is achieved by replacing specific aspartate/glutamate residues with alanine/glycine, creating a cavity within the active site.[28] Moreover, the primary coordination sphere of the non-heme iron enzyme can be modified by substitution of a ligand. For example, replacing α-ketoglutarate with N-oxalylglycine or acetate as the coordinating ligand introduces the capability for nitrene transfer reactions.[29] (Figure 3a)

Carbonic anhydrase, a zinc-containing metalloenzyme, has recently been discovered to exhibit catalytic activity in the asymmetric reduction of ketones. This intriguing reaction involves the generation of an abiotic zinc hydride intermediate, which represents a novel observation in biological systems. The introduction of a silane facilitates the transfer of a hydride to the zinc metal center, thereby enabling the observed catalytic behavior of carbonic anhydrase in ketone reduction.[30] (Figure 3b)

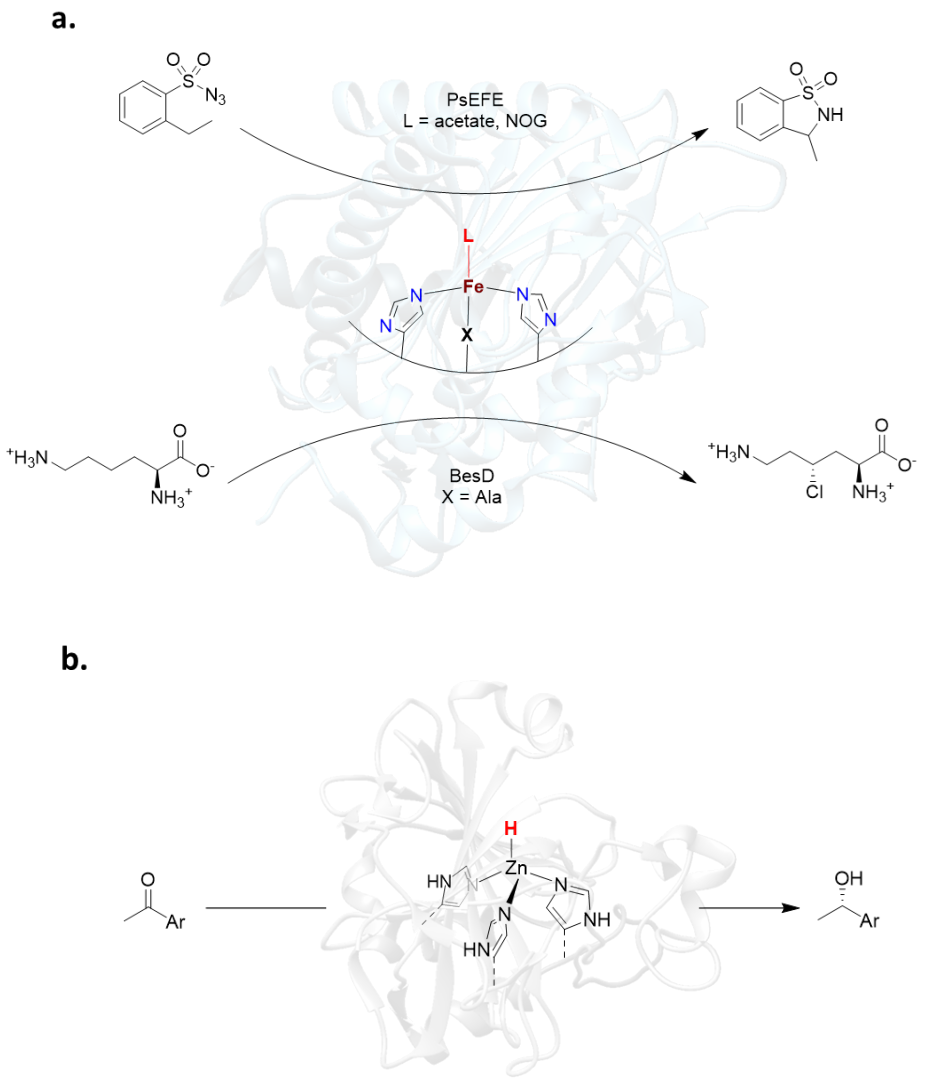

Figure 3. Promiscuous reactions introduced in metalloenzymes. a. nitrene transfer reaction and chlorination were introduced to FeII/αKG hydroxylase. b. asymmetric reduction of ketones was introduced to human carbonic anhydrase II (hCAII).

The promiscuous reactivity exhibited by natural metalloenzymes expands the potential for abiotic catalysis. However, the initial reactivity and selectivity of these enzymes are often low and require improvement. To address this challenge, directed evolution strategies have been employed to enhance both the reactivity and selectivity of these enzymatic reactions. These strategies are discussed in the next section.

1.2.2 Improvement of Abiotic Reactivity through Directed Evolution

Directed evolution is a technique that harnesses the principles of natural evolution to engineer enzymes or proteins with improved characteristics through iterative cycles of mutation and selection. Directed evolution has greatly improved enzymes in the biocatalytic process by enhancing the enzymes' tolerance to high temperatures,[31] organic solvents,[32] and pH changes, as

well as increasing the reaction specific and activity.[5,33] To establish directed evolution as a robust methodology for enzyme engineering in chemical synthesis and the production of natural products, a key component is the iterative rounds of high-throughput screening (HTS) from diversity generation. (Figure 4.) However, the cost and time required for high-throughput screening (HTS) can be substantial. To overcome this limitation, various tools and techniques have been developed to generate gene libraries and accelerate the directed evolution process. In the following section, the common strategies employed to generate mutant libraries for directed evolution will be introduced, including random mutagenesis, recombination, targeted random mutagenesis, and computational design.

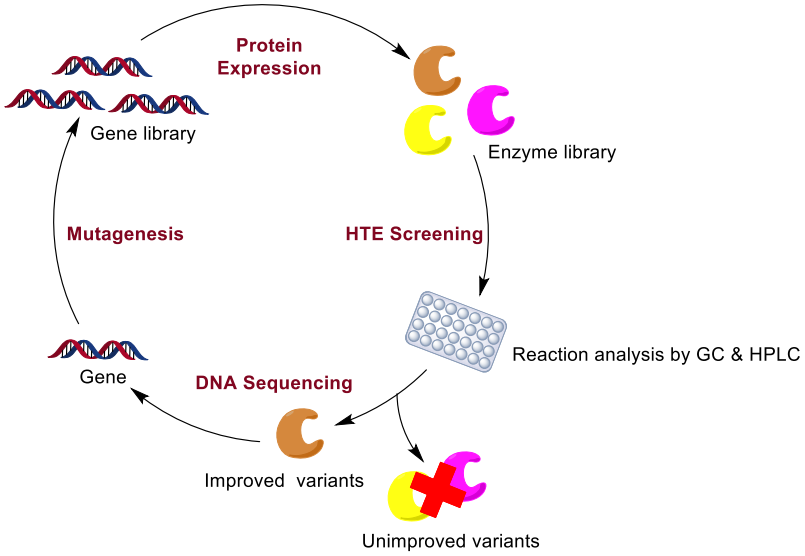

Figure 4. The process of iterative screening to discover the enzyme obtaining the desired properties.

Random mutagenesis and Recombination

Random mutagenesis is the strategy that is closest to natural evolution because it involves the random distribution of DNA base-pair changes throughout the target gene.[34] One well-established method for random mutagenesis is error-prone PCR, which allows for the construction of gene libraries with a broad range of mutations. The advantage of random mutagenesis lies in its ability to generate mutants from both the active site and the protein surface or positions distal from the active site. In contrast, targeted mutagenesis leads to changes at positions selected based on knowledge of the protein structure or hypotheses about positions important for reactivity.[35,36] Another technique, DNA shuffling, involves in vitro homologous recombination of pools of selected mutant genes by random fragmentation and PCR reassembly. This method enables random recombination between parent genes and retains a high proportion of functional progeny.[37,38]

Targeted random mutagenesis

Targeted random mutagenesis involves the pre-selection of specific sites or random distribution of sites for saturation mutagenesis. In saturation mutagenesis, all 20 amino acids are systematically

introduced at a single site, and this process is repeated iteratively. Site-saturation mutagenesis offers the advantage of comprehensive analysis of the original amino acid's function by covering all possible amino acids at a specific site.[39,40] Combinatorial mutagenesis is a site-directed protein engineering technique that combines multiple mutants obtained from site saturation mutagenesis. The goal is to leverage the additive effects arising from the combined activity of these mutants.[41,42] Finally, non-canonical amino acids can be incorporated into the natural amino acid pool to expand the range of amino acids that can be explored in site-directed saturation mutagenesis.[43]

Computational design

While random mutagenesis and targeted mutagenesis have been valuable in improving enzyme properties, they possess limitations, such as the need for extensive mutant screening generated by random mutagenesis. To overcome these limitations, protein engineering strategies have emerged that combine directed evolution with computational analysis, leading to more efficient enzyme reengineering.[44,45] In recent decades, protein engineering strategies that combine directed evolution and computational analysis improve the efficiency of reengineering enzymes. For computational investigations of catalytic reactivities,[46–48] the interaction and conformation between the active site and substrate are modeled by enzyme-substrate docking,[49] MD simulations,[50] QM/MM calculations, and analysis to rationalize the selectivity and reactivity of the enzymatic system. Furthermore, thermal stability[51,52] and solvent stability[53,54] are improved by using Rosetta[55] and FoldX[56] to predict the relative stability of the proteins. With the development of machine learning approaches, computational design methodologies are envisioned to establish smaller but smarter mutant libraries, thereby improving the efficiency of the screening process and expanding the capabilities of abiotic catalysis.

1.3 Artificial Metalloenzymes

Despite the potential of directed evolution to introduce abiotic reactivity into metalloenzymes, the inherent promiscuity of natural metalloenzymes remains limited and cannot cover the full spectrum of reactions that can be catalyzed by transition-metal catalysts. To overcome these limitations, artificial metalloenzymes (ArM) were introduced. These enzymes are often created by the incorporation of transition-metal cofactors within a protein scaffold.[7,8] The first examples of artificial metalloenzymes were developed in 1970s by Wilson and Whitesides by introducing a biotin-derivatized rhodium (I) complex that was bound to avidin, resulting in a homogeneous asymmetric hydrogenation catalyst.[9] However, the progress of ArMs was limited, due to the underdevelopment of both organometallic chemistry and protein engineering at that time. In recent decades, significant advancements have been made in the field of ArMs, enabling the realization of a wide range of non-natural reactions. In the following sections, the general methods to prepare ArMs and the abiotic reactions conducted by various ArMs will be introduced.

1.3.1 General Design and Preparation of Artificial Metalloenzymes

There are four general strategies to anchor abiotic transition metals into protein active sites to prepare artificial metalloenzymes.[57] The strategies can be classified by the interaction between the metal cofactor and host protein: (i) supramolecular anchoring, (ii) covalent anchoring, (iii) dative anchoring, and (iv) metal substitution. (Figure 5.)

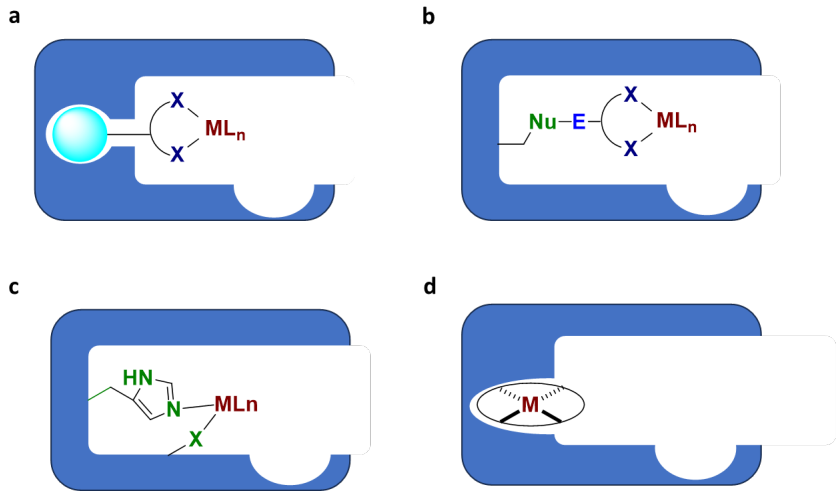

Figure 5. Four major strategies for the preparation of artificial metalloenzymes. a. supramolecular anchoring, b. covalent anchoring, c. dative anchoring, d. metal substitution.

Supramolecular anchoring

Supramolecular anchoring is a strategy that is based on the strong affinity between biomolecules containing a metal cofactor and a protein host, allowing for the immobilization of metal catalysts onto the secondary protein structure. Transition metals, such as Fe,[58] Rh,[59] Ru,[60] have been incorporated into artificial metalloenzymes using supramolecular anchoring techniques. One of the most well-known approaches involves the use of biotin-(strept)avidin interactions to generate enantioselective artificial metalloenzymes. The first Rh-biotin and avidin artificial metalloenzymes were prepared by Wilson and Whiteside for asymmetric hydrogenation.[9] Building upon this system, Ward's group further developed the biotin-streptavidin platform, hypothesizing that a deeper binding pocket would enhance enantioselectivity in the metalloenzyme. They introduced biotinylated d^6 half-sandwich Rh complexes into streptavidin, significantly expanding the scope of artificial hydrogenase systems.[61]

Moreover, supramolecular anchoring has been used to create artificial metalloenzymes with other protein scaffolds, including an artificial metathesase based on human carbonic anhydrase II and enzymes for asymmetric transfer hydrogenation using β-lactoglobulin. These approaches involve attaching specific anchors to protein scaffolds, allowing the incorporation of transition metal catalysts. The resulting artificial metalloenzymes exhibit enhanced catalytic activity and selectivity in metathesis and transfer hydrogenation reactions, respectively.[62,63] (Figure 6.)

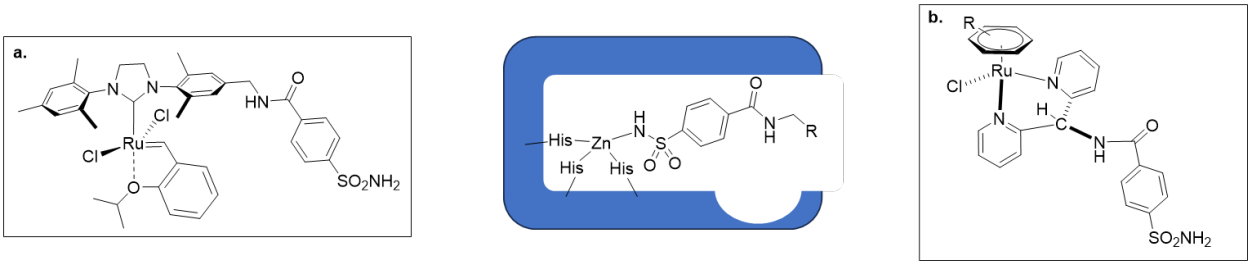

Figure 6. Artificial carbonic anhydrase prepared by anchoring arylsufonamide metallocofactors. a. Ruthenium cofactor catalyzes olefin metathesis, b. catalyzes asymmetric transfer hydrogenation.

Covalent anchoring

Covalent anchoring involves the formation of strong and irreversible bonds between reactive cofactors and specific amino acid residues on the protein. Common reactions utilized in this process include nucleophilic attack by residues such as cysteine,[64] serine,[65] lysine,[66] or other nucleophilic amino acids on maleimides or iodoacetamides. For example, Reetz and coworkers demonstrated the incorporation of a copper cofactor into papain by forming a covalent bond between a modified bipyridine moiety and a cysteine residue, showcasing the efficacy of this approach.[64] (Figure 7.)

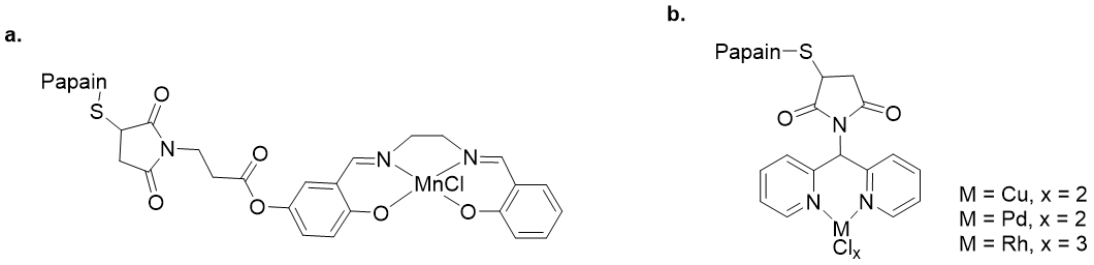

Figure 7. Incorporation of metallocofactors to papain through maleimide and cysteine crosslinking. a. incorporation of manganese salen complex, b. incorporation of bipyridine ligand coordinating with various metal.

Another common approach for covalent anchoring is the formation of a disulfide linkage between a cysteine residue and a cofactor with an electrophilic sulfur moiety. Lu and coworkers reported an artificial metalloprotein design by incorporating a Mn-Salen cofactor into myoglobin by the formation of two disulfide bonds between the sulfonate-containing salen and two cysteine residues on myoglobin which were introduced by mutation of Y103 and L72 of myoglobin to cysteines.[67] (Figure 8a.)

Finally, strain-promoted azide-alkyne cycloaddition (SPAAC) reactions between an unnatural amino acid containing a terminal alkyne or azide with the metal cofactor substituted with azide or alkyne is also a strategy to prepare artificial metalloenzyme through covalent anchoring. This was demonstrated by Lewis and coworkers in the preparation of artificial metalloenzymes containing Rh cofactors, which act as carbene transferases.[68] (Figure 8b.)

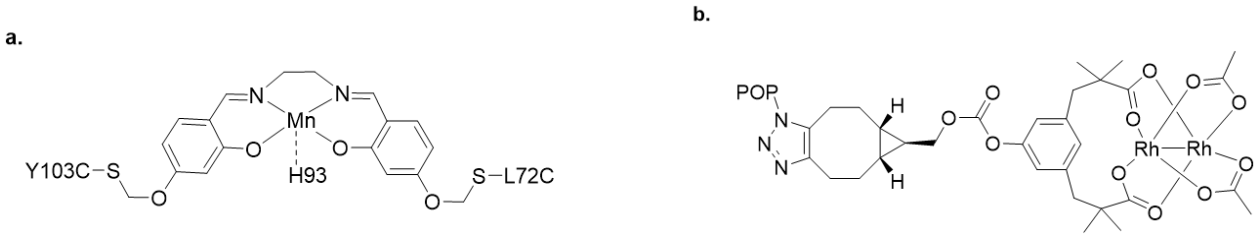

Figure 8. Covalent anchoring metallocofactors through a. disulfide bonds formation between sulfonate and cysteine and b. azide-alkyne cycloaddition between unnatural amino acids and cofactor containing alkyne.

Dative anchoring

The dative anchoring approach exploits the intrinsic property of amino acid residues that serve as Lewis bases (His, Cys, Glu, Asp, Ser, etc.), to incorporate cationic metals. The preparation of artificial metalloenzymes with dative anchoring requires the expression of apo protein, which is the metal-free protein, followed by addition of extrinsic metal salts. The earliest artificial metalloenzyme created by the dative anchoring strategy was reported by Kaiser and coworkers. They substituted copper for zinc in carboxypeptidase A,[69] which was the first report on oxidase activity by copper (II) carboxypeptidase.

Human carbonic anhydrase II (hCAII), a zinc containing enzyme that catalyzes the hydroxylation of carbon dioxide, is a common protein scaffold to prepare artificial metalloenzymes by the dative anchoring strategy. The zinc metal center can be removed by incubation with 2,6-pyridinedicarboxylate and the resulting apo protein further reconstituted with transition metal ions. Mn-hCAII was introduced to form an epoxidase that catalyzed asymmetric epoxidation of vinylarenes.[70] Rh-hCAII was reported to catalyze hydrogenation and hydroformylation, but the characterization and spectroscopy studies afforded deeper insights and implied that the active site in Rh-hCAII did not catalyze the claimed reactions.[71] (Figure 9.)

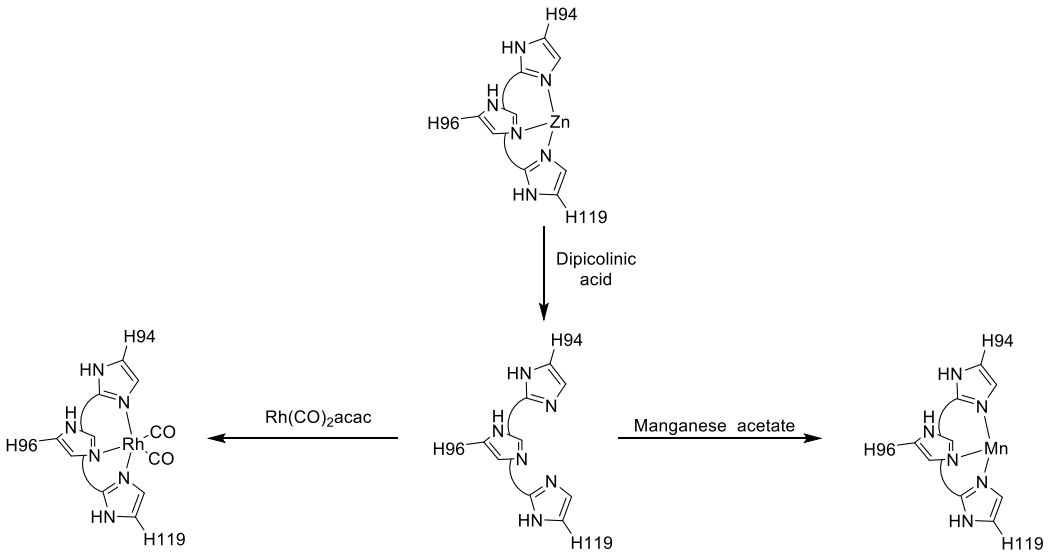

Figure 9. Preparation of artificial human carbonic anhydrase II (hCAII) through dative anchoring strategy. The zinc metal was first removed from the active site to form apo-hCAII and followed by metalation of desire metal salts.

Metal substitution

The metal substitution strategy involves replacing the natural transition metal in biosynthesized cofactors with unnatural transition metals, thereby introducing abiotic reactivity. Artificial

cofactors have been prepared by organic synthesis and subsequently reconstituted into the apo proteins. Hemoproteins, which is a family of protein containing the heme as metal cofactor, are particularly suitable for metal substitution strategies. Various synthetic analogs of natural porphyrin cofactors have been introduced to hemoproteins. For example, the incorporation of Mn porphycene into horseradish peroxidase by the Hayashi group led to the development of an oxidase catalyzing C-H bond hydroxylation.[72] In addition, a Co porphyrin complex was incorporated as a cofactor into myoglobin to enable hydrogen evolution catalysis.[73]

Recently, our group developed a system to incorporate noble transition metals into hemoproteins to generate carbene and nitrene transferases. The process involved preparing the apo hemoprotein in minimal media with low iron content, followed by purification using a standard protein purification protocol, followed by reconstitution of the protein with Ir(Me)mPIX (mPIX for mesoporphyrin IX). Ir(Me)mPIX was incorporated into apo-Mb (sperm whale myoglobin) containing a mutation of the axial histidine to glycine (H93A/G), resulting in the formation of an active carbene transferase.[74] This strategy was also applied to the thermophilic P450 scaffold, CYP119, resulting in the generation of a carbene transferase capable of catalyzing cyclopropanation of unactivated alkenes in natural terpenes with remarkable TON and diastereoselectivity.[75] (Figure 10.)

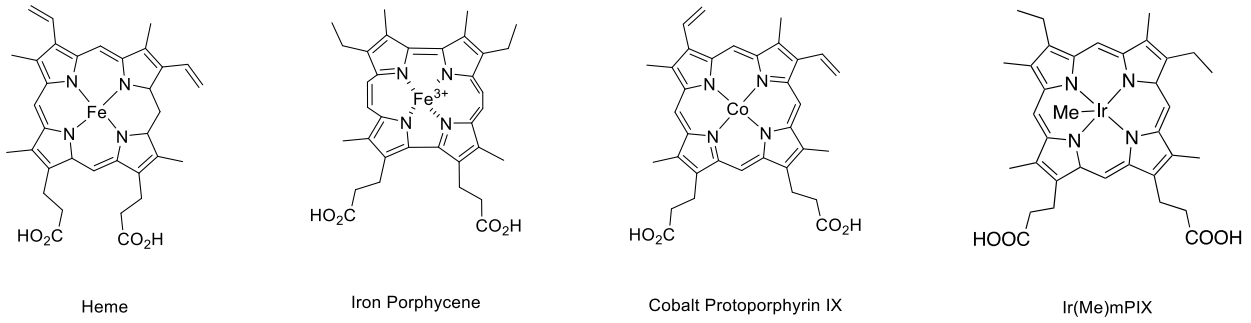

Figure 10. Metallocofactor for substitution of hemoprotein. The porphycene and porphyrin cofactors bear similar structures to the natural heme cofactor.

This approach was originally limited by the inability to conduct high-throughput screening. Each protein was purified and reconstituted with the artificial cofactor *in vitro*. To address this limitation, our group developed a platform for assembling the artificial metalloenzyme *in vivo*. With the application of a nonpathogenic *E. coli* strain that contains an outer-membrane receptor, Ir-CYP119 was assembled *in vivo* and catalyzed enantioselective carbene insertion into N-H bond of aniline derivatives. This platform was applied into biosynthetic pathway to produce unnatural terpenoids.[76,77]

1.3.2 Catalytic Reactions for Artificial Metalloenzymes

The incorporation of noble transition metals into protein scaffolds has enabled the creation of artificial metalloenzymes that catalyze a wide range of abiotic reactions. These transition metals or metal complexes offer reactivity that surpasses the capabilities of natural enzymes, while the intact secondary structure of the protein provides a chiral environment for highly enantioselective catalysis. Various abiotic reactions catalyzed by artificial metalloenzymes have been reported,

including reduction, oxidation, C-C bond formation, hydration, hydroformylation, etc. In the following section, reductions, oxidations, and C-C bond formations catalyzed by artificial metalloenzymes will be introduced.

Reduction

The first artificial metalloenzyme was developed as a hydrogenase with a biotinylated Rh(I)-bisphosphine incorporated to avidin and catalyzed the asymmetric hydrogenation of N-acetamidoacrylate obtaining N-acetamidoalanine with quantitative conversion and 41% ee.[9] More artificial metalloenzymes were developed by the anchoring strategies mentioned in the previous section. Reetz and coworkers reported a hydrogenase derived from papain in which Cu-, Pd- and Rh-complexes of maleimide-substituted dipyridine were covalently anchored to a cysteine side chain of the protein. However, these artificial metalloenzymes catalyzed hydrogenation with only low enantioselectivity.[78] Harada and coworkers reported the asymmetric hydrogenation of N-acetamido acrylic acid to produce N-acetyl-(S)-alanine with an ee over 98% using an achiral Rh-complex anchored in immunoglobin.[59] Watanabe and coworkers reported an artificial metalloenzyme that catalyzes size-selective olefin hydrogenation, with the metalloenzyme containing a Pd-nanocluster within the cage of an apo-ferritin, an iron-storage protein.[79] (Figure 11a.)

Artificial transfer hydrogenases have been designed for the reduction of various unsaturated substrates, including ketone,[80] imines,[81,82] and enones.[83] An artificial transfer hydrogenase was developed by Ward and coworkers by the incorporation of biotinylated, d^6, piano-stool Ru-complexes into streptavidin. The transfer hydrogenase catalyzed enantioselective transfer hydrogenation reactions of acetyl pyridine with up 90% ee and excellent conversion after two rounds of mutagenesis.[80] An imine reductase was developed by incorporating biotinylated [η5-(Cp*)IrCl] into streptavidin. The resulting imine reductase catalyzed asymmetric reduction of the salsolidine precursor with 57% ee. This enantioselectivity was improved to 91% ee with one round of mutagenesis, and the turnovers reached 100.[63] A similar system was also reported for the chemoselective reduction of enones to their corresponding ketones.[83] (Figure 11b.)

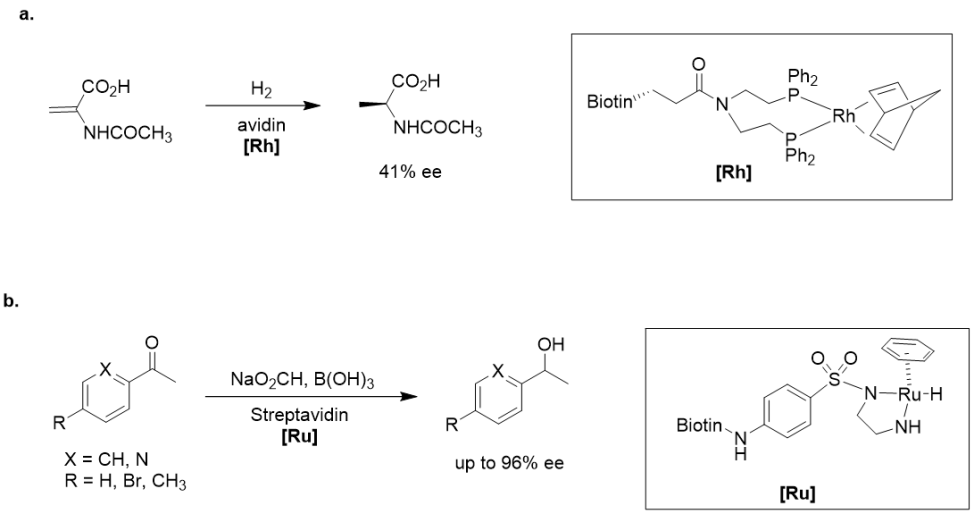

Figure 11. Asymmetric reduction reactions performed by artificial metalloenzymes based biotin-(Stept)avidin system. a. asymmetric hydrogenation of olefin and b. asymmetric transfer hydrogenation of acetophenone and acetyl pyridine.

Oxidation

Oxidation reactions are important in biology and synthetic organic chemistry, and enzymatic oxidation provides a selective and mild approach to these transformations. Natural enzymes, such as cytochrome P450, methane monooxygenase, and tyrosinase, generate metal-O_2 species in their active sites to catalyze oxidation reactions. However, natural enzymes are often limited to specific substrates. To overcome this limitation, many artificial metalloenzymes have been developed for various oxidation reactions such as alcohol oxidation,[84] sulfoxidation,[85] epoxidation,[70,86] dihydroxylation,[87] and peroxidation.[88]

Myoglobin (Mb) is a protein from the hemoprotein family with an original function to transport oxygen, and the heme cofactor was substituted with metallocofactors to transform myoglobin into an oxidase. Hayashi and co-workers introduced Fe-porphycene to apo-Mb, resulting 11-fold improvements, in the oxidation of guaiacol with hydrogen peroxide over the activity of wild-type Mb.[89,90] Watanabe and colleagues reconstituted achiral chromium and manganese salen and salophen complexes into apo-Mb, enabling abiotic and enantioselective sulfoxidation of thioanisole derivatives.[91] Moreover, Lu and coworkers discovered that covalent linkage of a salen cofactor to the protein scaffold significantly improved enantioselectivity. Double anchoring of the Mn-salen to Mb improved the enantioselectivity to 51% ee, compared to 0% ee for non-covalent binding of the cofactor and 12% ee for single anchoring of the cofactor and protein.[67,92] (Figure 12.)

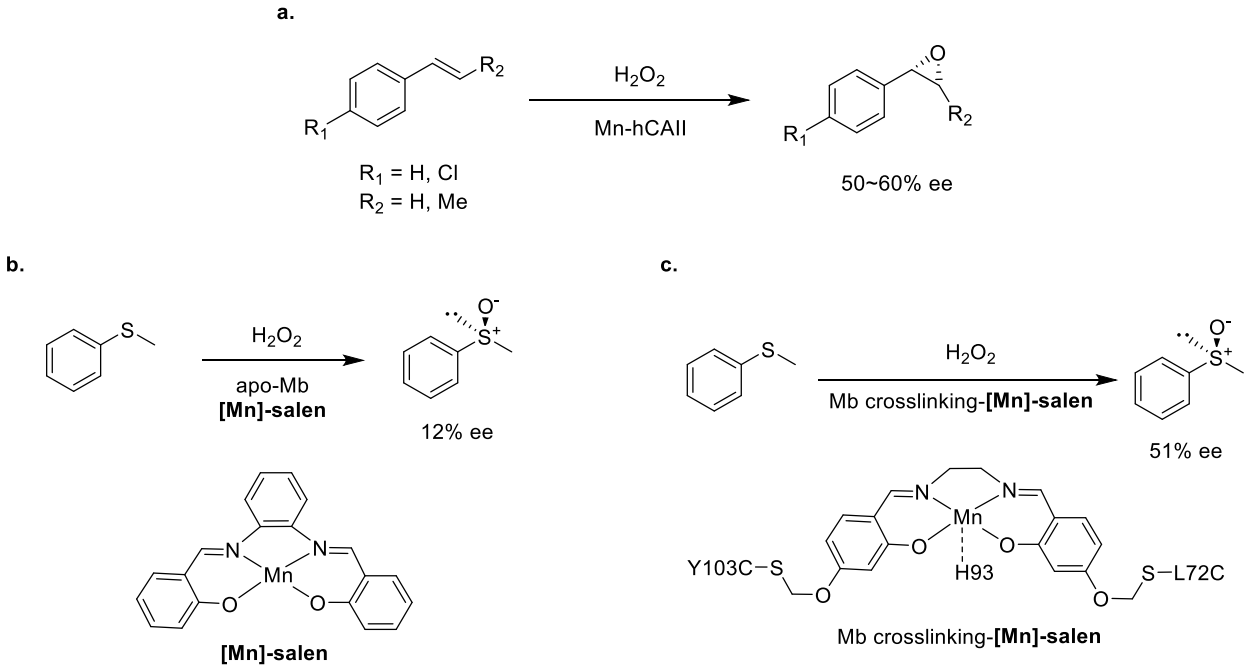

Figure 12. Asymmetric oxidation reactions performed by different artificial metalloenzyme systems. a. Mn-hCAII catalyzed epoxidation of styrene. b. Myoglobin substituted by Mn-salen cofactor performed enantioselective sulfoxidation of thioanisole derivatives, and c. The enantioselectivity was improved by introducing covalent linking between cofactor and protein host.

C-C Bond Formation

Enzymes modified with transition-metal catalysts have led to unnatural C-C bond-forming reactions, offering opportunities to synthesize important pharmaceutical building blocks. Despite the challenges of conducting these reactions under aqueous conditions, enzymes incorporated with transition-metal complexes catalyze various coupling reactions, including Suzuki cross-coupling,[93] allylic alkylation,[94] and the Heck reaction.[95]

Metal-porphyrin complexes catalyzing C-H insertion of various carbene or nitrene sources were introduced to hemoproteins. While the natural active site accommodates metal-oxo intermediates and substrates, the artificial metalloenzyme accommodates metal-carbene or metal-nitrene intermediates that catalyzed C-C or C-N bond formation reactions. Our group reported C-H and N-H insertion reaction catalyzed by Ir(Me)mPIX-substituted myoglobin and CYP119.[97,98] With mutation of the axial residue to accommodate the methyl group on Ir(Me)mPIX, the artificial metalloenzyme catalyzed intramolecular carbene insertions into C-H bonds with up to 7000 TON and up to 98% ee, cyclopropanation of olefins with up to 10,000 TON and 99% ee, and intermolecular carbene insertions into the benzylic C-H bonds of phthalane and its derivatives with moderate yield and ee.[74] (Figure 13.)

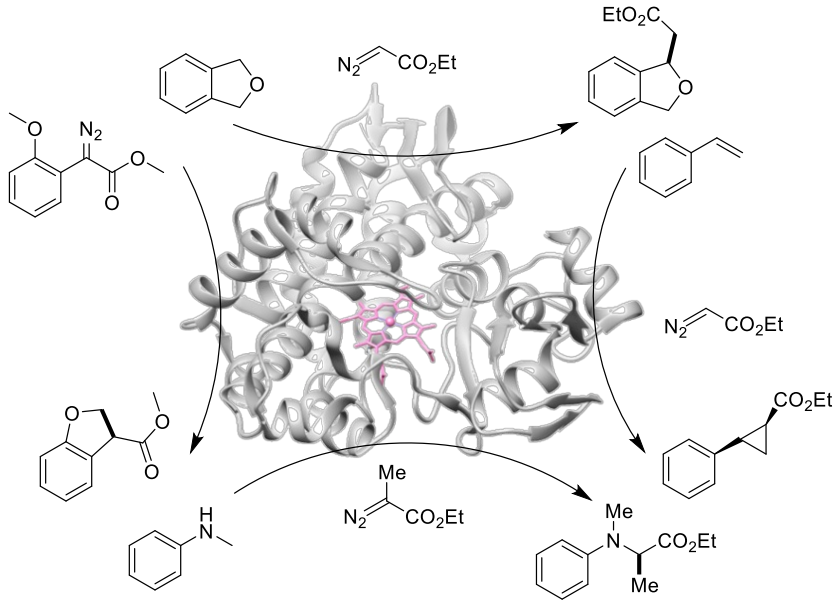

Figure 13. Enantioselective carbene transfer reactions catalyzed by Ir-CYP119 variants.

Transition metal catalyzed olefin metathesis is a highly versatile tool for C-C bond formation, and olefin metathesis has been catalyzed by various artificial metalloenzymes. The first two artificial

enzymes catalyzing olefin metathasis were introduced by the Hilvert group, in which biotinylated Grubbs-Hoveyda second generation catalyst was anchored to avidin or streptavidin through supramolecular interactions. These metalloenzymes catalyze the ring-closing metathesis of diallyl tosylamide.[99] Later, an artificial enzyme based on human carbonic anhydrase II (hCAII) catalyzing olefin metathesis was reported by the Ward group. A sulfonamide-tailed catalyst for ring closing metathesis that coordinates to the Zn metal center in hCAII was synthesized. Despite the similar reactivity between the free cofactor and the artificial enzyme, the reaction can be performed in a pH 7 buffer at 37 °C, which is similar to aerobic physiological conditions.[62] (Figure 14.)

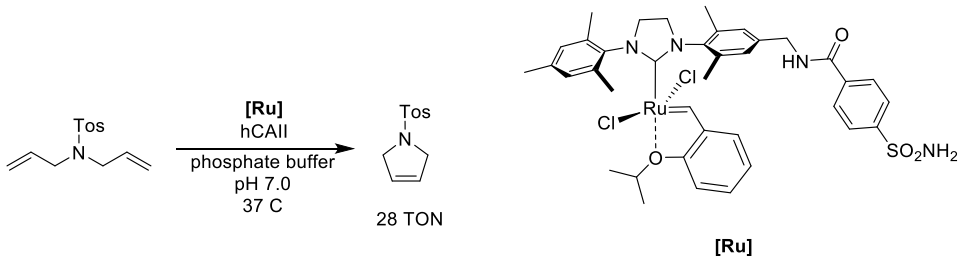

Figure 14. An artificial enzyme catalyzing olefin metathesis based on incorporation of the Hoveyda-Grubbs catalyst into hCAII, which catalyzed ring closing metathesis under aerobic physiological conditions.

1.4 Summary and Outlook

In conclusion, this chapter highlights the utilization of protein promiscuity and directed evolution to catalyze abiotic reactions with proteins. Various strategies have been employed to accelerate the generation of mutant library reactivity, including random mutagenesis, site-directed mutagenesis, and computational design. Moreover, the emergence of artificial metalloenzymes has expanded the capabilities of metalloproteins to catalyze non-natural reactions with proteins containing synthetic cofactors. By harnessing the advantages of protein promiscuity, directed evolution, and synthetic metallocofactors, the field of biocatalysis demonstrates tremendous potential for future advancements.

1.5 References

(1) Wu, S.; Snajdrova, R.; Moore, J. C.; Baldenius, K.; Bornscheuer, U. T. Biocatalysis: Enzymatic Synthesis for Industrial Applications. *Angew. Chem. Int. Ed.* **2021**, *60* (1), 88–119.
(2) Huffman, M. A.; Fryszkowska, A.; Alvizo, O.; Borra-Garske, M.; Campos, K. R.; Canada, K. A.; Devine, P. N.; Duan, D.; Forstater, J. H.; Grosser, S. T.; Halsey, H. M.; Hughes, G. J.; Jo, J.; Joyce, L. A.; Kolev, J. N.; Liang, J.; Maloney, K. M.; Mann, B. F.; Marshall, N. M.; McLaughlin, M.; Moore, J. C.; Murphy, G. S.; Nawrat, C. C.; Nazor, J.; Novick, S.; Patel, N. R.; Rodriguez-Granillo, A.; Robaire, S. A.; Sherer, E. C.; Truppo, M. D.; Whittaker, A. M.; Verma, D.; Xiao, L.; Xu, Y.; Yang, H. Design of an in Vitro Biocatalytic Cascade for the Manufacture of Islatravir. *Science* **2019**, *366* (6470), 1255–1259.
(3) McLaughlin, M.; Kong, J.; Belyk, K. M.; Chen, B.; Gibson, A. W.; Keen, S. P.; Lieberman, D. R.; Milczek, E. M.; Moore, J. C.; Murray, D.; Peng, F.; Qi, J.; Reamer, R. A.; Song, Z. J.; Tan, L.; Wang, L.; Williams, M. J. Enantioselective Synthesis of 4′-Ethynyl-2-Fluoro-2′-Deoxyadenosine (EFdA) via Enzymatic Desymmetrization. *Org. Lett.* **2017**, *19* (4), 926–929.

(4) Kageyama, M.; Nagasawa, T.; Yoshida, M.; Ohrui, H.; Kuwahara, S. Enantioselective Total Synthesis of the Potent Anti-HIV Nucleoside EFdA. *Org. Lett.* **2011**, *13* (19), 5264–5266.
(5) Cherry, J. R.; Fidantsef, A. L. Directed Evolution of Industrial Enzymes: An Update. *Curr. Opin. Biotechnol.* **2003**, *14* (4), 438–443.
(6) Arnold, F. H.; Volkov, A. A. Directed Evolution of Biocatalysts. *Curr Opin Chem Biol.* **1999**, *3*(1), 54-59
(7) Davis, H. J.; Ward, T. R. Artificial Metalloenzymes: Challenges and Opportunities. *ACS Cent. Sci.* **2019**, *5* (7), 1120–1136.
(8) Schwizer, F.; Okamoto, Y.; Heinisch, T.; Gu, Y.; Pellizzoni, M. M.; Lebrun, V.; Reuter, R.; Köhler, V.; Lewis, J. C.; Ward, T. R. Artificial Metalloenzymes: Reaction Scope and Optimization Strategies. *Chem. Rev.* **2018**, *118* (1), 142–231.
(9) Wilson, M. E.; Whitesides, G. M. Conversion of a Protein to a Homogeneous Asymmetric Hydrogenation Catalyst by Site-Specific Modification with a Diphosphinerhodium(I) Moiety. *J. Am. Chem. Soc.* **1978**, *100* (1), 306–307.
(10) Gupta, R. D. Recent Advances in Enzyme Promiscuity. *Sustain. Chem. Process.* **2016**, *4* (1), 2.
(11) Singla, P.; Bhardwaj, R. D. Enzyme promiscuity – A light on the "darker" side of enzyme specificity. *Biocatalysis and Biotransformation* **2020**, *38*(2), 81-92
(12) Sevrioukova, I. F.; Poulos, T. L. Understanding the Mechanism of Cytpchrome P450 3A4: Recnet Advances and Remaining Problems. *Dalton Trans. Camb. Engl. 2003* **2013**, *42* (9), 3116–3126.
(13) Rittle, J.; Green, M. T. Cytochrome P450 Compound I: Capture, Characterization, and C-H Bond Activation Kinetics. *Science* **2010**, *330*(6006), 933-937
(14) Lu, H.; Zhang, X. P. Catalytic C–H Functionalization by Metalloporphyrins: Recent Developments and Future Directions. *Chem Soc Rev* **2011**, *40* (4), 1899–1909..
(15) Che, C.-M.; Lo, V. K.-Y.; Zhou, C.-Y.; Huang, J.-S. Selective Functionalisation of Saturated C–H Bonds with Metalloporphyrin Catalysts. *Chem. Soc. Rev.* **2011**, *40* (4), 1950.
(16) Yang, Y.; Arnold, F. H. Navigating the Unnatural Reaction Space: Directed Evolution of Heme Proteins for Selective Carbene and Nitrene Transfer. *Acc. Chem. Res.* **2021**, *54* (5), 1209–1225.
(17) Coelho, P. S.; Brustad, E. M.; Kannan, A.; Arnold, F. H. Olefin Cyclopropanation via Carbene Transfer Catalyzed by Engineered Cytochrome P450 Enzymes. *Science* **2012**, *339*(6117), 307-310
(18) Knight, A. M.; Kan, S. B. J.; Lewis, R. D.; Brandenberg, O. F.; Chen, K.; Arnold, F. H. Diverse Engineered Heme Proteins Enable Stereodivergent Cyclopropanation of Unactivated Alkenes. *ACS Cent. Sci.* **2018**, *4* (3), 372–377.
(19) Chen, K.; Huang, X.; Kan, S. B. J.; Zhang, R. K.; Arnold, F. H. Enzymatic Construction of Highly Strained Carbocycles. *Science* **2018**, *360* (6384), 71–75.
(20) Sreenilayam, G.; Fasan, R. Myoglobin-Catalyzed Intermolecular Carbene N–H Insertion with Arylamine Substrates. *Chem. Commun.* **2015**, *51* (8), 1532–1534.
(21) Wang, Z. J.; Peck, N. E.; Renata, H.; Arnold, F. H. Cytochrome P450-Catalyzed Insertion of Carbenoids into N–H Bonds. *Chem Sci* **2014**, *5* (2), 598–601.
(22) Tyagi, V.; Bonn, R. B.; Fasan, R. Intermolecular Carbene S–H Insertion Catalysed by Engineered Myoglobin-Based Catalysts. *Chem. Sci.* **2015**, *6* (4), 2488–2494.
(23) Kan, S. B. J.; Lewis, R. D.; Chen, K.; Arnold, F. H. Directed Evolution of Cytochrome c for Carbon–Silicon Bond Formation: Bringing Silicon to Life. *Science* **2016**, *354* (6315),

(24) Kan, S. B. J.; Huang, X.; Gumulya, Y.; Chen, K.; Arnold, F. H. Genetically Programmed Chiral Organoborane Synthesis. *Nature* **2017**, *552* (7683), 132–136.
(25) Prier, C. K.; Zhang, R. K.; Buller, A. R.; Brinkmann-Chen, S.; Arnold, F. H. Enantioselective, Intermolecular Benzylic C–H Amination Catalysed by an Engineered Iron-Haem Enzyme. *Nat. Chem.* **2017**, *9* (7), 629–634.
(26) Yang, Y.; Cho, I.; Qi, X.; Liu, P.; Arnold, F. H. An Enzymatic Platform for the Asymmetric Amination of Primary, Secondary and Tertiary C(Sp3)-H Bonds. *Nat. Chem.* **2019**, *11* (11), 987–993.
(27) Farwell, C. C.; Zhang, R. K.; McIntosh, J. A.; Hyster, T. K.; Arnold, F. H. Enantioselective Enzyme-Catalyzed Aziridination Enabled by Active-Site Evolution of a Cytochrome P450. *ACS Cent. Sci.* **2015**, *1* (2), 89–93.
(28) Neugebauer, M. E.; Kissman, E. N.; Marchand, J. A.; Pelton, J. G.; Sambold, N. A.; Millar, D. C.; Chang, M. C. Y. Reaction Pathway Engineering Converts a Radical Hydroxylase into a Halogenase. *Nat. Chem. Biol.* **2022**, *18* (2), 171–179.
(29) Goldberg, N. W.; Knight, A. M.; Zhang, R. K.; Arnold, F. H. Nitrene Transfer Catalyzed by a Non-Heme Iron Enzyme and Enhanced by Non-Native Small-Molecule Ligands. *J. Am. Chem. Soc.* **2019**, *141* (50), 19585–19588.
(30) Ji, P.; Park, J.; Gu, Y.; Clark, D. S.; Hartwig, J. F. Abiotic Reduction of Ketones with Silanes Catalysed by Carbonic Anhydrase through an Enzymatic Zinc Hydride. *Nat. Chem.* **2021**, *13* (4), 312–318.
(31) Yano, J. K.; Poulos, T. L. New Understandings of Thermostable and Peizostable Enzymes. *Curr. Opin. Biotechnol.* **2003**, *14* (4), 360–365.
(32) Reetz, M. T.; Soni, P.; Fernández, L.; Gumulya, Y.; Carballeira, J. D. Increasing the Stability of an Enzyme toward Hostile Organic Solvents by Directed Evolution Based on Iterative Saturation Mutagenesis Using the B-FIT Method. *Chem. Commun.* **2010**, *46* (45), 8657.
(33) Dalby, P. A. Strategy and Success for the Directed Evolution of Enzymes. *Curr. Opin. Struct. Biol.* **2011**, *21* (4), 473–480.
(34) Miyazaki, K.; Arnold, F. H. Exploring Nonnatural Evolutionary Pathways by Saturation Mutagenesis: Rapid Improvement of Protein Function. *J. Mol. Evol.* **1999**, *49* (6), 716–720.
(35) Zaccolo, M.; Gherardi, E. The Effect of High-Frequency Random Mutagenesis on in Vitro Protein Evolution: A Study on TEM-1 β-Lactamase. *Journal of Molecular Biology* **1999**, *285*(2), 775-783
(36) Chen, K.; Arnold, F. H. Tuning the Activity of an Enzyme for Unusual Environments: Sequential Random Mutagenesis of Subtilisin E for Catalysis in Dimethylformamide. *Proc. Natl. Acad. Sci.* **1993**, *90* (12), 5618–5622.
(37) Zhao, H.; Giver, L.; Shao, Z.; Affholter', J. A.; Arnold, F. H. Molecular Evolution by Staggered Extension Process (StEP) in Vitro Recotnbination. **1998**, *16*.
(38) Stemmer, W. P. C. Rapid Evolution of a Protein in Vitro by DNA Shuffling. *Nature* **1994**, *370* (6488), 389–391.
(39) Reetz, M. T.; Kahakeaw, D.; Sanchis, J. Shedding Light on the Efficacy of Laboratory Evolution Based on Iterative Saturation Mutagenesis. *Mol BioSyst* **2009**, *5* (2), 115–122.
(40) Siloto, R. M. P.; Weselake, R. J. Site Saturation Mutagenesis: Methods and Applications in Protein Engineering. *Biocatal. Agric. Biotechnol.* **2012**, *1* (3), 181–189.
(41) Sandberg, W. S.; Terwilliger, T. C. Engineering multiple properties of a protein by combinatorial mutagenesis. *PNAS* **1993**, *90*(18), 8367-8371

(42) Chen, C.; Guan, B.-H.; Geng, Q.; Zheng, Y.-C.; Chen, Q.; Pan, J.; Xu, J.-H. Enhanced Thermostability of *Candida* Ketoreductase by Computation-Based Cross-Regional Combinatorial Mutagenesis. *ACS Catal.* **2023**, *13* (11), 7407–7416.
(43) Anthony-Cahill, S. J.; Griffith, M. C.; Noren, C. J.; Suich, D. J.; Schultz, P. G. Site-Specific Mutagenesis with Unnatural Amino Acids *TIBS* **1989**, *14*(10), 400-403
(44) Zhao, H., Lee, S. Y., Nielsen, J., Stephanopoulos, G., Protein Engineering: Tools and Applications *John Wiley& Sons* **2021**.
(45) Arnold, F. H. Combinatorial and Computational Challenges for Biocatalyst Design. *Nature* **2001**, *409* (6817), 253–257.
(46) Li, R.; Wijma, H. J.; Song, L.; Cui, Y.; Otzen, M.; Tian, Y.; Du, J.; Li, T.; Niu, D.; Chen, Y.; Feng, J.; Han, J.; Chen, H.; Tao, Y.; Janssen, D. B.; Wu, B. Computational Redesign of Enzymes for Regio- and Enantioselective Hydroamination. *Nat. Chem. Biol.* **2018**, *14* (7), 664–670.
(47) Cadet, F.; Fontaine, N.; Li, G.; Sanchis, J.; Ng Fuk Chong, M.; Pandjaitan, R.; Vetrivel, I.; Offmann, B.; Reetz, M. T. A Machine Learning Approach for Reliable Prediction of Amino Acid Interactions and Its Application in the Directed Evolution of Enantioselective Enzymes. *Sci. Rep.* **2018**, *8* (1), 16757.
(48) Mai, B. K.; Neris, N. M.; Yang, Y.; Liu, P. C–N Bond Forming Radical Rebound Is the Enantioselectivity-Determining Step in P411-Catalyzed Enantioselective C(Sp^3)–H Amination: A Combined Computational and Experimental Investigation. *J. Am. Chem. Soc.* **2022**, *144* (25), 11215–11225.
(49) Morris, G. M.; Huey, R.; Lindstrom, W.; Sanner, M. F.; Belew, R. K.; Goodsell, D. S.; Olson, A. J. AutoDock4 and AutoDockTools4: Automated Docking with Selective Receptor Flexibility. *J. Comput. Chem.* **2009**, *30* (16), 2785–2791.
(50) Salomon-Ferrer, R.; Götz, A. W.; Poole, D.; Le Grand, S.; Walker, R. C. Routine Microsecond Molecular Dynamics Simulations with AMBER on GPUs. 2. Explicit Solvent Particle Mesh Ewald. *J. Chem. Theory Comput.* **2013**, *9* (9), 3878–3888.
(51) Soh, L. M. J.; Mak, W. S.; Lin, P. P.; Mi, L.; Chen, F. Y.-H.; Damoiseaux, R.; Siegel, J. B.; Liao, J. C. Engineering a Thermostable Keto Acid Decarboxylase Using Directed Evolution and Computationally Directed Protein Design. *ACS Synth. Biol.* **2017**, *6* (4), 610–618.
(52) Huang, J.; Xie, D.-F.; Feng, Y. Engineering Thermostable (R)-Selective Amine Transaminase from Aspergillus Terreus through in Silico Design Employing B-Factor and Folding Free Energy Calculations. *Biochem. Biophys. Res. Commun.* **2017**, *483* (1), 397–402.
(53) Wallraf, A.-M.; Liu, H.; Zhu, L.; Khalfallah, G.; Simons, C.; Alibiglou, H.; Davari, M. D.; Schwaneberg, U. A Loop Engineering Strategy Improves Laccase Lcc2 Activity in Ionic Liquid and Aqueous Solution. *Green Chem.* **2018**, *20* (12), 2801–2812.
(54) Lehmann, C.; Bocola, M.; Streit, W. R.; Martinez, R.; Schwaneberg, U. Ionic Liquid and Deep Eutectic Solvent-Activated CelA2 Variants Generated by Directed Evolution. *Appl. Microbiol. Biotechnol.* **2014**, *98* (12), 5775–5785.
(55) Liu, Y.; Kuhlman, B. RosettaDesign Server for Protein Design. *Nucleic Acids Res.* **2006**, *34*, 235–238.
(56) Van Durme, J.; Delgado, J.; Stricher, F.; Serrano, L.; Schymkowitz, J.; Rousseau, F. A Graphical Interface for the FoldX Forcefield. *Bioinformatics* **2011**, *27* (12), 1711–1712.
(57) Rosati, F.; Roelfes, G. Artificial Metalloenzymes. *ChemCatChem* **2010**, *2* (8), 916–927.

(58) Ricoux, R.; Lukowska, E.; Pezzotti, F.; Mahy, J.-P. New Activities of a Catalytic Antibody with a Peroxidase Activity: Formation of Fe(II)-RNO Complexes and Stereoselective Oxidation of Sulfides. *Eur. J. Biochem.* **2004**, *271* (7), 1277–1283.
(59) Yamaguchi, H.; Hirano, T.; Kiminami, H.; Taura, D.; Harada, A. Asymmetric Hydrogenation with Antibody-Achiral Rhodium Complex. *Org. Biomol. Chem.* **2006**, *4* (19), 3571.
(60) Chevalley, A.; Cherrier, M. V.; Fontecilla-Camps, J. C.; Ghasemi, M.; Salmain, M. Artificial Metalloenzymes Derived from Bovine β-Lactoglobulin for the Asymmetric Transfer Hydrogenation of an Aryl Ketone – Synthesis, Characterization and Catalytic Activity. *Dalton Trans* **2014**, *43* (14), 5482–5489.
(61) Skander, M.; Humbert, N.; Collot, J.; Gradinaru, J.; Klein, G.; Loosli, A.; Sauser, J.; Zocchi, A.; Gilardoni, F.; Ward, T. R. Artificial Metalloenzymes: (Strept)Avidin as Host for Enantioselective Hydrogenation by Achiral Biotinylated Rhodium−Diphosphine Complexes. *J. Am. Chem. Soc.* **2004**, *126* (44), 14411–14418.
(62) Zhao, J.; Kajetanowicz, A.; Ward, T. R. Carbonic Anhydrase II as Host Protein for the Creation of a Biocompatible Artificial Metathesase. *Org. Biomol. Chem.* **2015**, *13* (20), 5652–5655.
(63) Monnard, F. W.; Heinisch, T.; Nogueira, E. S.; Schirmer, T.; Ward, T. R. Human Carbonic Anhydrase II as a Host for Piano-Stool Complexes Bearing a Sulfonamide Anchor. *Chem. Commun.* **2011**, *47* (29), 8238. h.
(64) Reetz, M. T.; Rentzsch, M.; Pletsch, A.; Maywald, M. Towards the Directed Evolution of Hybrid Catalysts. *CHIMIA* **2002**, *56* (12), 721.
(65) Kruithof, C. A.; Dijkstra, H. P.; Lutz, M.; Spek, A. L.; Egmond, M. R.; Klein Gebbink, R. J. M.; van Koten, G. Non-Tethered Organometallic Phosphonate Inhibitors for Lipase Inhibition: Positioning of the Metal Center in the Active Site of Cutinase. *Eur. J. Inorg. Chem.* **2008**, *2008* (28), 4425–4432.
(66) Garner, D. K.; Liang, L.; Barrios, D. A.; Zhang, J.-L.; Lu, Y. Covalent Anchor Positions Play an Important Role in Tuning Catalytic Properties of a Rationally Designed MnSalen-Containing Metalloenzyme. *ACS Catal.* **2011**, *1* (9), 1083–1089.
(67) Carey, J. R.; Ma, S. K.; Pfister, T. D.; Garner, D. K.; Kim, H. K.; Abramite, J. A.; Wang, Z.; Guo, Z.; Lu, Y. A Site-Selective Dual Anchoring Strategy for Artificial Metalloprotein Design. *J. Am. Chem. Soc.* **2004**, *126* (35), 10812–10813.
(68) Srivastava, P.; Yang, H.; Ellis-Guardiola, K.; Lewis, J. C. Engineering a Dirhodium Artificial Metalloenzyme for Selective Olefin Cyclopropanation. *Nat. Commun.* **2015**, *6* (1), 7789.
(69) Emilthomaksaiser, Yamamu. Studies on the Oxidase Activity of Copper(I1) Carboxypeptidase A. *J.C.S. CHEM. COMM.* **1976**, *20*, 830-831
(70) Fernández-Gacio, A.; Codina, A.; Fastrez, J.; Riant, O.; Soumillion, P. Transforming Carbonic Anhydrase into Epoxide Synthase by Metal Exchange *ChemBioChem* **2006**, *7*, 1013-1016
(71) Key, H. M.; Clark, D. S.; Hartwig, J. F. Generation, Characterization, and Tunable Reactivity of Organometallic Fragments Bound to a Protein Ligand. *J. Am. Chem. Soc.* **2015**, *137* (25), 8261–8268.
(72) Matsuo, T.; Murata, D.; Hisaeda, Y.; Hori, H.; Hayashi, T. Porphyrinoid Chemistry in Hemoprotein Matrix: Detection and Reactivities of Iron(IV)-Oxo Species of Porphycene Incorporated into Horseradish Peroxidase. *J. Am. Chem. Soc.* **2007**, *129* (43), 12906–12907.

(73) Sommer, D. J.; Vaughn, M. D.; Ghirlanda, G. Protein Secondary-Shell Interactions Enhance the Photoinduced Hydrogen Production of Cobalt Protoporphyrin IX. *Chem Commun* **2014**, *50* (100), 15852–15855..
(74) Key, H. M.; Dydio, P.; Clark, D. S.; Hartwig, J. F. Abiological Catalysis by Artificial Haem Proteins Containing Noble Metals in Place of Iron. *Nature* **2016**, *534* (7608), 534–537.
(75) Key, H. M.; Dydio, P.; Liu, Z.; Rha, J. Y.-E.; Nazarenko, A.; Seyedkazemi, V.; Clark, D. S.; Hartwig, J. F. Beyond Iron: Iridium-Containing P450 Enzymes for Selective Cyclopropanations of Structurally Diverse Alkenes. *ACS Cent. Sci.* **2017**, *3* (4), 302–308..
(76) Huang, J.; Quest, A.; Cruz-Morales, P.; Deng, K.; Pereira, J. H.; Van Cura, D.; Kakumanu, R.; Baidoo, E. E. K.; Dan, Q.; Chen, Y.; Petzold, C. J.; Northen, T. R.; Adams, P. D.; Clark, D. S.; Balskus, E. P.; Hartwig, J. F.; Mukhopadhyay, A.; Keasling, J. D. Complete Integration of Carbene-Transfer Chemistry into Biosynthesis. *Nature* **2023**, *617* (7960), 403–408.
(77) Liu, Z.; Huang, J.; Gu, Y.; Clark, D. S.; Mukhopadhyay, A.; Keasling, J. D.; Hartwig, J. F. Assembly and Evolution of Artificial Metalloenzymes within *E. Coli* Nissle 1917 for Enantioselective and Site-Selective Functionalization of C─H and C═C Bonds. *J. Am. Chem. Soc.* **2022**, *144* (2), 883–890.
(78) Reetz, M. T.; Rentzsch, M.; Pletsch, A.; Maywald, M.; Maiwald, P.; Peyralans, J. J.-P.; Maichele, A.; Fu, Y.; Jiao, N.; Hollmann, F.; Mondière, R.; Taglieber, A. Directed Evolution of Enantioselective Hybrid Catalysts: A Novel Concept in Asymmetric Catalysis. *Tetrahedron* **2007**, *63* (28), 6404–6414.
(79) Ueno, T.; Suzuki, M.; Goto, T.; Matsumoto, T.; Nagayama, K.; Watanabe, Y. Size-Selective Olefin Hydrogenation by a Pd Nanocluster Provided in an Apo-Ferritin Cage. *Angew. Chem.* **2004**, *116* (19), 2581–2584.
(80) Letondor, C.; Humbert, N.; Ward, T. R. Artificial Metalloenzymes Based on Biotin-Avidin Technology for the Enantioselective Reduction of Ketones by Transfer Hydrogenation. *Proc. Natl. Acad. Sci.* **2005**, *102* (13), 4683–4687.
(81) Schwizer, F.; Köhler, V.; Dürrenberger, M.; Knörr, L.; Ward, T. R. Genetic Optimization of the Catalytic Efficiency of Artificial Imine Reductases Based on Biotin–Streptavidin Technology. *ACS Catal.* **2013**, *3* (8), 1752–1755.
(82) Dürrenberger, M.; Heinisch, T.; Wilson, Y. M.; Rossel, T.; Nogueira, E.; Knörr, L.; Mutschler, A.; Kersten, K.; Zimbron, M. J.; Pierron, J.; Schirmer, T.; Ward, T. R. Artificial Transfer Hydrogenases for the Enantioselective Reduction of Cyclic Imines. *Angew. Chem. Int. Ed.* **2011**, *50* (13), 3026–3029.
(83) Heinisch, T.; Langowska, K.; Tanner, P.; Reymond, J.-L.; Meier, W.; Palivan, C.; Ward, T. R. Fluorescence-Based Assay for the Optimization of the Activity of Artificial Transfer Hydrogenase within a Biocompatible Compartment. *ChemCatChem* **2013**, *5* (3), 720–723.
(84) Thomas, C. M.; Letondor, C.; Humbert, N.; Ward, T. R. Aqueous Oxidation of Alcohols Catalyzed by Artificial Metalloenzymes Based on the Biotin–Avidin Technology. *J. Organomet. Chem.* **2005**, *690* (20), 4488–4491.
(85) Raffy, Q.; Ricoux, R.; Mahy, J.-P. Synthesis of a New Estradiol–Iron Metalloporphyrin Conjugate Used to Build up a New Hybrid Biocatalyst for Selective Oxidations by the 'Trojan Horse' Strategy. *Tetrahedron Lett.* **2008**, *49* (11), 1865–1869.
(86) Okrasa, K.; Kazlauskas, R. J. Manganese-Substituted Carbonic Anhydrase as a New Peroxidase. *Chem. – Eur. J.* **2006**, *12* (6), 1587–1596.

(87) Köhler, V.; Mao, J.; Heinisch, T.; Pordea, A.; Sardo, A.; Wilson, Y. M.; Knörr, L.; Creus, M.; Prost, J.-C.; Schirmer, T.; Ward, T. R. OsO4·Streptavidin: A Tunable Hybrid Catalyst for the Enantioselective Cis-Dihydroxylation of Olefins. *Angew. Chem.* **2011**, *123* (46), 11055–11058.
(88) Cochran, A. G.; Schultz, P. G. Peroxidase Activity of an Antibody-Heme Complex. *J. Am. Chem. Soc.* **1990**, *112* (25), 9414–9415.
(89) Hayashi, T.; Murata, D.; Makino, M.; Sugimoto, H.; Matsuo, T.; Sato, H.; Shiro, Y.; Hisaeda, Y. Crystal Structure and Peroxidase Activity of Myoglobin Reconstituted with Iron Porphycene. *Inorg. Chem.* **2006**, *45* (26), 10530–10536.
(90) Oohora, K.; Onoda, A.; Hayashi, T. Hemoproteins Reconstituted with Artificial Metal Complexes as Biohybrid Catalysts. *Acc. Chem. Res.* **2019**, *52* (4), 945–954.
(91) Ueno, T.; Koshiyama, T.; Abe, S.; Yokoi, N.; Ohashi, M.; Nakajima, H.; Watanabe, Y. Design of Artificial Metalloenzymes Using Non-Covalent Insertion of a Metal Complex into a Protein Scaffold. *J. Organomet. Chem.* **2007**, *692* (1–3), 142–147.
(92) Liu, X.; Yu, Y.; Hu, C.; Zhang, W.; Lu, Y.; Wang, J. Significant Increase of Oxidase Activity through the Genetic Incorporation of a Tyrosine–Histidine Cross-Link in a Myoglobin Model of Heme–Copper Oxidase. *Angew. Chem. Int. Ed.* **2012**, *51* (18), 4312–4316.
(93) Abe, S.; Niemeyer, J.; Abe, M.; Takezawa, Y.; Ueno, T.; Hikage, T.; Erker, G.; Watanabe, Y. Control of the Coordination Structure of Organometallic Palladium Complexes in an Apo-Ferritin Cage. *J. Am. Chem. Soc.* **2008**, *130* (32), 10512–10514.
(94) Pierron, J.; Malan, C.; Creus, M.; Gradinaru, J.; Hafner, I.; Ivanova, A.; Sardo, A.; Ward, T. R. Artificial Metalloenzymes for Asymmetric Allylic Alkylation on the Basis of the Biotin–Avidin Technology. *Angew. Chem. Int. Ed.* **2008**, *47* (4), 701–705.
(95) Filice, M.; Romero, O.; Aires, A.; Guisan, J. M.; Rumbero, A.; Palomo, J. M. Preparation of an Immobilized Lipase-Palladium Artificial Metalloenzyme as Catalyst in the Heck Reaction: Role of the Solid Phase. *Adv. Synth. Catal.* **2015**, *357* (12), 2687–2696.
(96) Natoli, S. N.; Hartwig, J. F. Noble−Metal Substitution in Hemoproteins: An Emerging Strategy for Abiological Catalysis. *Acc. Chem. Res.* **2019**, *52* (2), 326–335.
(97) Gu, Y.; Bloomer, B. J.; Liu, Z.; Chen, R.; Clark, D. S.; Hartwig, J. F. Directed Evolution of Artificial Metalloenzymes in Whole Cells. *Angew. Chem.* **2022**, *134* (5), e202110519.
(98) Mayer, C.; Gillingham, D. G.; Ward, T. R.; Hilvert, D. An Artificial Metalloenzyme for Olefin Metathesis. *Chem. Commun.* **2011**, *47* (44), 12068.
(99) Okrasa, K.; Kazlauskas, R. J. Manganese-Substituted Carbonic Anhydrase as a New Peroxidase. *Chem.Eur. J.* **2006**, *12*, 1587-1596

Chapter 2

Abiotic Reduction of Dialkyl Ketones Catalyzed by Carbonic Anhydrase

2.1 Introduction

Unnatural biocatalytic reactions can be achieved by exploiting the promiscuity of existing enzymes or by conducting extensive directed evolution to forge active sites suitable for unnatural reactants.[1–4] Rarely does an enzyme catalyze a process that is far from that of the native function and rarely do enzymes catalyze reactions with a broad scope of substrates.

We recently reported the reduction of aryl ketones catalyzed by carbonic anhydrase.[5] This reaction was noteworthy because our mechanistic data implied the intermediacy of a monomeric zinc hydride, and monomeric metal-hydrides, particularly of electrophilic metal centers, are rare or unknown in biology.[6,7] It was also noteworthy because this enzyme has evolved to catalyze the hydrolysis of achiral carbon dioxide to form achiral carbonic acid.[8,9]

The chiral benzylic alcohols formed by this ketone reduction and hydrolysis are components of pharmaceuticals (Figure 1a).[10–12] Dialkyl carbinols are also common structures in biological active compounds, but the asymmetric reduction of dialkyl ketones to form them difficult to achieve with small molecule catalysts that must differentiate between sterically and electronically similar alkyl substituents;[13–16] only recently have catalysts reduced methyl alkyl ketones with ee values over 90%, and only with catalysts containing complex ligands.[17] Alcohol dehydrogenases (ADHs) reduce ketones to alcohols, but even individual enzymes and their accompanying cofactor regeneration systems[18] each react with limited scope.[19–21] Nevertheless, ADHs have been commercialized and cat-alyze reactions that produce pharmaceutical active ingredients at large scales[22–24] showing the value of enzymatic reductions of ketones.

We report the reduction of a wide scope of dialkyl ketones with high enantioselectivity by reduction catalyzed by wild type carbonic anhydrase or one double mutant with a larger binding site created to accommodate larger ketones. (Figure 1d) Remarkable enantioselectivities are achieved with ketones containing groups that would be seemingly impossible to differentiate by a small-molecule catalysts and that have not been shown previously to be differentiated by the various types of ketoreductases. Computational data explain the origins of high selectivity.

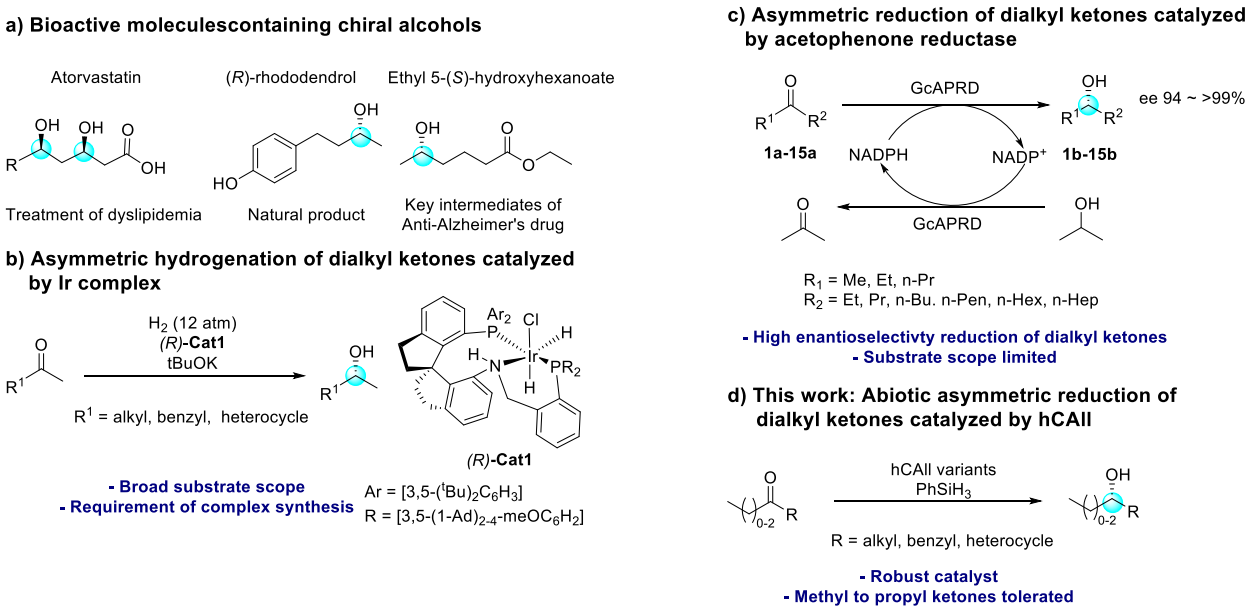

Figure 1. Chiral alcohols and catalytic asymmetric synthesis of chiral dialkyl alcohols. (a) Chiral alcohols in bioactive molecules (b) Asymmetric hydrogenation of dialkyl ketones catalyzed by an iridium complex (c) Asymmetric reduction of dialkyl ketones catalyzed by acetophenone reductase (d) Asymmetric reduction of dialkyl ketones catalyzed by hCAII

2.2 Results and Discussions

Our studies on the reduction of dialkyl ketones began with 2-heptanone, a simple dialkyl ketone, as the model substrate with phenylsilane as the reducing agent and purified wild-type, human carbonic anhydrase (wt hCAII) as catalyst. To our surprise, this reaction occurred in a high 99% yield and 99% enantioselectivity. The reaction was conducted at 50 mM concentration of ketone in tris buffer at pH 8.0 by simply adding neat substrates and phenylsilane to purified protein and shaking at room temperature for 16 h.

The scope of reduction of methyl alkyl ketones catalyzed by wt hCAII is broad and is shown in Scheme 1. Substrates with simple alkyl chains (**S1-S6**) underwent re-duction with high yields and excellent enantioselectivity. Evaluation of the chain length on the methyl ketones showed that those up to seven carbons reacted to full conversion. The ketone with a nonyl chain reacted to lower, albeit substantial, conversion, revealing the size of the substrate binding site. The ketone containing a more sterically demanding cyclohexyl methyl group (**S7**) reacted to lower yield, but with high enantioselectivity. Methyl ketones containing a chlorine, ether, ester, olefin, or alkyne functionality all reacted in high yield and enantioselectivity (**S8-S12**). Substituted arenes (**S13-S19**) and heterocyclic groups on the alkyl chain were also tolerated (**S20-S24**).Particularly noteworthy are reactions of ketones with heteroarenes bearing basic nitrogens, which often poison small-molecule, transition-metal catalysts. Reactions of enones also gave allylic alcohols with high enantiomeric excess.

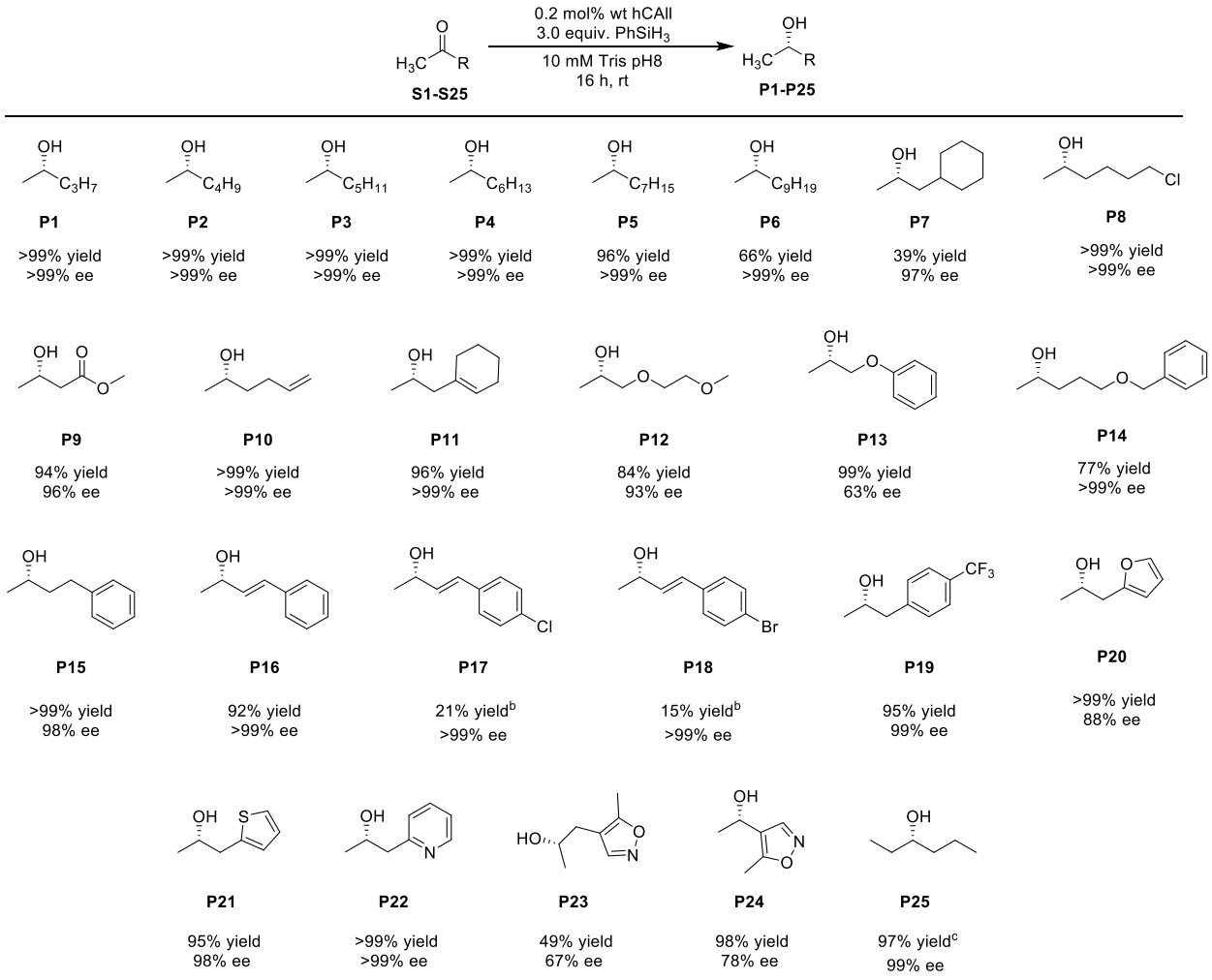

aStandard reaction conditions: 0.1 umol of hCAII, 2.0 mL of 10 mM tris pH 8.0 buffer, 50.0 umol of ketone, 150.0 umol of PhSiH3 (3.0 equiv versus ketone). Yields were determined by 1H NMR spectroscopy, enantiomeric excess was determined by chiral HPLC or GC. bThe substrate was dissolved in DMSO and added to the reaction as a stock solution. cThe reaction was conducted with 0.2 umol of wt hCAII

Scheme 1. Scope of the reduction of dialkyl ketones catalyzed by wt hCAII.[a]

Although wt hCAII catalyzed the reduction of methyl ketones (Figure 2 (Left), entry 1) with broad scope, reactions of ethyl ketones (Figure 2 (Left), entry 2) occurred to a lower 65% conversion, albeit with the same high enantioselectivity. Reactions of propyl ketones gave no product (Figure 2 (Left), entry 4). The selective binding of an ethyl vs propyl group by wt hCAII was demonstrated by the reduction of 3-hexanone, which gave (S)-3-hexanol in 99% ee (Scheme 1, S25). These data imply that the binding site of wt hCAII readily accommodates an acetyl unit, can accommodate a propionyl group, but binding of larger acyl groups is less favorable or prohibited.

Site-directed mutagenesis is a powerful tool to address the limitations of biocatalysts.[25–28] We mutated four amino acids (L204, V207, L198, W209) that are located on the upper loop embedded in the hydrophobic pocket to smaller ones to enable the protein to accommodate a larger ketone (Figure 2a). Because these four residues are embedded in the active site, mutants containing hydrophobic residues (A, L, V, I, F) at these sites were evaluated first. By decreasing the size of

the sidechain at the 209 position from tryptophan to leucine, the enzyme catalyzed the reaction of 3-octanone in 99% yield (entry 3) and with high (>99%) enantioselectivity. We note that the reaction was con-ducted under whole-cell conditions, resulting in consistent enantioselectivity and TTN what were 8-fold higher than those of the reaction catalyzed by the purified protein (60% yield, >99% ee). (See Figure S1 and Figure S2 for detail)

A second round of mutagenesis was conducted to im-prove enzyme performance toward 4-nonanone (Figure 2(Left), entry 5). Site saturation mutagenesis (SSM)[29–31] on all residues around the active site led to a variant (W209L/ V134I) that catalyzed the reduction of 4-nonanone with twice the activity as that of the single mutant (entry 6) and with over 99% ee with enzyme in intact E. coli.

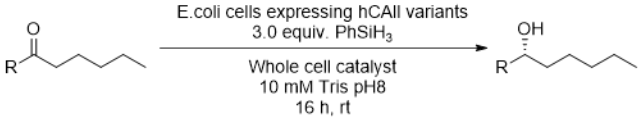

Entry	R	Variant	GC Conversion	e.e.
1	Me	wt	>99%	>99%
2	Et	wt	65%	>99%
3	Et	W209L	>99% (60%)[b]	>99% (99%)[b]
4	nPr	wt	0%	-
5	nPr	W209L	63%	>99%
6	nPr	W209L V134I	>99% (83%)[b]	>99% (99%)[b]

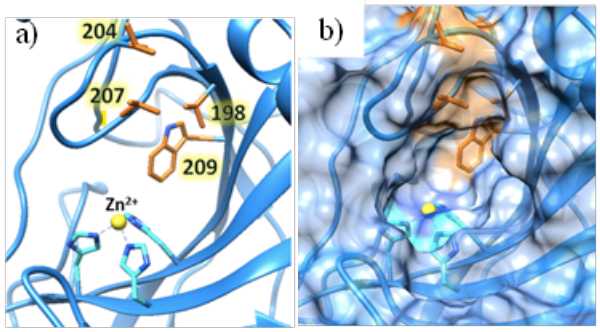

[a]Reaction catalyzed by purified protein.

Figure 2. (Left) Reduction of dialkyl ketones catalyzed by E. coli cells harboring hCAII variants.[a] (a) Amino acid positions targeted in evolution (orange) shown on the wt hCAII homology model (blue) in relation to the zinc metal center (yellow). (b) Protein surface shown to indicate the targeted amino acids lo-cated in the inner pocket of the active site of hCAII

The scope and limitations of the reactions catalyzed by the variants of hCAII are shown in Scheme 2. Dialkyl ketones with one long chain and one ethyl substituent underwent reduction in excellent yield with high enantioselectivity (S29-S31). Like the reactions of methyl ketones, the reactions of ethyl and propyl ketones tolerated various functional groups, including olefins (S36-S38), ethers (S40, 44), and heterocycles (S45- S47), to form the corresponding alcohols with good to excellent yields and enantioselectivities. Phenyl ethyl (S41) and benzyl ethyl ketones (S42) also were reduced to the corresponding alcohol with excellent ee and with moderate to excellent yield.

Dialkyl ketones possessing alkyl groups of similar size (S26-S28) are particularly difficult to reduce with high enantioselectivity with few examples.[19] Yet, hCAII variants catalyzed reduction of these substrates in excellent yield and enantioselectivity. For ex-ample, the reduction of 4-nonanone (S28) occurred to high conversion and with high enantioselectivity (>99% yield, >99% ee), showing that this mutant of hCAII can differentiate between a propyl and pentyl group. Even 3-hexanone (S27), which contains an ethyl and propyl group on the carbonyl unit reacted with a remarkably high enantioselectivity (97% ee) when catalyzed by the mutant containing alanine in place of leucine at position 209. The enantiodivergent reduction of a dialkyl ketone, 2-pentanone, also was achieved. The wild type hCAII formed (S)-2-pentanol (P25) as the major product (99%

yield, >99% ee), while the W209L mutant formed (R)-2-pentanol (P26) as the major product (99% yield, 65% ee).

Branched ketones (S32-S34) reacted with distinct yields and enantioselectivities. The α-branched ketone 2-methyl-3-penanone (S32) formed the corresponding alcohol in 85% yield, but with just 40% ee. We hypothesized that the ethyl and isopropyl moieties in the α-branched ketone have sufficiently similar size to fit in the active site with both orientations to form the two enantiomers (Figure S3). The β-branched ketone 5-methyl-3-hexanone (S33) converted to the corresponding alcohol in 50% yield and with a higher 75% ee, due to diminishing of the hydrogen bonding between T199 and the carbonyl group, which is a critical interaction for the reduction to occur.5 (Figure S4a) In contrast, the γ-branched ketone 6-methyl-3-heptanone (S34) converted to the corresponding alcohol in excellent 85% yield and 97% ee, due to the presence of hydrogen bonding be-tween T199 and the carbonyl group, as indicated by the pose of the ketone in the computational docking model. (Figure S4b)

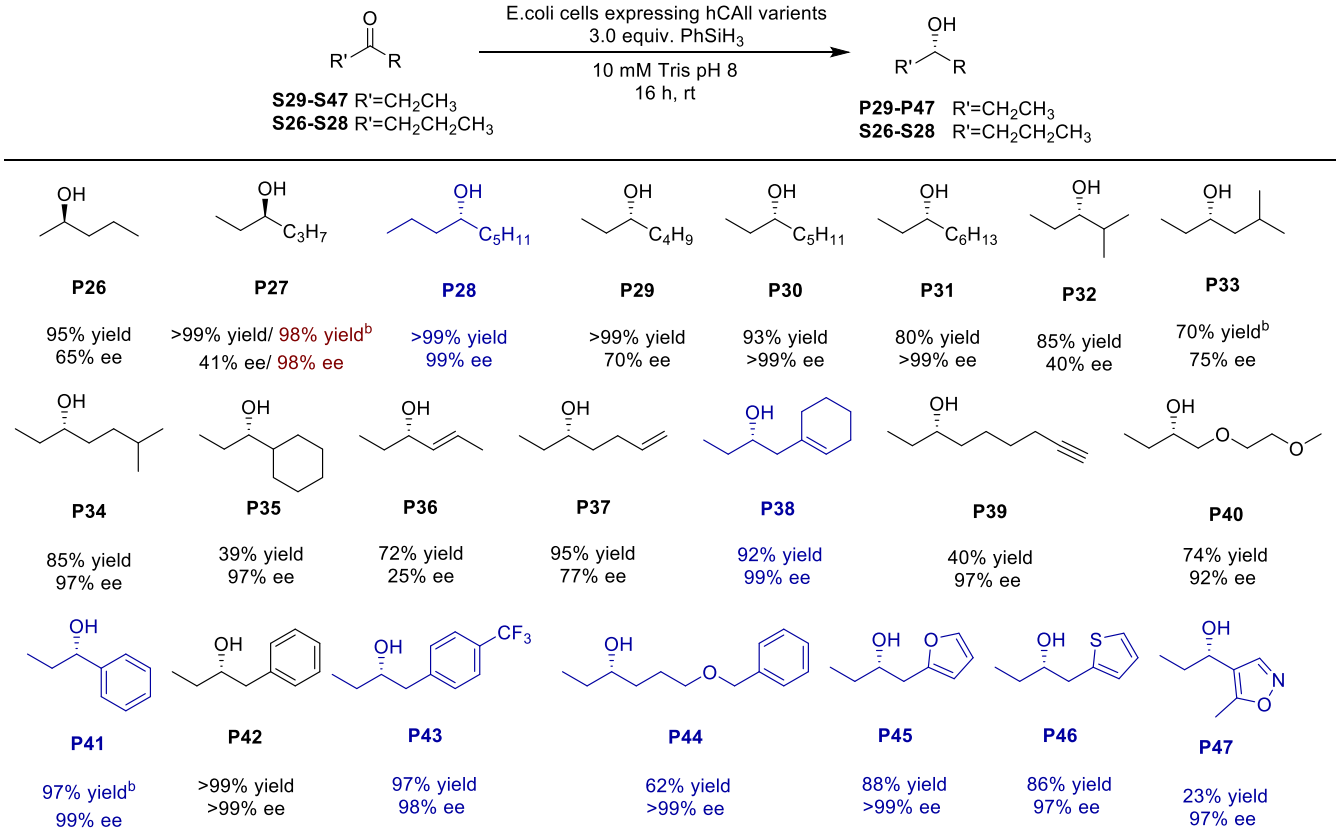

[a]Standard reaction conditions: 10 mL culture of hCAII variants expressed with E. coli, 2.0 mL of 10 mM tris pH 8.0 buffer, 50.0 umol of ketone, 150.0 umol of $PhSiH_3$ (3.0 equiv with respect to ketone). Entries colored in black were conducted with hCAII variant W209L; blue with hCAII variant W209L/V134I; and red with hCAII variant W209A. [b]The reaction was conducted with 20 mL culture of hCAII variants.

Scheme 2. Scope of the reduction of 2-, 3-, and 4-alkanones.

The reduction can be conducted on multi-millimole scale with purified protein or protein in whole cells (Scheme 3). The reaction of 2.5 mmol of 2-heptanone with purified, wild type hCAII formed

P4 in high yield and enantioselectivity, as shown in Scheme 3A (82% yield, >99% ee). The reactions also can be conducted on multi-millimole scale with whole cells. The reaction of 3-octanone shown in Scheme 3B catalyzed by the enzyme in whole E. coli cells on a 4.8 mmol scale formed alcohol P29 in excellent yield and selectivity (86% yield, >99% ee). The yield and enantioselectivity for reaction of 2-heptanone on this scale is comparable to that from small scale reactions with purified protein (99% yield, >99% ee), and the reaction of 3-octanone is comparable to that of the reaction catalyzed by the enzyme in whole cells in small scale (99% yield, >99% ee).

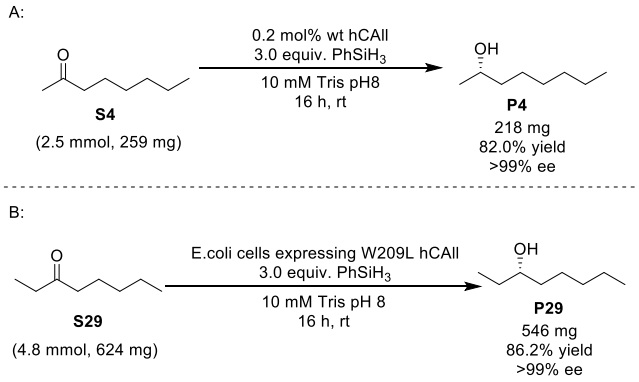

[a]Reactions by A: Purified protein and B: Whole Cell.

Scheme 3. Reductions of dialkyl ketones on multi-mmol scale.

To elucidate the origins of enantioselectivity and effect of mutations, we investigated the structural differ-ences between wt hCAII and the W209 variant. By expanding the size of the active size, we hypothesized that 4-nonanone would lie deeper in the active site of the W209L mutant of hCAII than it did in the wt hCAII. To test the hypothesis, we docked 4-nonanone to both wild type hCAII (4-nonanone in white) and W209L hCAII (4-nonanone in gray). (Figure 3). The W209L mutant contains a deep pocket in the active site that allows 4-nonanone to bind with the propyl moiety embedded within the enzyme and the carbonyl of 4-nonanone to approach the zinc hydride. This binding mode contrasts that for binding of 4-nonanone to wt hCAII. 4-Nonanone appears to bind to the surface of the protein at a position distal from the zinc hydride. Thus, the difference in the reactivity of the variants towards 4-nonanone can be rationalized by the hydride — C=O distance, which is 3.97 Å in wt hCAII and 3.73 Å in W209L hCAII. These computations support our hypothesis that the W209L mutation creates a pocket to accommodate the large propyl moiety of 4-nonanone.

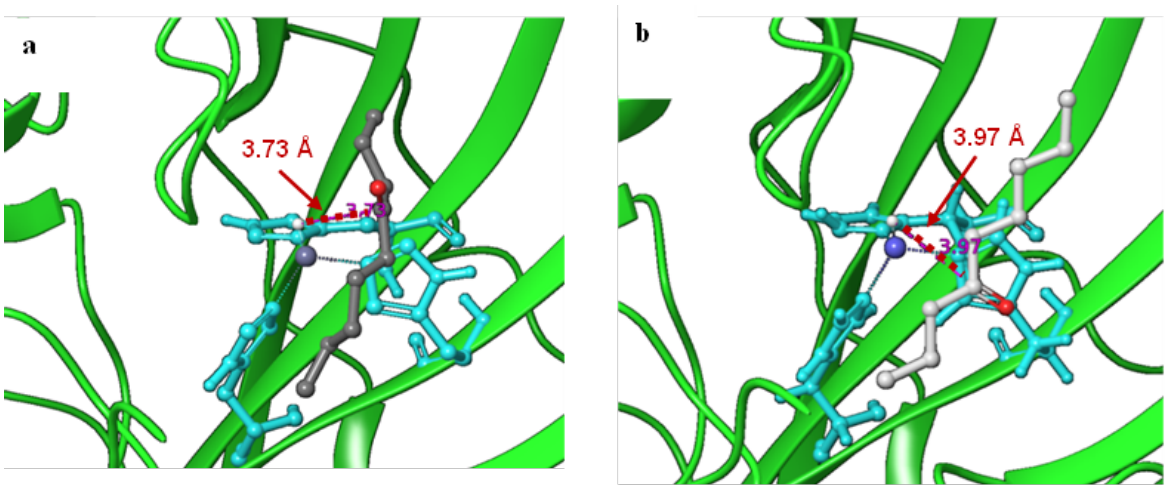

Figure 3. Computational study of the substrate selectivity of the variants of hCAII a. the docking modes of 4-nonanone in W209L hCAII b. the docking modes of 4-nonanone in wt hCAII. All distances between atoms are shown in Å.

2.3 Conclusion

Our studies show that an enzyme whose native function is to catalyze the reaction of an achiral substrate with water to form an achiral product can catalyze the reduction of nearly symmetrical dialkyl ketones with high reactivity and enantioselectivity via a zinc-hydride intermediate.Furthermore, site-directed mutagenesis generates new variants of hCAII that overcome the limitations in scope of the wild-type protein. The system tolerates a broad range of sizes and auxiliary functionality of the substrates, while differentiating substituents with steric properties as similar as pentyl and ethyl or pentyl and propyl groups. The broad scope of substrates that react suggest that this system could become a synthetically viable approach to prepare enantioenriched secondary aliphatic alcohols as pharmaceutical building blocks.

2.4 Experimental Information

2.4.1 General information

Unless otherwise noted, all chemicals, salts and solvent were obtained from commercial suppliers (Sigma-Aldrich, Acros, etc.) and used without further purification. ^{1}H and ^{13}C NMR spectra were recorded on NEO-500 MHz or Bruker AV-600 MHz spectrometers. Chemical shifts (δ) are reported in ppm relative to the residual solvent signal (CDCl3: 7.26 ppm for ^{1}H NMR and 77.16 ppm for ^{13}C NMR spectroscopy). NMR multiplicities are abbreviated as follows: s = singlet, d = doublet, t= triplet, q = quartet, pent = pentet, sext = sextet, dd = doublet of doublets, td = triplet of doublets, m = multiples, br = broad signal. All expression media and buffers were prepared with ddH_2O (MilliQ A10 Advantage purification system, Millipore). Expression media was sterilized either by autoclave (20 min, 121 °C) or a sterile syringe filter (0.22 um). To maintain sterile conditions, sterile materials and E. coli cells were manipulated near a lit Bunsen burner. Oligonucleotides were obtained from Integrated DNA Technologies. Enzymes and reagents used for cloning were obtained from New England BioLabs and Thermo Fisher Scientific.

2.4.2 Experimental procedures

2.4.2.1 *E.coli* strains and expression plasmids

The plasmid encoding wild type hCAII (UniProt ID P00918) was prepared by the procedure previously reported by our group.[5,32]

The highlight letters indicate the residues that were mutated compared to the wt hCAII sequence.

DNA Sequence of hCAII

ATGAAATCTTCTCACCATCACCATCACCATGAAAACCTGTACTTCCAATCCAATGCA
ATGTCCCATCACTGGGGGTACGGCAAACACAACGGACCTGAGCATTGGCATAAGGA
CTTCCCCATTGCCAAGGGAGAGCGCCAGTCCCCTGTTGACATCGACACTCACACAGC
CAAGTATGACCCTTCCCTGAAGCCCCTGTCTGTTTCCTATGATCAAGCAACTTCCCTG
AGGATCCTCAACAATGGTCATGCTTTCAACGTGGAGTTTGATGACTCTCAGGACAAA
GCAGTGCTCAAGGGAGGACCCCTGGATGGCACTTACAGATTGATTCAGTTTCACTTT
CACTGGGGTTCACTTGATGGACAAGGTTCAGAGCATACTGTGGATAAAAAGAAATA
TGCTGCAGAACTTCACTTGGTTCATTGGAACACCAAATATGGGGATTTTGGGAAAGC
TGTGCAGCAACCTGATGGACTGGCCGTTCTAGGTATTTTTTTGAAGGTTGGCAGCGC
TAAACCGGGCCTTCAGAAAGTTGTTGATGTGCTGGATTCCATTAAAACAAAGGGCA
AGAGTGCTGACTTCACTAACTTCGATCCTCGTGGCCTCCTTCCTGAATCCCTGGATTA
CTGGACCTACCCAGGCTCACTGACCACCCCTCCTCTTCTGGAATGTGTGACCTGGAT
TGTGCTCAAGGAACCCATCAGCGTCAGCAGCGAGCAGGTGTTGAAATTCCGTAAAC
TTAACTTCAATGGGGAGGGTGAACCCGAAGAACTGATGGTGGACAACTGGCGCCCA
GCTCAGCCACTGAAGAACAGGCAAATCAAAGCTTCCTTCAAATAA

Protein Sequence of hCAII

MKSSHHHHHHENLYFQSNAMSHHWGYGKHNGPEHWHKDFPIAKGERQSPVDIDTHTA
KYDPSLKPLSVSYDQATSLRILNNGHAFNVEFDDSQDKAVLKGGPLDGTYRLIQFHFHW
GSLDGQGSEHTVDKKKYAAELHLVHWNTKYGDFGKAVQQPDGLAVLGIFLKVGSAKP
GLQKVVDVLDSIKTKGKSADFTNFDPRGLLPESLDYWTYPGSLTTPPLLECVTWIVLKEP
ISVSSEQVLKFRKLNFNGEGEPEELMVDNWRPAQPLKNRQIKASFK*

2.4.2.2 hCAII library and protein sequences

KOD Hot Start Master Mix was used to amplify the parent plasmid with primers containing NNK codons at the target sites. After DpnI digestion, the PCR product was transformed into XL1-blue cells. DNA extraction and sequencing was conducted by UC Berkeley DNA Sequencing Facility.

First-round	Primer sequence
L204NNK-F	CCT CCT CTT **NNK** GAA TGT GTG ACC TGG ATT G
L204NNK-R	CAC ACA TTC **MNN** AAG AGG AGG GGT G
L198NNK-F	AGG CTC A**NN K**AC CAC CCC TCC
L198NNK-R	GTG GT**M NN**T GAG CCT GGG TAG GT
W209NNK-F	GTG TGA CC**N NK**A TTG TGC TCA AGG AA

W209NNK-R	AGC ACA AT**M** **NN**G GTC ACA CAT TCC AGA
V207NNK -F	GGA ATG T**NN** **K**AC CTG GAT TGT GCT CA
V207NNK -R	CAA TCC AGG T**MN** **N**AC ATT CCA GAA GAG G

DNA sequence of W209L hCAII

ATGAAATCTTCTCACCATCACCATCACCATGAAAACCTGTACTTCCAATCCAATGCA
ATGTCCCATCACTGGGGGTACGGCAAACACAACGGACCTGAGCATTGGCATAAGGA
CTTCCCCATTGCCAAGGGAGAGCGCCAGTCCCCTGTTGACATCGACACTCACACAGC
CAAGTATGACCCTTCCCTGAAGCCCCTGTCTGTTTCCTATGATCAAGCAACTTCCCTG
AGGATCCTCAACAATGGTCATGCTTTCAACGTGGAGTTTGATGACTCTCAGGACAAA
GCAGTGCTCAAGGGAGGACCCCTGGATGGCACTTACAGATTGATTCAGTTTCACTTT
CACTGGGGTTCACTTGATGGACAAGGTTCAGAGCATACTGTGGATAAAAAGAAATA
TGCTGCAGAACTTCACTTGGTTCATTGGAACACCAAATATGGGGATTTTGGGAAAGC
TGTGCAGCAACCTGATGGACTGGCCGTTCTAGGTATTTTTTTGAAGGTTGGCAGCGC
TAAACCGGGCCTTCAGAAAGTTGTTGATGTGCTGGATTCCATTAAAACAAAGGGCA
AGAGTGCTGACTTCACTAACTTCGATCCTCGTGGCCTCCTTCCTGAATCCCTGGATTA
CTGGACCTACCCAGGCTCACTGACCACCCCTCCTCTTCTGGAATGTGTGACCTTGATT
GTGCTCAAGGAACCCATCAGCGTCAGCAGCGAGCAGGTGTTGAAATTCCGTAAACT
TAACTTCAATGGGGAGGGTGAACCCGAAGAACTGATGGTGGACAACTGGCGCCCAG
CTCAGCCACTGAAGAACAGGCAAATCAAAGCTTCCTTCAAATAAT

Protein sequence of W209L hCAII

MKSSHHHHHHENLYFQSNAMSHHWGYGKHNGPEHWHKDFPIAKGERQSPVDIDTHTA
KYDPSLKPLSVSYDQATSLRILNNGHAFNVEFDDSQDKAVLKGGPLDGTYRLIQFHFHW
GSLDGQGSEHTVDKKKYAAELHLVHWNTKYGDFGKAVQQPDGLAVLGIFLKVGSAKP
GLQKVVDVLDSIKTKGKSADFTNFDPRGLLPESLDYWTYPGSLTTPPLLECVTLIVLKEPI
SVSSEQVLKFRKLNFNGEGEPEELMVDNWRPAQPLKNRQIKASFK*

DNA sequence of W209A hCAII

ATGAAATCTTCTCACCATCACCATCACCATGAAAACCTGTACTTCCAATCCAATGCA
ATGTCCCATCACTGGGGGTACGGCAAACACAACGGACCTGAGCATTGGCATAAGGA
CTTCCCCATTGCCAAGGGAGAGCGCCAGTCCCCTGTTGACATCGACACTCACACAGC
CAAGTATGACCCTTCCCTGAAGCCCCTGTCTGTTTCCTATGATCAAGCAACTTCCCTG
AGGATCCTCAACAATGGTCATGCTTTCAACGTGGAGTTTGATGACTCTCAGGACAAA
GCAGTGCTCAAGGGAGGACCCCTGGATGGCACTTACAGATTGATTCAGTTTCACTTT
CACTGGGGTTCACTTGATGGACAAGGTTCAGAGCATACTGTGGATAAAAAGAAATA
TGCTGCAGAACTTCACTTGGTTCATTGGAACACCAAATATGGGGATTTTGGGAAAGC

TGTGCAGCAACCTGATGGACTGGCCGTTCTAGGTATTTTTTTGAAGGTTGGCAGCGC
TAAACCGGGCCTTCAGAAAGTTGTTGATGTGCTGGATTCCATTAAAACAAAGGGCA
AGAGTGCTGACTTCACTAACTTCGATCCTCGTGGCCTCCTTCCTGAATCCCTGGATTA
CTGGACCTACCCAGGCTCACTGACCACCCCTCCTCTTCTGGAATGTGTGACCGCTAT
TGTGCTCAAGGAACCCATCAGCGTCAGCAGCGAGCAGGTGTTGAAATTCCGTAAAC
TTAACTTCAATGGGGAGGGTGAACCCGAAGAACTGATGGTGGACAACTGGCGCCCA
GCTCAGCCACTGAAGAACAGGCAAATCAAAGCTTCCTTCAAATAA

Protein sequence of W209A hCAII

MKSSHHHHHHENLYFQSNAMSHHWGYGKHNGPEHWHKDFPIAKGERQSPVDIDTHTA
KYDPSLKPLSVSYDQATSLRILNNGHAFNVEFDDSQDKAVLKGGPLDGTYRLIQFHFHW
GSLDGQGSEHTVDKKKYAAELHLVHWNTKYGDFGKAVQQPDGLAVLGIFLKVGSAKP
GLQKVVDVLDSIKTKGKSADFTNFDPRGLLPESLDYWTYPGSLTTPPLLECVTAIVLKEPI
SVSSEQVLKFRKLNFNGEGEPEELMVDNWRPAQPLKNRQIKASFK*

Second-round	Primer sequence
RC335-F131NNK-F	GGG ATN **NK**G GGA AAG CTG TGC AG
RC335-F131NNK-R	CAG CTT TCC C**MN** **N**AT CCC CAT ATT TG
RC335-V134NNK-F	GGG AAA GCT **NNK** CAG CAA CCT GAT
RC335-V134NNK-R	AGG TTG CTG **MNN** AGC TTT CCC AAA ATC
RC335-L141NNK-F	CCT GAT GGA **NNK** GCC GTT CTA GGT ATT TTT TT
RC335-L141NNK-R	TAG AAC GG**M** **NN**C TCC ATC AGG TTG
RC335-V143NNK-F	GGA CTG GCC **NNK** CTA GGT ATT TTT TTG AAG
RC335-V143NNK-R	AAA TAC CTA G**MM** **N**GG CCA GTC CAT CA

DNA sequence of W209L/V134I hCAII

ATGAAATCTTCTCACCATCACCATCACCATGAAAACCTGTACTTCCAATCCAATGCA
ATGTCCCATCACTGGGGGTACGGCAAACACAACGGACCTGAGCATTGGCATAAGGA
CTTCCCCATTGCCAAGGGAGAGCGCCAGTCCCCTGTTGACATCGACACTCACACAGC
CAAGTATGACCCTTCCCTGAAGCCCCTGTCTGTTTCCTATGATCAAGCAACTTCCCTG
AGGATCCTCAACAATGGTCATGCTTTCAACGTGGAGTTTGATGACTCTCAGGACAAA
GCAGTGCTCAAGGGAGGACCCCTGGATGGCACTTACAGATTGATTCAGTTTCACTTT
CACTGGGGTTCACTTGATGGACAAGGTTCAGAGCATACTGTGGATAAAAAGAAATA
TGCTGCAGAACTTCACTTGGTTCATTGGAACACCAAATATGGGGATTTTGGGAAAGC
TATTCAGCAACCTGATGGACTGGCCGTTCTAGGTATTTTTTTGAAGGTTGGCAGCGC
TAAACCGGGCCTTCAGAAAGTTGTTGATGTGCTGGATTCCATTAAAACAAAGGGCA
AGAGTGCTGACTTCACTAACTTCGATCCTCGTGGCCTCCTTCCTGAATCCCTGGATTA
CTGGACCTACCCAGGCTCACTGACCACCCCTCCTCTTCTGGAATGTGTGACCTTGATT
GTGCTCAAGGAACCCATCAGCGTCAGCAGCGAGCAGGTGTTGAAATTCCGTAAACT
TAACTTCAATGGGGAGGGTGAACCCGAAGAACTGATGGTGGACAACTGGCGCCCAG
CTCAGCCACTGAAGAACAGGCAAATCAAAGCTTCCTTCAAATA

Protein sequence of W209L/V134I hCAII

MKSSHHHHHHENLYFQSNAMSHHWGYGKHNGPEHWHKDFPIAKGERQSPVDIDTHTA
KYDPSLKPLSVSYDQATSLRILNNGHAFNVEFDDSQDKAVLKGGPLDGTYRLIQFHFHW
GSLDGQGSEHTVDKKKYAAELHLVHWNTKYGDFGKAIQQPDGLAVLGIFLKVGSAKP
GLQKVVDVLDSIKTKGKSADFTNFDPRGLLPESLDYWTYPGSLTTPPLLECVTLIVLKEPI
SVSSEQVLKFRKLNFNGEGEPEELMVDNWRPAQPLKNRQIKASFK

2.4.2.3 Protein expression and purification

Protein expression for purified protein reactions

hCAII was overexpressed in chemically competent Rosetta2 (DE3) pLysS *E. coli.* cells (obtained from UC Berkeley Macro Lab) with Luria Broth (LB) Media. Freshly transformed cells were plated on ampicillin/LB (100 mg/L) media and grown overnight at 37 °C in the oven. Single colonies were used to grow the starting culture in 5 mL LB/amp media, which were shaken at 37 °C overnight. Overnight culture was added to 4 × 1 L of LB/amp media and shaken at 37 °C/ 250 rpm for 8 h. After the optical density (OD) of cell culture was measured at 1.0 to 1.2, the temperature was reduced to 25 °C. The cell culture was induced with IPTG (1 mM/L) and shaken for additional 16 h. After this time, the cells were collected by centrifugation (5000 rpm, 15 minutes, 4 °C). Cell pellets were resuspended in Ni-NTA lysis buffer (50 mM NaPi, 300 mM NaCl, 10 mM imidazole, pH 8.0) and frozen at -80 °C.

Protein expression for whole-cell reactions

The hCAII starting culture was prepared identical to the previous culture described in *Protein expression for purified protein reactions.* To a 50 mL culture tube containing 10 mL of LB/amp media was added 50 µL of starting culture. The tube was covered with an air permeable membrane and shaken at 37 °C with 250 rpm for 8 h. After the optical density (OD) of cell culture was measured to be 1.0 to 1.2, the temperature was reduced to 25 °C. The cell culture was induced with IPTG (1 mM/L) and shaken for an additional 16 h. After this time, the cells were collected by centrifugation (10,000 rpm, 15 minutes, 4°C). LB media was discarded, and cells pellets were resuspended in 2 mL tris buffer (10 mM, pH 8.0) for whole-cell reactions.

Protein purification

Cell suspensions were thawed in a room-temperature water bath and transferred to a glass beaker. The cell suspensions were lysed on ice by sonication (5 × 10 min on, 5 × 10 min off, 60% amplitude) The cell debris was removed by centrifugation (10,000 rpm, 30 min, 4 °C), and Ni-NTA was added to the cell lysate. The lysate was mixed in Ni-NTA for 30 min at 4°C, and the resulting material poured onto a glass frit. The resin was washed with Ni-NTA lysis buffer twice and eluted with Ni-NTA elution buffer (50 mM NaPi, 250 mM NaCl, 250 mM Imidazole, pH = 8.0). The eluted protein was dialyzed against tris buffer twice (50 mM, pH = 8.0, 12 h/ 2h, 4 °C). The protein concentration was determined by measuring the absorption at 280 nm with a NanoDrop UV-vis spectrophotometer. The purified protein was divided into Eppendorf tubes (3 mg/tube) and stored at -80 °C.

2.4.2.4 Catalytic reactions

Reactions catalyzed by purified hCAII

The solution containing 1 μmol hCAII in tris buffer (10 mM, pH 8.0) was thawed to room temperature. To a 4 mL screw-capped glass vial was added the protein solution diluted with the same buffer to 2 mL (final concentration as 0.05 mM solution of hCAII) and followed by ketone (100 μmol) and phenylsilane (37 μL, 300 μmol). The reaction was conducted on an orbital shaker (20 °C, 300 rpm) for 16 h. After completion, the reaction mixture was extracted with 2 mL of $CDCl_3$ twice. To the chloroform solution was added mesitylene as the internal standard to calculate NMR yield. The yields were measured by ^1H NMR spectroscopy. The ee of the chiral alcohols were determined by gas chromatography (GC) after acetylation (**Ac**) with acetic anhydride with DMAP as base in DCM unless otherwise noted or high performance liquid chromatography (HPLC).

Reactions catalyzed by hCAII in whole *E. coli* cells

The amount of hCAII in whole *E. coli* cells was determined by SDS-PAGE stained by Coomassie blue and imaged by a Bio rad Gel Imaging System. A calibration curve to determine the concentration of purified wt hCAII was generated by analyzing the image of an SDS PAGE gel with four samples of varying protein concentration (2.2 mg/ mL, 1.1 mg/ mL, 0.55 mg/ mL, 0.275 mg/ mL, Figure S1). For the reactions, cell pellets from 10 mL-cultures were lysed with B-PER Bacterial Cell Lysis, and the protein concentration in the cell lysate was determined by running an SDS PAGE gel of the cell lysate and converting the image intensity to concentration with the calibration curve. The data were processed by ImageJ to subtract background noise from cell lysate and protein gel. (Figure S2.)

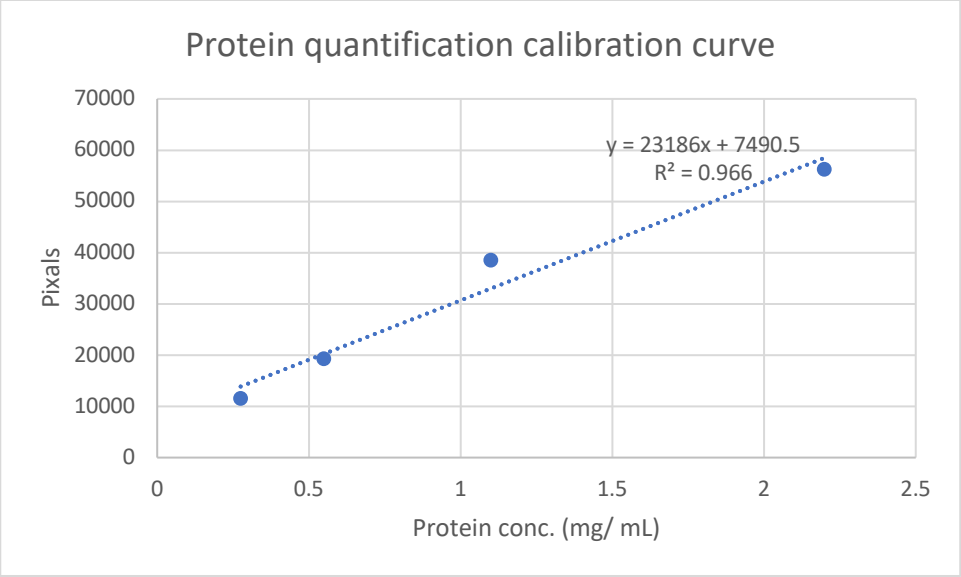

Figure S1. Calibration curved from SDS-PAGE of purified protein processed by ImageJ.

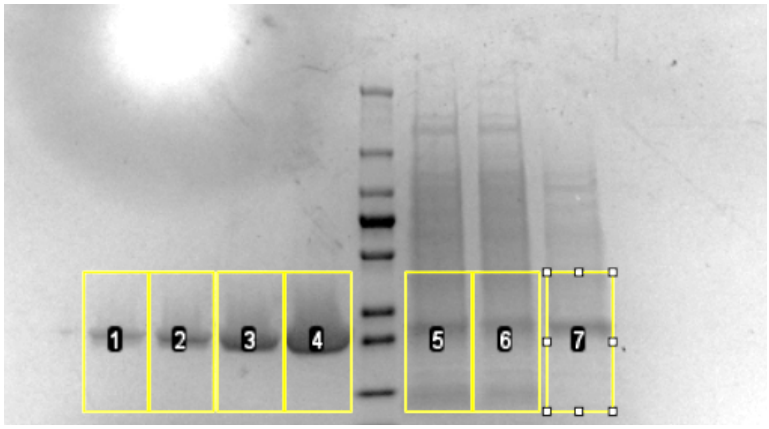

Figure S2. SDS-PAGE imaged by Bio rad Gel Imaging System and the selected area containing protein of interest and background for background subtraction by ImageJ.

The 10 mL-cultured cell pellets suspended in tris buffer (2 mL, 10 mM, pH 8.0) were transferred into 4 mL screw-capped glass vials. The ketone (100 µmol) and phenylsilane (37 µL, 300 µmol) were added to the cell solution. The resulting solution was allowed to react on an orbital shaker (20 °C, 300 rpm) for 16 h. After completion, the reaction mixture was extracted with 2 mL of $CDCl_3$ twice. To the chloroform solution was added mesitylene as the internal standard to calculate NMR yield. The yields were measured by ^1H NMR spectroscopy. The ee of the chiral alcohols were determined by gas chromatography (GC) after acetylation with acetic anhydride with DMAP as base in DCM, unless otherwise noted, or by high performance liquid chromatography (HPLC).

2.4.2.5 Preparation and Analytical Data of Substrates

General procedures for synthesis of ketones

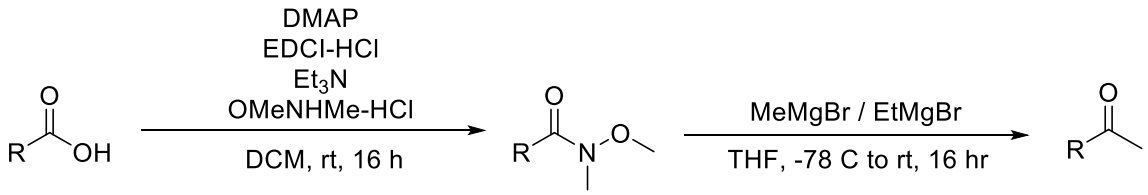

A previously reported procedure was followed.[17] To a 250 mL round-bottomed flask, the carboxylic acid (10 mmol), EDCI-HCl (2.9 g, 15 mmol, 1.5 equiv), NH(OMe)Me-HCl (1.5 g, 15 mmol, 1.5 equiv), DMAP (240 mg, 2 mmol, 0.2 equiv), and DCM (100 mL) were added sequentially, followed by Et_3N (2.8 mL, 20 mmol, 2.0 equiv). The reaction was stirred at room temperature for 16 h. Upon completion, the reaction mixture was diluted with 200 mL of H_2O and extracted with DCM (150 mL × 3). The combined organic layers were dried over Na_2SO_4, and the solvent was evaporated. The residue was purified by silica gel column chromatography with ethyl acetate/hexane as the elution solvent.

Synthesis of methyl ketones

To a 50 mL round-bottomed flask, the Weinreb amide (1.5 mmol) was dissolved in dried THF (15 mL) and cooled to -78 °C. The solution of amide was added the solution of MeMgBr (1.2 mL, 3 mmol, 2.5 M in THF, 2 equiv) dropwise. The reaction was stirred at -78 °C for 2 h and warmed to room temperature for another 14 h. Upon completion, the reaction was quenched with saturated aqueous NH_4Cl and extracted with DCM (30 mL × 3). The combined organic layers were dried over Na_2SO_4, and the solvent was evaporated. The residue was purified by silica gel column chromatography with ethyl acetate/hexanes as the elution solvent.

Synthesis of ethyl ketones

To a 50 mL round-bottomed flask, the Weinreb amide (1.5 mmol) was dissolved in dried THF (15 mL) and cooled to -78 °C. The solution of EtMgBr (1.0 mL, 3 mmol, 3.0 M in diethyl ether, 2 equiv) was added dropwise to the solution of amide. The reaction was stirred at -78 °C for 2 h and warmed to room temperature for another 14 h. Upon completion, the reaction was quenched with aqueous NH_4Cl and extracted with DCM (30 mL × 3). The combined organic layers were dried over Na_2SO_4, and the solvent was evaporated. The residue was purified by silica gel column chromatography with ethyl acetate/hexanes as the elution solvent.

Data for **S11**

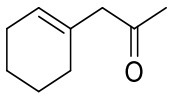

Following the general procedure for methyl ketones, a colorless oil was obtained (127 mg, 62% yield) with ethyl acetate/hexane (4:1) as the eluent.

Spectral data match those previously reported.

^{1}H NMR (600 MHz, $CDCl_3$) δ5.58-5.54 (m, 1H), δ3.00 (s, 2H), δ2.12 (s, 3H), δ2.06-2.01 (m, 2H), δ1.93-1.89 (m, 2H), δ1.65-1.59 (m, 2H), δ1.58-1.53 (m, 2H)

^{13}C NMR (151MHz, $CDCl_3$) δ208.05, 131.89, 126.44, 53.57, 29.13, 28.71, 25.53, 22.89, 22.13.

Data for **S12**

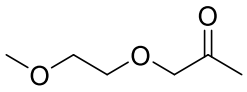

Following the general procedure for methyl ketones, a colorless oil (174 mg, 88% yield) was obtained with ethyl acetate/hexane (3:1) as the eluent.

^{1}H NMR (500 MHz, $CDCl_3$) δ4.11 (s, 2H), δ3.68-3.66 (m, 2H), δ3.59-3.57 (m, 2H), δ3.38 (s, 3H), δ2.15 (s, 3H)

^{13}C NMR (125 MHz, $CDCl_3$) δ207.02, 76.92, 72.13, 71.01, 59.19, 26.38

HR MS (pESI): calcd. For $C_6H_{13}O_3$ $[M+H]^+$: 133.08, found: 133.0859

Data for **S14**

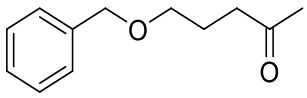

Following the general procedure for methyl ketones, a colorless oil (163 mg, 56% yield) was obtained with ethyl acetate/hexane (4:1) as the eluent.

Spectral data match those previously reported.[33]

^{1}H NMR (600 MHz, $CDCl_3$) δ7.37-7.28 (m, 5H), 4.50 (s, 2H), δ3.51 (t, J = 7.3 Hz, 2H), δ2.57 (t, J = 8.7 Hz, 2H), δ2.16 (s, 3H), δ1.93-1.90 (t, J = 8.1 Hz, 2H)

^{13}C NMR (151MHz, $CDCl_3$) δ208.80, 138.54, 128.52, 127.77, 127.72, 73.01, 69.41, 40.47, 30.11, 24.03

Data for **S19**

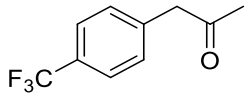

Following the general procedure for methyl ketones, a white solid (176 mg, 60% yield) was obtained with Ethyl acetate/hexane (4:1) as the eluent.

Spectral data match those previously reported.[34]

^{1}H NMR (600 MHz, $CDCl_3$) δ 7.66 – 7.55 (m, 2H), 7.35 – 7.29 (m, 2H), 3.78 (s, 2H), 2.20 (s, 3H).

^{13}C NMR (151 MHz, $CDCl_3$) δ 205.11, 138.21, 129.98, 125.82, 125.80, 125.77, 125.75, 50.56, 29.77.

Data for **S21**

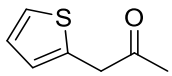

Following the general procedure for methyl ketones, a yellow oil was obtained (162 mg, 76% yield) with ethyl acetate/hexane (4:1) as the eluent.

Spectral data match those previously reported.[35]

^{1}H NMR (600 MHz, $CDCl_3$) δ7.23 (dd, J = 6.2, 1.5, 1Hf), δ6.98 (dd, J = 5.9, 4.0, 1H), δ6.90-6.88 (m, 1H), δ3.90 (s, 2H), δ2.21 (s, 3H)

^{13}C NMR (151MHz, $CDCl_3$) δ204.92, 135.37, 127.21, 126.99, 125.26, 44.59, 29.11

Data for **S23**

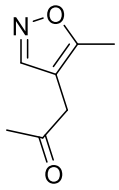

Following the general procedure for methyl ketones, a colorless oil was obtained (110 mg, 65% yield) with ethyl acetate/hexane (4:1) as the eluent.

^{1}H NMR (600 MHz, $CDCl_3$) δ 6.08 (s, 1H), 3.86 (s, 2H), 2.31 (s, 3H), 2.26 (s, 3H).

^{13}C NMR (151 MHz, $CDCl_3$) δ 201.42, 165.19, 160.24, 104.38, 41.48, 29.85, 29.40, 11.55.

HR MS (pESI): calcd. For $C_7H_{10}O_2N$ $[M+H]^+$: 140.06, found: 140.0706

Data for **S24**

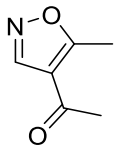

Following the general procedure for methyl ketones, a white solid was obtained (95 mg, 51% yield) with ethyl acetate/hexane (4:1) as the eluent.

Spectral data match those previously reported.[36]

^{1}H NMR (600 MHz, $CDCl_3$) δ 8.47 (s, 1H), 2.72 (s, 3H), 2.46 (s, 3H).

^{13}C NMR (151 MHz, $CDCl_3$) δ 191.29, 173.67, 149.72, 117.11, 29.17.

Data for **S38**

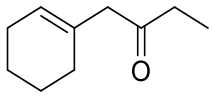

Following the general procedure for ethyl ketones, a colorless oil was obtained (141 mg, 62% yield) with ethyl acetate/hexane (4:1) as the eluent.

^{1}H NMR (600 MHz, $CDCl_3$) δ 5.53 (qd, J = 3.0, 1.4 Hz, 1H), 3.00 (d, J = 1.7 Hz, 2H), 2.45 (q, J = 7.3 Hz, 2H), 2.07 – 1.99 (m, 2H), 1.91 (td, J = 6.0, 2.6 Hz, 2H), 1.61 (qq, J = 5.0, 2.8 Hz, 2H), 1.58 – 1.53 (m, 2H), 1.03 (t, J = 7.3 Hz, 3H).

^{13}C NMR (151 MHz, $CDCl_3$) δ 210.51, 132.06, 126.14, 52.32, 35.05, 28.80, 25.54, 22.92, 22.16, 7.99.

HR MS (pESI): calcd. For $C_{10}H_{17}O$ $[M+H]^+$: 153.12, found: 153.1274

Data for **S39**

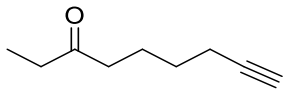

Following the general procedure for ethyl ketones, a colorless oil was obtained (65 mg, 35% yield) with ethyl acetate/hexane (4:1) as the eluent.

Spectral data match those previously reported.[37]

^{1}H NMR (600 MHz, $CDCl_3$) δ 2.42 (q, J = 7.3 Hz, 4H), 2.20 (td, J = 7.1, 2.7 Hz, 2H), 1.94 (d, J = 2.7 Hz, 1H), 1.73 – 1.66 (m, 2H), 1.56 – 1.48 (m, 2H), 1.05 (t, J = 7.3 Hz, 3H).

^{13}C NMR (151 MHz, $CDCl_3$) δ 211.26, 84.07, 68.51, 41.72, 35.88, 22.94, 22.69, 18.26, 7.83.

Data for **S43**

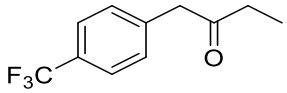

Following the general procedure for ethyl ketones, a white solid was obtained (87 mg, 29% yield) with ethyl acetate/hexane (4:1) as the eluent.

Spectral data match those previously reported.[38]

^{1}H NMR (600 MHz, $CDCl_3$) δ 7.61 (d, *J* = 8.0 Hz, 2H), 7.34 (d, *J* = 7.9 Hz, 2H), 3.79 (s, 2H), 2.53 (q, *J* = 7.3 Hz, 2H), 1.09 (t, *J* = 7.3 Hz, 3H).

^{13}C NMR (151 MHz, $CDCl_3$) δ 207.82, 129.95, 125.73, 125.70, 49.33, 35.86, 7.88.

Data for **S44**

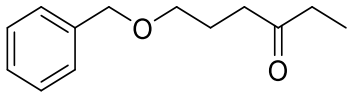

Following the general procedure for ethyl ketones, a colorless oil (174 mg, 56% yield) was obtained with ethyl acetate/hexane (4:1) as the eluent.

Spectral data match those previously reported.[39]

^{1}H NMR (600 MHz, $CDCl_3$) δ7.38-7.28 (m, 5H), 4.50 (s, 2H), δ3.50 (t, J = 7.4 Hz, 2H), δ2.54 (t, J = 8.7 Hz, 2H), δ2.44 (q, J= 8.8 Hz, 2H), δ1.93-1.90 (m, 2H), δ1.06 (t, J = 8.8, 3H)

^{13}C NMR (151 MHz, $CDCl_3$) δ211.46, 138.57, 128.51, 127.78, 127.71, 72.99, 69.52, 39.06, 36.10, 24.07, 7.96

Data for **S45**

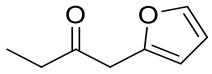

Following the general procedure for ethyl ketones, the reaction was quenched after 4 h at -78 °C, and a colorless oil was obtained (31 mg, 15% yield) with ethyl acetate/hexane (4:1) as the eluent.

Spectral data match those previously reported.[40]

^{1}H NMR (600 MHz, $CDCl_3$) δ 7.36 (dd, *J* = 1.9, 0.9 Hz, 1H), 6.34 (dd, *J* = 3.2, 1.9 Hz, 1H), 6.19 (dd, *J* = 3.2, 0.9 Hz, 1H), 3.70 (s, 2H), 2.47 (q, *J* = 7.3 Hz, 2H), 1.05 (t, *J* = 7.3 Hz, 3H).

^{13}C NMR (151 MHz, $CDCl_3$) δ 206.91, 148.60, 142.22, 110.80, 108.28, 42.28, 35.29, 7.75.

Data for **S46**

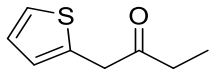

Following the general procedure for ethyl ketones, a yellow oil was obtained (78 mg, 34% yield) with ethyl acetate/hexane (4:1) as the eluent.

Spectral data match those previously reported.[41]

^{1}H NMR (600 MHz, $CDCl_3$) δ 7.21 (dd, J = 5.1, 1.2 Hz, 1H), 6.97 (dd, J = 5.2, 3.4 Hz, 1H), 6.89 (dq, J = 3.3, 1.0 Hz, 1H), 3.89 (d, J = 0.9 Hz, 2H), 2.53 (q, J = 7.3 Hz, 2H), 1.06 (t, J = 7.3 Hz, 3H).

^{13}C NMR (151 MHz, $CDCl_3$) δ 207.42, 135.51, 127.01, 126.71, 125.01, 43.30, 34.99, 7.77

Data for **S47**

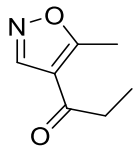

Following the general procedure for ethyl ketones, a colorless oil was obtained (45 mg, 21% yield) with ethyl acetate/hexane (4:1) as the eluent.

^{1}H NMR (600 MHz, $CDCl_3$) δ 8.48 (t, J = 0.7 Hz, 1H), 2.78 (q, J = 7.3 Hz, 2H), 2.73 (d, J = 0.7 Hz, 3H), 1.19 (t, J = 7.2 Hz, 3H).

^{13}C NMR (151 MHz, $CDCl_3$) δ 194.44, 173.53, 149.34, 116.54, 34.77, 13.13, 7.57.

HR MS (pESI): calcd. For $C_7H_{10}O_2N$ $[M+H]^+$: 140.06, found: 140.0706

2.4.2.6 Preparation of Authentic Products and Analytical Data of Chiral Products

General procedure for synthesis of racemic alcohols

The racemic alcohols were prepared by a previously reported procedure.[2] To a 20 mL screw-capped glass vial, the ketone (1 mmol) was dissolved in 4 mL of methanol and cooled to 0 °C in ice. $NaBH_4$ (10 mmol, 380 mg) was added to the solution portion wise. The mixture was stirred for 3 h at room temperature. Upon completion, the mixture was diluted with 3 mL of H_2O and extracted with 50 mL of DCM, and the organic layer was dried with Na_2SO_4. The solvent was evaporated, and the residue was purified by silica column chromatography, eluting with ethyl acetate/hexane (1:3). The ee of the chiral alcohols were determined by gas chromatography (GC) after acetylation with acetic anhydride with DMAP as base in DCM, unless otherwise noted, or by high performance liquid chromatography (HPLC).

(S)-2-pentanol (**P1**)

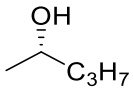

^{1}H NMR (600 MHz, $CDCl_3$) δ 3.90 – 3.75 (m, 1H), 1.53 – 1.31 (m, 5H), 1.20 (d, J = 6.1 Hz, 3H), 1.03 – 0.88 (m, 3H).

^{13}C NMR (151 MHz, $CDCl_3$) δ 68.03, 41.68, 23.61, 19.07, 14.19.

$[\alpha]_D^{25}$ = +6.0 (ethyl acetate)

Spectral data match those previously reported.[42]

Separation of corresponding acetate enantiomers (**P1-Ac**): Chirasil-Dex CB, inject temperature = 250 °C, detector temperature = 300 °C, inlet pressure = 12.5 psi, flow rate = 1.3 mL/ min, split ratio = 50:1, temperature program = 50 °C (0 min) - 10 °C/min - 180 °C

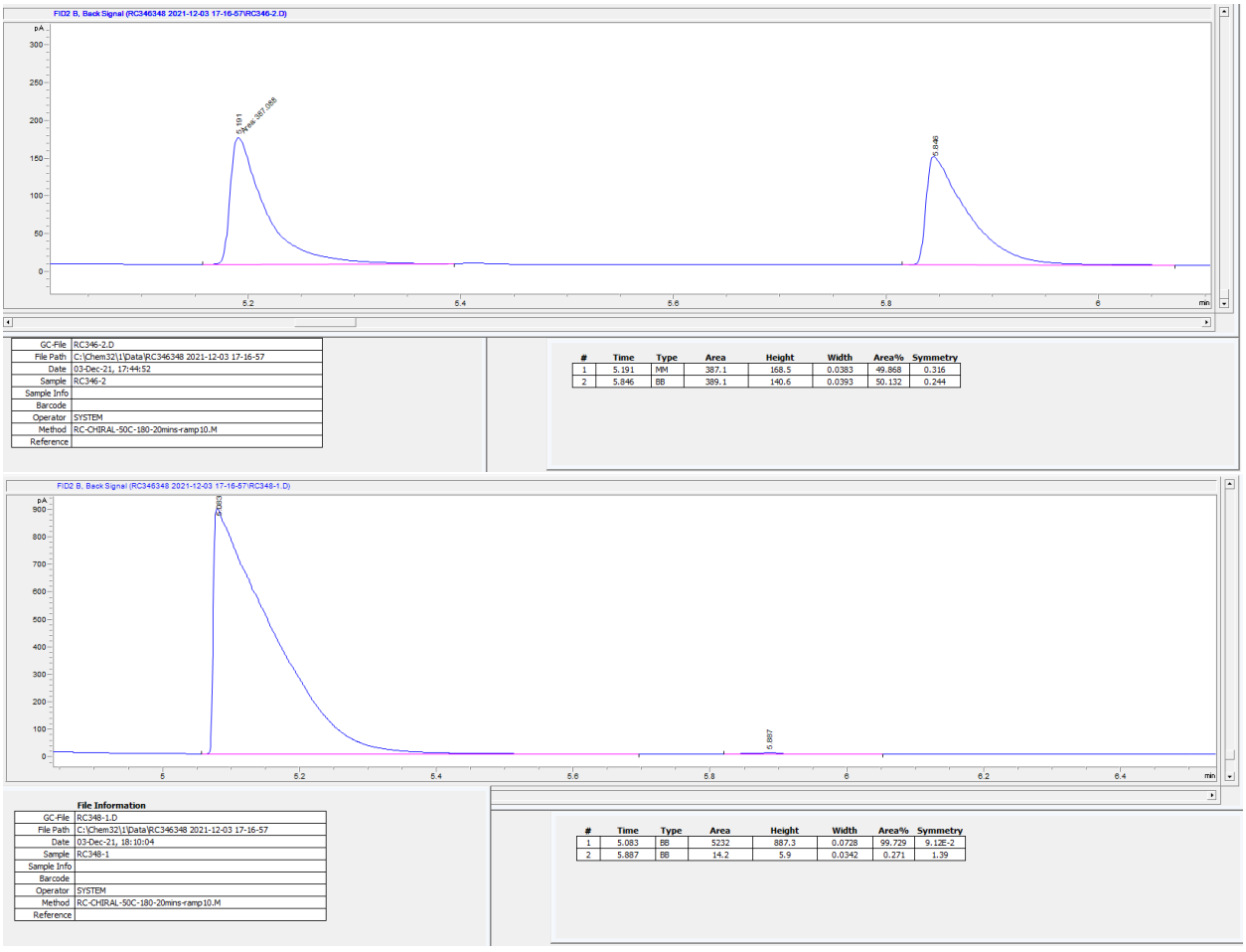

(S)-2-hexanol (**P2**)

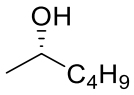

^{1}H NMR (600 MHz, $CDCl_3$) δ 3.87 – 3.71 (m, 1H), 1.55 – 1.24 (m, 7H), 1.18 (d, *J* = 6.2 Hz, 3H), 0.90 (t, *J* = 6.9 Hz, 3H).

^{13}C NMR (151 MHz, $CDCl_3$) δ 68.32, 39.21, 28.09, 23.61, 22.85, 14.19.

Spectral data match those previously reported.[43]

Separation of corresponding acetate enantiomers (**P2-Ac**): Chirasil-Dex CB, inject temperature = 250 °C, detector temperature = 300 °C, inlet pressure = 12.5 psi, flow rate = 1.3 mL/ min, split ratio = 50:1, temperature program = 50 °C (0 min) - 10 °C/min - 180 °C

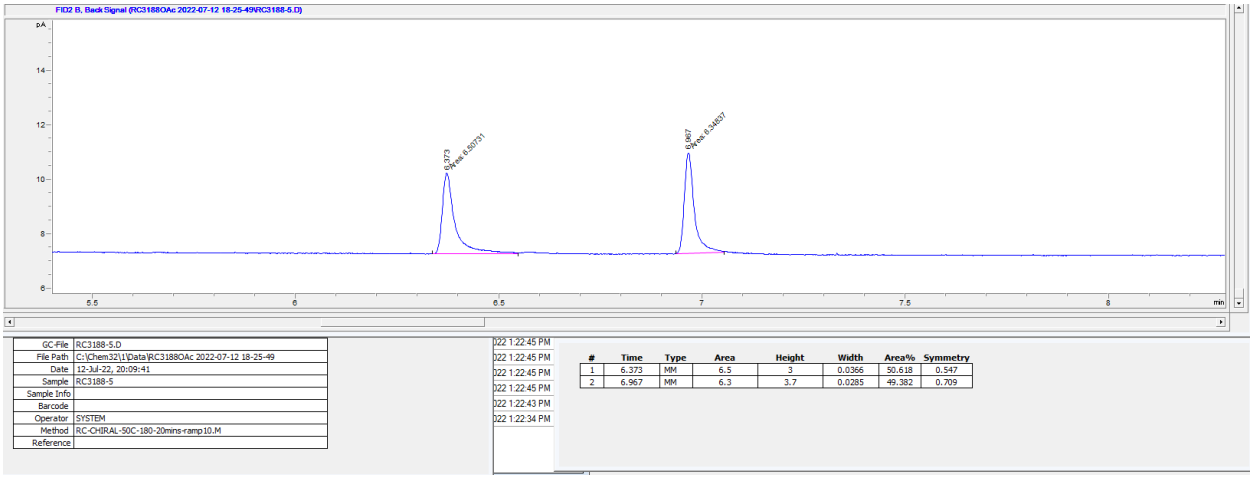

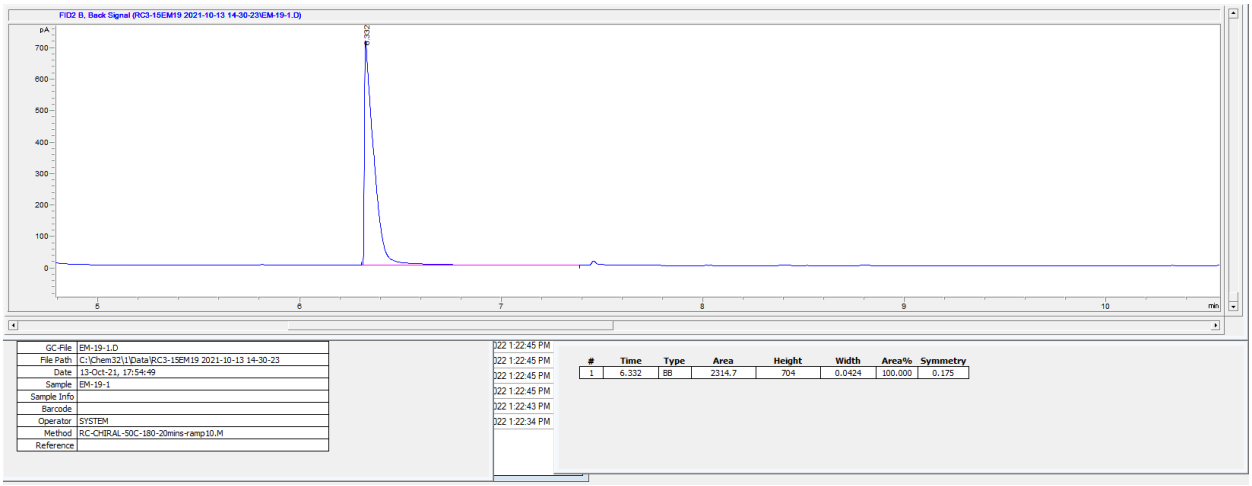

(S)-2-heptanol (**P3**)

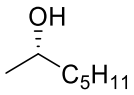

^{1}H NMR (600 MHz, $CDCl_3$) δ 3.79 (dqt, J = 7.1, 6.1, 4.9 Hz, 1H), 1.51 – 1.38 (m, 4H), 1.35 – 1.26 (m, 5H), 1.18 (d, J = 6.1 Hz, 3H), 0.89 (t, J = 7.0 Hz, 3H).

^{13}C NMR (151 MHz, $CDCl_3$) δ 68.20, 39.35, 31.85, 25.45, 23.48, 22.63, 14.02.

$[\alpha]_D^{25}$ = +4.9 (ethyl acetate)

Spectral data match those previously reported.[42]

Separation of corresponding acetate enantiomers (**P3-Ac**): Chirasil-Dex CB, inject temperature = 250 °C, detector temperature = 300 °C, inlet pressure = 12.5 psi, flow rate = 1.3 mL/ min, split ratio = 50:1, temperature program = 50 °C (0 min) - 10 °C/min - 180 °C

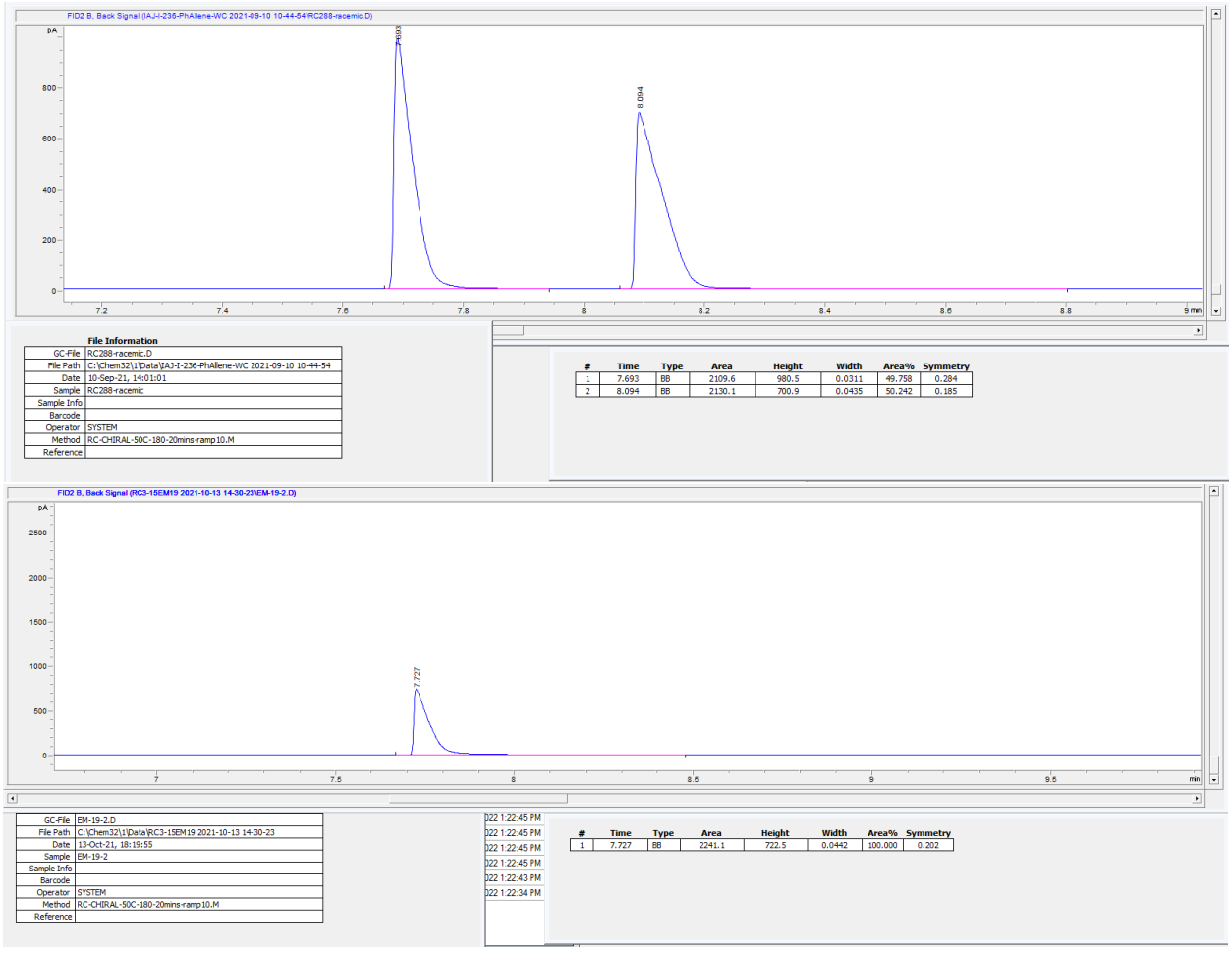

(S)-2-Octanol (**P4**)

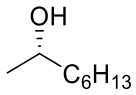

^{1}H NMR (600 MHz, $CDCl_3$) δ 3.84 – 3.74 (m, 1H), 1.58 – 1.35 (m, 4H), 1.35 – 1.24 (m, 7H), 1.18 (dd, *J* = 6.2, 0.7 Hz, 3H), 0.88 (t, *J* = 6.9 Hz, 3H).

^{13}C NMR (151 MHz, $CDCl_3$) δ 68.34, 39.54, 31.98, 29.46, 25.88, 23.63, 22.75, 22.63, 14.21.

Spectral data match those previously reported.[43]

Separation of corresponding acetate enantiomers (**P4-Ac**): Chirasil-Dex CB, inject temperature = 250 °C, detector temperature = 300 °C, inlet pressure = 12.5 psi, flow rate = 1.3 mL/ min, split ratio = 50:1, temperature program = 50 °C (0 min) - 10 °C/min - 180 °C

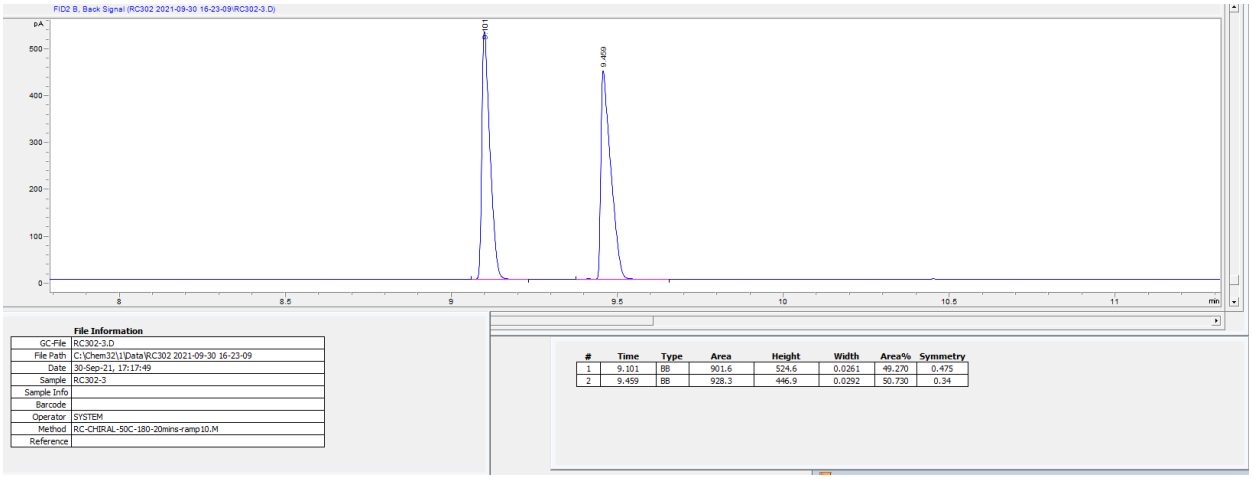

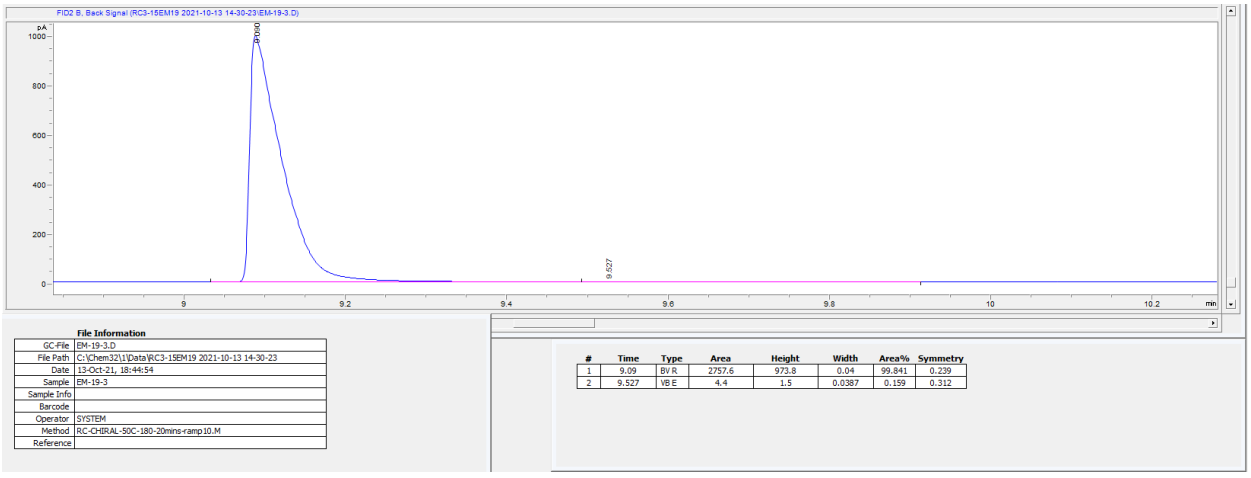

(S)-2-nonanol (**P5**)

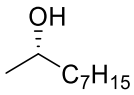

^{1}H NMR (600 MHz, $CDCl_3$) δ 3.85 – 3.71 (m, 1H), 1.52 – 1.35 (m, 4H), 1.28 (tt, *J* = 10.6, 6.1 Hz, 9H), 1.18 (d, *J* = 6.1 Hz, 3H), 0.88 (t, *J* = 7.0 Hz, 3H).

^{13}C NMR (151 MHz, $CDCl_3$) δ 68.20, 39.39, 31.82, 29.61, 29.29, 25.78, 23.49, 22.66, 14.08.

Spectral data match those previously reported.[44]

Separation of corresponding acetate enantiomers (**P5-Ac**): Chirasil-Dex CB, inject temperature = 250 °C, detector temperature = 300 °C, inlet pressure = 12.5 psi, flow rate = 1.3 mL/ min, split ratio = 50:1, temperature program = 50 °C (0 min) - 10 °C/min - 180 °C

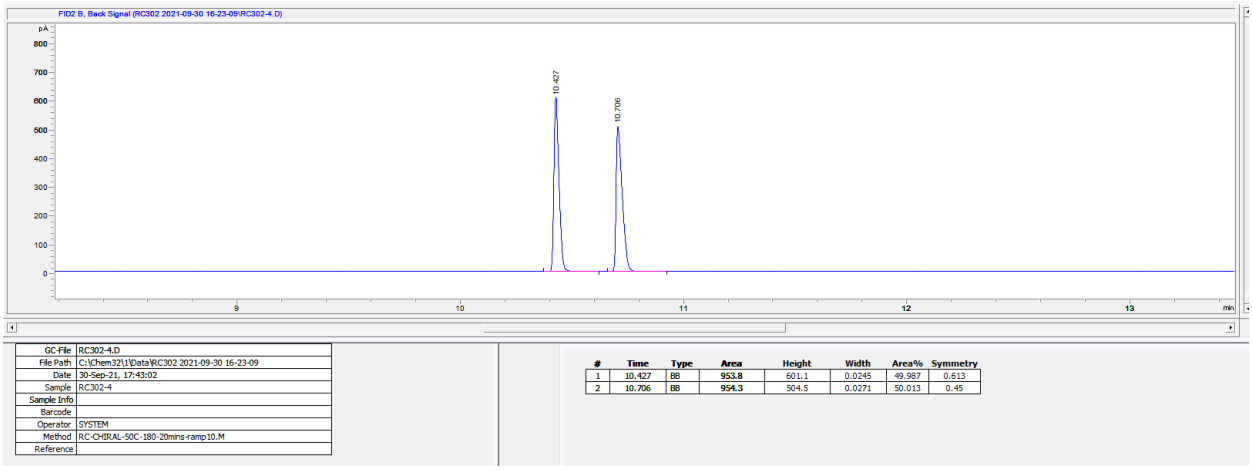

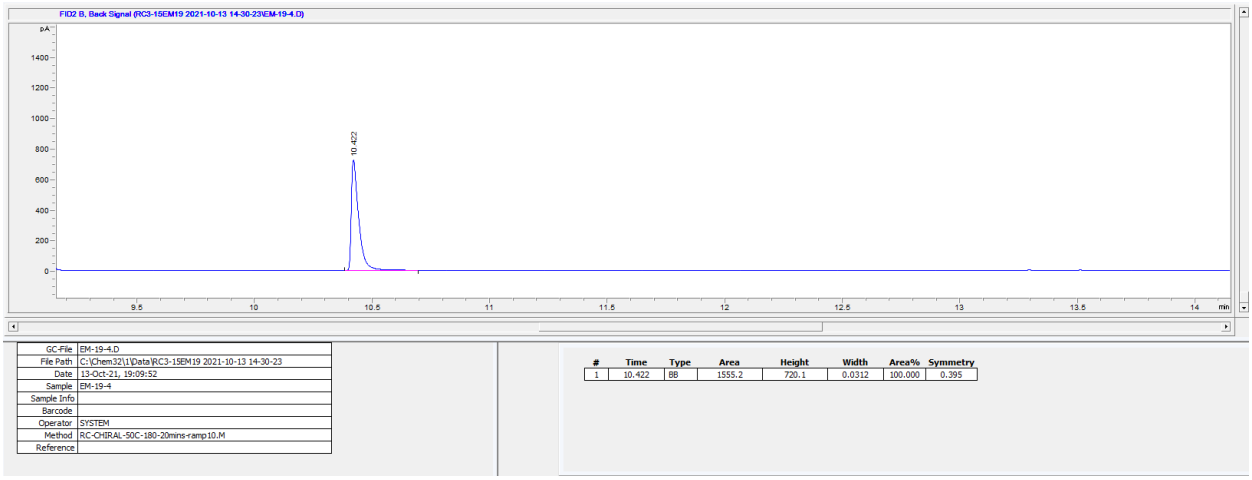

(S)-2-undecanol (**P6**)

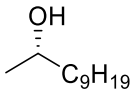

^{1}H NMR (600 MHz, $CDCl_3$) δ 3.90 – 3.69 (m, 1H), 1.54 – 1.20 (m, 17H), 1.18 (d, J = 6.2 Hz, 3H), 0.88 (t, J = 7.0 Hz, 3H).

^{13}C NMR (151 MHz, $CDCl_3$) δ 68.21, 39.40, 31.90, 29.65, 29.63, 29.57, 29.32, 25.78, 23.49, 22.68, 14.10.

Spectral data match those previously reported.[43]

Separation of corresponding acetate enantiomers (**P6-Ac**): Chirasil-Dex CB, inject temperature = 250 °C, detector temperature = 300 °C, inlet pressure = 12.5 psi, flow rate = 1.3 mL/ min, split ratio = 50:1, temperature program = 50 °C (0 min) - 10 °C/min - 180 °C

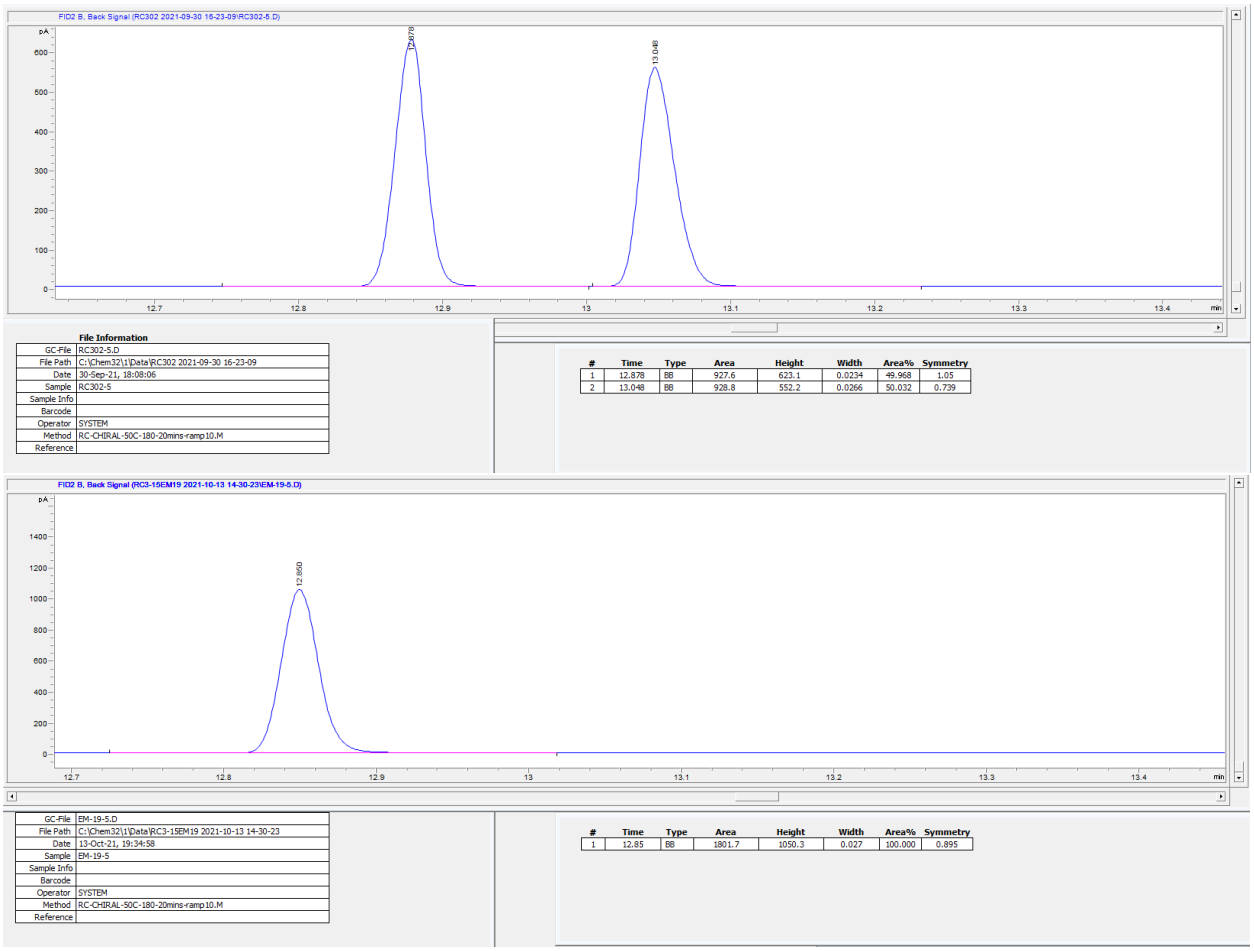

(S)-1-cyclohexyl-propan-2-ol (**P7**)

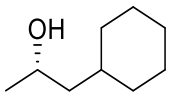

^{1}H NMR (600 MHz, $CDCl_3$) δ 3.90 (dqd, *J* = 7.6, 6.2, 4.9 Hz, 1H), 1.82 – 1.21 (m, 12H), 1.20 – 1.12 (m, 4H), 0.98 – 0.80 (m, 2H).

^{13}C NMR (151 MHz, $CDCl_3$) δ 65.66, 47.40, 34.48, 34.10, 33.24, 26.72, 26.47, 26.35, 24.21.

Spectral data match those previously reported.[45]

Separation of corresponding acetate enantiomers (**P7-Ac**): Chirasil-Dex CB, inject temperature = 250 °C, detector temperature = 300 °C, inlet pressure = 12.5 psi, flow rate = 1.3 mL/ min, split ratio = 50:1, temperature program = 50 °C (0 min) - 10 °C/min - 180 °C

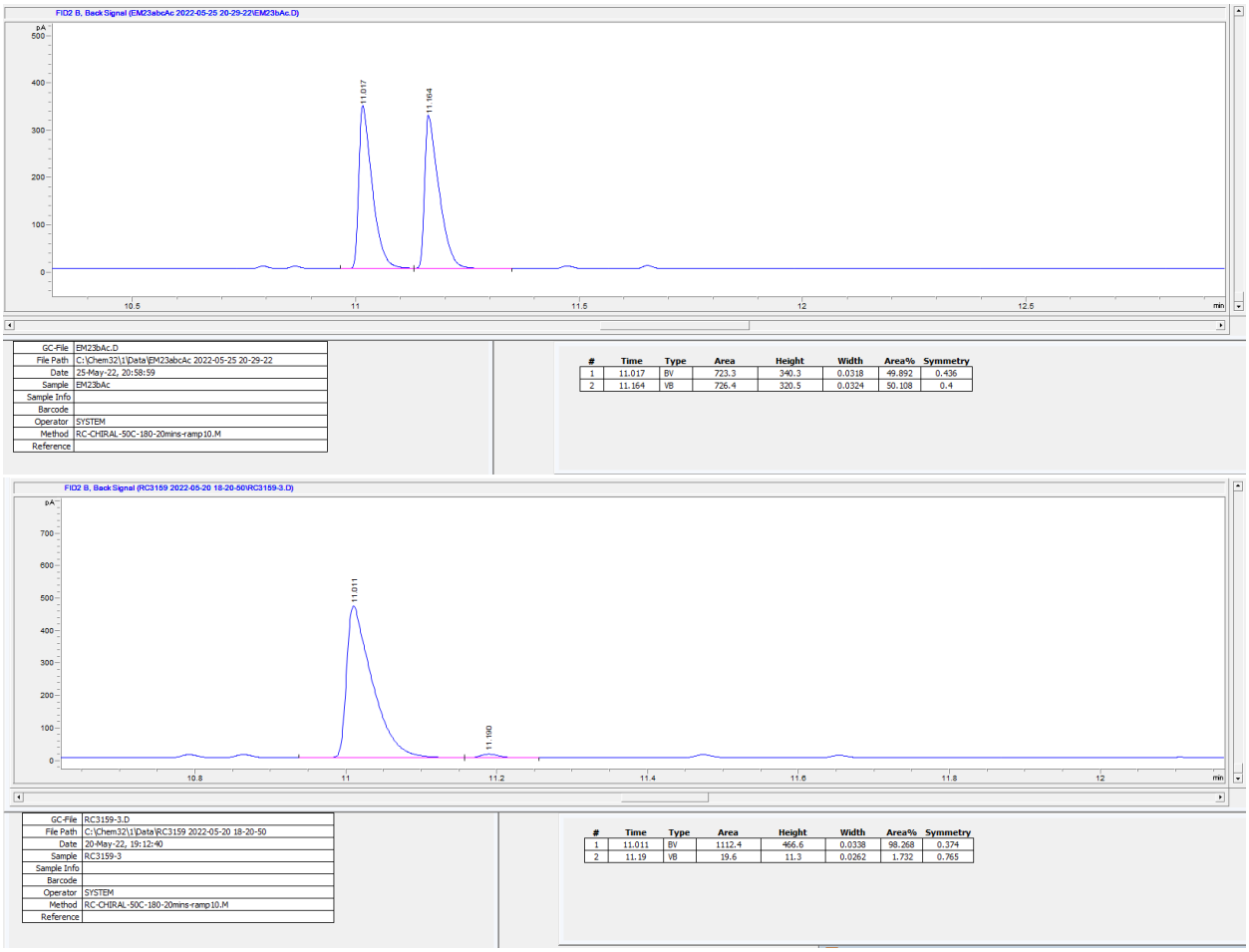

(S)-6-chlorohexan-2-ol (**P8**)

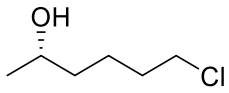

^{1}H NMR (600 MHz, $CDCl_3$) δ 3.78 (h, *J* = 6.1 Hz, 1H), 3.52 (t, *J* = 6.7 Hz, 2H), 1.86 – 1.64 (m, 3H), 1.59 – 1.40 (m, 4H), 1.18 (d, *J* = 6.2 Hz, 3H).

^{13}C NMR (151 MHz, $CDCl_3$) δ 67.92, 45.06, 38.49, 32.64, 23.62, 23.20.

Spectral data match those previously reported.[43]

Separation of corresponding acetate enantiomers (**P8-Ac**): Chirasil-Dex CB, inject temperature = 250 °C, detector temperature = 300 °C, inlet pressure = 12.5 psi, flow rate = 1.3 mL/ min, split ratio = 50:1, temperature program = 50 °C (0 min) - 10 °C/min - 180 °C

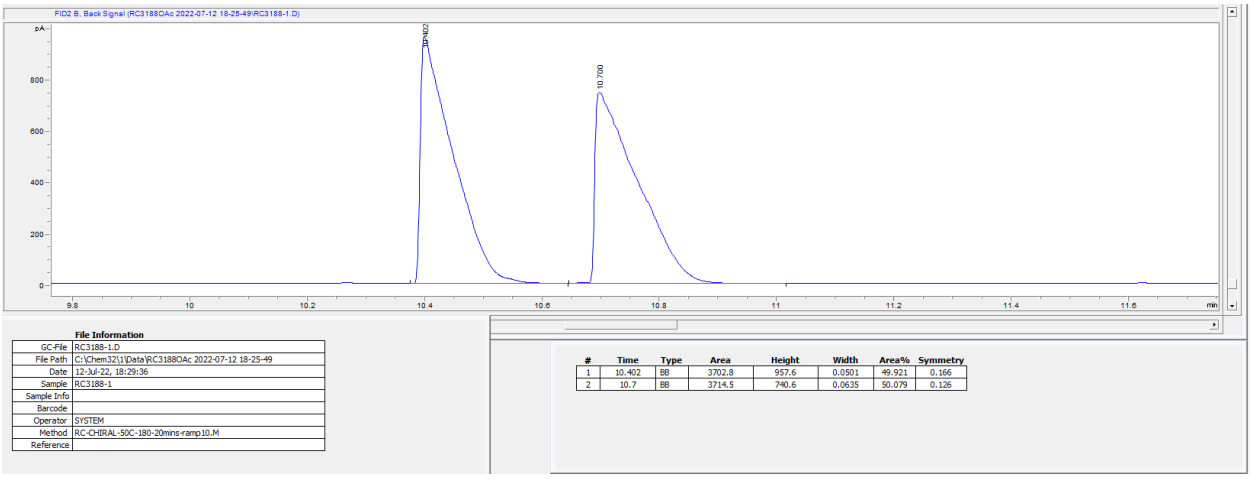

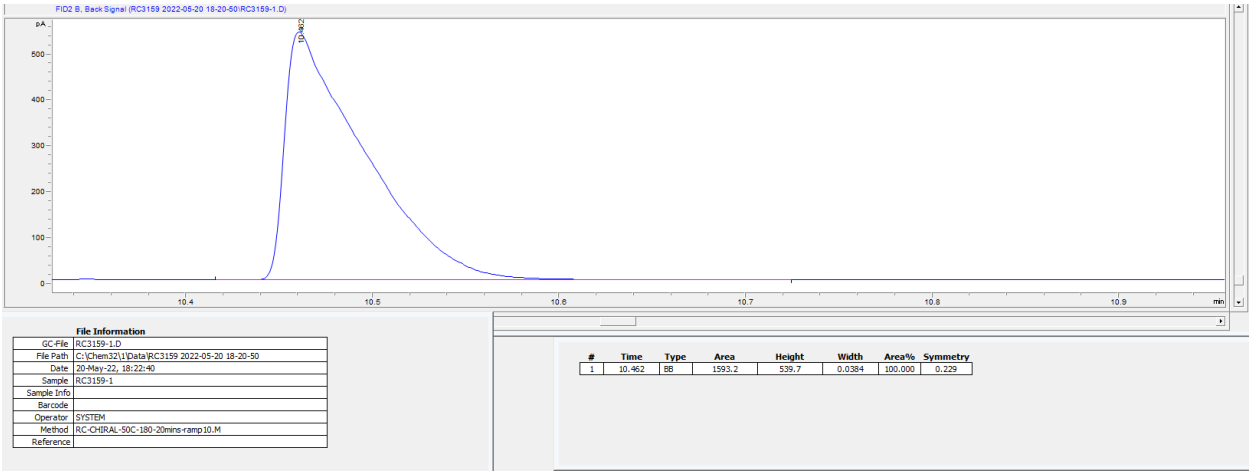

(S)-3-hydroxybutyric acid methyl ester (**P9**)

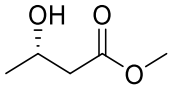

^{1}H NMR (500 MHz, $CDCl_3$) δ 4.18 (dqd, *J* = 8.7, 6.3, 3.6 Hz, 1H), 3.69 (s, 3H), 2.73 (s, 1H), 2.57 – 2.33 (m, 2H), 1.21 (d, *J* = 6.4 Hz, 3H).

^{13}C NMR (126 MHz, $CDCl_3$) δ 173.42, 64.34, 51.83, 42.69, 22.56.

Spectral data match those previously reported.[46]

Separation of corresponding acetate enantiomers (**P9-Ac**): Chirasil-Dex CB, inject temperature = 250 °C, detector temperature = 300 °C, inlet pressure = 12.5 psi, flow rate = 1.3 mL/ min, split ratio = 50:1, temperature program = 50 °C (0 min) - 10 °C/min - 180 °C

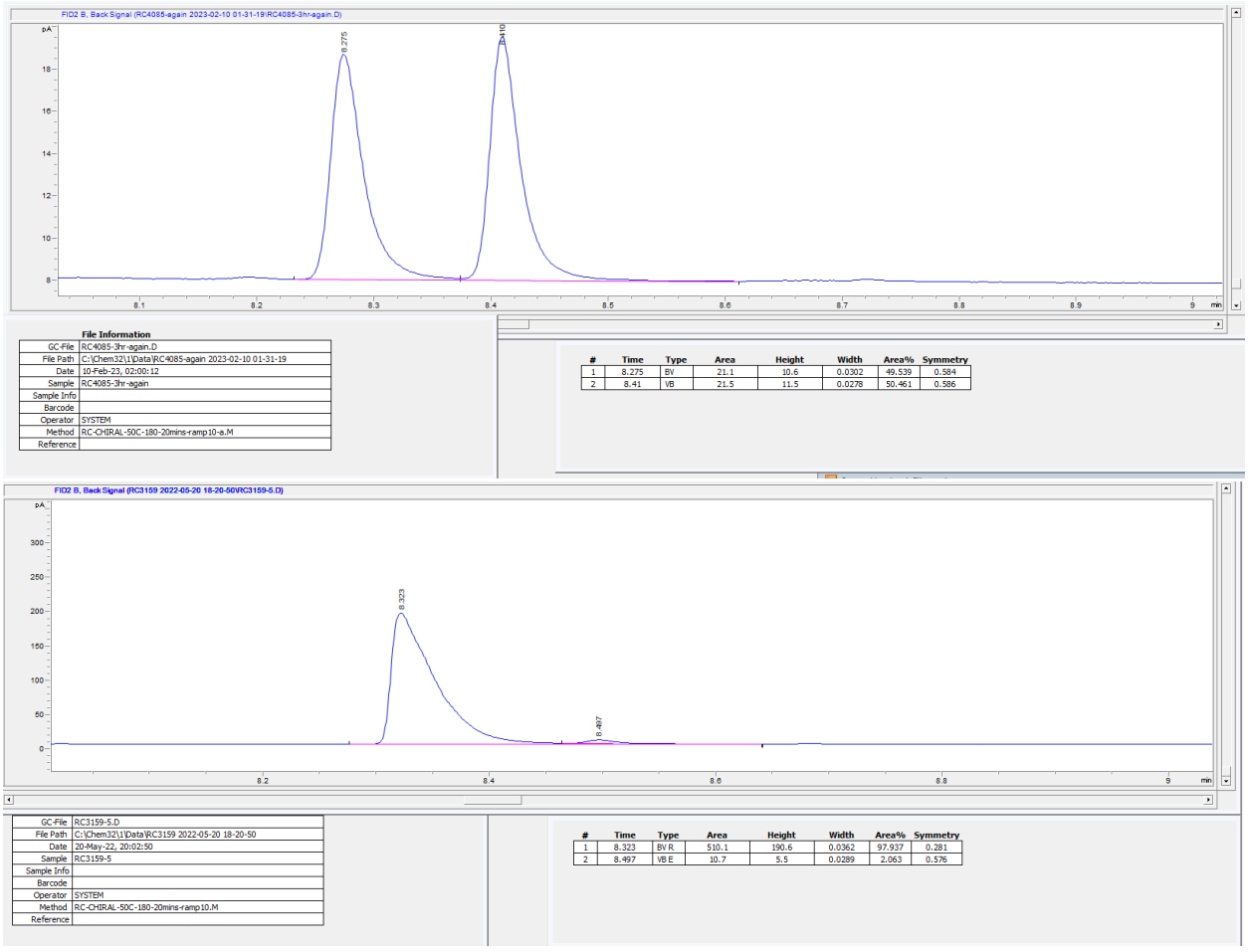

(S)-5-hexen-2-ol (**P10**)

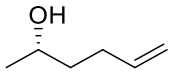

^{1}H NMR (500 MHz, $CDCl_3$) δ 5.83 (ddt, J = 16.9, 10.1, 6.6 Hz, 1H), 5.04 (dq, J = 17.1, 1.7 Hz, 1H), 4.96 (ddt, J = 10.2, 2.3, 1.3 Hz, 1H), 3.82 (dqd, J = 7.3, 6.2, 5.1 Hz, 1H), 2.22 – 2.06 (m, 2H), 1.64 – 1.45 (m, 3H), 1.19 (d, J = 6.2 Hz, 3H).

^{13}C NMR (126 MHz, $CDCl_3$) δ 138.62, 114.87, 77.36, 67.79, 38.39, 30.28, 23.58.

Spectral data match those previously reported.[47]

Separation of corresponding acetate enantiomers (**P10-Ac**): Chirasil-Dex CB, inject temperature = 250 °C, detector temperature = 300 °C, inlet pressure = 12.5 psi, flow rate = 1.3 mL/ min, split ratio = 50:1, temperature program = 50 °C (0 min) - 10 °C/min - 180 °C

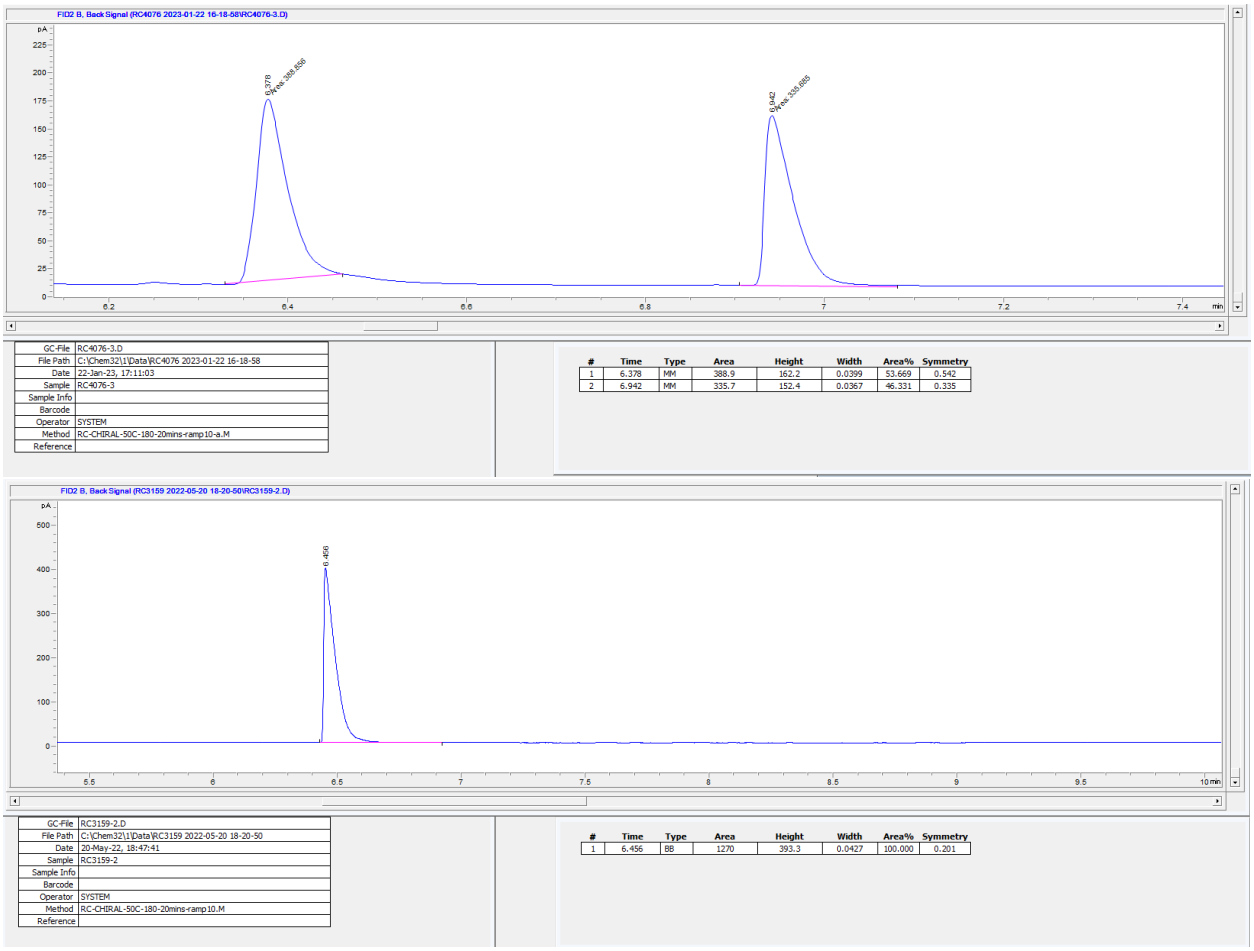

(S)-1-Cyclohex-1-enyl-propan-2-ol (**P11**)

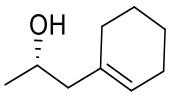

^{1}H NMR (500 MHz, $CDCl_3$) δ 5.56 – 5.50 (m, 1H), 3.87 (dqd, *J* = 12.4, 6.2, 3.9 Hz, 1H), 2.13 – 2.07 (m, 1H), 2.05 – 1.98 (m, 4H), 1.66 – 1.53 (m, 4H), 1.18 (d, *J* = 6.0 Hz, 3H).

^{13}C NMR (126 MHz, $CDCl_3$) δ 134.99, 125.08, 77.36, 65.03, 48.51, 28.52, 25.41, 23.01, 22.96, 22.48.

Spectral data match those previously reported.[48]

Separation of corresponding acetate enantiomers (**P11-Ac**): Chirasil-Dex CB, inject temperature = 250 °C, detector temperature = 300 °C, inlet pressure = 12.5 psi, flow rate = 1.3 mL/ min, split ratio = 50:1, temperature program = 50 °C (0 min) - 10 °C/min - 180 °C

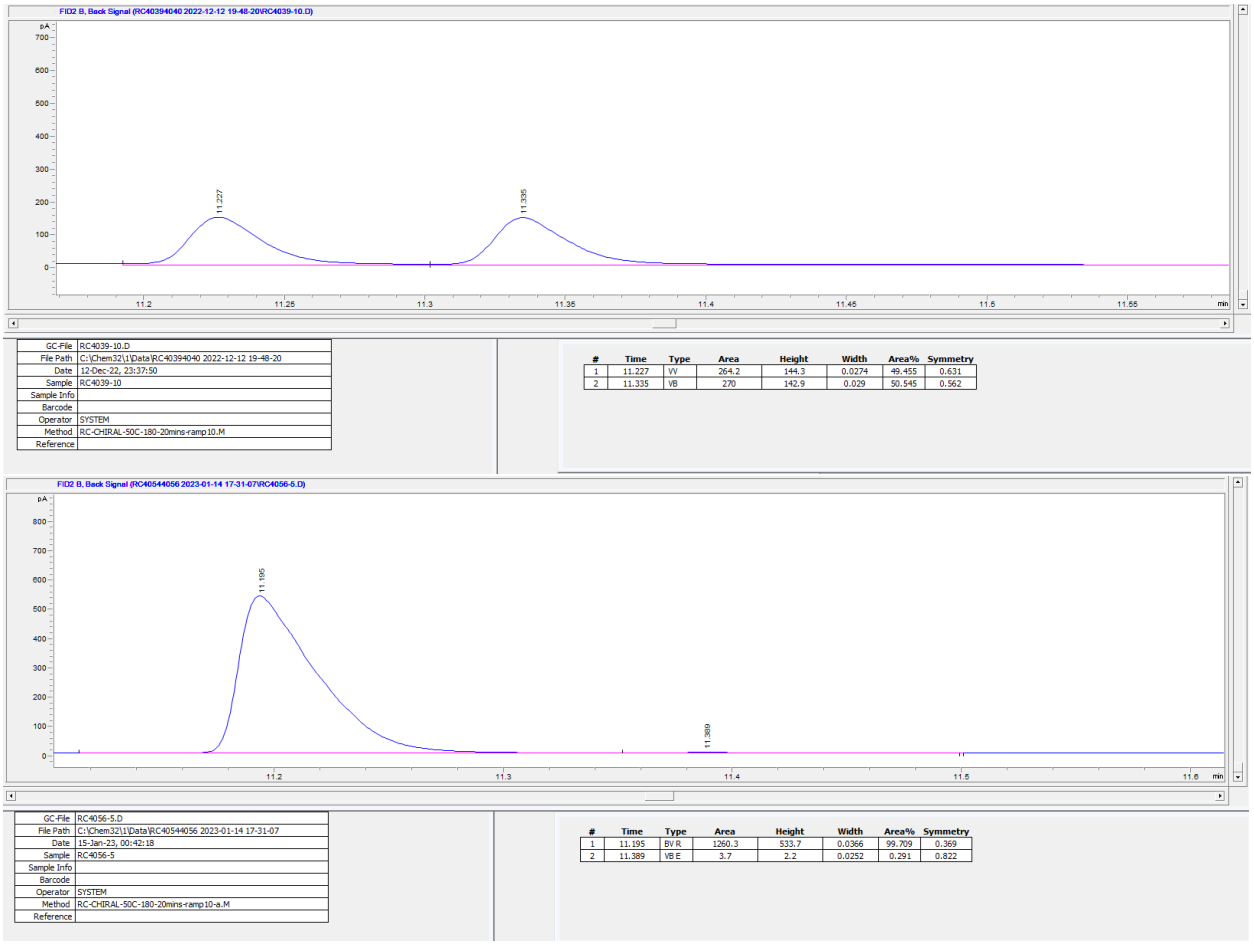

(S)-1-(2-Methoxy-ethoxy)-propan-2-ol (**P12**)

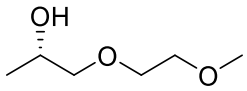

^{1}H NMR (600 MHz, $CDCl_3$) δ 3.99 (dqd, *J* = 9.3, 6.4, 2.8 Hz, 1H), 3.67 (dddd, *J* = 31.3, 11.0, 5.9, 3.3 Hz, 2H), 3.59 – 3.49 (m, 3H), 3.40 (s, 3H), 3.26 (dd, *J* = 9.8, 8.5 Hz, 1H), 1.13 (d, *J* = 6.4 Hz, 3H).

^{13}C NMR (151 MHz, $CDCl_3$) δ 77.22, 72.10, 70.71, 66.49, 59.20, 18.55.

Spectral data match those previously reported.[49]

Separation of corresponding acetate enantiomers (**P12-Ac**): Chirasil-Dex CB, inject temperature = 250 °C, detector temperature = 300 °C, inlet pressure = 12.5 psi, flow rate = 1.3 mL/ min, split ratio = 50:1, temperature program = 50 °C (0 min) - 10 °C/min - 180 °C

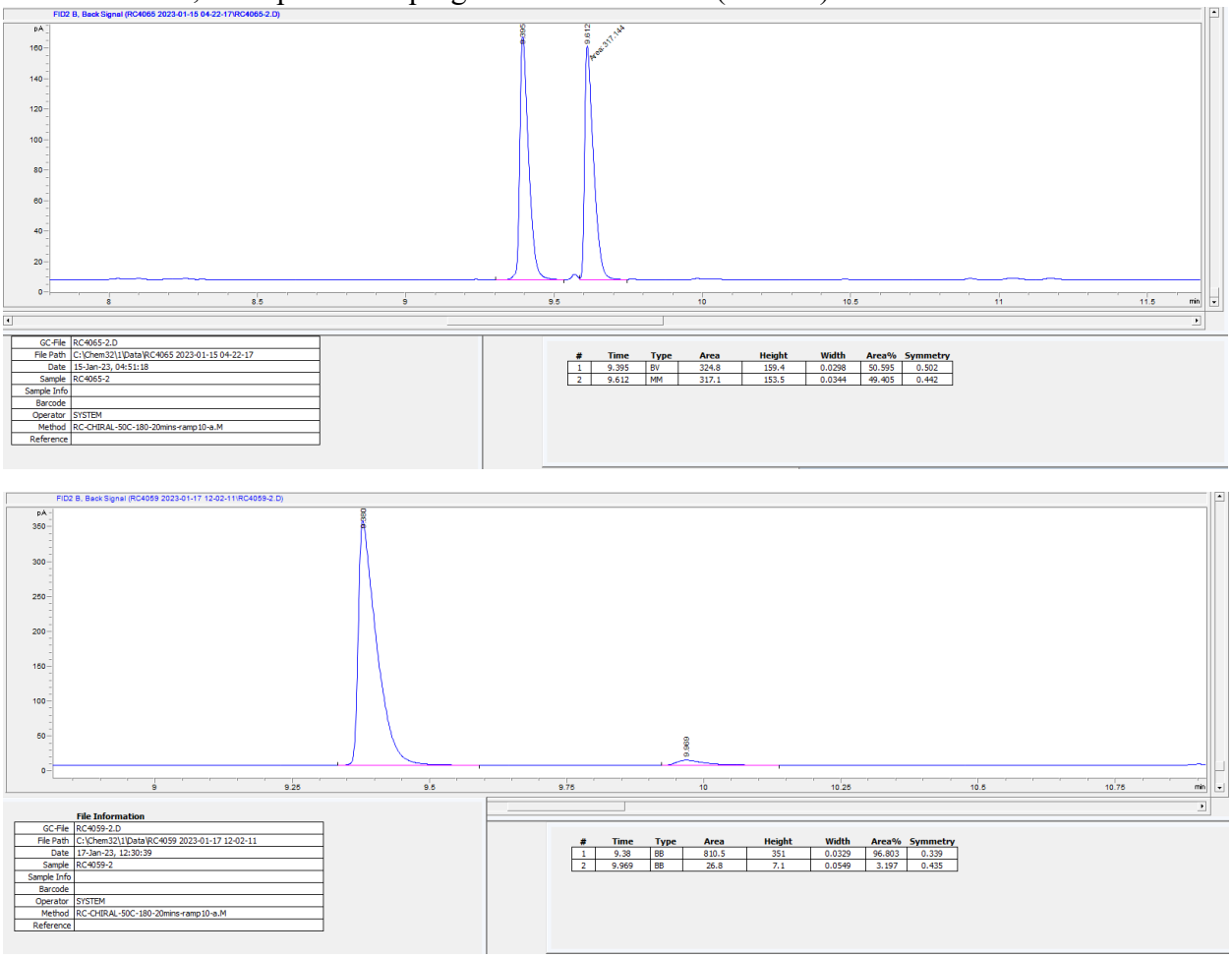

(S)-1-Phenoxypropan-2-ol (**P13**)

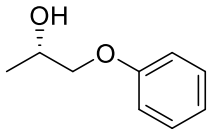

^{1}H NMR (600 MHz, $CDCl_3$) δ 7.32 – 7.27 (m, 2H), 6.97 (tt, *J* = 7.3, 1.1 Hz, 1H), 6.94 – 6.89 (m, 2H), 4.20 (dqd, *J* = 7.8, 6.4, 3.2 Hz, 1H), 3.95 (dd, *J* = 9.2, 3.1 Hz, 1H), 3.80 (dd, *J* = 9.2, 7.8 Hz, 1H), 2.33 (s, 1H), 1.29 (d, *J* = 6.4 Hz, 3H).
^{13}C NMR (151 MHz, $CDCl_3$) δ 158.57, 129.54, 121.15, 114.59, 73.23, 66.31, 18.74.

Spectral data match those previously reported.[50]

Separation of corresponding acetate enantiomers (**P13-Ac**): Chirasil-Dex CB, inject temperature = 250 °C, detector temperature = 300 °C, inlet pressure = 12.5 psi, flow rate = 1.3 mL/ min, split ratio = 50:1, temperature program = 50 °C (0 min) - 10 °C/min - 180 °C

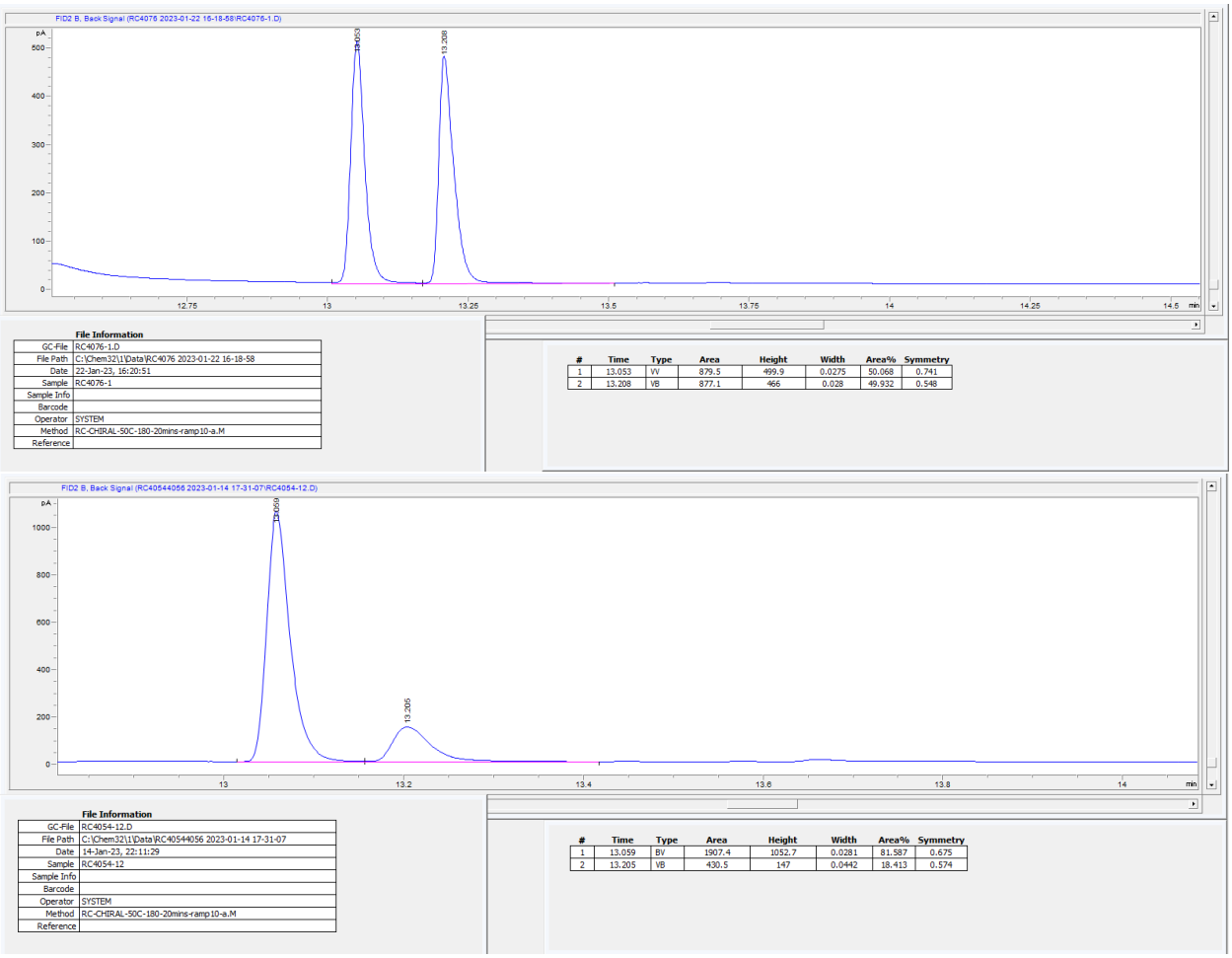

(S)-5-hydroxypentan-2-ol benzyl ether (**P14**)

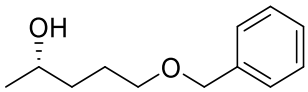

^{1}H NMR (600 MHz, $CDCl_3$) δ 7.34 (dtd, *J* = 7.2, 6.3, 1.3 Hz, 4H), 7.30 – 7.26 (m, 1H), 4.52 (s, 2H), 3.81 (dqd, *J* = 8.0, 6.2, 4.3 Hz, 1H), 3.52 (td, *J* = 6.2, 1.0 Hz, 2H), 1.77 – 1.68 (m, 2H), 1.61 (dddd, *J* = 14.0, 8.1, 6.8, 4.3 Hz, 1H), 1.55 – 1.46 (m, 1H), 1.19 (d, *J* = 6.2 Hz, 3H).

^{13}C NMR (151 MHz, $CDCl_3$) δ 138.34, 128.57, 127.85, 127.79, 73.22, 70.72, 67.95, 36.77, 26.49, 23.61.

Spectral data match those previously reported.[51]

Separation of corresponding acetate enantiomers (**P14-Ac**): Chirasil-Dex CB, inject temperature = 250 °C, detector temperature = 300 °C, inlet pressure = 12.5 psi, flow rate = 1.3 mL/ min, split ratio = 50:1, temperature program = 50 °C (0 min) - 10 °C/min - 180 °C

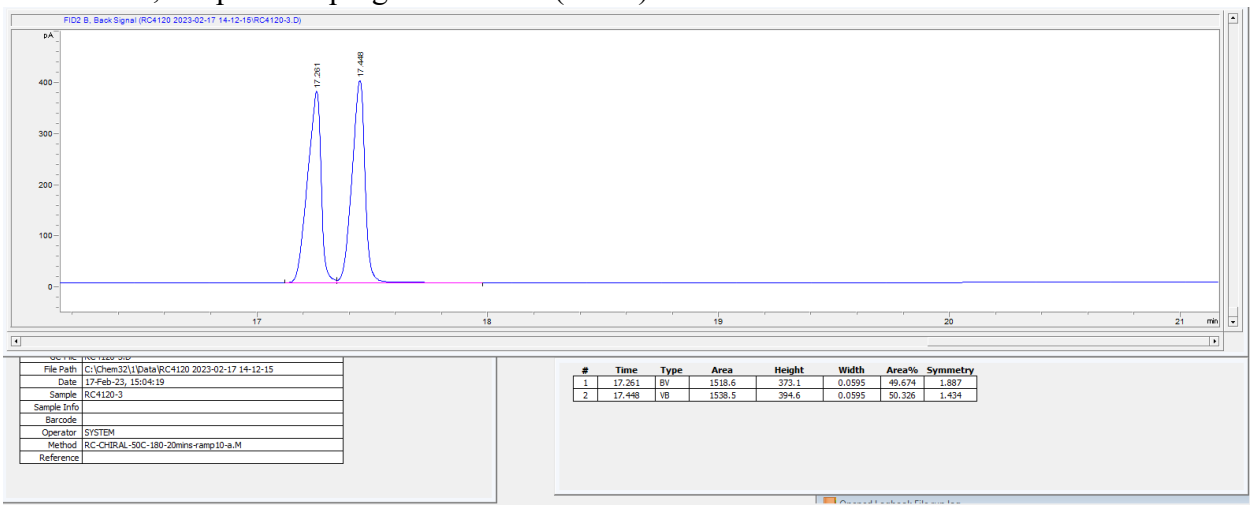

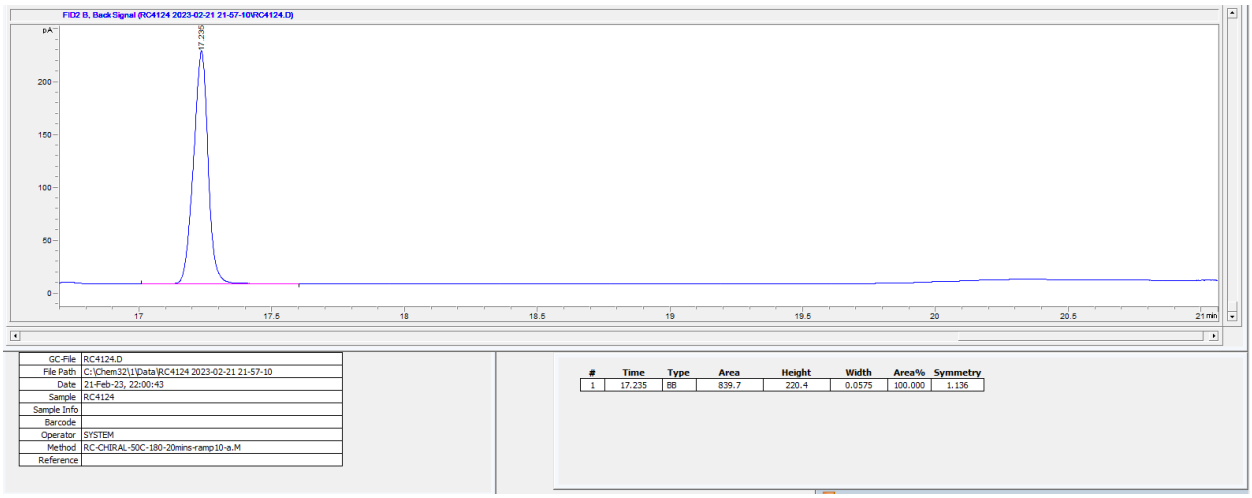

(S)-4-phenylbutan-2-ol (**P15**)

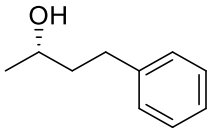

^{1}H NMR (600 MHz, $CDCl_3$) δ 7.30 (t, *J* = 7.6 Hz, 2H), 7.24 – 7.19 (m, 3H), 3.90 – 3.79 (m, 1H), 2.73 (dddd, *J* = 51.6, 13.8, 9.5, 6.4 Hz, 2H), 1.87 – 1.73 (m, 2H), 1.24 (d, *J* = 6.2 Hz, 3H).

^{13}C NMR (151 MHz, $CDCl_3$) δ 142.18, 128.49, 125.90, 67.56, 40.94, 32.23, 23.69.

Spectral data match those previously reported.[16,43]

Separation of enantiomers: HPLC OD-H column, 10% iPrOH in hexane, 1.0 mL/min flow rate

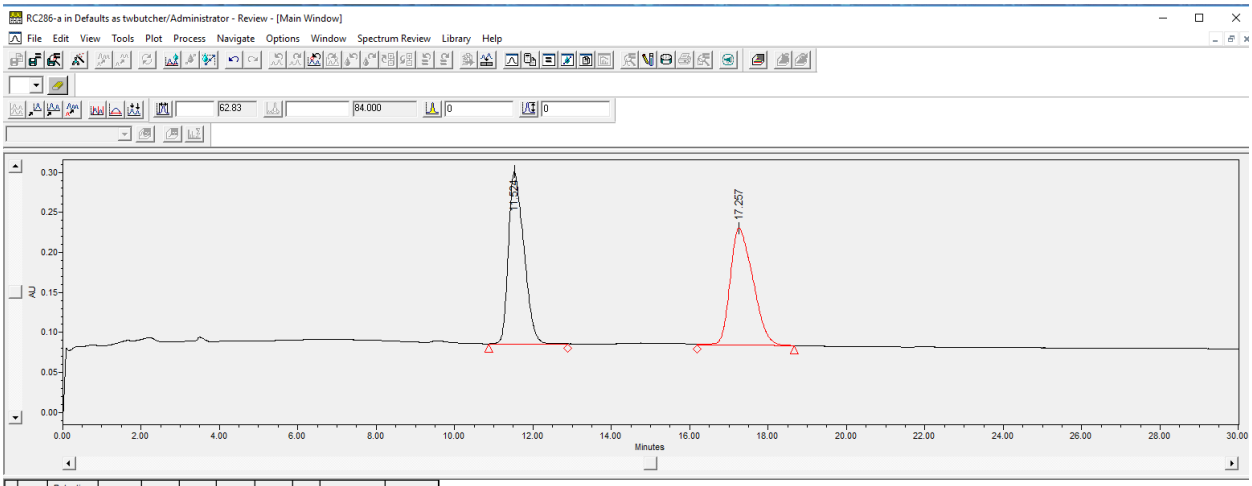

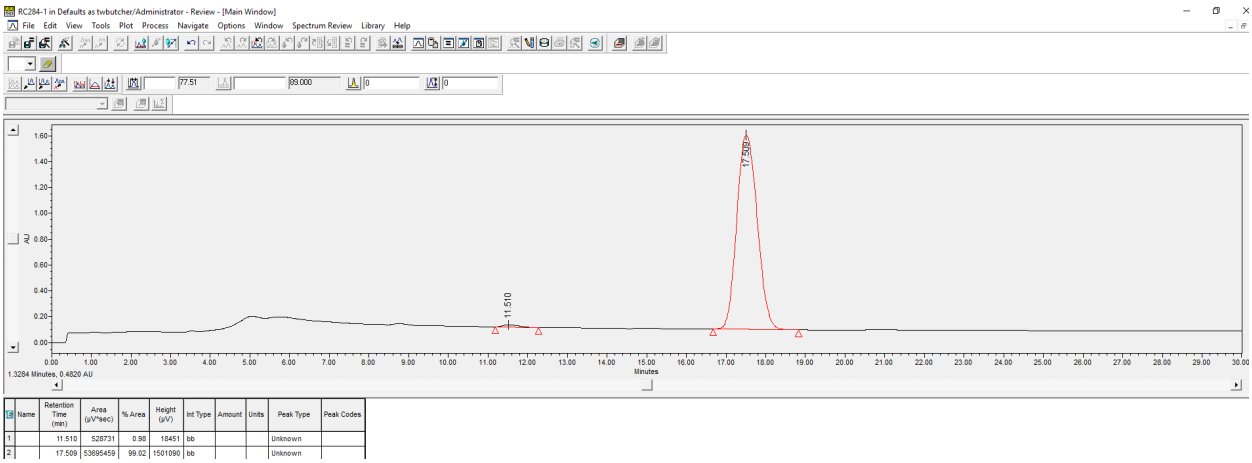

(S)-(E)-4-phenyl-3-buten-2-ol (**P16**)

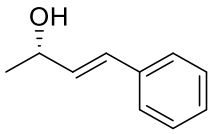

^{1}H NMR (600 MHz, $CDCl_3$) δ 7.41 – 7.36 (m, 2H), 7.35 – 7.29 (m, 2H), 7.26 – 7.21 (m, 1H), 6.60 – 6.55 (m, 1H), 6.27 (dd, *J* = 15.9, 6.4 Hz, 1H), 4.53 – 4.46 (m, 1H), 1.58 (d, *J* = 3.5 Hz, 2H), 1.38 (d, *J* = 6.4 Hz, 3H).

^{13}C NMR (151 MHz, $CDCl_3$) δ 136.84, 133.71, 129.57, 128.73, 127.79, 126.60, 69.11, 23.58.

Spectral data match those previously reported.[50]

Separation of corresponding acetate enantiomers (**P16-Ac**): Chirasil-Dex CB, inject temperature = 250 °C, detector temperature = 300 °C, inlet pressure = 12.5 psi, flow rate = 1.3 mL/ min, split

ratio = 50:1, temperature program = 50 °C (0 min) - 10 °C/min - 180 °C

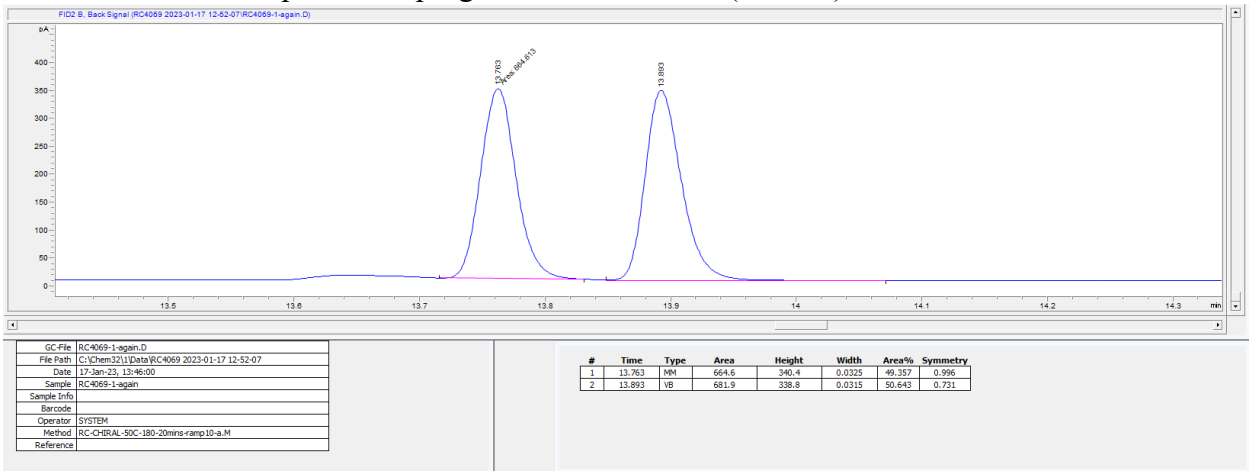

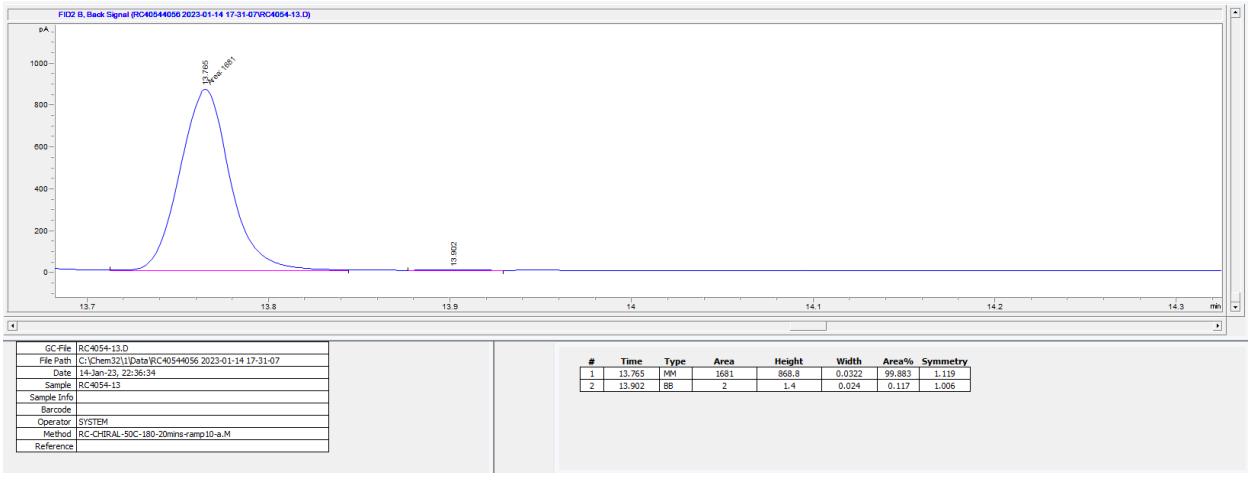

(S,E)-4-(4-chlorophenyl)but-3-en-2-ol (**P17**)

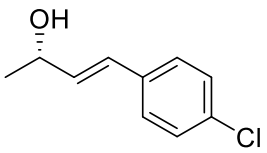

^{1}H NMR (500 MHz, $CDCl_3$) δ 7.38 – 7.17 (m, 4H), 6.50 (dd, *J* = 15.9, 1.3 Hz, 1H), 6.22 (dd, *J* = 16.0, 6.2 Hz, 1H), 4.45 (p, *J* = 6.4 Hz, 1H), 1.35 (d, *J* = 6.5 Hz, 3H).

^{13}C NMR (126 MHz, $CDCl_3$) δ 135.36, 134.34, 133.07, 128.67, 127.86, 127.63, 68.50, 53.51, 50.33, 23.26.

Spectral data match those previously reported.

Separation of enantiomers: HPLC AD-H column, 1% iPrOH in hexane, 1.0 mL/min flow rate

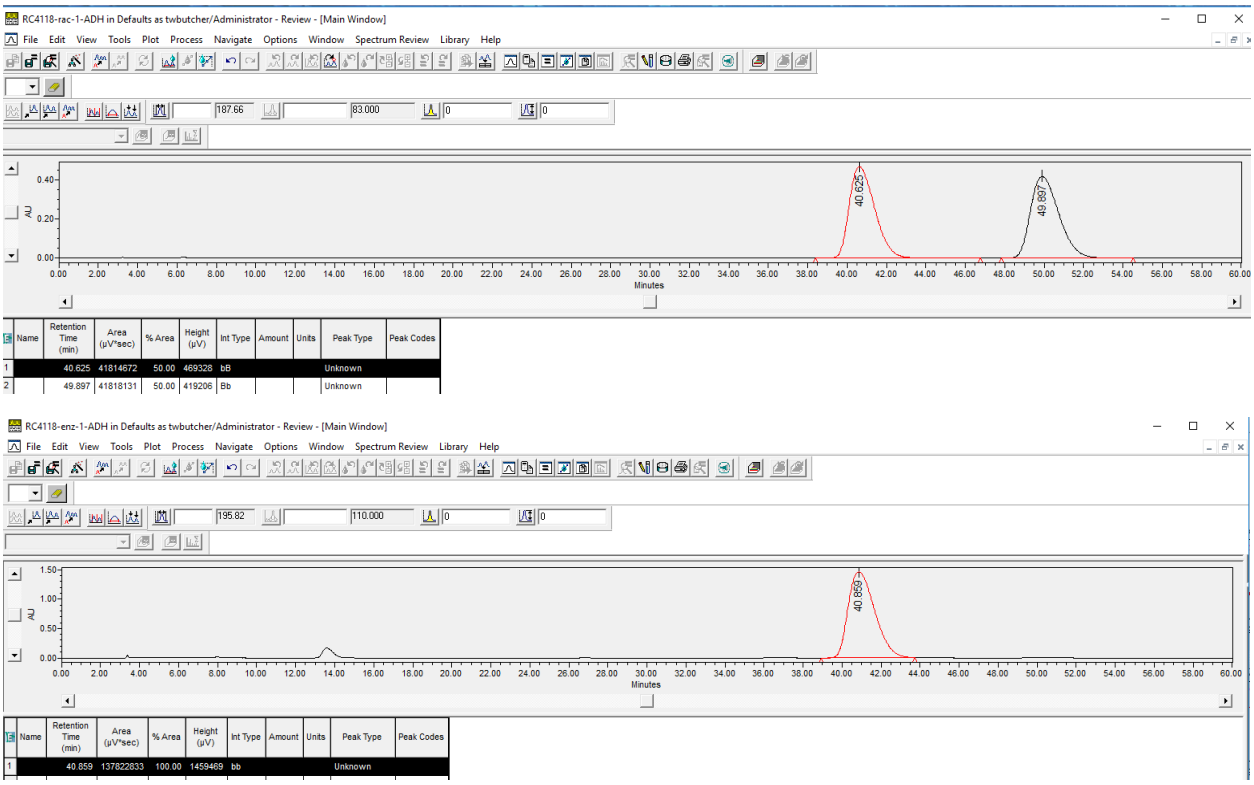

(S,E)-4-(4-bromophenyl)but-3-en-2-ol (**P18**)

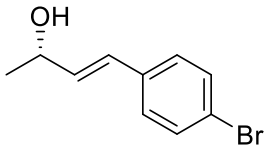

^{1}H NMR (600 MHz, $CDCl_3$) δ 7.45 – 7.41 (m, 2H), 7.26 – 7.22 (m, 2H), 6.54 – 6.48 (m, 1H), 6.25 (dd, J = 15.9, 6.2 Hz, 1H), 4.48 (pd, J = 6.4, 1.3 Hz, 1H), 1.37 (d, J = 6.4 Hz, 3H).

^{13}C NMR (151 MHz, $CDCl_3$) δ 135.83, 134.49, 131.84, 128.34, 128.14, 121.53, 68.92, 23.56.

Spectral data match those previously reported.[52]

Separation of enantiomers: HPLC OD-H column, 1% iPrOH in hexane, 1.0 mL/min flow rate.

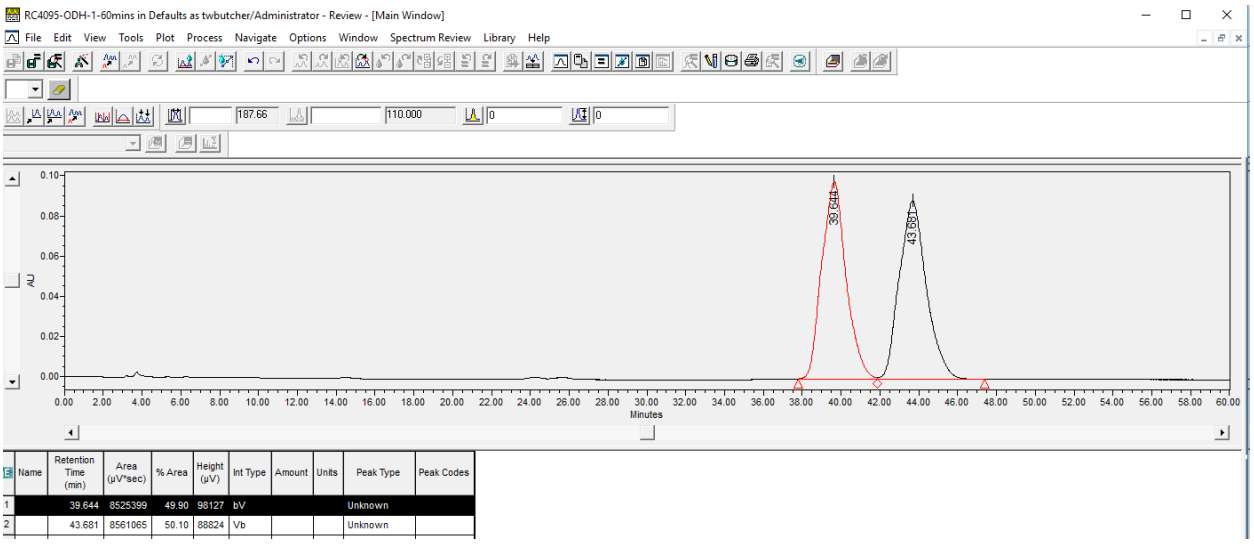

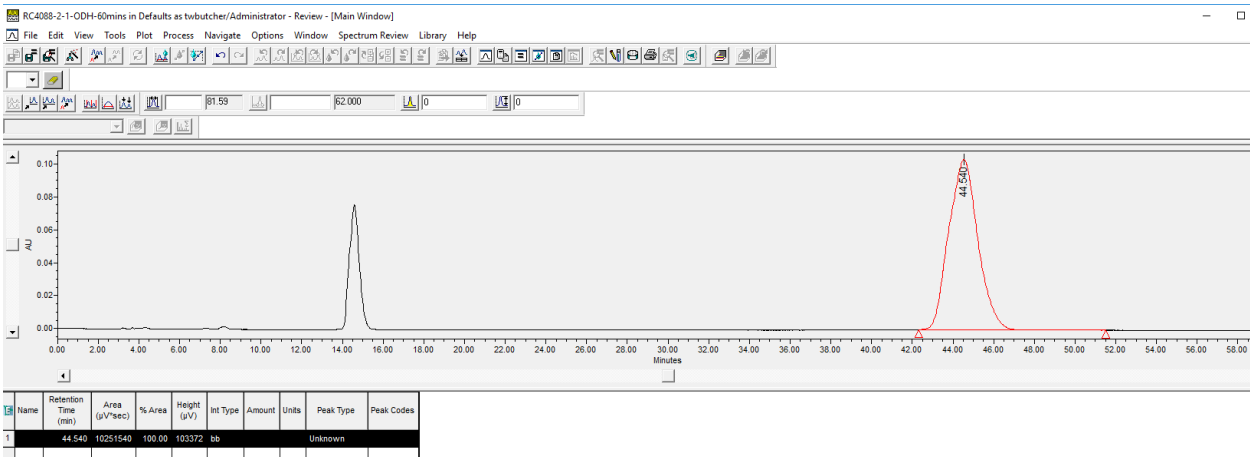

(S)-1-[4-(trifluoromethyl)phenyl]propan-2-ol (**P19**)

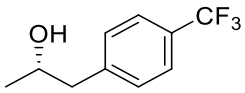

^{1}H NMR (600 MHz, $CDCl_3$) δ 7.57 (d, J = 8.0 Hz, 2H), 7.34 (d, J = 7.9 Hz, 2H), 4.06 (dqd, J = 7.8, 6.1, 4.8 Hz, 1H), 2.87 – 2.74 (m, 2H), 1.44 (s, 1H), 1.26 (d, J = 6.2 Hz, 3H).

^{13}C NMR (151 MHz, $CDCl_3$) δ 142.90, 129.87, 128.90, 125.58, 125.56, 125.53, 125.51, 125.32, 123.52, 68.80, 45.58, 23.23.

Spectral data match those previously reported.[53]

Separation of corresponding acetate enantiomers (**P19-Ac**): Chirasil-Dex CB, inject temperature = 250 °C, detector temperature = 300 °C, inlet pressure = 12.5 psi, flow rate = 1.3 mL/ min, split ratio = 50:1, temperature program = 50 °C (0 min) - 10 °C/min - 180 °C

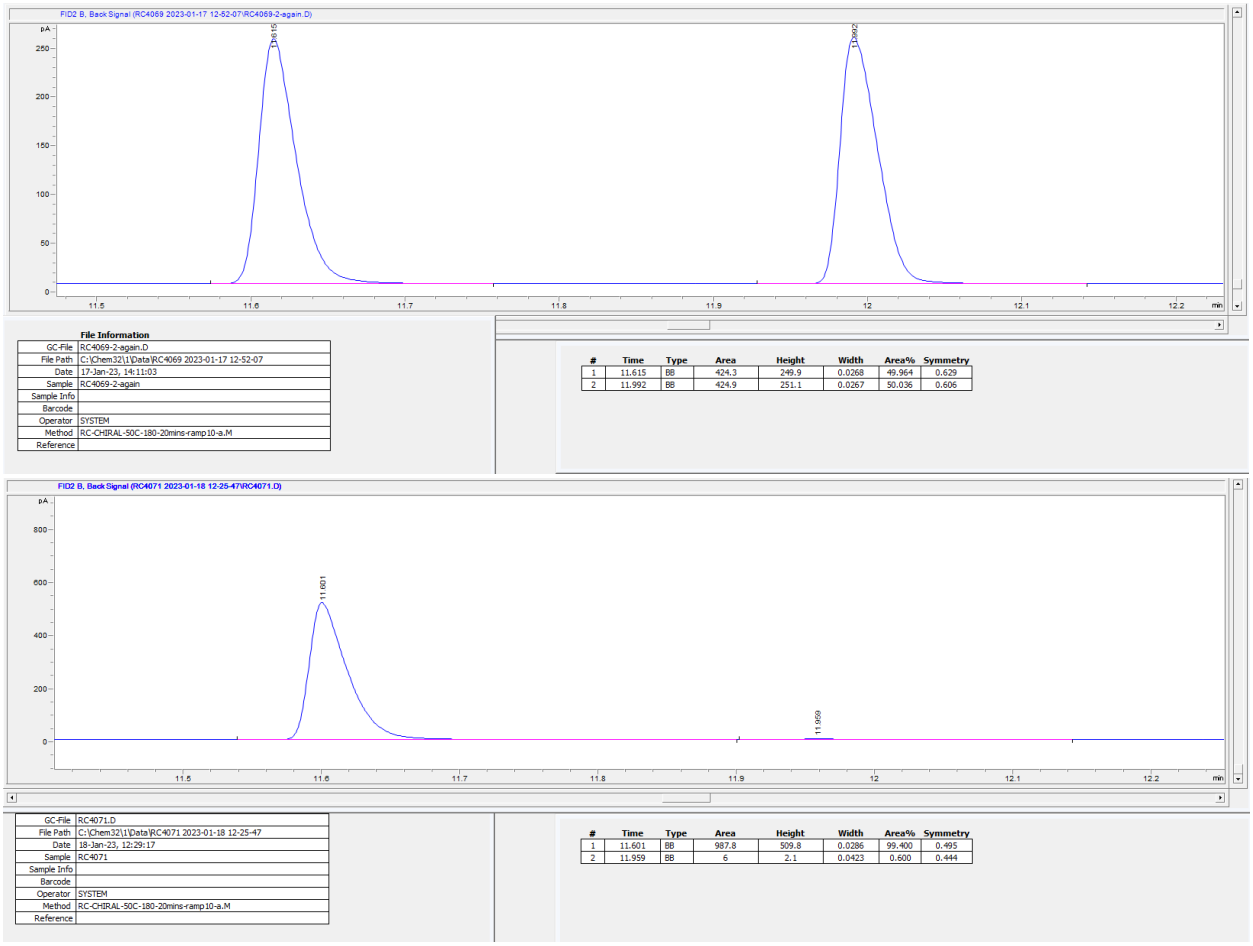

(S)-2-(2-hydroxypropyl)furan (**P20**)

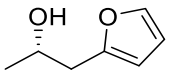

^{1}H NMR (600 MHz, $CDCl_3$) δ 7.35 (dd, *J* = 1.9, 0.8 Hz, 1H), 6.32 (dd, *J* = 3.2, 1.9 Hz, 1H), 6.15 – 6.07 (m, 1H), 4.10 (dqd, *J* = 7.4, 6.2, 4.5 Hz, 1H), 2.86 – 2.71 (m, 2H), 1.75 (s, 1H), 1.24 (d, *J* = 6.2 Hz, 4H).

^{13}C NMR (151 MHz, $CDCl_3$) δ 152.99, 141.81, 110.45, 107.15, 66.94, 37.99, 22.88.

Spectral data match those previously reported.[54]

Separation of corresponding acetate enantiomers (**P20-Ac**): Chirasil-Dex CB, inject temperature = 250 °C, detector temperature = 300 °C, inlet pressure = 12.5 psi, flow rate = 1.3 mL/ min, split ratio = 50:1, temperature program = 50 °C (0 min) - 10 °C/min - 180 °C

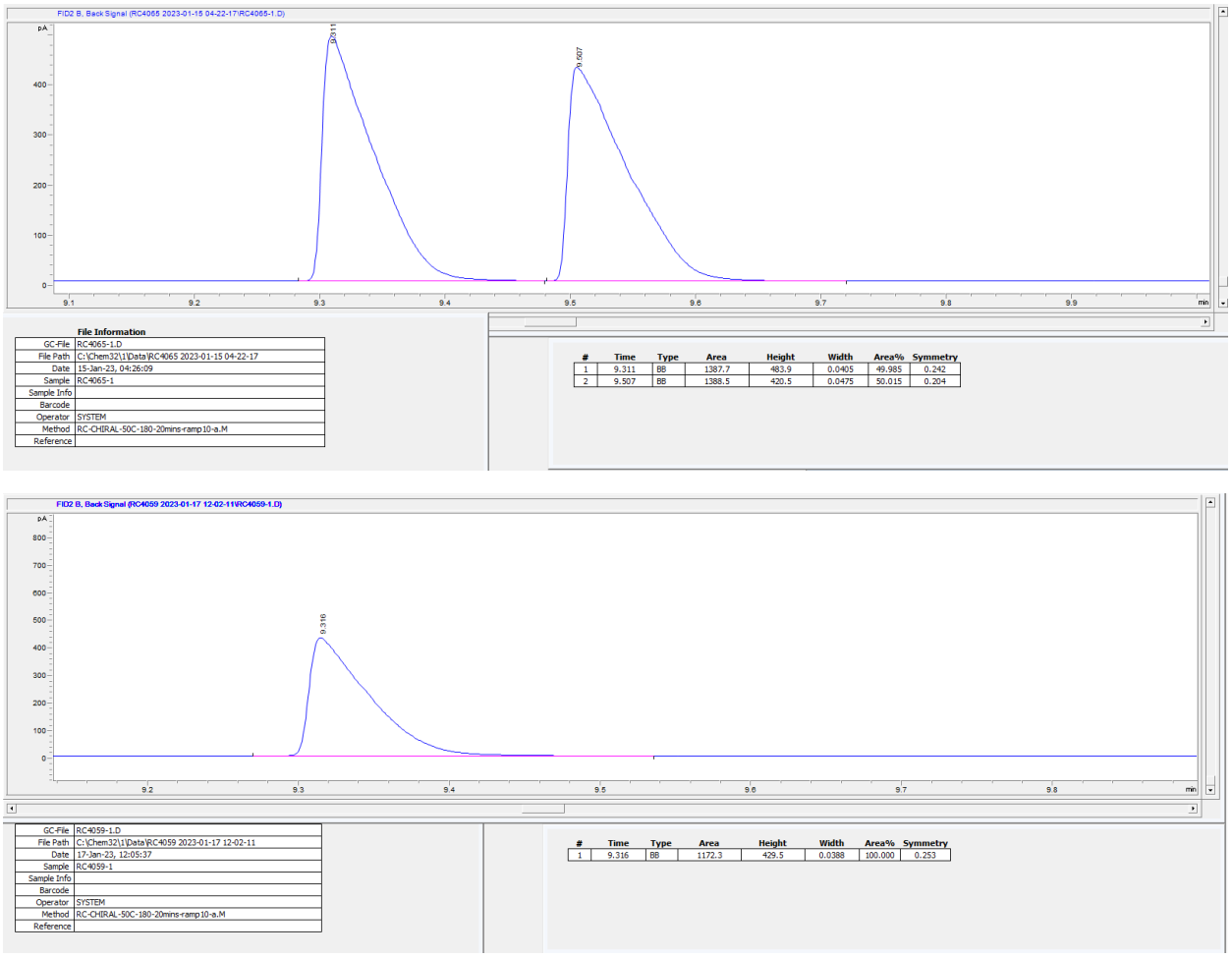

(S)-2-(2-thienyl)-1-hydroxy-1-methylethane (**P21**)

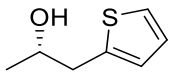

^{1}H NMR (500 MHz, $CDCl_3$) δ 7.18 (dd, J = 5.2, 1.2 Hz, 1H), 6.96 (dd, J = 5.1, 3.4 Hz, 1H), 6.87 (dd, J = 3.4, 1.1 Hz, 1H), 4.02 (dqd, J = 7.9, 6.2, 4.4 Hz, 1H), 3.08 – 2.81 (m, 2H), 1.26 (d, J = 6.2 Hz, 3H).

^{13}C NMR (126 MHz, $CDCl_3$) δ 140.66, 127.13, 126.13, 124.34, 68.78, 39.77, 22.66.

Spectral data match those previously reported.[55]

Separation of corresponding acetate enantiomers (**P21-Ac**): Chirasil-Dex CB, inject temperature = 250 °C, detector temperature = 300 °C, inlet pressure = 12.5 psi, flow rate = 1.3 mL/ min, split ratio = 50:1, temperature program = 50 °C (0 min) - 10 °C/min - 180 °C

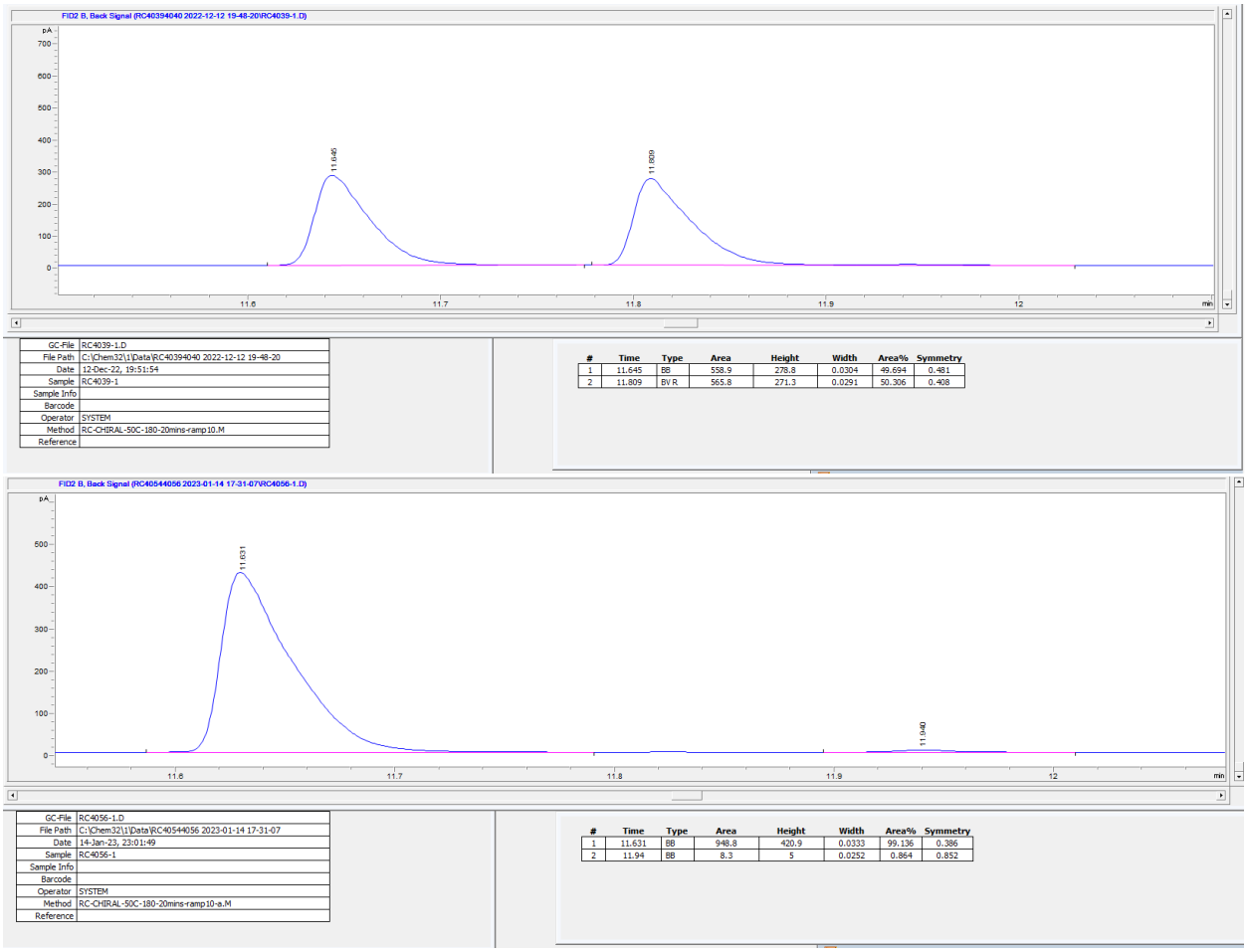

(S)-1-(pyridin-2-yl)propan-2-ol (**P22**)

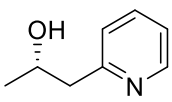

^{1}H NMR (600 MHz, $CDCl_3$) δ 8.48 (ddd, *J* = 5.0, 1.9, 1.0 Hz, 1H), 7.61 (td, *J* = 7.7, 1.9 Hz, 1H), 7.18 – 7.09 (m, 2H), 4.23 (ddp, *J* = 12.4, 6.2, 3.2 Hz, 1H), 2.94 – 2.74 (m, 2H), 1.27 (d, *J* = 6.2 Hz, 3H).

^{13}C NMR (151 MHz, $CDCl_3$) δ 160.25, 148.59, 136.74, 123.66, 121.51, 67.17, 44.97, 22.99.

Spectral data match those previously reported.[56]

Separation of corresponding acetate enantiomers (**P22-Ac**): Chirasil-Dex CB, inject temperature = 250 °C, detector temperature = 300 °C, inlet pressure = 12.5 psi, flow rate = 1.3 mL/ min, split ratio = 50:1, temperature program = 50 °C (0 min) - 10 °C/min - 180 °C

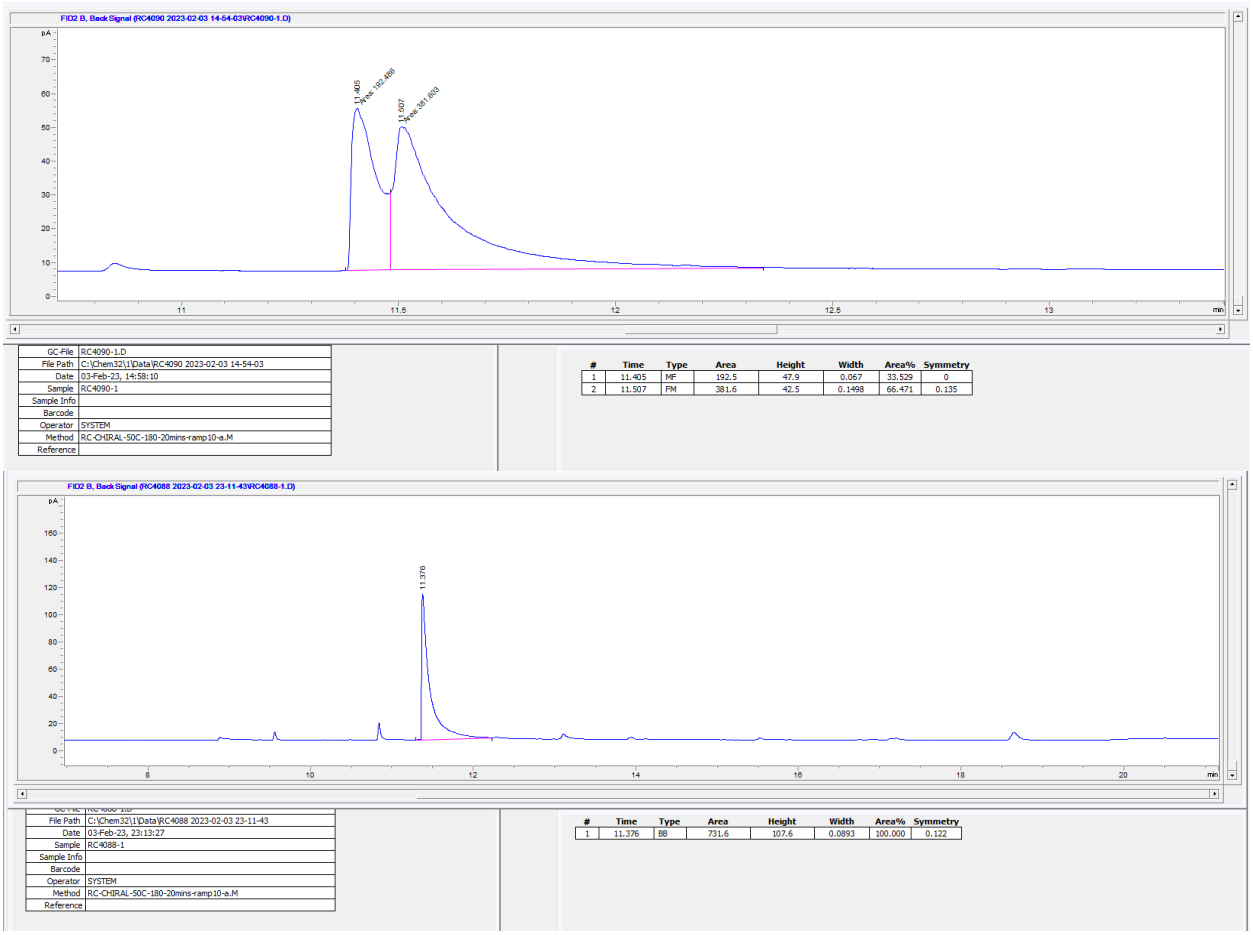

(S)-1-(5-methyl-1,2-oxazol-4-yl)propan-2-ol (**P23**)

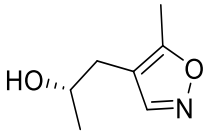

^{1}H NMR (500 MHz, $CDCl_3$) δ 5.93 (s, 1H), 4.18 (h, J = 6.2 Hz, 1H), 2.93 – 2.81 (m, 2H), 2.27 (s, 3H), 1.28 (d, J = 6.3 Hz, 3H).

^{13}C NMR (126 MHz, $CDCl_3$) δ 170.12, 160.07, 103.33, 66.35, 36.52, 23.23, 11.54.

HR MS (pESI): calcd. For $C_7H_{12}O_2N$ $[M+H]^+$: 142.08, found: 142.0863

Separation of corresponding acetate enantiomers (**P23-Ac**): Chirasil-Dex CB, inject temperature = 250 °C, detector temperature = 300 °C, inlet pressure = 12.5 psi, flow rate = 1.3 mL/ min, split ratio = 50:1, temperature program = 50 °C (0 min) - 10 °C/min - 180 °C

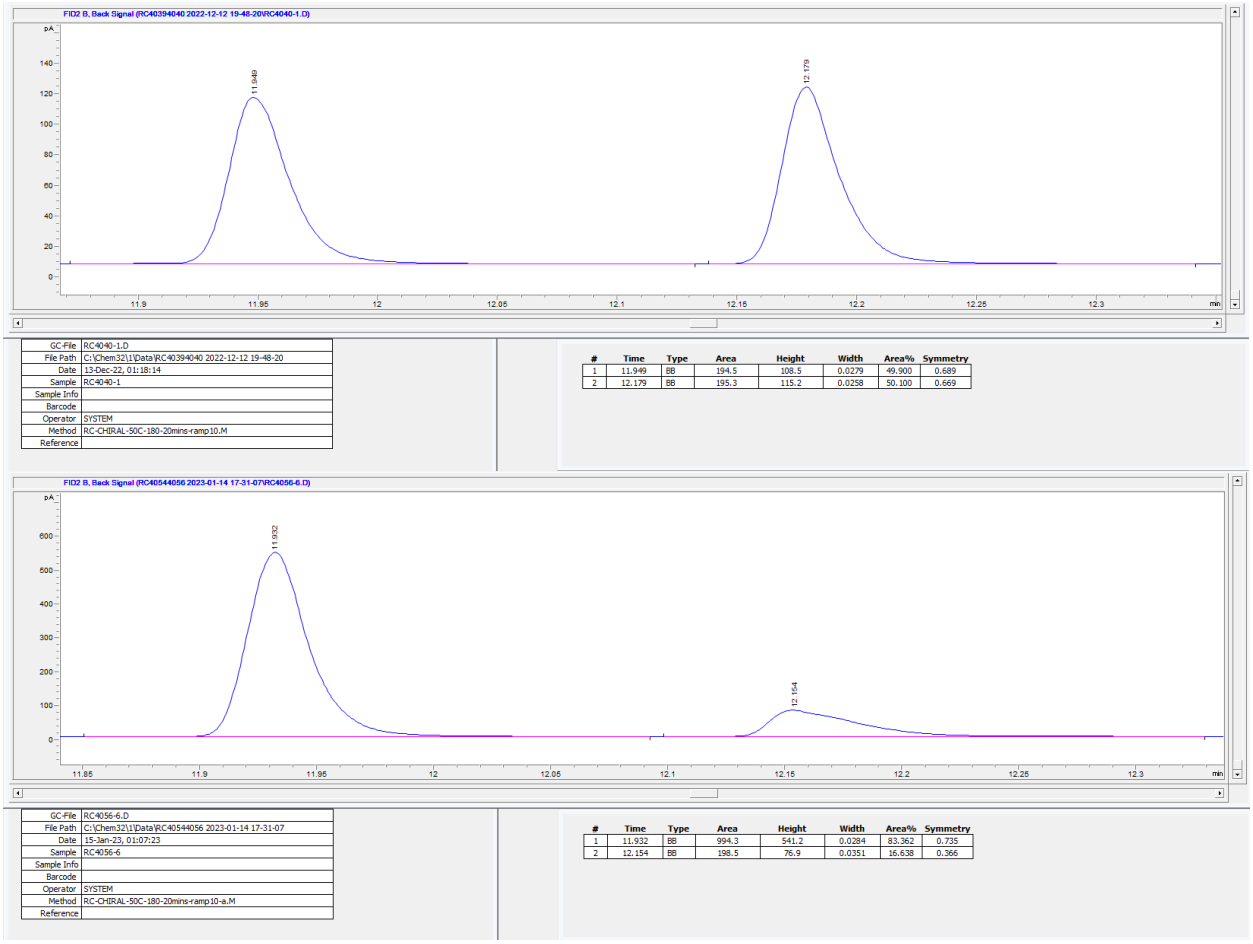

(S)-1-(5-methyl-1,2-oxazol-4-yl) ethanol (**P24**)

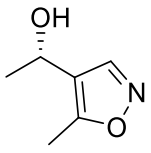

^{1}H NMR (500 MHz, $CDCl_3$) δ 8.20 (s, 1H), 4.87 (q, *J* = 6.5 Hz, 1H), 2.44 (s, 3H), 1.50 (d, *J* = 6.4 Hz, 3H).

^{13}C NMR (126 MHz, $CDCl_3$) δ 164.80, 149.13, 119.08, 77.36, 61.42, 24.31, 11.25.

HR MS (pESI): calcd. For $C_6H_{10}O_2N$ $[M+H]^+$: 128.14, found: 128.0706

Separation of corresponding acetate enantiomers (**P24-Ac**): Chirasil-Dex CB, inject temperature = 250 °C, detector temperature = 300 °C, inlet pressure = 12.5 psi, flow rate = 1.3 mL/ min, split ratio = 50:1, temperature program = 50 °C (0 min) - 10 °C/min - 180 °C

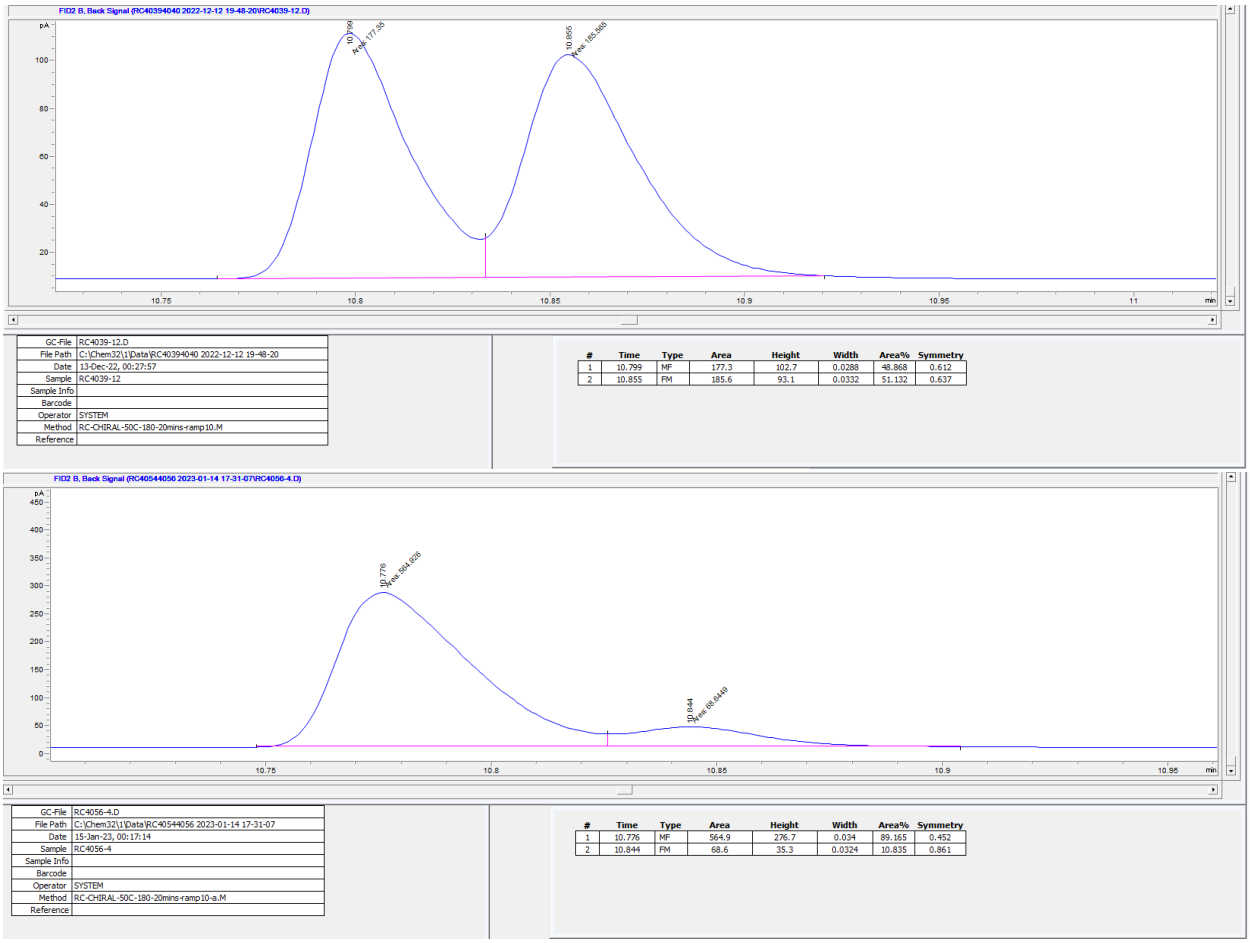

(S)-3-hexanol (**P25**)

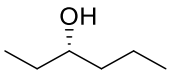

^{1}H NMR (500 MHz, $CDCl_3$) δ 3.53 (tt, *J* = 7.2, 4.5 Hz, 1H), 1.54 – 1.30 (m, 7H), 0.93 (td, *J* = 7.2, 5.2 Hz, 6H).

^{13}C NMR (126 MHz, $CDCl_3$) δ 73.18, 39.28, 30.29, 18.97, 14.25, 9.99.

Spectral data match those previously reported.[57]

Separation of corresponding acetate enantiomers (**P25-Ac**): Chirasil-Dex CB, inject temperature = 250 °C, detector temperature = 300 °C, inlet pressure = 12.5 psi, flow rate = 1.3 mL/ min, split ratio = 50:1, temperature program = 50 °C (0 min) - 10 °C/min - 180 °C

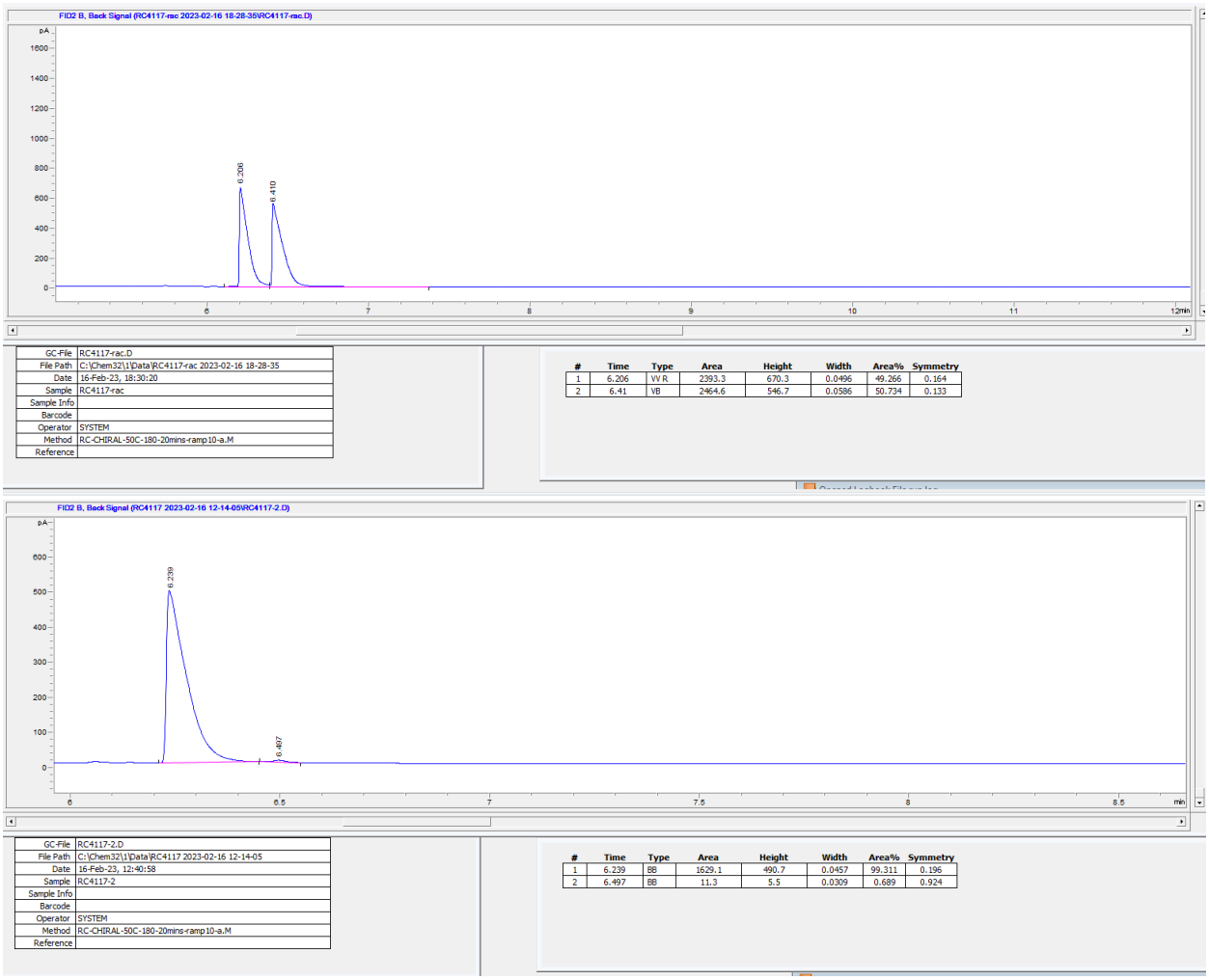

(R)-2-pentanol (**P26**)

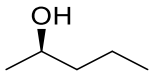

^{1}H NMR (600 MHz, $CDCl_3$) δ 3.90 – 3.75 (m, 1H), 1.53 – 1.31 (m, 5H), 1.20 (d, J = 6.1 Hz, 3H), 1.03 – 0.88 (m, 3H).

^{13}C NMR (151 MHz, $CDCl_3$) δ 68.03, 41.68, 23.61, 19.07, 14.19.

Spectral data match those previously reported.[42]

Separation of corresponding acetate enantiomers (**P26-Ac**): Chirasil-Dex CB, inject temperature = 250 °C, detector temperature = 300 °C, inlet pressure = 12.5 psi, flow rate = 1.3 mL/ min, split ratio = 50:1, temperature program = 50 °C (0 min) - 10 °C/min - 180 °C

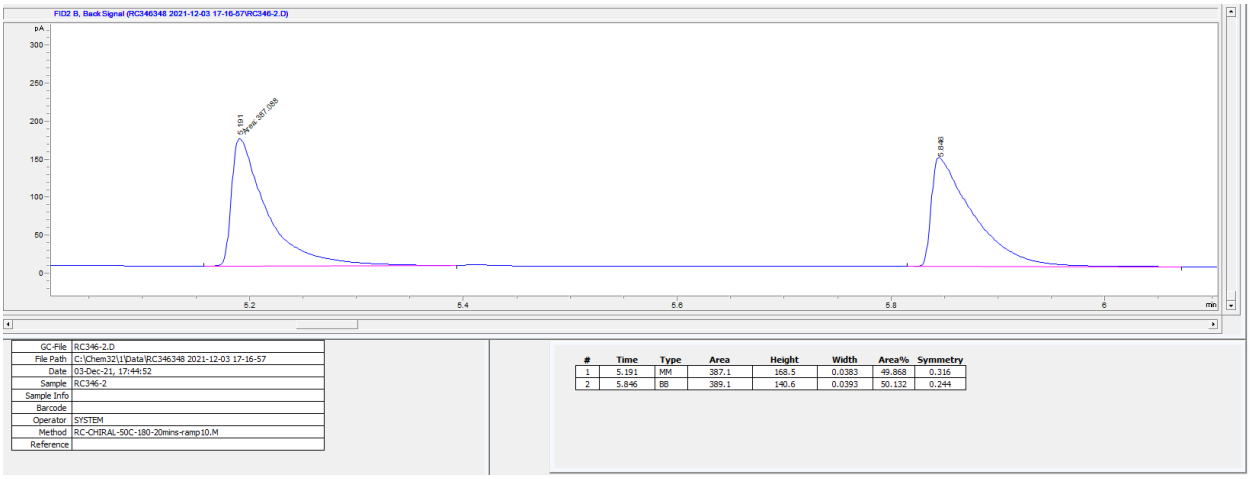

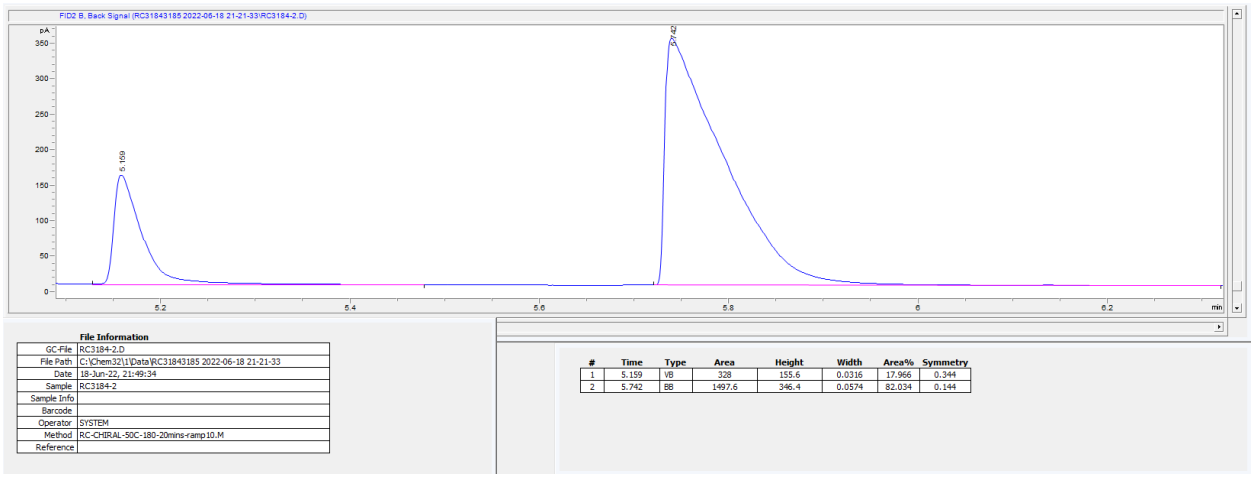

(R)-3-hexanol (**P27**) catalyzed by W209L

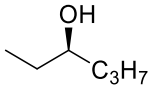

^{1}H NMR (500 MHz, $CDCl_3$) δ 3.53 (tt, J = 7.2, 4.5 Hz, 1H), 1.54 – 1.30 (m, 7H), 0.93 (td, J = 7.2, 5.2 Hz, 6H).

^{13}C NMR (126 MHz, $CDCl_3$) δ 73.18, 39.28, 30.29, 18.97, 14.25, 9.99.

$[\alpha]_D^{25}$ = -118.3 ($CDCl_3$)

Spectral data match those previously reported.[57]

Separation of corresponding acetate enantiomers (**P27-Ac**): Chirasil-Dex CB, inject temperature = 250 °C, detector temperature = 300 °C, inlet pressure = 12.5 psi, flow rate = 1.3 mL/ min, split ratio = 50:1, temperature program = 50 °C (0 min) - 10 °C/min - 180 °C

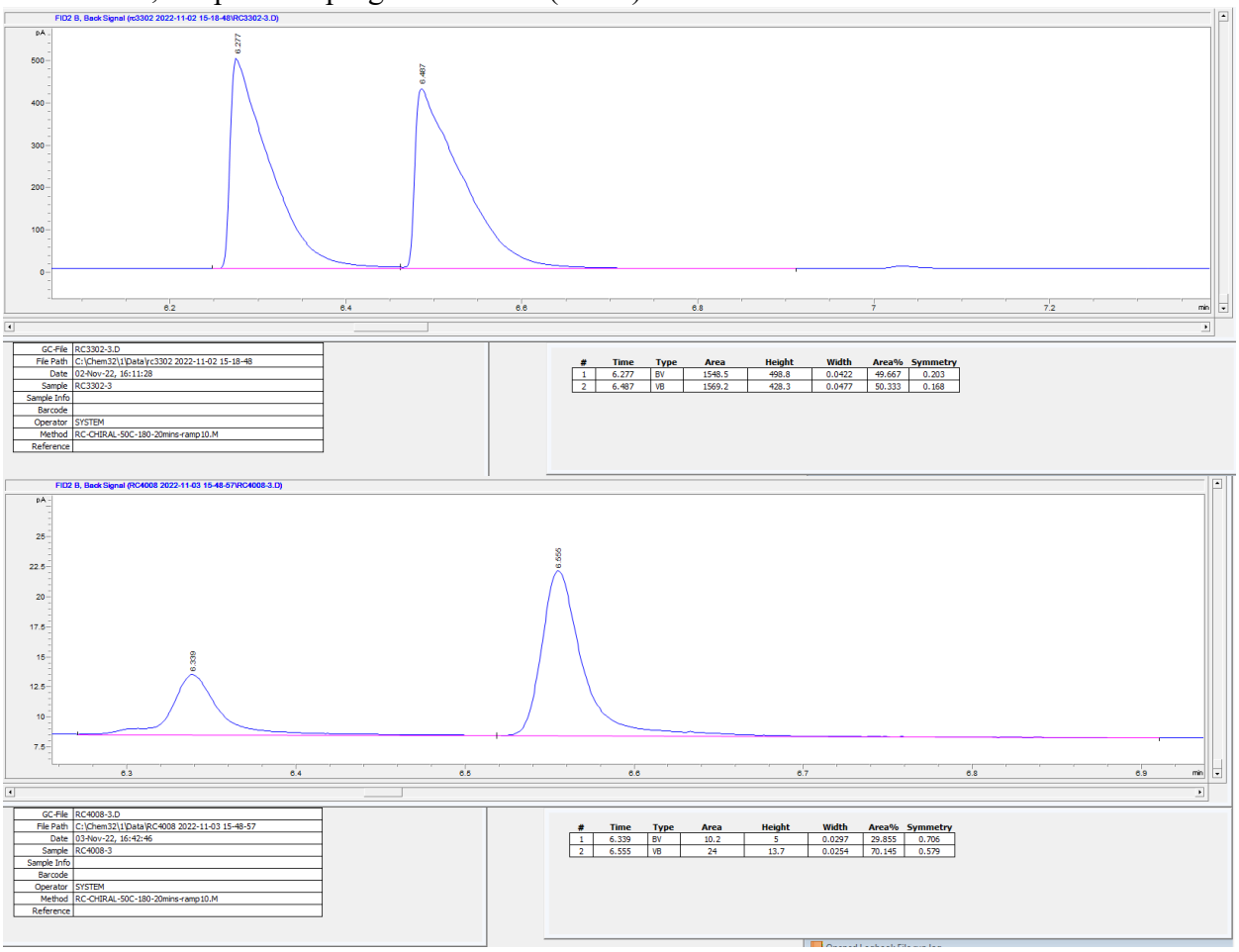

(R)-3-hexanol (**P27**) catalyzed by W209A

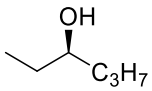

^{1}H NMR (600 MHz, $CDCl_3$) δ 3.52 (tt, J = 7.3, 4.5 Hz, 1H), 1.57 – 1.36 (m, 6H), 1.36 – 1.22 (m, 4H), 0.92 (dt, J = 18.4, 7.3 Hz, 6H).

^{13}C NMR (151 MHz, $CDCl_3$) δ 73.47, 36.79, 30.28, 27.99, 22.91, 14.20, 10.00.

Spectral data match those previously reported.[57]

Separation of corresponding acetate enantiomers (**P27-Ac**): Chirasil-Dex CB, inject temperature = 250 °C, detector temperature = 300 °C, inlet pressure = 12.5 psi, flow rate = 1.3 mL/ min, split ratio = 50:1, temperature program = 50 °C (0 min) - 10 °C/min - 180 °C

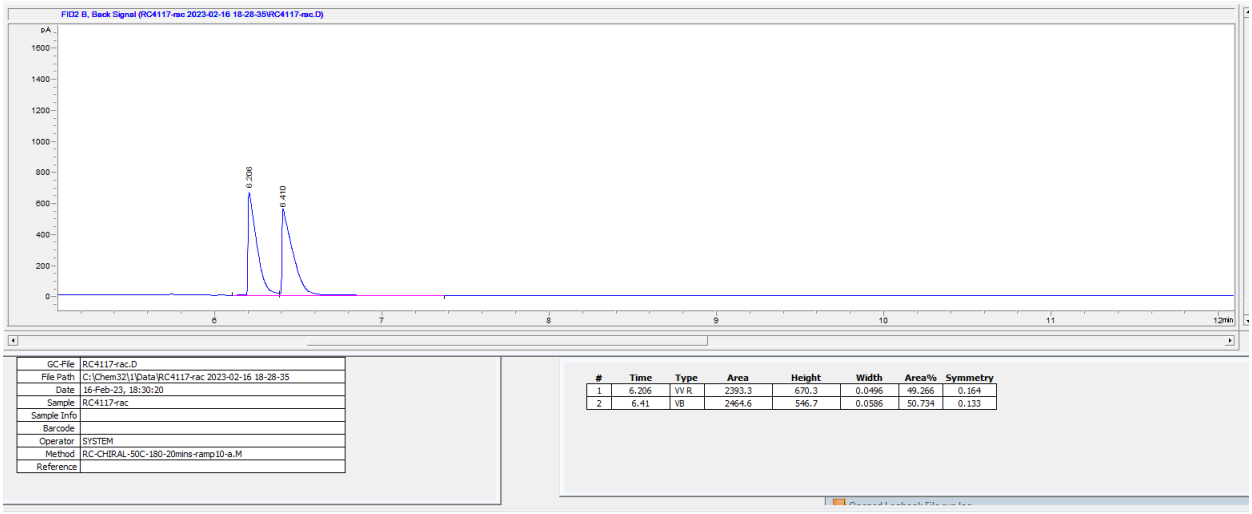

GC-File	RC4117-rac.D
File Path	C:\Chem32\1\Data\RC4117-rac 2023-02-16 18-28-35
Date	16-Feb-23, 18:30:20
Sample	RC4117-rac
Sample Info	
Barcode	
Operator	SYSTEM
Method	RC-CHIRAL-50C-180-20mins-ramp10-a.M
Reference	

#	Time	Type	Area	Height	Width	Area%	Symmetry
1	6.206	VV R	2393.3	670.3	0.0496	49.266	0.164
2	6.41	VB	2464.6	546.7	0.0586	50.734	0.133

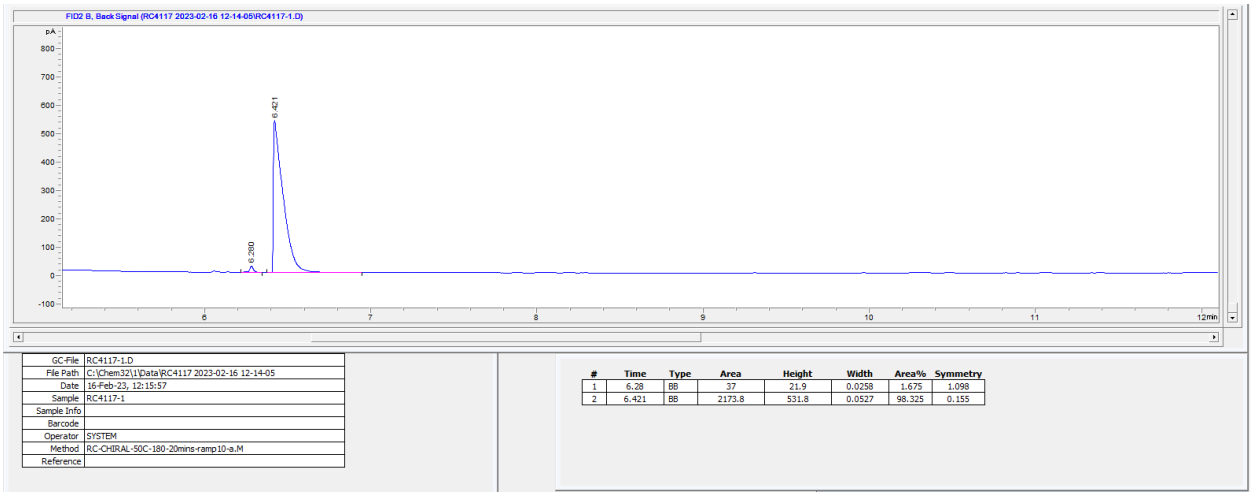

GC-File	RC4117-1.D
File Path	C:\Chem32\1\Data\RC4117 2023-02-16 12-14-05
Date	16-Feb-23, 12:15:57
Sample	RC4117-1
Sample Info	
Barcode	
Operator	SYSTEM
Method	RC-CHIRAL-50C-180-20mins-ramp10-a.M
Reference	

#	Time	Type	Area	Height	Width	Area%	Symmetry
1	6.28	BB	37	21.9	0.0258	1.675	1.098
2	6.421	BB	2173.8	531.8	0.0527	98.325	0.155

(S)-4-nonanol (**P28**)

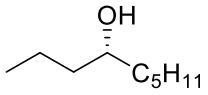

^{1}H NMR (500 MHz, $CDCl_3$) δ 3.64 – 3.54 (m, 1H), 1.59 – 1.15 (m, 14H), 0.90 (dt, *J* = 17.4, 6.9 Hz, 6H).

^{13}C NMR (126 MHz, $CDCl_3$) δ 71.85, 39.80, 37.60, 32.06, 25.46, 22.78, 18.96, 14.24, 14.17.

Spectral data match those previously reported.[58]

Separation of corresponding acetate enantiomers (**P28-Ac**): Chirasil-Dex CB, inject temperature = 250 °C, detector temperature = 300 °C, inlet pressure = 12.5 psi, flow rate = 1.3 mL/ min, split ratio = 50:1, temperature program = 50 °C (0 min) - 10 °C/min - 180 °C

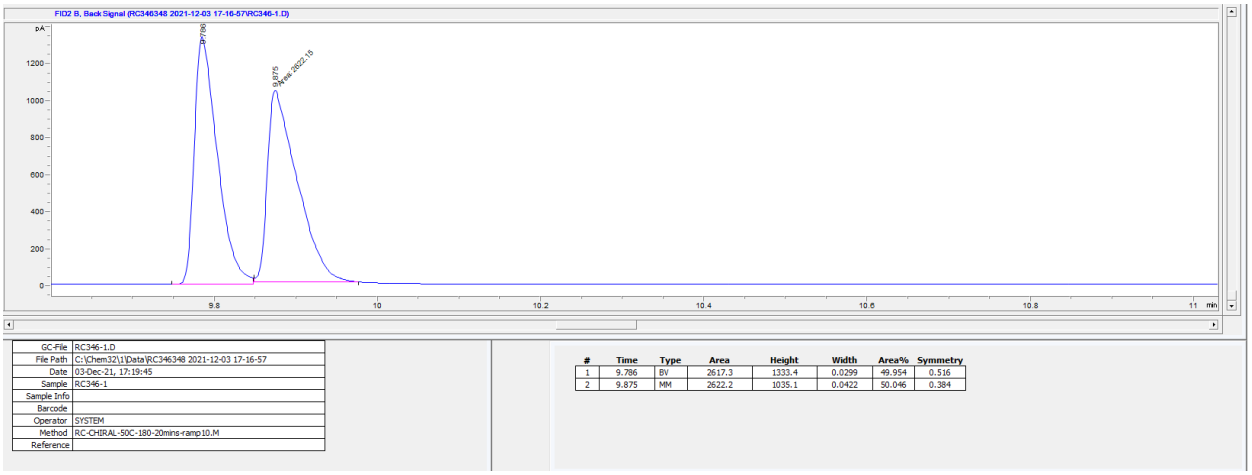

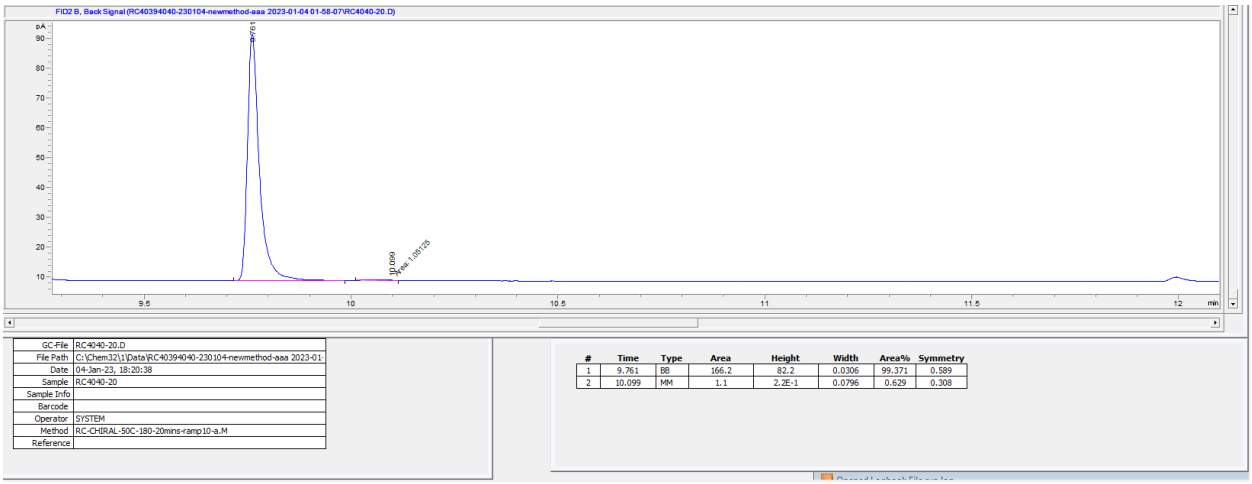

(S)-3-heptanol (**P29**)

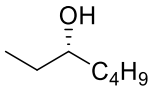

^{1}H NMR (600 MHz, $CDCl_3$) δ 3.52 (tt, *J* = 7.3, 4.6 Hz, 1H), 1.56 – 1.37 (m, 6H), 1.32 (ddddd, *J* = 14.2, 12.3, 8.4, 7.0, 1.9 Hz, 4H), 0.92 (dt, *J* = 18.5, 7.3 Hz, 6H).

^{13}C NMR (151 MHz, $CDCl_3$) δ 73.47, 36.79, 30.28, 27.99, 22.91, 14.20, 10.00.

Spectral data match those previously reported.[59]

Separation of corresponding acetate enantiomers (**P29-Ac**): Chirasil-Dex CB, inject temperature = 250 °C, detector temperature = 300 °C, inlet pressure = 12.5 psi, flow rate = 1.3 mL/ min, split ratio = 50:1, temperature program = 50 °C (0 min) - 10 °C/min - 180 °C

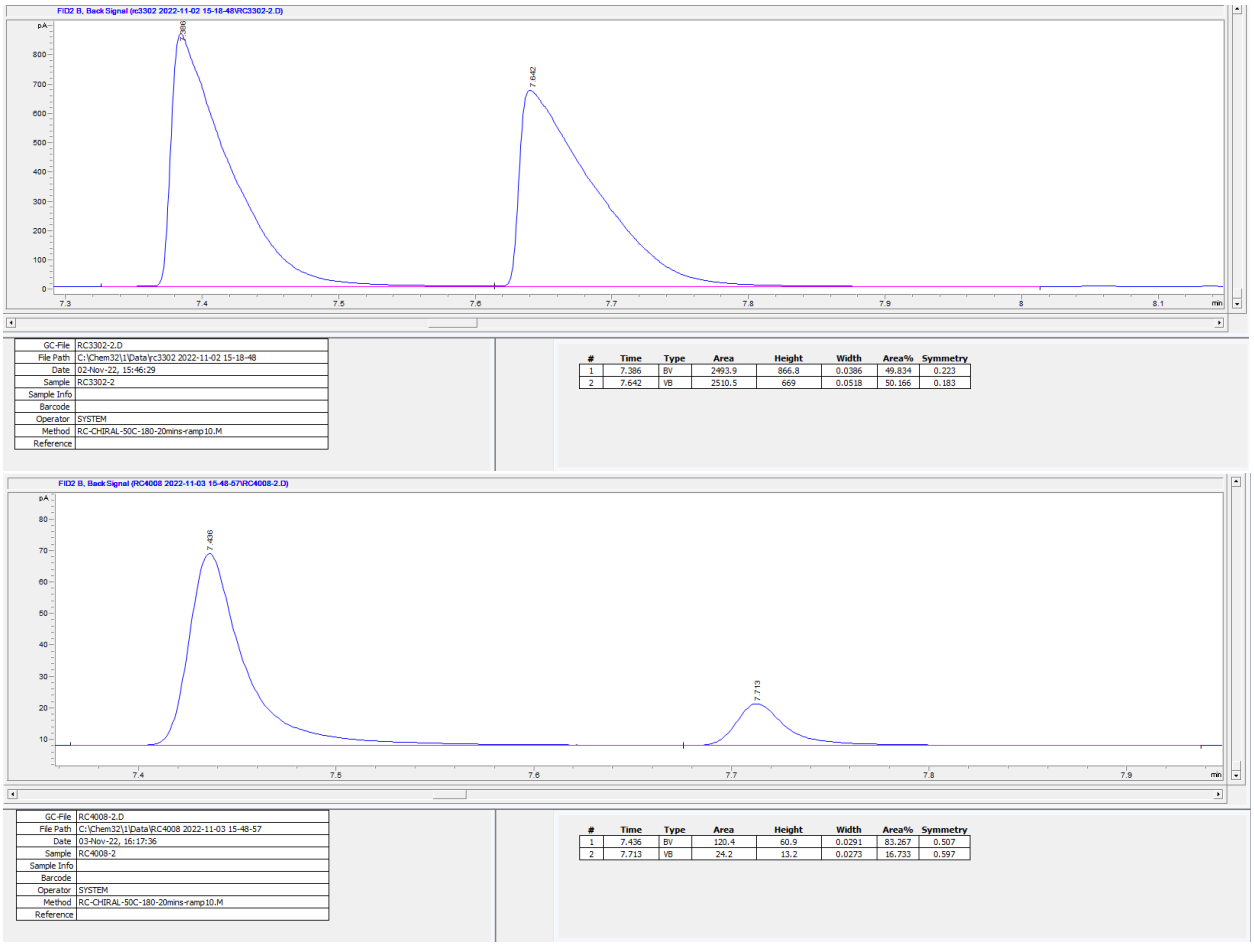

(S)-3-octanol (**P30**)

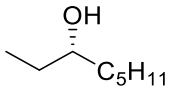

^{1}H NMR (600 MHz, $CDCl_3$) δ 3.51 (tq, J = 7.3, 4.4 Hz, 1H), 1.57 – 1.36 (m, 6H), 1.35 – 1.20 (m, 5H), 0.93 (t, J = 7.5 Hz, 3H), 0.88 (t, J = 6.8 Hz, 3H).

^{13}C NMR (151 MHz, $CDCl_3$) δ 73.46, 37.06, 32.06, 30.27, 25.47, 22.78, 14.16, 9.99.

$[\alpha]_D^{25}$ = +29.1 ($CDCl_3$)

Spectral data match those previously reported.[60]

Separation of corresponding acetate enantiomers (**P30-Ac**): Chirasil-Dex CB, inject temperature = 250 °C, detector temperature = 300 °C, inlet pressure = 12.5 psi, flow rate = 1.3 mL/ min, split ratio = 50:1, temperature program = 50 °C (0 min) - 10 °C/min - 180 °C

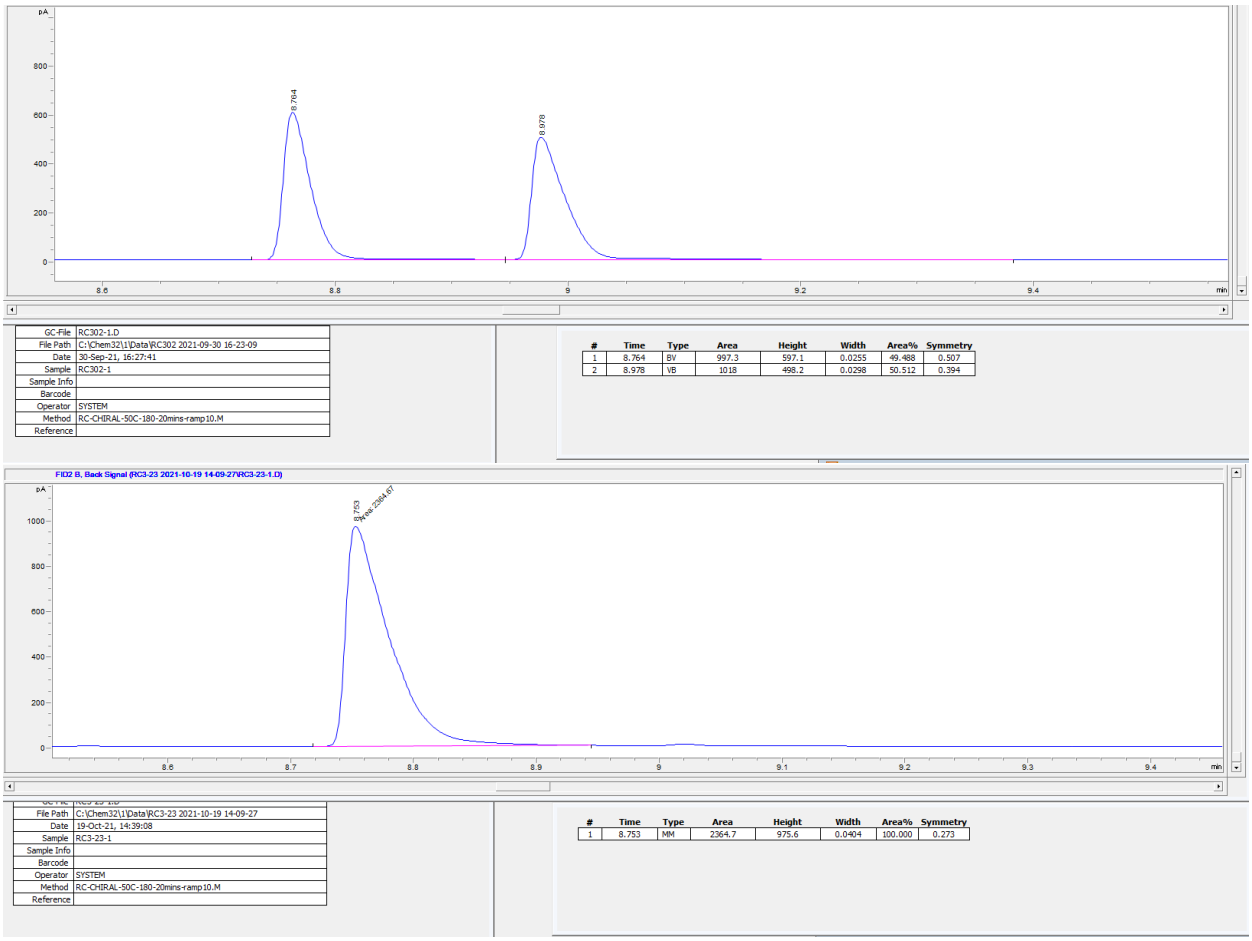

(S)-3-nonanol (**P31**)

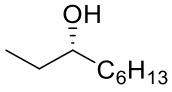

^{1}H NMR (600 MHz, $CDCl_3$) δ 3.62 – 3.46 (m, 1H), 1.59 – 1.21 (m, 14H), 0.95 (t, J = 7.4 Hz, 3H), 0.90 (t, J = 6.9 Hz, 3H).

^{13}C NMR (151 MHz, $CDCl_3$) δ 73.48, 37.11, 31.99, 30.28, 29.53, 25.77, 22.76, 14.21, 10.00.

Spectral data match those previously reported.[61]

Separation of corresponding acetate enantiomers (**P31-Ac**): Chirasil-Dex CB, inject temperature = 250 °C, detector temperature = 300 °C, inlet pressure = 12.5 psi, flow rate = 1.3 mL/ min, split ratio = 50:1, temperature program = 50 °C (0 min) - 10 °C/min - 180 °C

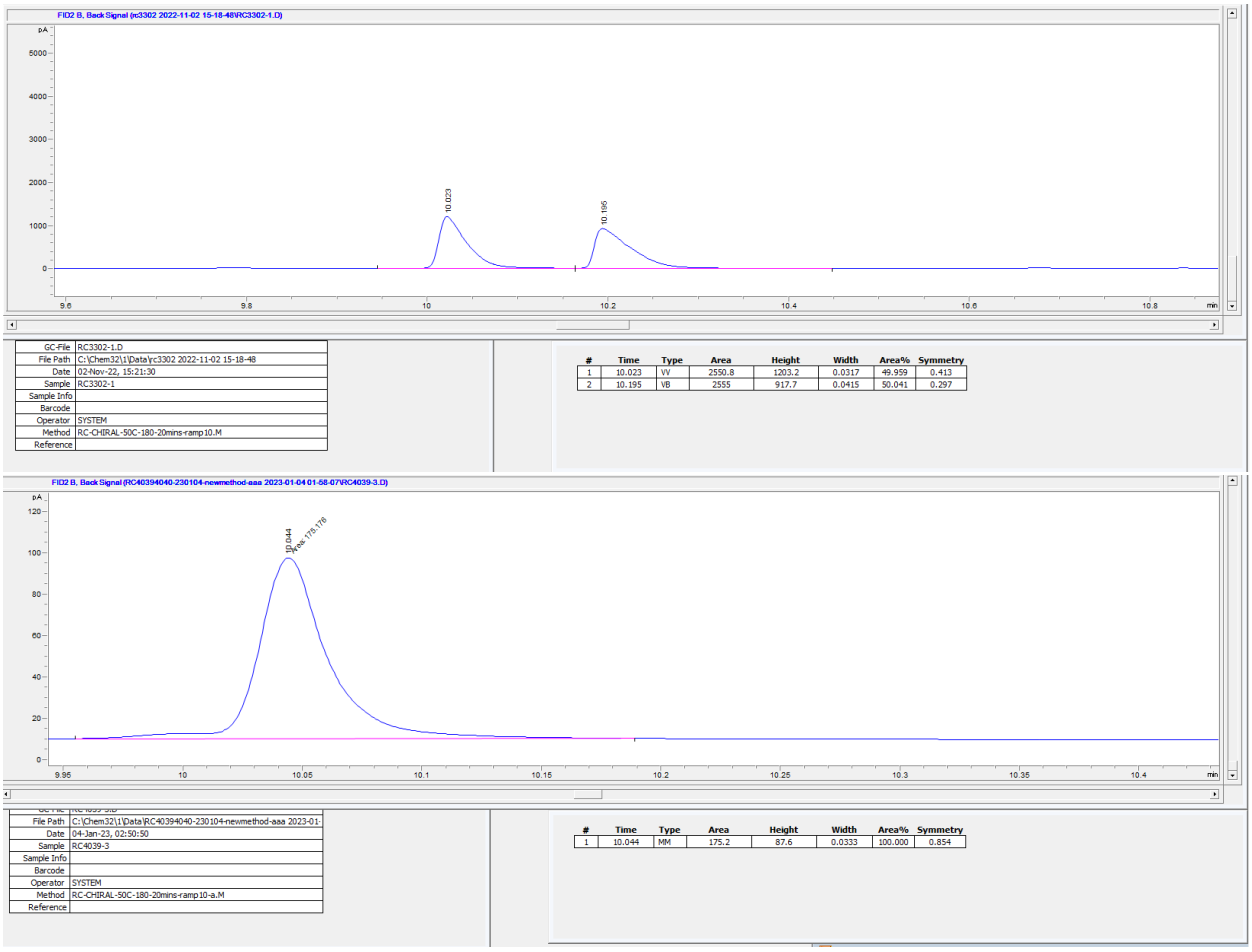

(S)-2-methyl-3-pentanol (**P32**)

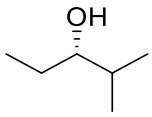

^{1}H NMR (600 MHz, $CDCl_3$) δ 3.28 (ddd, J = 8.7, 5.2, 3.8 Hz, 1H), 1.66 (pd, J = 6.8, 5.2 Hz, 1H), 1.53 (dqd, J = 13.8, 7.5, 3.8 Hz, 1H), 1.45 – 1.35 (m, 2H), 0.96 (t, J = 7.4 Hz, 3H), 0.91 (dd, J = 6.8, 5.2 Hz, 6H).

^{13}C NMR (151 MHz, $CDCl_3$) δ 78.37, 33.21, 27.09, 19.07, 17.22, 10.43.

Spectral data match those previously reported.[62]

Separation of corresponding acetate enantiomers (**P32-Ac**): Chirasil-Dex CB, inject temperature = 250 °C, detector temperature = 300 °C, inlet pressure = 12.5 psi, flow rate = 1.3 mL/ min, split ratio = 50:1, temperature program = 50 °C (0 min) - 10 °C/min - 180 °C

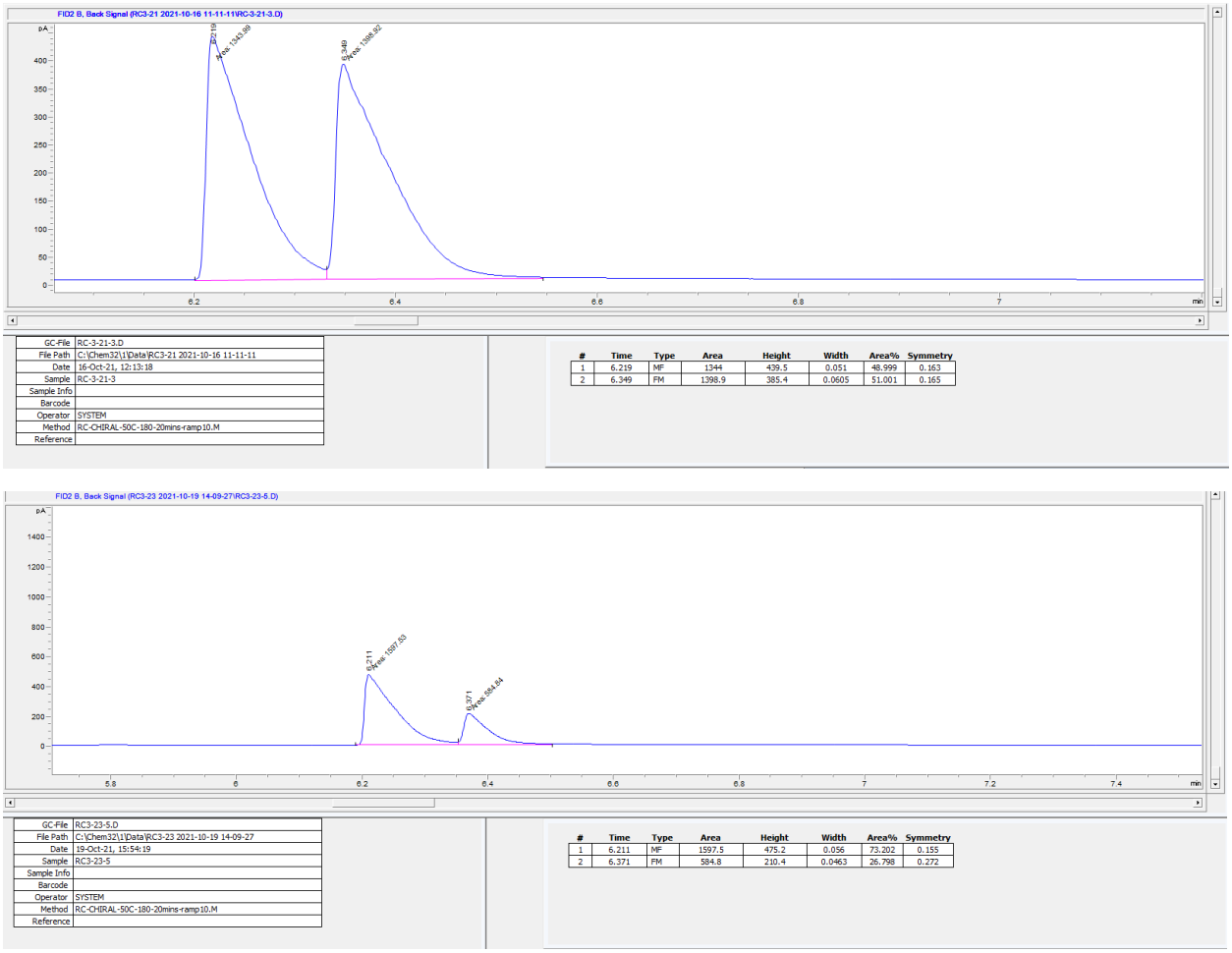

(S)-5-methylhexan-3-ol (**P33**)

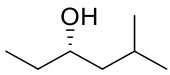

^{1}H NMR (600 MHz, $CDCl_3$) δ 3.60 (ddt, *J* = 8.8, 7.3, 4.3 Hz, 1H), 1.77 (dddd, *J* = 13.3, 11.9, 8.9, 6.6 Hz, 1H), 1.56 – 1.16 (m, 9H), 0.98 – 0.88 (m, 10H).

^{13}C NMR (151 MHz, $CDCl_3$) δ 71.47, 46.47, 30.90, 24.79, 23.68, 22.20, 9.98.

Spectral data match those previously reported.[63]

Separation of corresponding acetate enantiomers (**P33-Ac**): Chirasil-Dex CB, inject temperature = 250 °C, detector temperature = 300 °C, inlet pressure = 12.5 psi, flow rate = 1.3 mL/ min, split ratio = 50:1, temperature program = 50 °C (0 min) - 10 °C/min - 180 °C

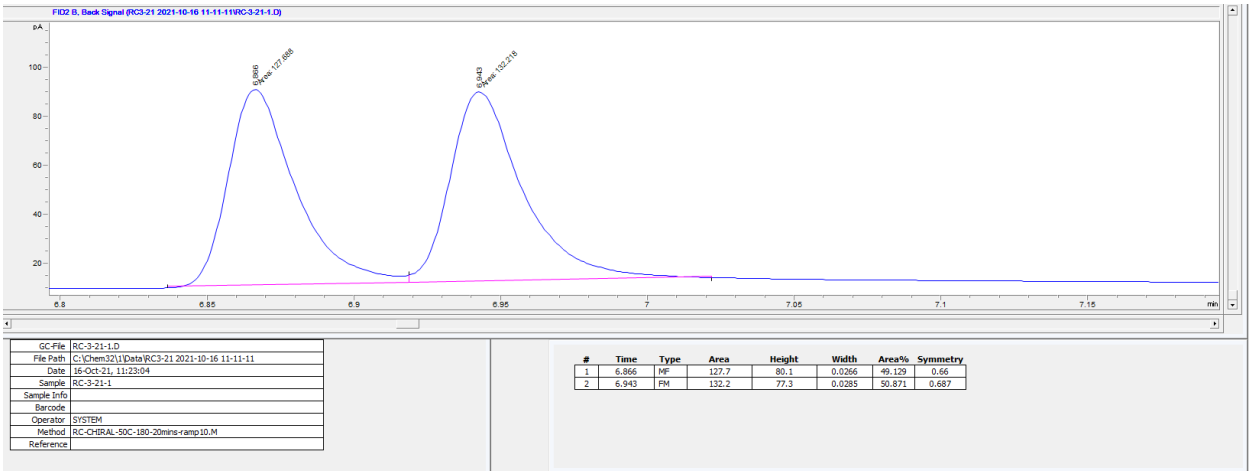

GC-File	RC-3-21-1.D
File Path	C:\Chem32\1\Data\RC3-21 2021-10-16 11-11-11
Date	16-Oct-21, 11:23:04
Sample	RC-3-21-1
Sample Info	
Barcode	
Operator	SYSTEM
Method	RC-CHIRAL-50C-180-20mins-ramp10.M
Reference	

#	Time	Type	Area	Height	Width	Area%	Symmetry
1	6.866	MF	127.7	80.1	0.0266	49.129	0.66
2	6.943	FM	132.2	77.3	0.0285	50.871	0.687

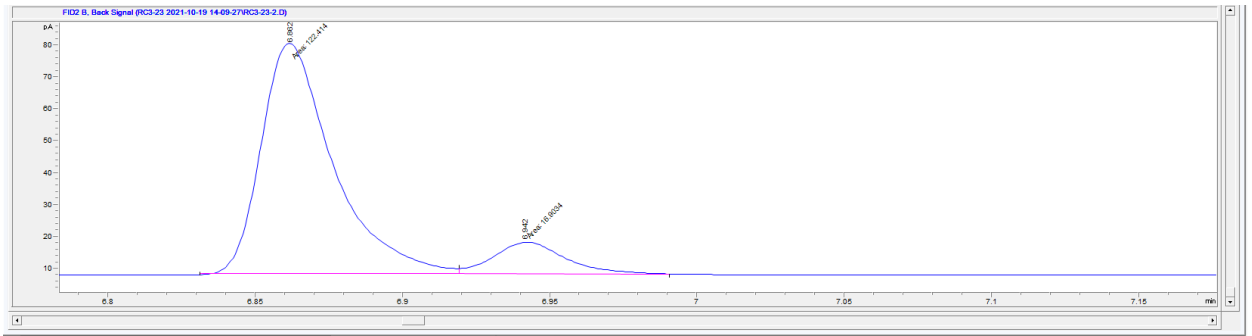

GC-File	RC3-23-2.D
File Path	C:\Chem32\1\Data\RC3-23 2021-10-19 14-09-27
Date	19-Oct-21, 15:04:08
Sample	RC3-23-2
Sample Info	
Barcode	
Operator	SYSTEM
Method	RC-CHIRAL-50C-180-20mins-ramp10.M
Reference	

#	Time	Type	Area	Height	Width	Area%	Symmetry
1	6.862	MF	122.4	72.6	0.0281	87.867	0.62
2	6.942	FM	16.9	9.9	0.0285	12.133	0

(S)-6-methylheptan-3-ol (**P34**)

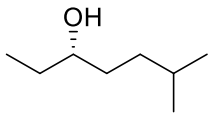

^{1}H NMR (600 MHz, $CDCl_3$) δ 3.51 (tt, *J* = 7.5, 4.7 Hz, 1H), 1.65 – 1.38 (m, 6H), 1.34 (dddd, *J* = 13.1, 11.5, 6.9, 4.7 Hz, 1H), 1.21 (dddd, *J* = 13.0, 11.6, 6.6, 5.4 Hz, 1H), 0.96 (t, *J* = 7.5 Hz, 3H), 0.91 (dd, *J* = 6.6, 4.0 Hz, 6H).

^{13}C NMR (151 MHz, CDCl3) δ 73.73, 34.92, 34.86, 30.24, 28.25, 22.78, 22.61, 9.95.

Spectral data match those previously reported.[64]

Separation of corresponding acetate enantiomers (**P34-Ac**): Chirasil-Dex CB, inject temperature = 250 °C, detector temperature = 300 °C, inlet pressure = 12.5 psi, flow rate = 1.3 mL/ min, split ratio = 50:1, temperature program = 50 °C (0 min) - 10 °C/min - 180 °C

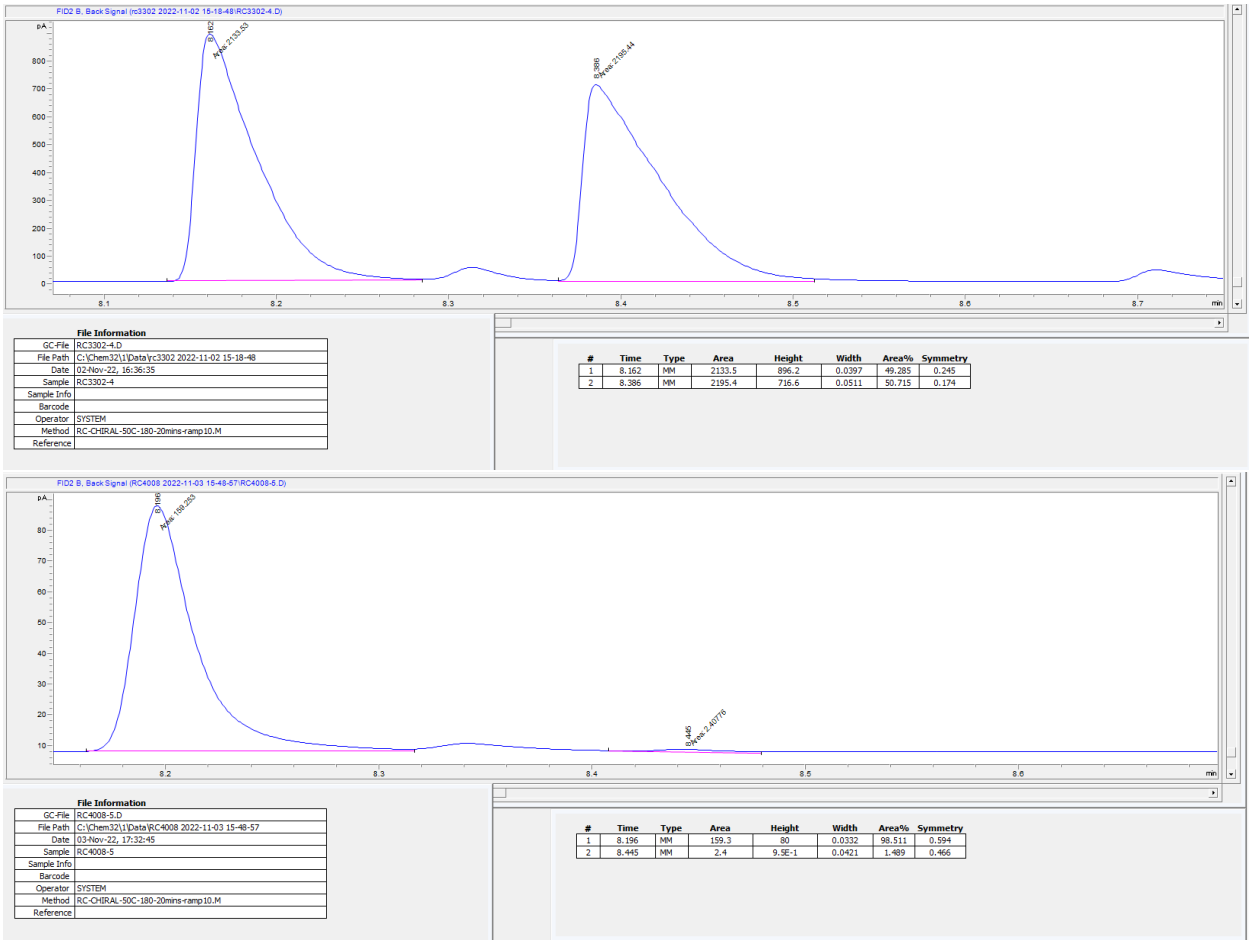

(S)-1-cyclohexylpropan-1-ol (**P35**)

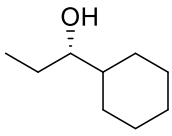

^{1}H NMR (600 MHz, $CDCl_3$) δ 3.26 (ddd, *J* = 8.9, 5.4, 3.8 Hz, 1H), 1.83 – 1.71 (m, 3H), 1.68 – 1.60 (m, 2H), 1.53 (dqd, *J* = 13.8, 7.5, 3.8 Hz, 1H), 1.45 – 0.97 (m, 9H), 0.94 (t, *J* = 7.4 Hz, 3H).

^{13}C NMR (151 MHz, $CDCl_3$) δ 77.73, 43.29, 29.44, 27.86, 26.95, 26.69, 26.51, 26.34, 10.33.

Spectral data match those previously reported.[60]

Separation of corresponding acetate enantiomers (**P35-Ac**): Chirasil-Dex CB, inject temperature = 250 °C, detector temperature = 300 °C, inlet pressure = 12.5 psi, flow rate = 1.3 mL/ min, split ratio = 50:1, temperature program = 50 °C (0 min) - 10 °C/min - 180 °C

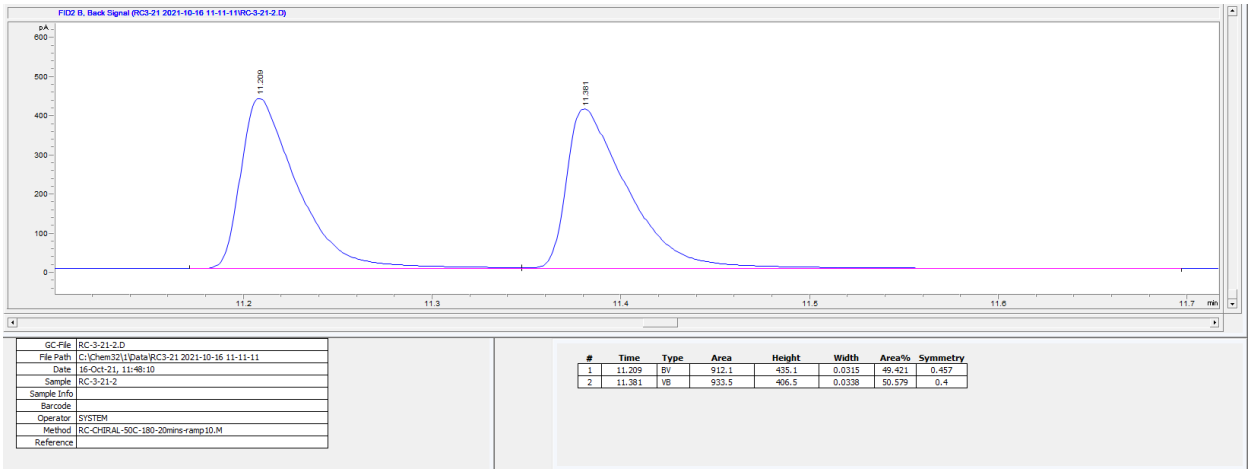

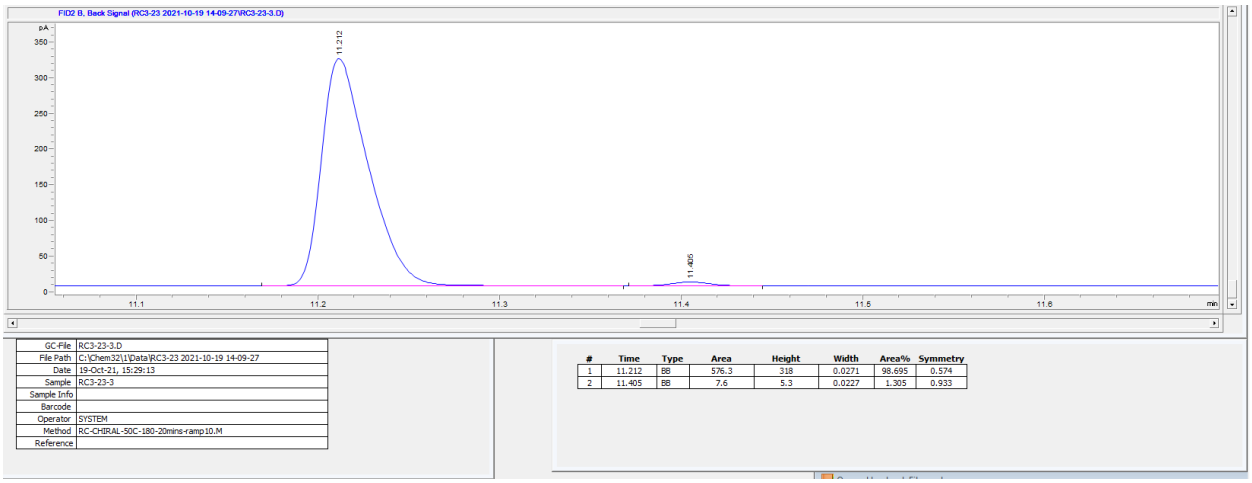

(S)-(E)-4-hexen-3-ol (**P36**)

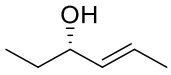

^{1}H NMR (500 MHz, $CDCl_3$) δ 5.83 (ddt, *J* = 16.9, 10.1, 6.6 Hz, 1H), 5.10 – 4.92 (m, 2H), 3.82 (dqd, *J* = 7.3, 6.2, 5.1 Hz, 1H), 2.27 – 2.01 (m, 2H), 1.62 – 1.47 (m, 3H), 1.19 (d, *J* = 6.2 Hz, 3H).

^{13}C NMR (126 MHz, $CDCl_3$) δ 138.62, 114.87, 67.79, 38.39, 30.28, 23.58.

Spectral data match those previously reported.[65]

Separation of corresponding acetate enantiomers (**P36-Ac**): Chirasil-Dex CB, inject temperature = 250 °C, detector temperature = 300 °C, inlet pressure = 12.5 psi, flow rate = 1.3 mL/ min, split ratio = 50:1, temperature program = 50 °C (0 min) - 10 °C/min - 180 °C

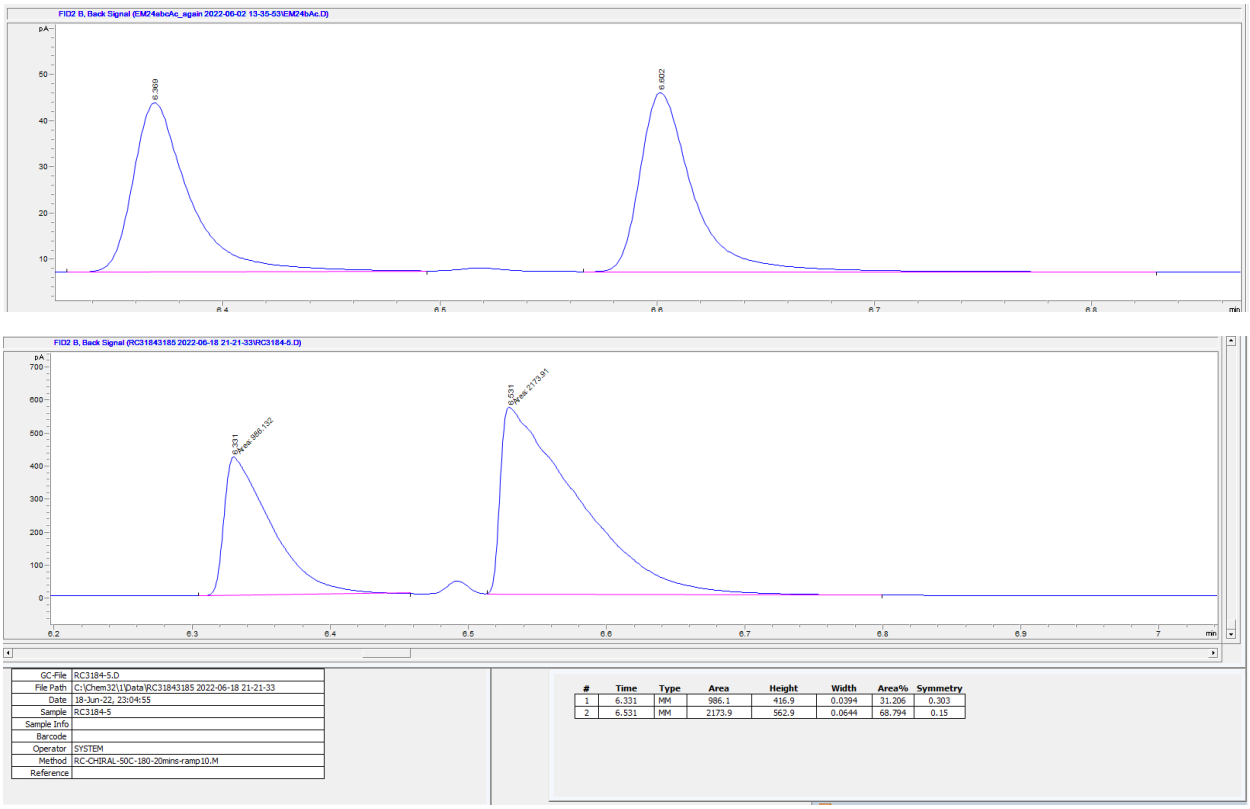

(S)-6-hepten-3-ol (**P37**)

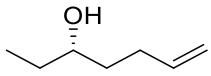

^{1}H NMR (600 MHz, $CDCl_3$δ 5.84 (ddt, J = 16.9, 10.2, 6.7 Hz, 1H), 5.04 (dq, J = 17.1, 1.8 Hz, 1H), 4.96 (ddt, J = 10.2, 2.4, 1.3 Hz, 1H), 3.54 (tt, J = 7.6, 4.5 Hz, 1H), 2.29 – 2.00 (m, 2H), 1.65 – 1.36 (m, 6H), 0.94 (t, J = 7.5 Hz, 3H).

^{13}C NMR (151 MHz, $CDCl_3$) δ 138.67, 114.72, 72.86, 35.99, 30.20, 30.09, 9.85.

Spectral data match those previously reported.

Separation of corresponding acetate enantiomers (**P37-Ac**): Chirasil-Dex CB, inject temperature = 250 °C, detector temperature = 300 °C, inlet pressure = 12.5 psi, flow rate = 1.3 mL/ min, split ratio = 50:1, temperature program = 50 °C (0 min) - 10 °C/min - 180 °C

(S)-2-(cyclohexen-1-yl)butan-3-ol (**P38**)

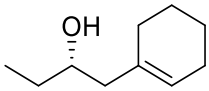

^{1}H NMR (500 MHz, $CDCl_3$) δ 5.53 (td, *J* = 3.3, 2.0 Hz, 1H), 3.69 – 3.52 (m, 1H), 2.17 – 1.93 (m, 5H), 1.72 – 1.40 (m, 8H), 0.96 (t, *J* = 7.5 Hz, 3H).

^{13}C NMR (126 MHz, $CDCl_3$) δ 135.00, 125.08, 77.36, 70.03, 46.21, 29.97, 28.51, 25.44, 23.03, 22.51, 10.18.

HR MS (pESI): calcd. For $C_{10}H_{19}O$ $[M+H]^+$: 155.14, found: 155.1431

Separation of enantiomers (**P38**): Chirasil-Dex CB, inject temperature = 250 °C, detector temperature = 300 °C, inlet pressure = 12.5 psi, flow rate = 1.3 mL/ min, split ratio = 50:1, temperature program = 50 °C (0 min) - 10 °C/min - 180 °C

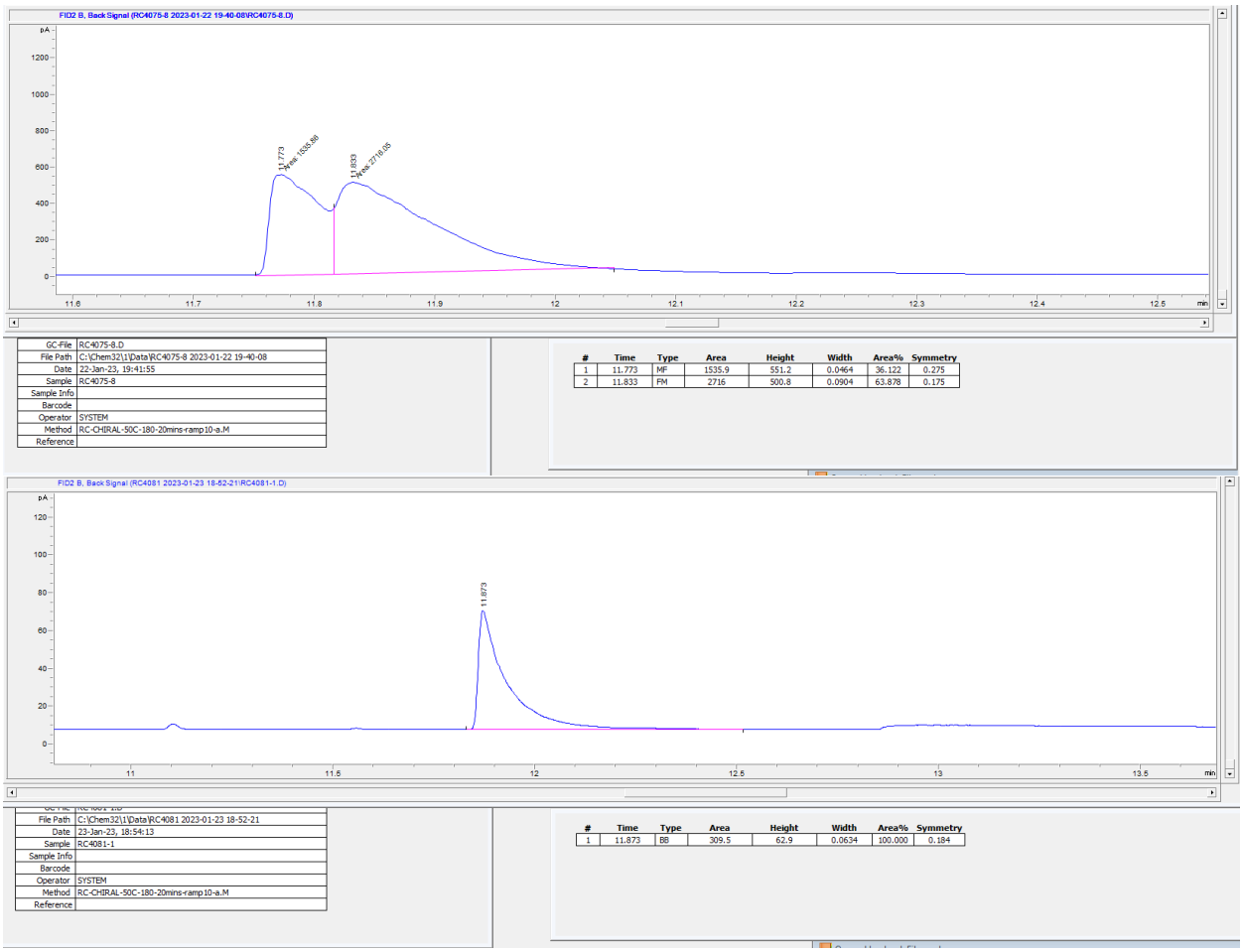

(S)-oct-7-yn-3-ol (**P39**)

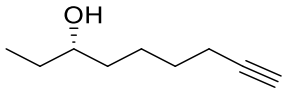

^{1}H NMR (600 MHz, $CDCl_3$) δ 3.54 (td, *J* = 7.4, 4.6 Hz, 1H), 2.21 (td, *J* = 6.9, 2.7 Hz, 2H), 1.94 (d, *J* = 5.3 Hz, 1H), 1.63 – 1.38 (m, 9H), 0.95 (t, *J* = 7.5 Hz, 3H).

^{13}C NMR (151 MHz, $CDCl_3$) δ 73.30, 68.43, 36.51, 30.34, 28.64, 24.96, 18.54, 10.01.

Spectral data match those previously reported.[66]

Separation of corresponding acetate enantiomers (**P39-Ac**): Chirasil-Dex CB, inject temperature = 250 °C, detector temperature = 300 °C, inlet pressure = 12.5 psi, flow rate = 1.3 mL/ min, split ratio = 50:1, temperature program = 50 °C (0 min) - 10 °C/min - 180 °C

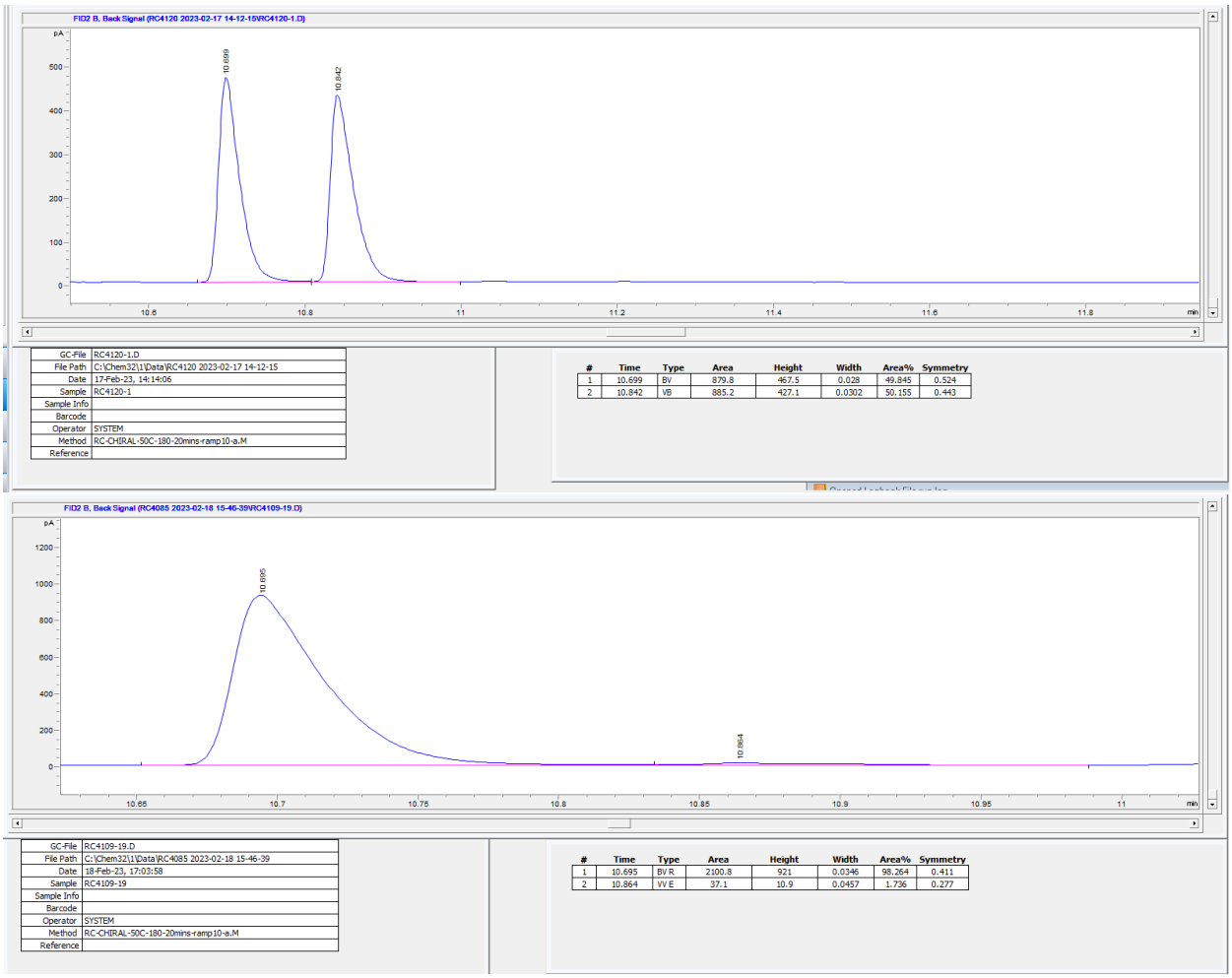

(S)-1-(Methoxymethoxy)butan-2-ol (**P40**)

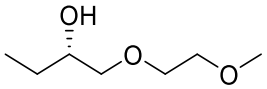

^{1}H NMR (600 MHz, $CDCl_3$) δ 3.76 – 3.61 (m, 3H), 3.59 – 3.50 (m, 3H), 3.39 (s, 3H), 3.31 (dd, *J* = 9.9, 8.3 Hz, 1H), 1.51 – 1.41 (m, 2H), 0.96 (t, *J* = 7.5 Hz, 3H).

^{13}C NMR (151 MHz, $CDCl_3$) δ 75.73, 72.10, 71.76, 70.71, 59.19, 26.10, 10.05.

HR MS (pESI): calcd. For $C_7H_{17}O_3$ $[M+H]^+$: 149.11, found: 149.1172

Separation of corresponding acetate enantiomers (**P40-Ac**): Chirasil-Dex CB, inject temperature = 250 °C, detector temperature = 300 °C, inlet pressure = 12.5 psi, flow rate = 1.3 mL/ min, split ratio = 50:1, temperature program = 50 °C (0 min) - 10 °C/min - 180 °C

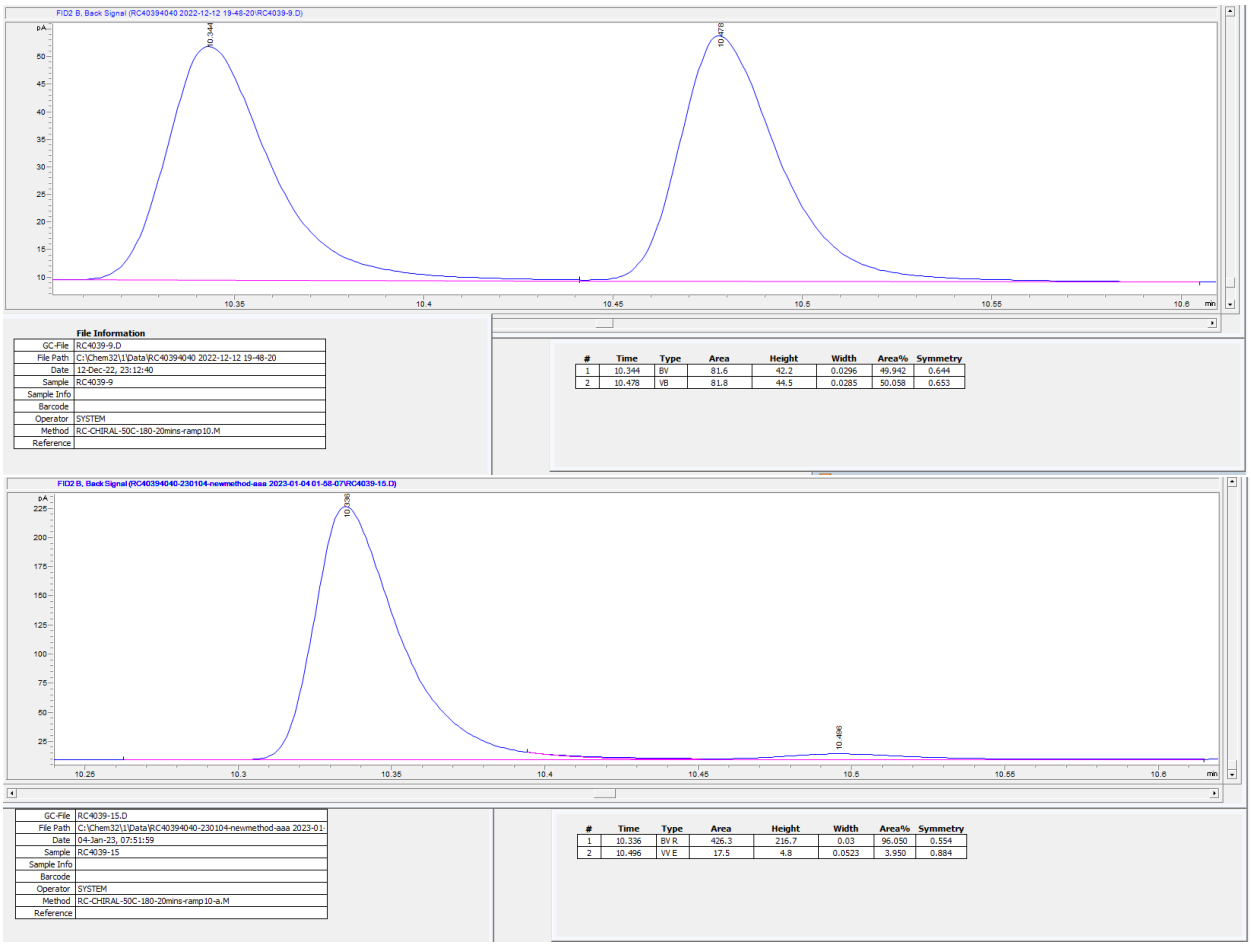

(S)-1-phenyl-1-propanol (**P41**)

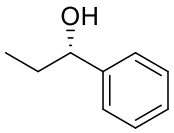

^{1}H NMR (600 MHz, $CDCl_3$) δ 7.38 – 7.33 (m, 4H), 7.30 – 7.26 (m, 1H), 4.61 (dd, J = 7.2, 6.0 Hz, 1H), 1.87 – 1.72 (m, 3H), 0.93 (t, J = 7.4 Hz, 3H).

^{13}C NMR (151 MHz, $CDCl_3$) δ 144.75, 128.57, 127.67, 126.12, 76.20, 32.06, 10.29.

Spectral data match those previously reported.[60]

Separation of corresponding acetate enantiomers (**P41-Ac**): Chirasil-Dex CB, inject temperature = 250 °C, detector temperature = 300 °C, inlet pressure = 12.5 psi, flow rate = 1.3 mL/ min, split ratio = 50:1, temperature program = 50 °C (0 min) - 10 °C/min - 180 °C

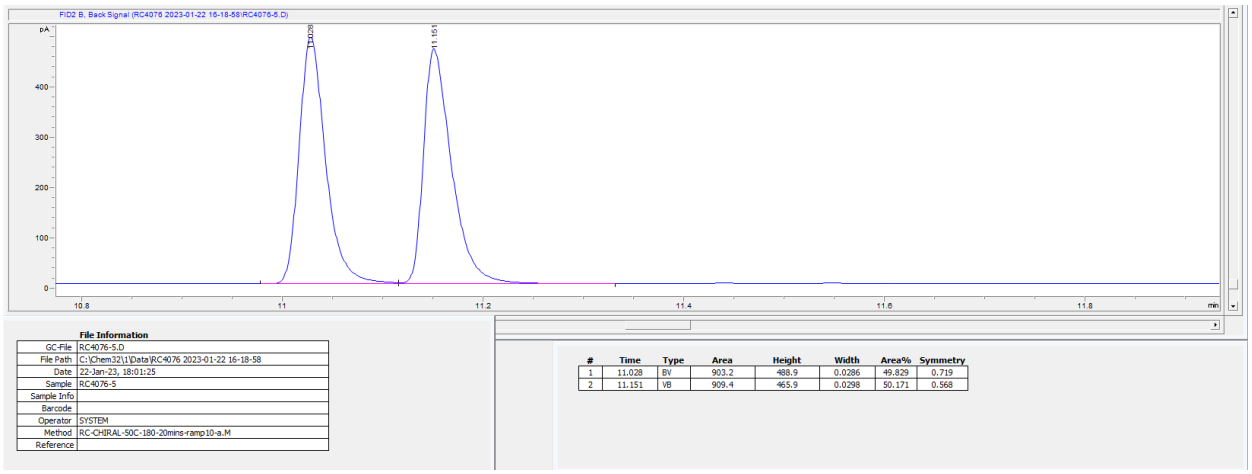

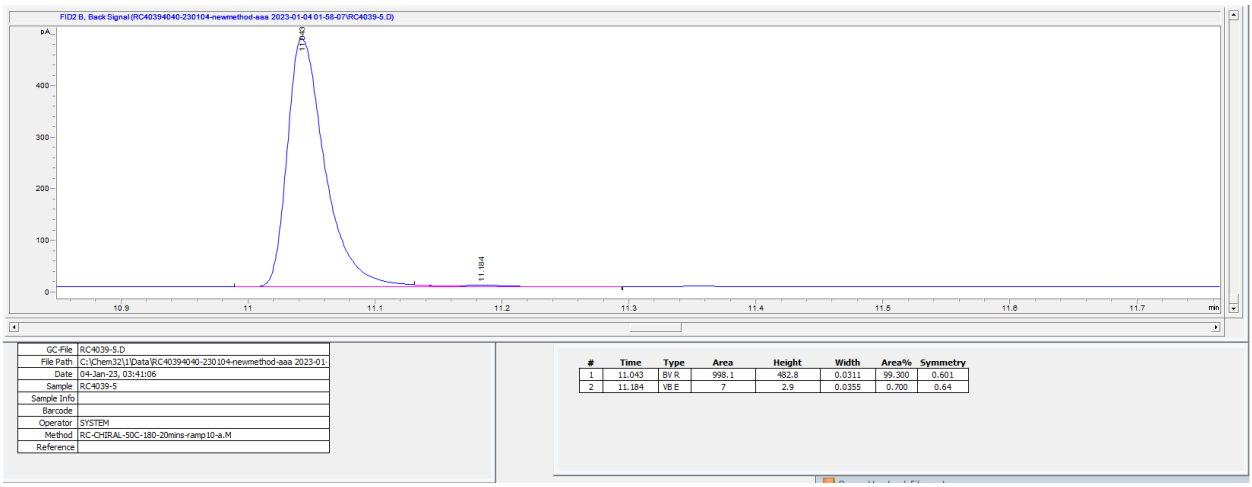

(S)-1-phenylbutan-2-ol (**P42**)

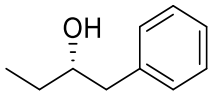

^{1}H NMR (600 MHz, $CDCl_3$) δ 7.35 (t, *J* = 7.7 Hz, 2H), 7.26 (t, *J* = 8.8 Hz, 3H), 3.79 (tt, *J* = 8.5, 4.5 Hz, 1H), 2.87 (dd, *J* = 13.6, 4.3 Hz, 1H), 2.74 – 2.62 (m, 1H), 1.68 – 1.48 (m, 3H), 1.10 – 0.98 (m, 3H).

^{13}C NMR (151 MHz, $CDCl_3$) δ 138.79, 129.56, 128.69, 126.57, 74.18, 43.73, 29.74, 10.18.

Spectral data match those previously reported.[59]

Separation of enantiomers: HPLC OD-H column, 5% iPrOH in hexane, 1.0 mL/min flow rate.

(S)-1-[4-(Trifluoromethyl)phenyl]butan-2-ol (**P43**)

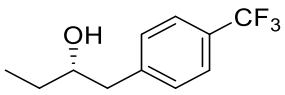

^{1}H NMR (600 MHz, $CDCl_3$) δ 7.59 – 7.53 (m, 2H), 7.34 (d, J = 7.9 Hz, 2H), 3.78 (tt, J = 8.4, 3.8 Hz, 1H), 2.88 (dd, J = 13.7, 4.3 Hz, 1H), 2.73 (dd, J = 13.7, 8.3 Hz, 1H), 1.64 – 1.48 (m, 5H), 1.01 (t, J = 7.5 Hz, 3H).

^{13}C NMR (151 MHz, $CDCl_3$) δ 143.13, 129.88, 129.02, 128.80, 125.54, 125.52, 125.49, 125.47, 125.34, 123.53, 73.98, 43.44, 29.96, 10.11.

Separation of enantiomers: HPLC AD-H column, 1% iPrOH in hexane, 1.0 mL/min flow rate.

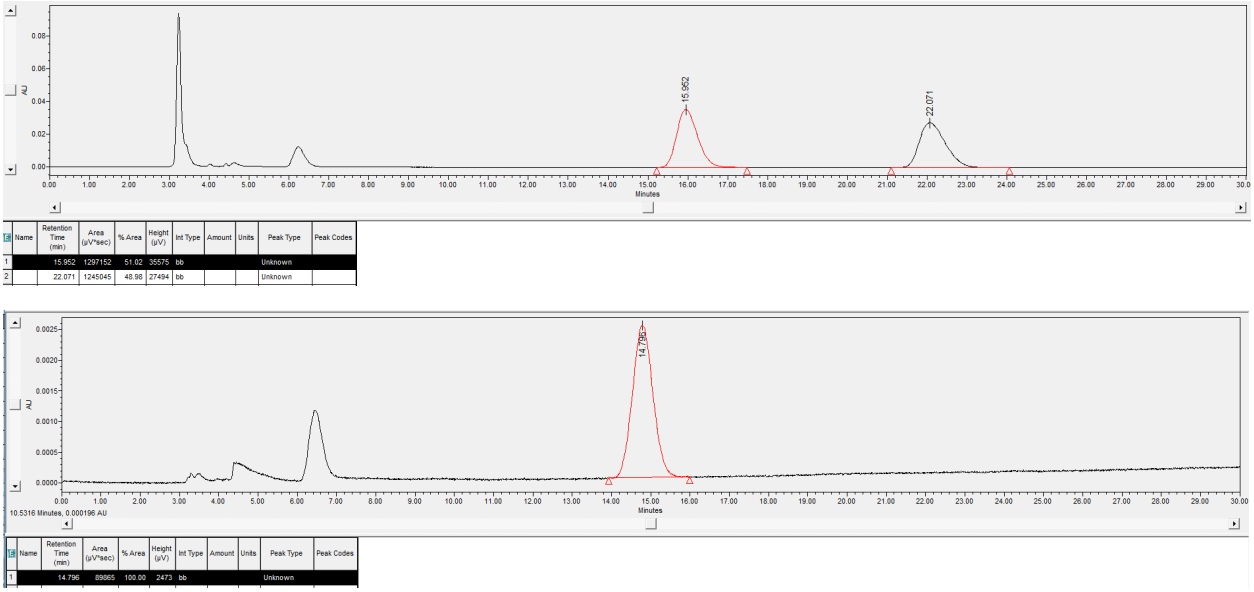

(S)-6-Benzyloxy-hexan-3-ol (**P44**)

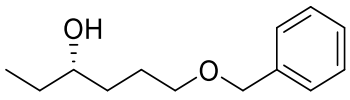

^{1}H NMR (600 MHz, $CDCl_3$) δ 7.44 – 7.26 (m, 5H), 4.52 (s, 2H), 3.58 – 3.48 (m, 3H), 1.84 – 1.59 (m, 4H), 1.54 – 1.42 (m, 3H), 0.94 (t, J = 7.4 Hz, 3H).

^{13}C NMR (151 MHz, $CDCl_3$) δ 138.39, 128.56, 127.86, 127.78, 73.19, 73.16, 70.73, 34.35, 30.37, 26.38, 10.16.

Spectral data match those previously reported. [67]

Separation of corresponding acetate enantiomers (**P44-Ac**): Chirasil-Dex CB, inject temperature = 250 °C, detector temperature = 300 °C, inlet pressure = 12.5 psi, flow rate = 1.3 mL/ min, split ratio = 50:1, temperature program = 50 °C (0 min) - 10 °C/min - 180 °C

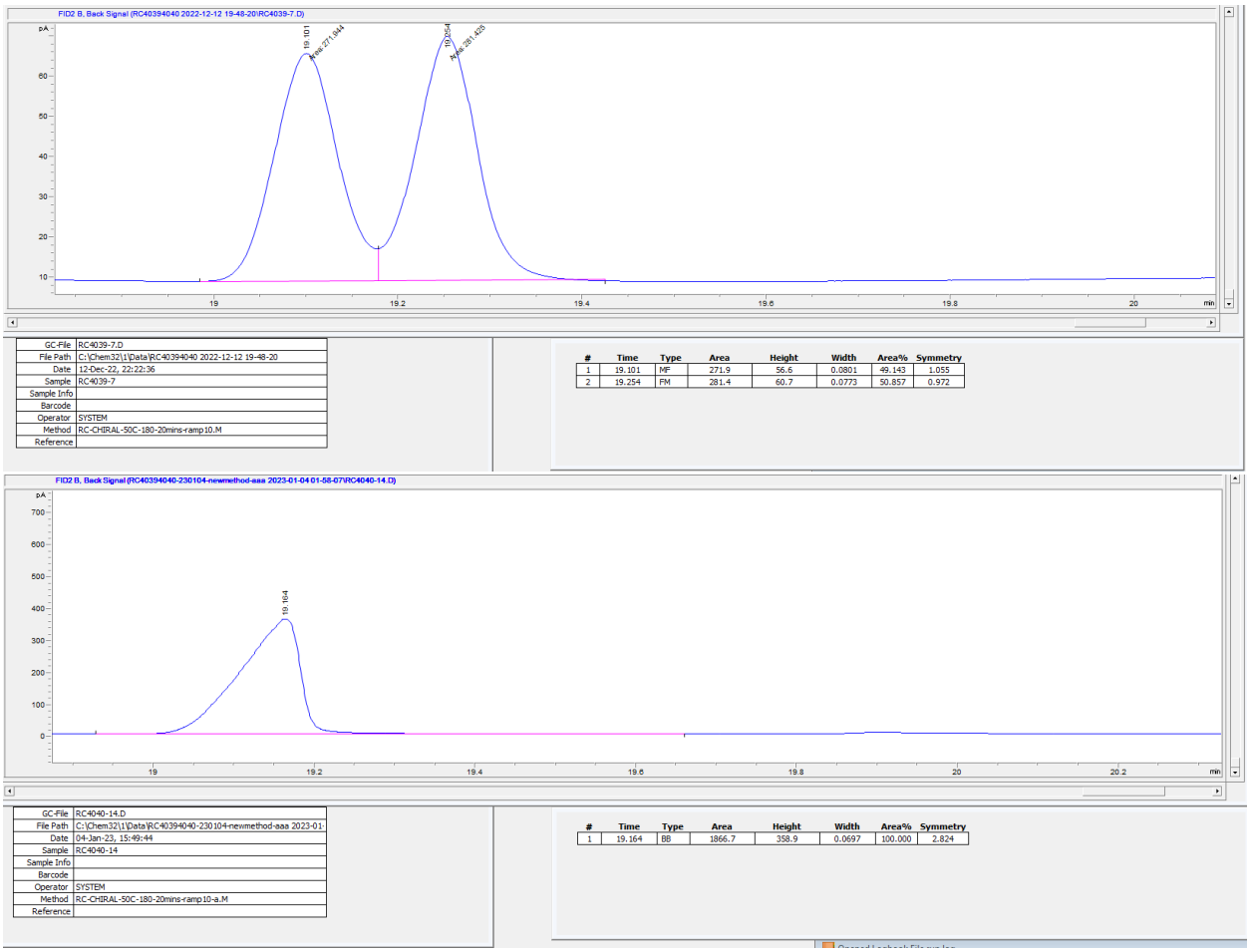

(S)-1-Furyl-butan-2-ol (**P45**)

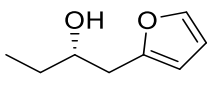

^{1}H NMR (600 MHz, $CDCl_3$) δ 7.34 (dd, *J* = 1.9, 0.8 Hz, 1H), 6.31 (dd, *J* = 3.2, 1.9 Hz, 1H), 6.14 – 6.07 (m, 1H), 2.85 (ddd, *J* = 15.0, 4.1, 0.8 Hz, 1H), 2.72 (dd, *J* = 15.0, 8.0 Hz, 1H), 1.54 – 1.49 (m, 4H), 0.98 (t, *J* = 7.5 Hz, 3H).

^{13}C NMR (151 MHz, $CDCl_3$) δ 141.74, 110.45, 107.12, 71.99, 51.01, 35.82, 29.67, 10.06.

Spectral data match those previously reported.[68]

Separation of corresponding acetate enantiomers (**P45-Ac**): Chirasil-Dex CB, inject temperature = 250 °C, detector temperature = 300 °C, inlet pressure = 12.5 psi, flow rate = 1.3 mL/ min, split ratio = 50:1, temperature program = 50 °C (0 min) - 10 °C/min - 180 °C

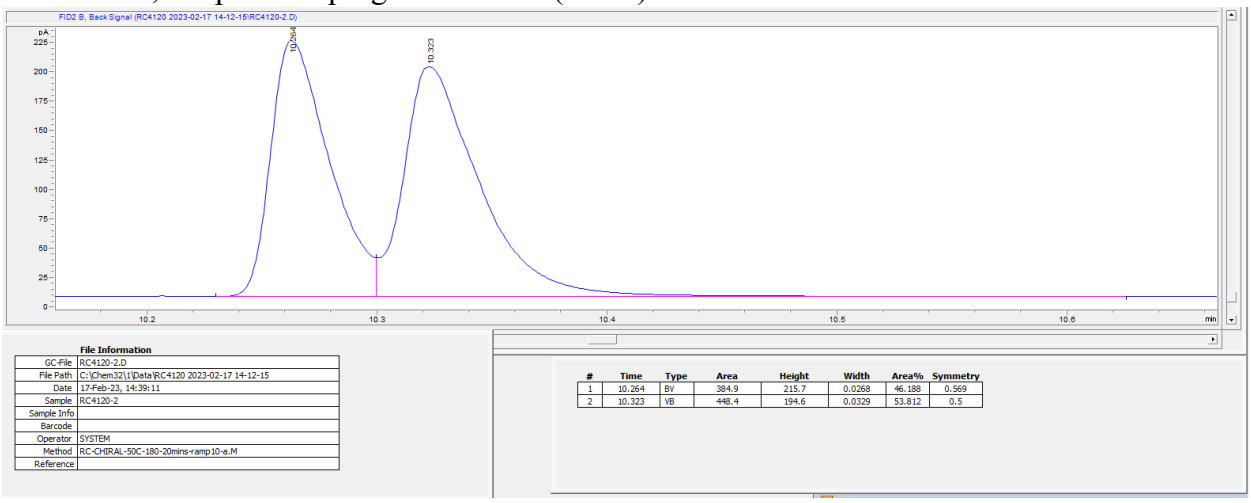

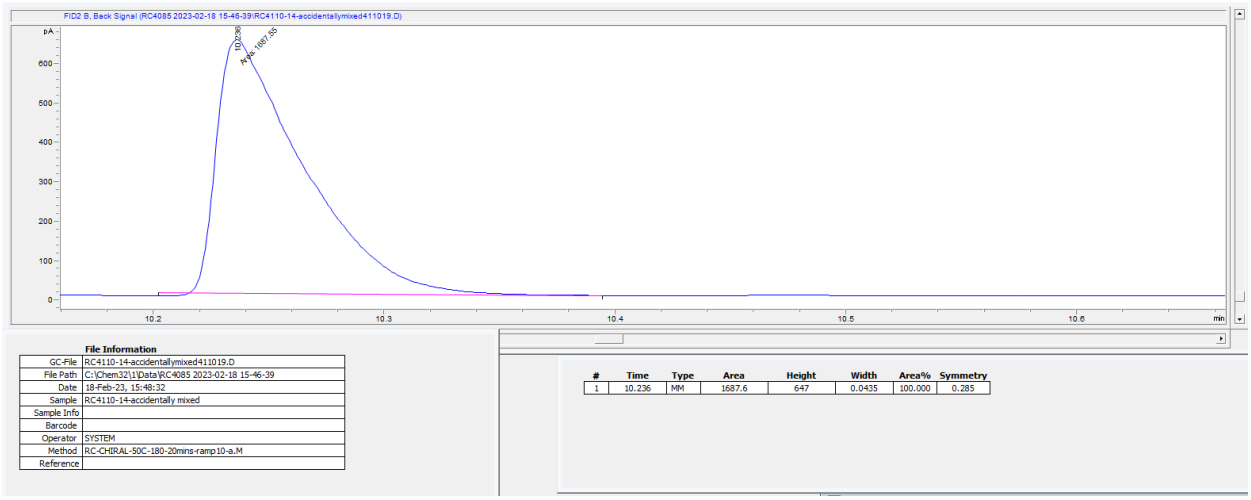

(S)-1-(2-thienyl)-2-butanol (**P46**)

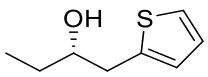

^{1}H NMR (600 MHz, $CDCl_3$) δ 7.18 (dd, *J* = 5.2, 1.2 Hz, 1H), 6.96 (dd, *J* = 5.1, 3.4 Hz, 1H), 6.87 (dt, *J* = 3.5, 1.0 Hz, 1H), 3.75 (tt, *J* = 8.2, 4.5 Hz, 1H), 3.04 (ddd, *J* = 14.7, 4.0, 0.9 Hz, 1H), 2.89 (ddd, *J* = 14.7, 8.2, 0.7 Hz, 1H), 1.63 – 1.50 (m, 5H), 1.00 (t, *J* = 7.5 Hz, 3H).

^{13}C NMR (151 MHz, $CDCl_3$) δ 140.80, 127.14, 126.13, 124.34, 73.92, 37.66, 29.51, 10.14.

Spectral data match those previously reported.[41]

Separation of corresponding acetate enantiomers (**P46-Ac**): Chirasil-Dex CB, inject temperature = 250 °C, detector temperature = 300 °C, inlet pressure = 12.5 psi, flow rate = 1.3 mL/ min, split ratio = 50:1, temperature program = 50 °C (0 min) - 10 °C/min - 180 °C

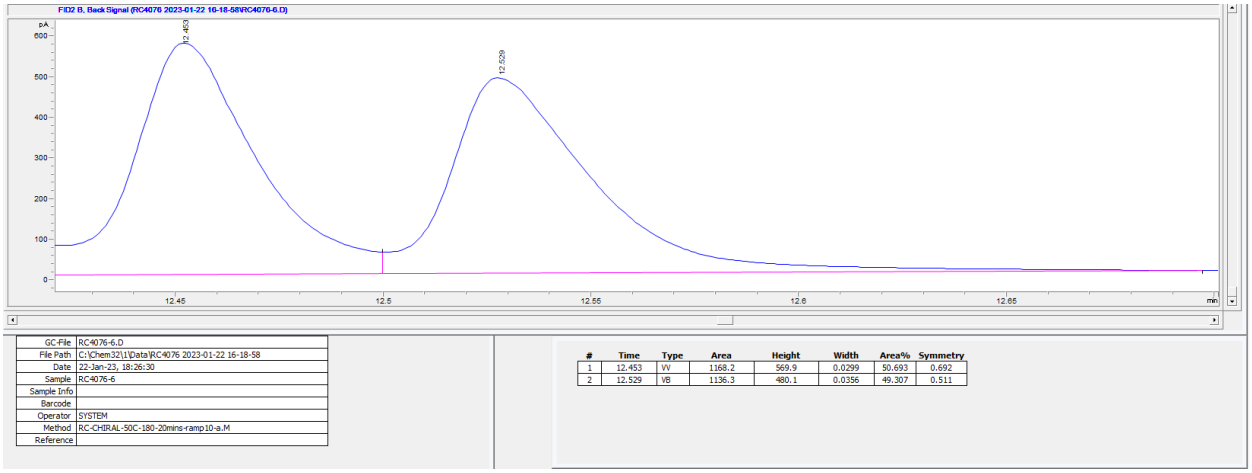

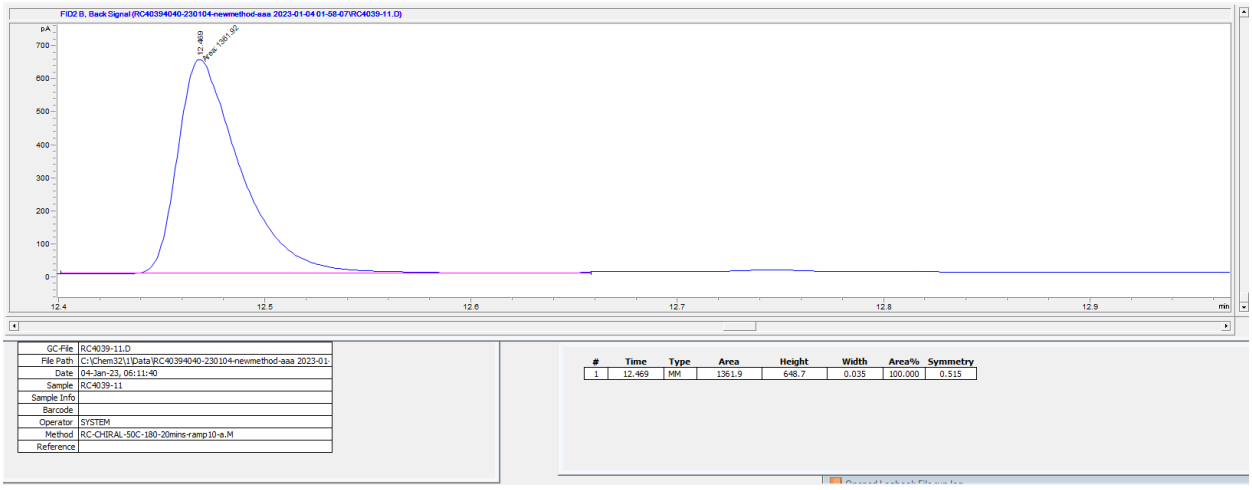

(S)-1-(5-Methyl-1,2-oxazol-4-yl)propan-1-ol (**P47**)

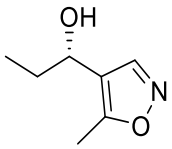

^{1}H NMR (500 MHz, $CDCl_3$) δ 8.18 (s, 1H), 4.56 (t, *J* = 6.8 Hz, 1H), 2.42 (s, 3H), 1.78 (ddq, *J* = 55.6, 13.8, 7.0 Hz, 5H), 0.92 (t, *J* = 7.4 Hz, 3H).

^{13}C NMR (126 MHz, $CDCl_3$) δ 165.01, 149.20, 117.76, 77.23, 66.75, 30.99, 11.13, 9.90.

HR MS (pESI): calcd. For $C_7H_{12}O_2N$ $[M+H]^+$: 142.08, found: 142.0863

Separation of corresponding acetate enantiomers (**P47-Ac**): Chirasil-Dex CB, inject temperature = 250 °C, detector temperature = 300 °C, inlet pressure = 12.5 psi, flow rate = 1.3 mL/ min, split ratio = 50:1, temperature program = 50 °C (0 min) - 10 °C/min - 180 °C

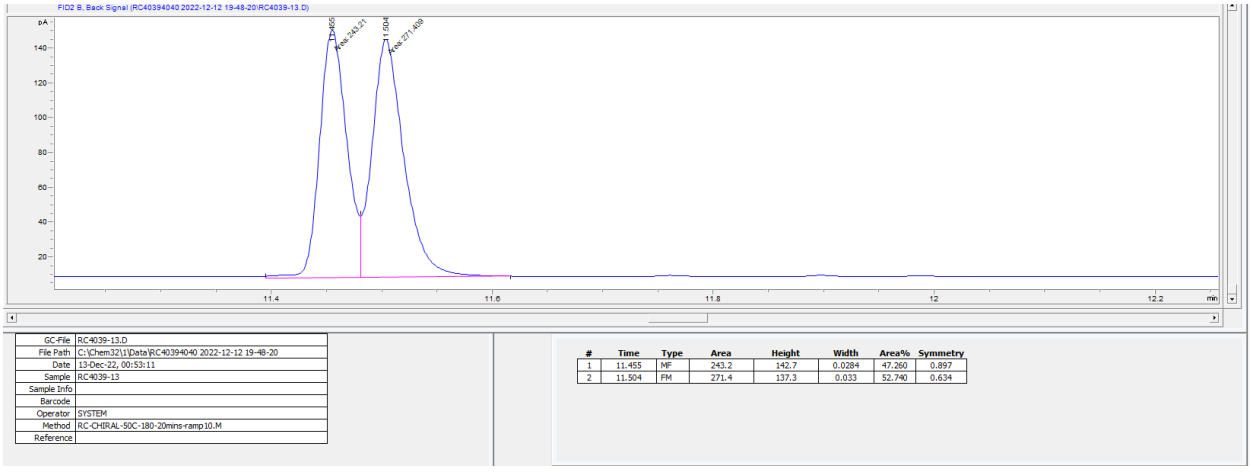

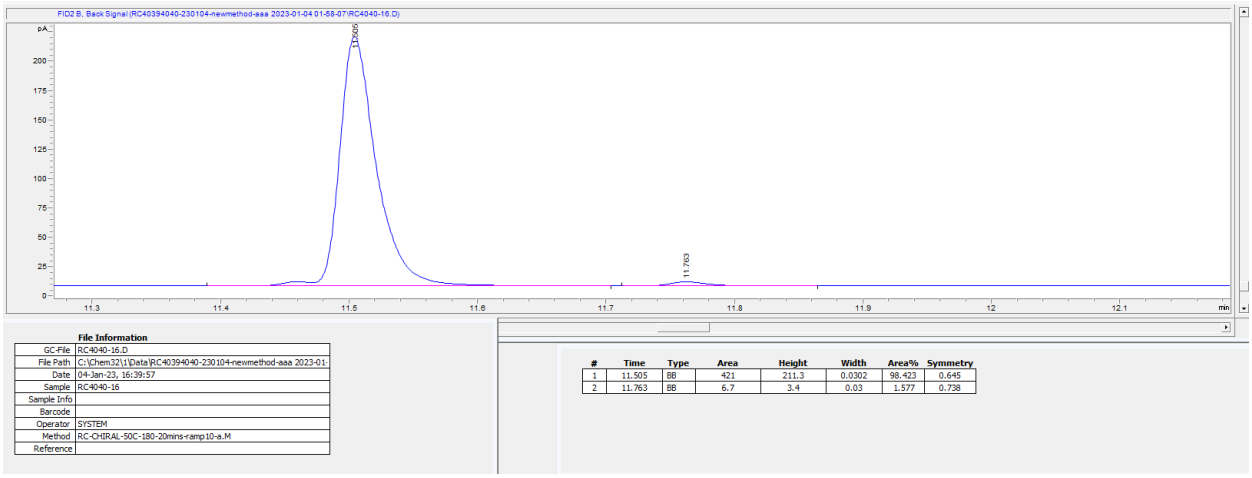

2.4.2.7 Computational study

The hCAII structure with the PDB code of 1BN1 was used as the starting structure of the modeling of ligand docking to hCAII variants. Schrödinger was used to correct errors and add hydrogens for the preparation of the protein receptor from the crystal model. The receptor structure was prepared by setting the simulation pH at 7.4, deleting water molecules >5Å distance from the ligand, and converging heavy atoms to RMSD by 0.30Å. The hydrogen-bonding interactions within the protein were optimized with the OPLS_2005 force field to generate the protein acceptor. The native sulfamide ligand was replaced with the hydride group, and the charge of the zinc-hydride complex was changed to neutral. The receptor grid was generated with a box length of 20 Å centering at the hydride.

All the molecules for docking were prepared with the 3D Builder within Schrodinger and optimized with the OPLS_2005 force field using Minimization in MacroModel. Substrates were docked to the active site of hCAII using Glide Ligand Docking Generation. The ligand docking setting was optimized by setting the ligand to rigid with the docking performance at the SP (standard precision) level with the same OPLS_2005 force field.

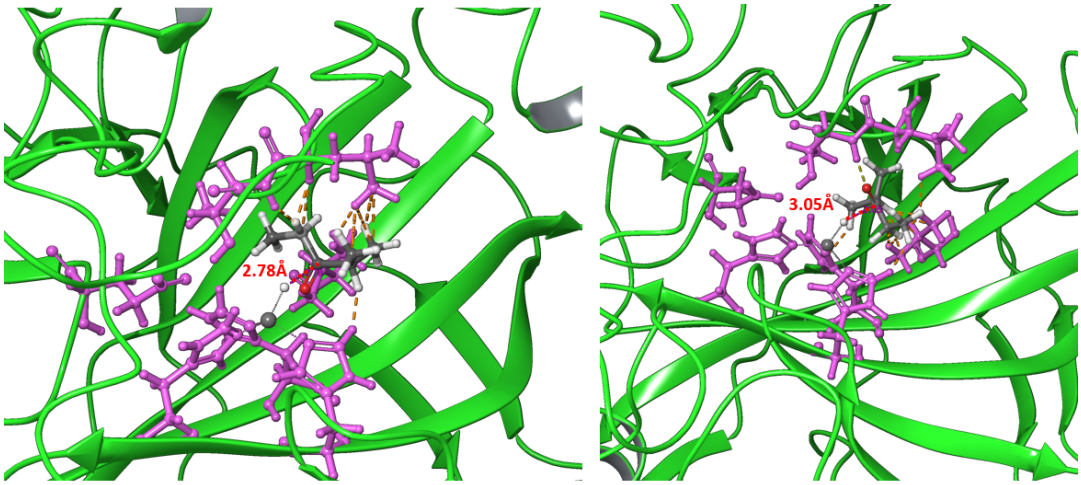

Figure S3. The docking model of ethyl isopropyl ketone to W209L hCAII with two conformations.

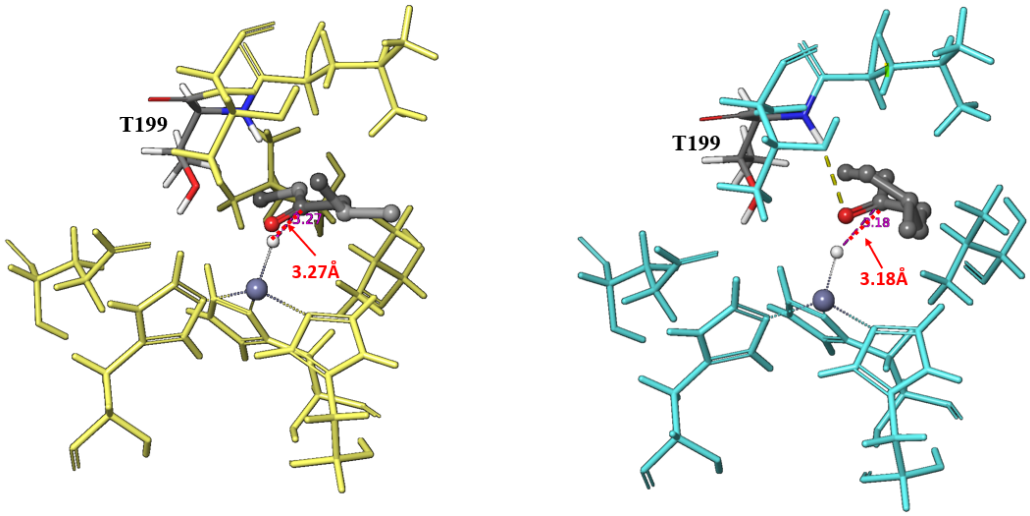

Figure S4. The docking model of (a) 5-methyl-3-hexanone and (b) 6-methyl-3-heptanone to W209L. The yellow dash line indicated the hydrogen bonding between oxygen on the ketone and nitrogen on T199.

2.4.2.8 NMR spectra

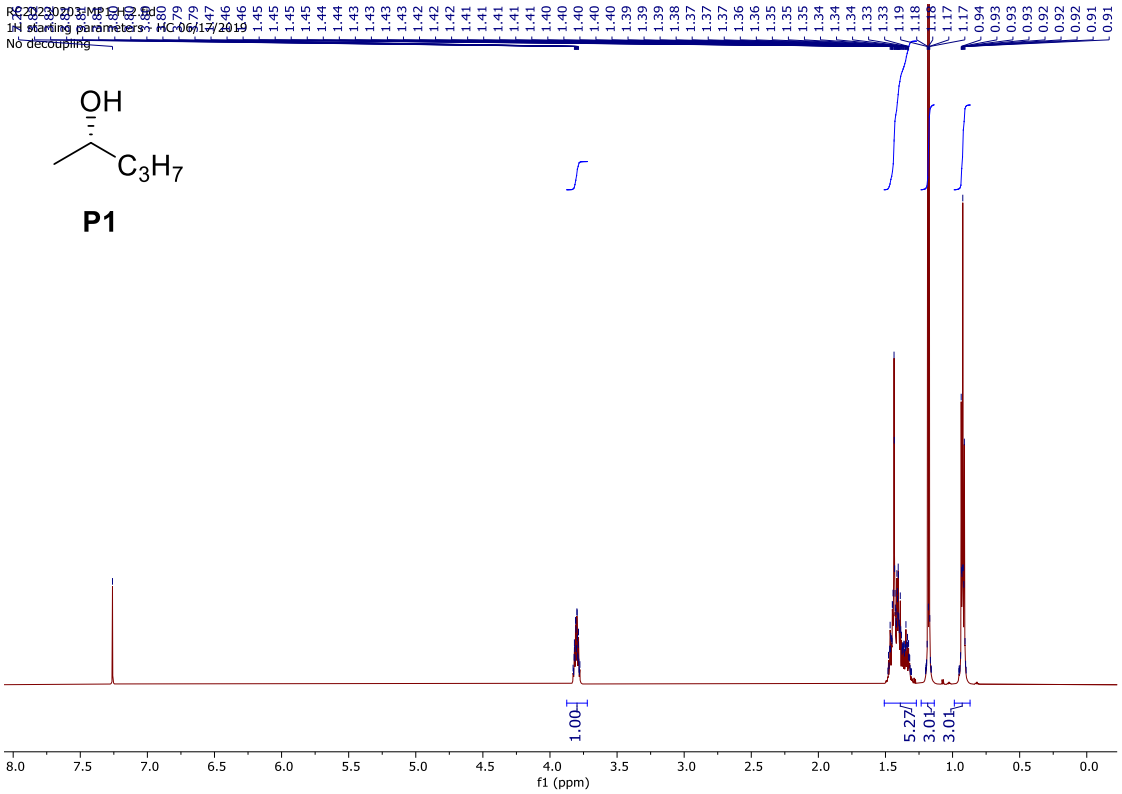

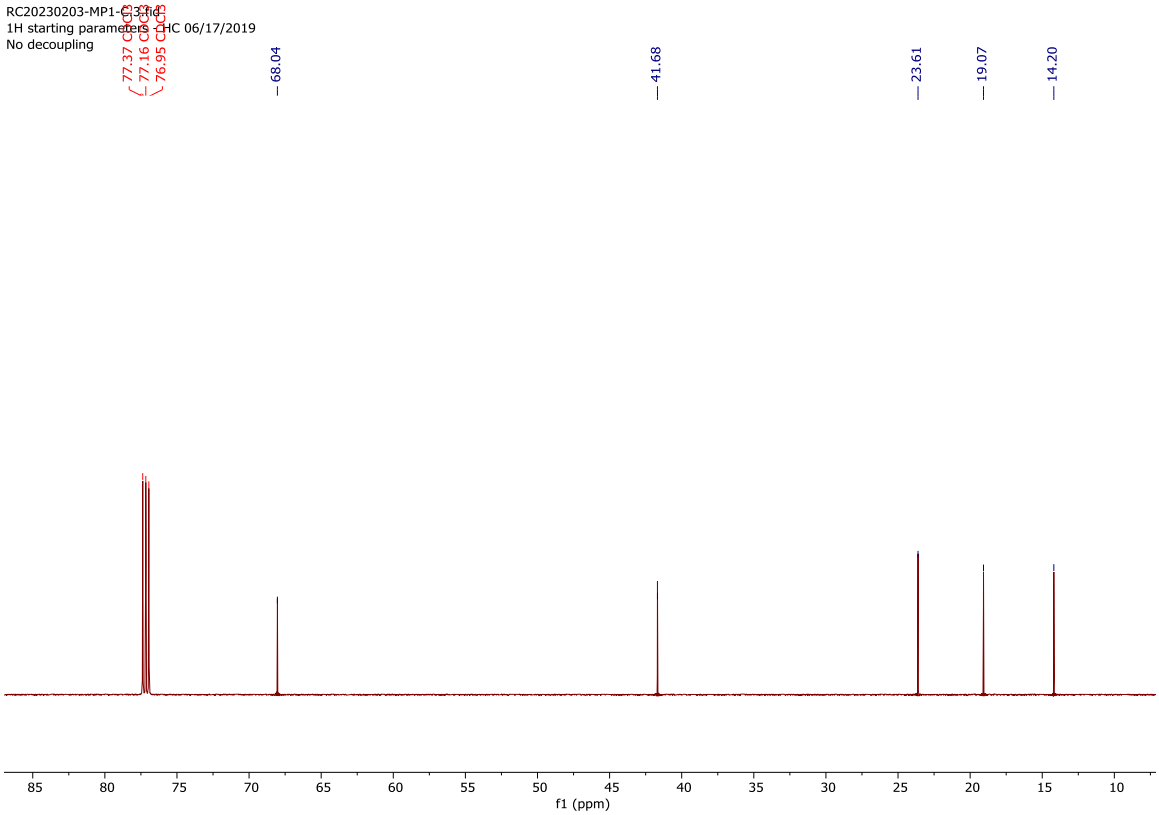

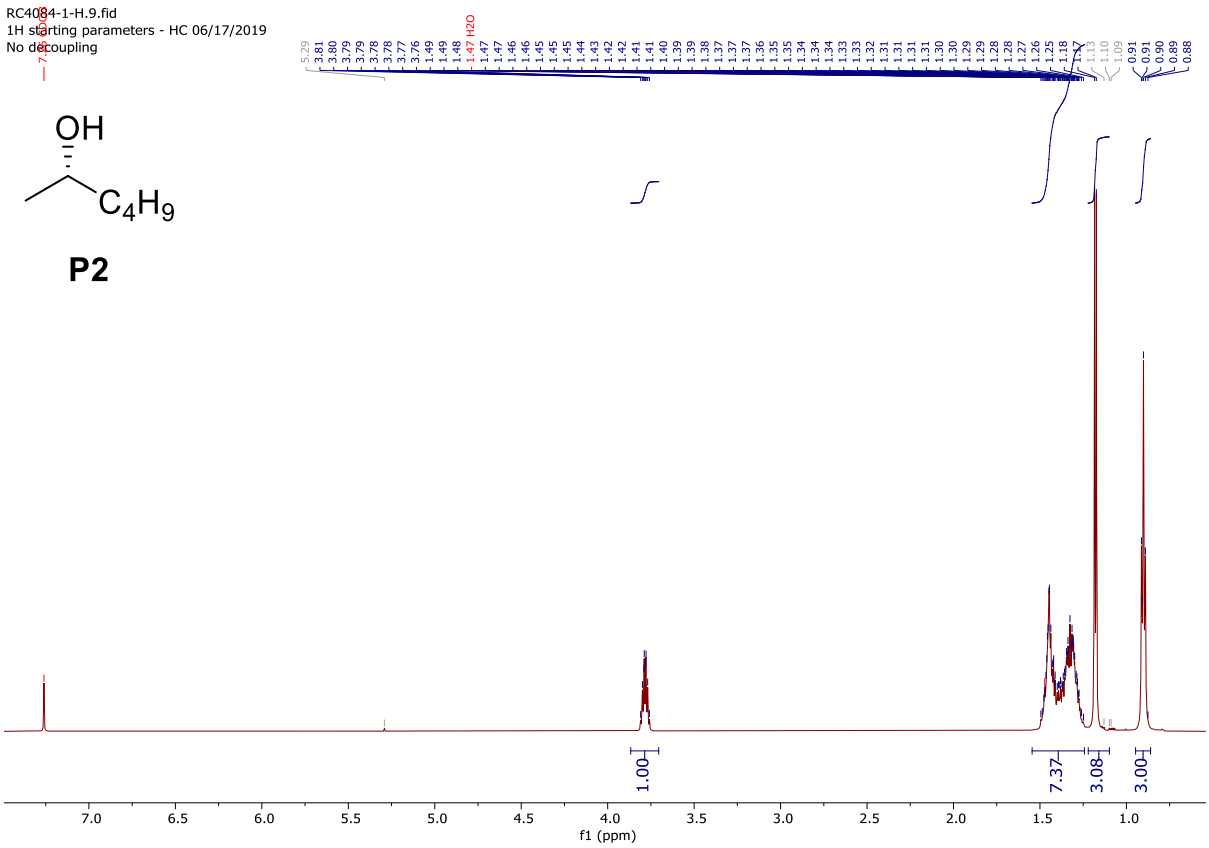
RC4084-1-H.9.fid
1H starting parameters - HC 06/17/2019
No decoupling
OH
C4H9
P2
1.00
7.37
3.08
3.00
f1 (ppm)

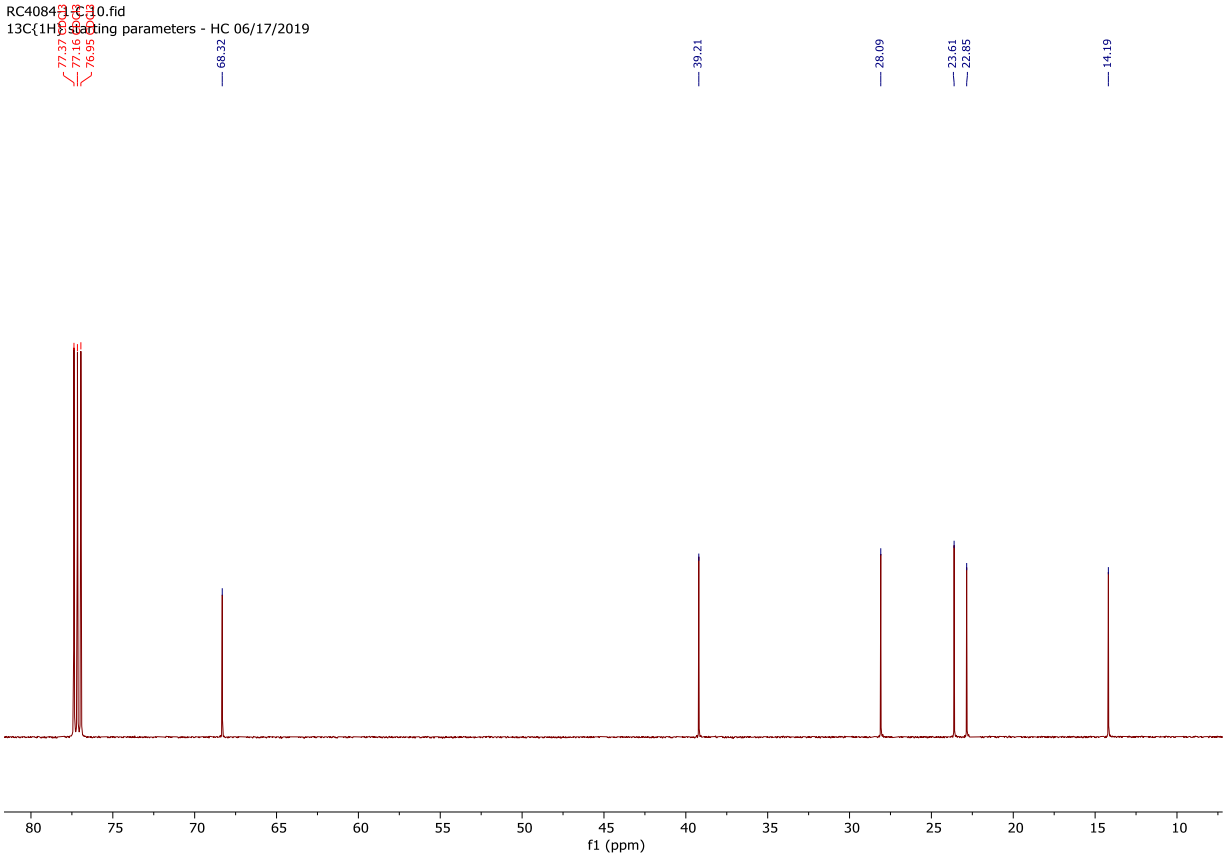
RC4084-1-C.10.fid
13C{1H} starting parameters - HC 06/17/2019
77.37
77.16
76.95
68.32
39.21
28.09
23.61
22.85
14.19
f1 (ppm)

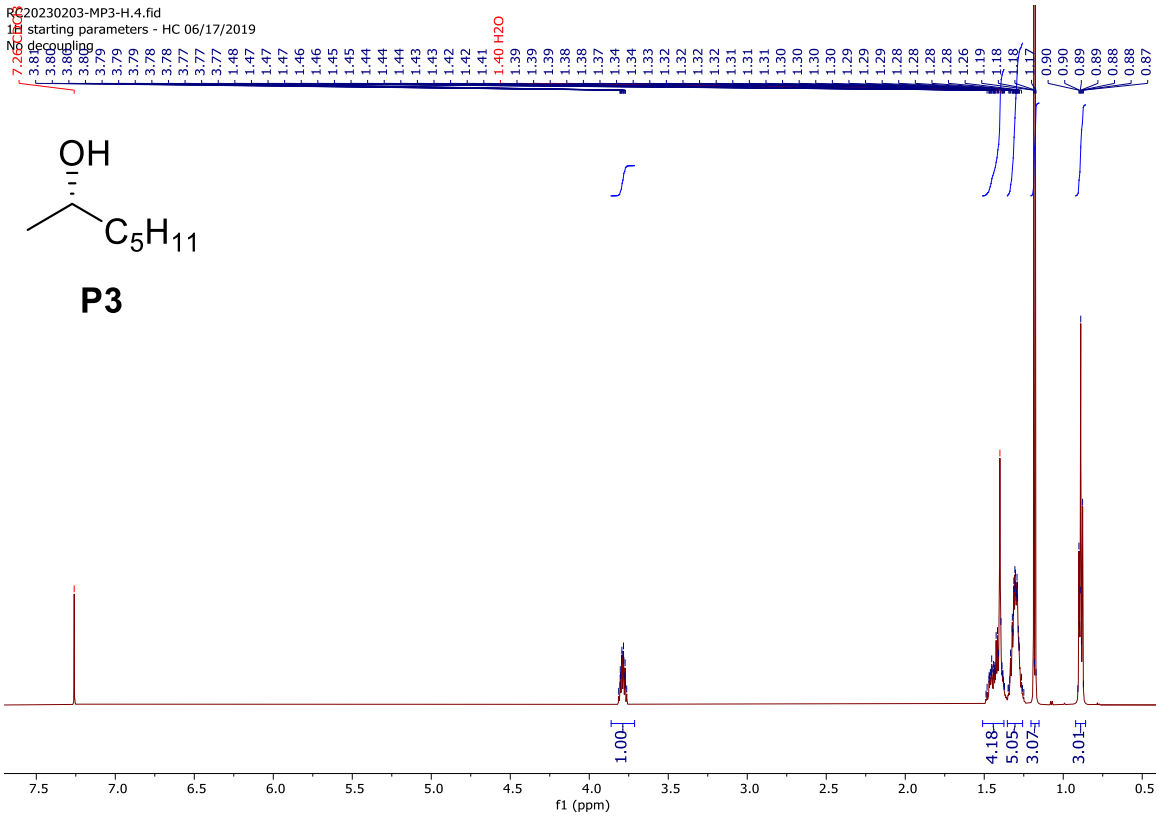
RC20230203-MP3-H.4.fid
1H starting parameters - HC 06/17/2019
No decoupling
OH
C5H11
P3
1.40 H2O
1.00
4.18
5.05
3.07
3.01
f1 (ppm)

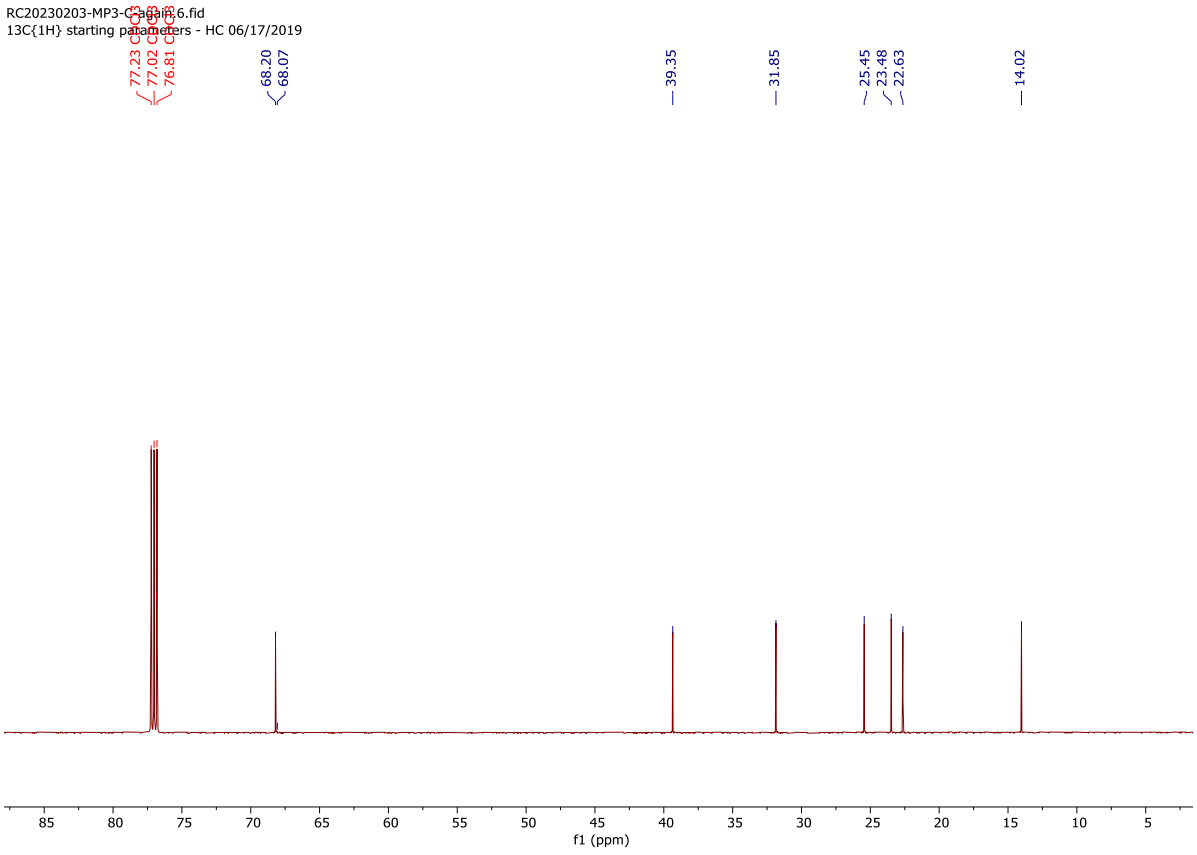
RC20230203-MP3-C.13.fid
13C{1H} starting parameters - HC 06/17/2019
77.23 CDCl3
77.02 CDCl3
76.81 CDCl3
68.20
68.07
39.35
31.85
25.45
23.48
22.63
14.02
f1 (ppm)

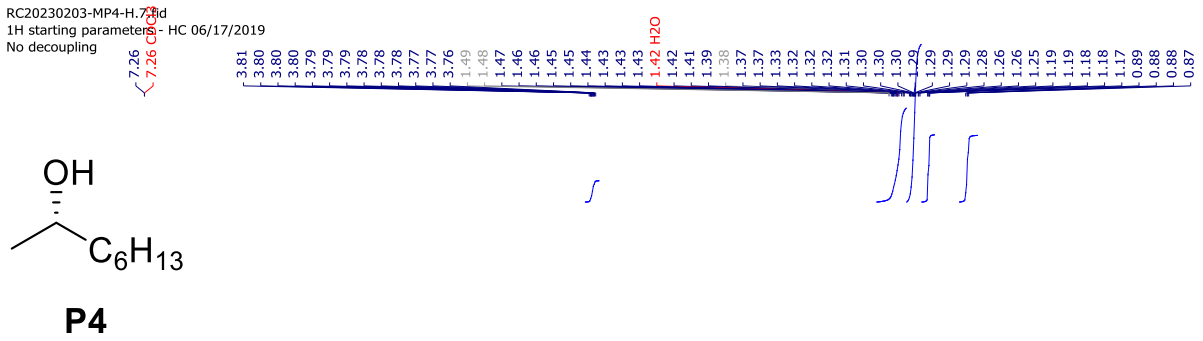
RC20230203-MP4-H.7.fid
1H starting parameters - HC 06/17/2019
No decoupling
7.26 CDCl3
1.42 H2O
OH
C6H13

P4

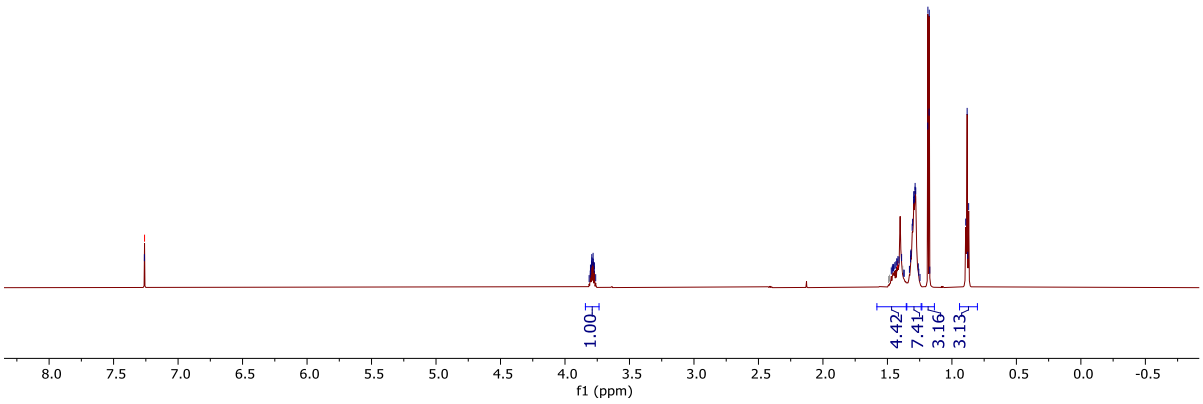
1.00
4.42
7.41
3.16
3.13
f1 (ppm)

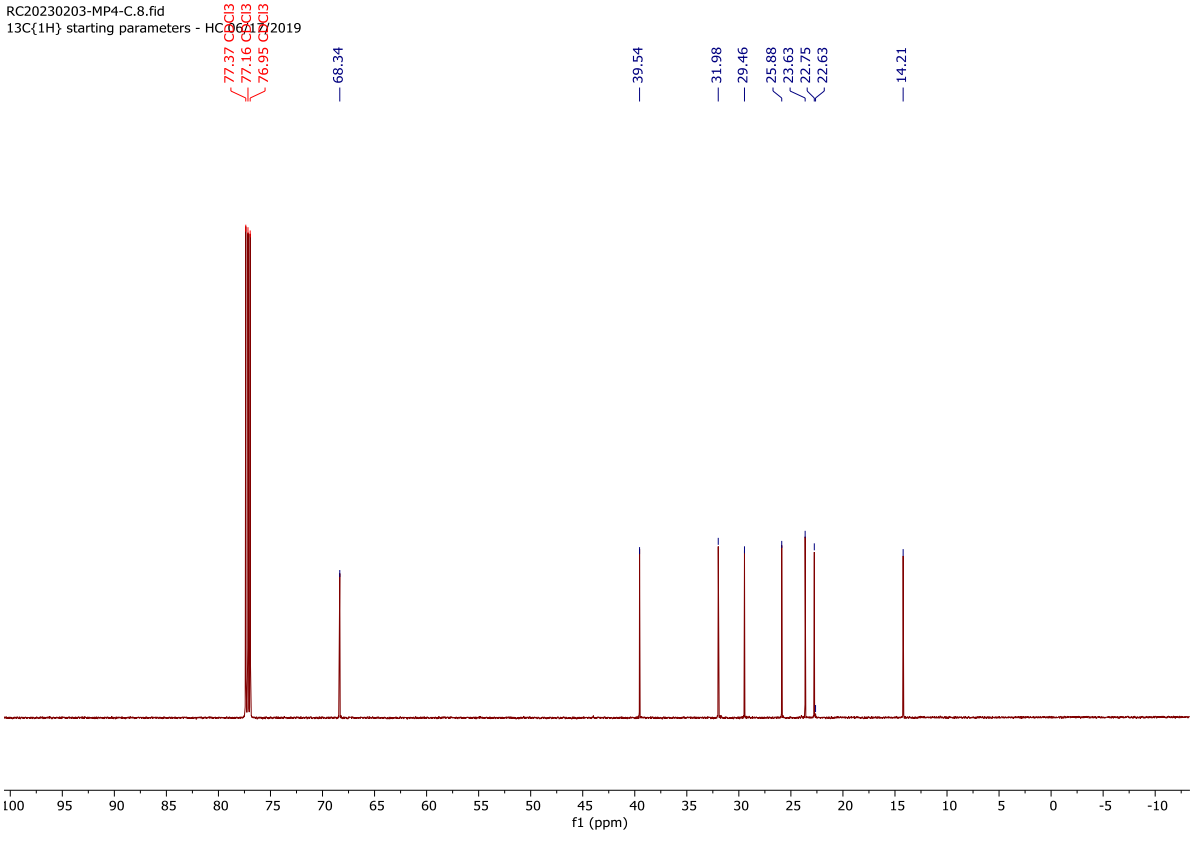
RC20230203-MP4-C.8.fid
13C{1H} starting parameters - HC 06/17/2019
77.37 CDCl3
77.16 CDCl3
76.95 CDCl3
68.34
39.54
31.98
29.46
25.88
23.63
22.75
22.63
14.21
f1 (ppm)

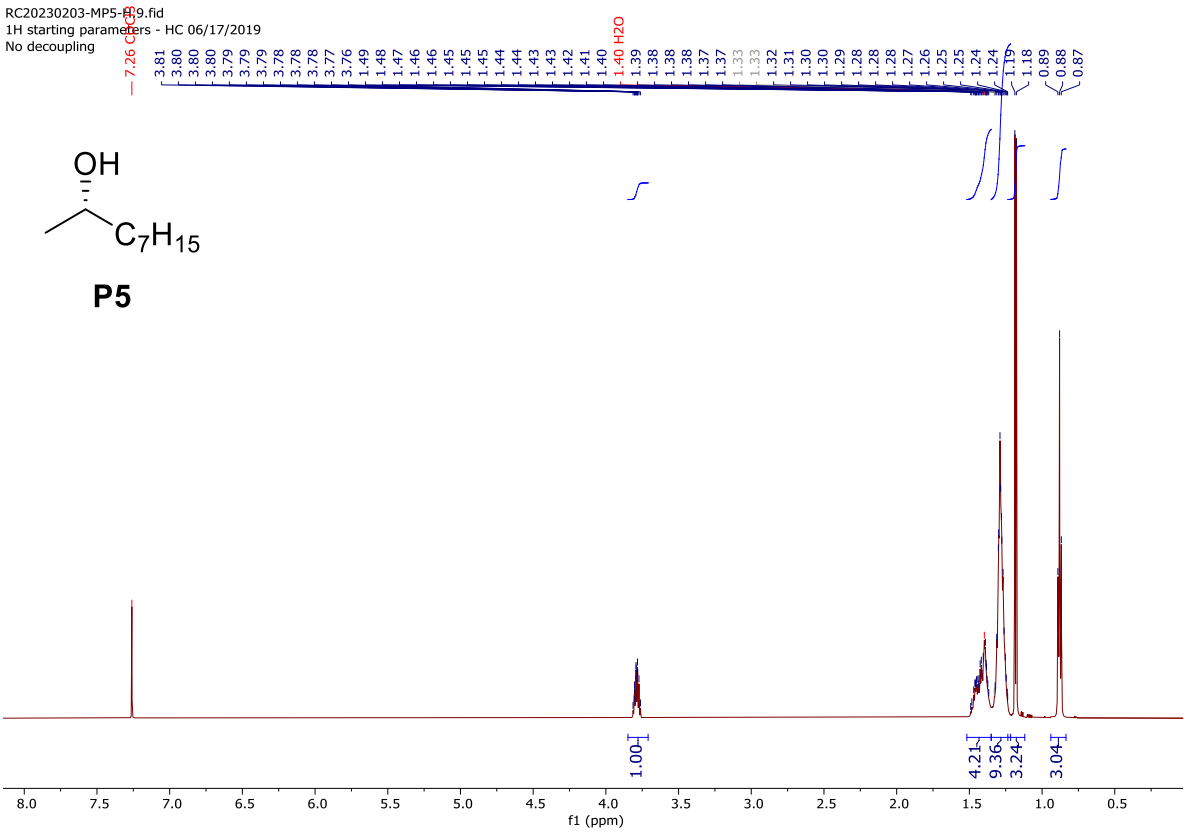
RC20230203-MP5-H.9.fid
1H starting parameters - HC 06/17/2019
No decoupling
7.26 CDCl3
1.40 H2O
OH
C7H15
P5
1.00
4.21
9.36
3.24
3.04
f1 (ppm)

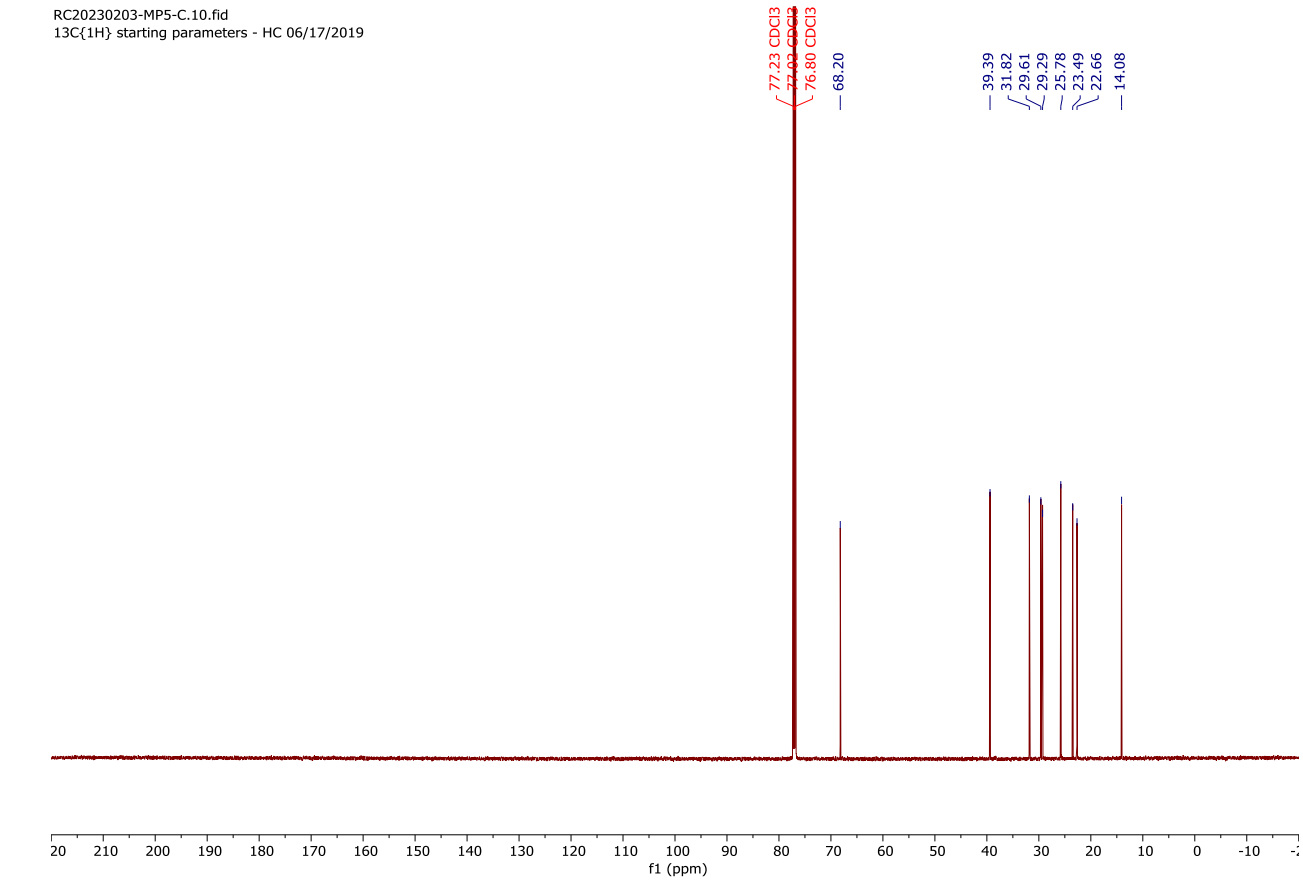
RC20230203-MP5-C.10.fid
13C{1H} starting parameters - HC 06/17/2019
77.23 CDCl3
77.01 CDCl3
76.80 CDCl3
68.20
39.39
31.82
29.61
29.29
25.78
23.49
22.66
14.08
f1 (ppm)

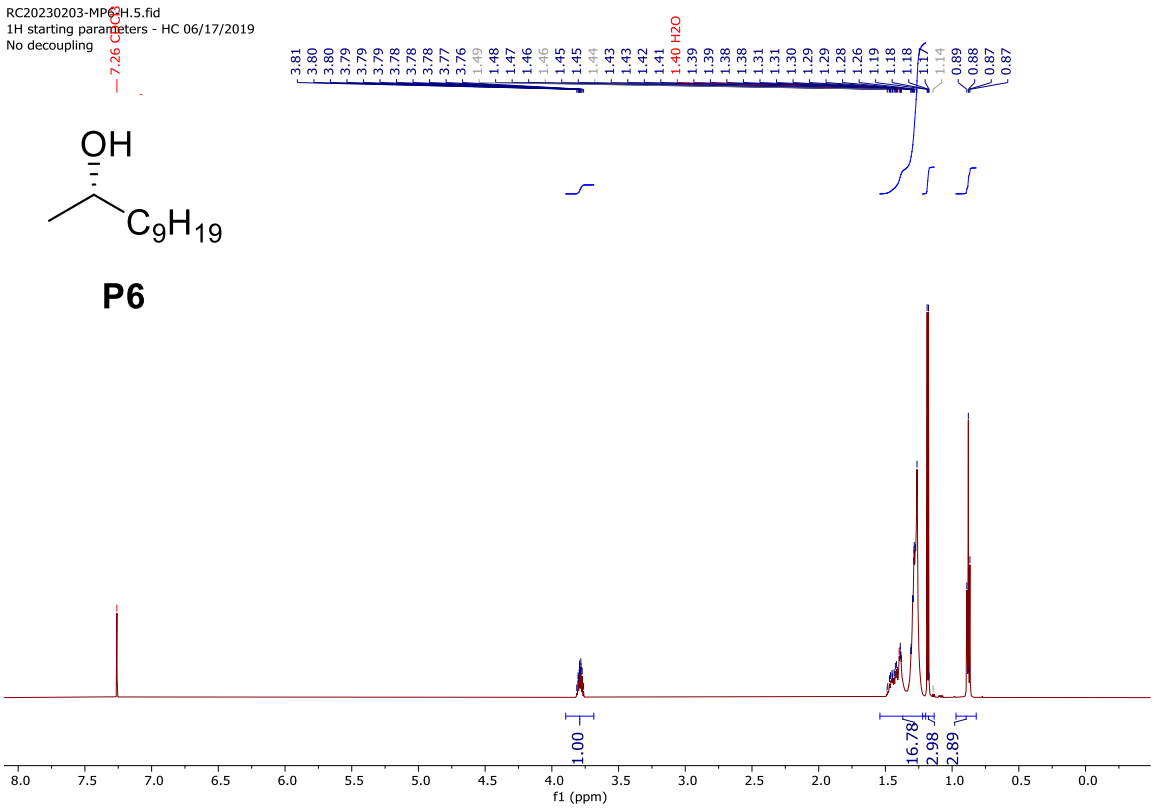
RC20230203-MP6-H.5.fid
1H starting parameters - HC 06/17/2019
No decoupling
7.26 CDCl3
1.40 H2O
OH
C9H19
P6
1.00
16.78
2.98
2.89
f1 (ppm)

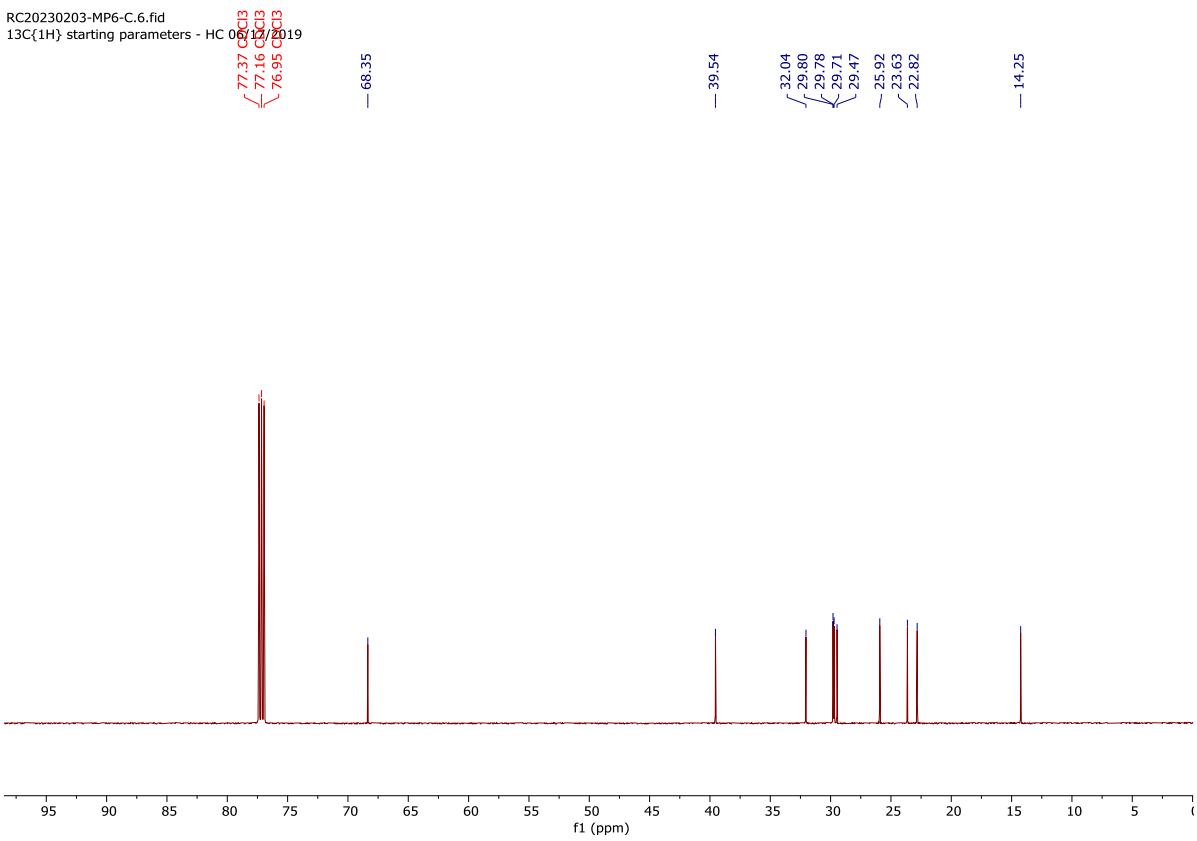
RC20230203-MP6-C.6.fid
13C{1H} starting parameters - HC 06/17/2019
77.37 CDCl3
77.16 CDCl3
76.95 CDCl3
68.35
39.54
32.04
29.80
29.78
29.71
29.47
25.92
23.63
22.82
14.25
f1 (ppm)

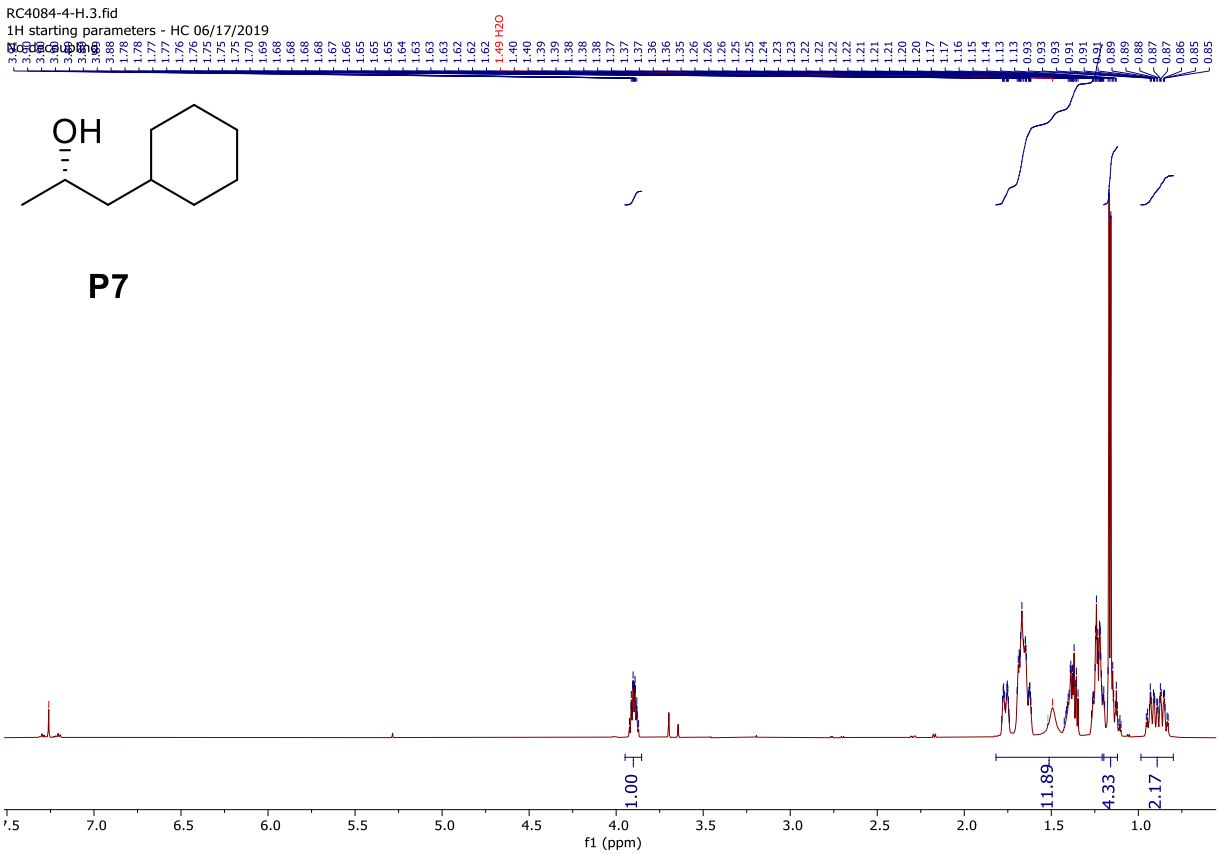
RC4084-4-H.3.fid
1H starting parameters - HC 06/17/2019
OH
P7
1.49 H2O
1.00
11.89
4.33
2.17
f1 (ppm)

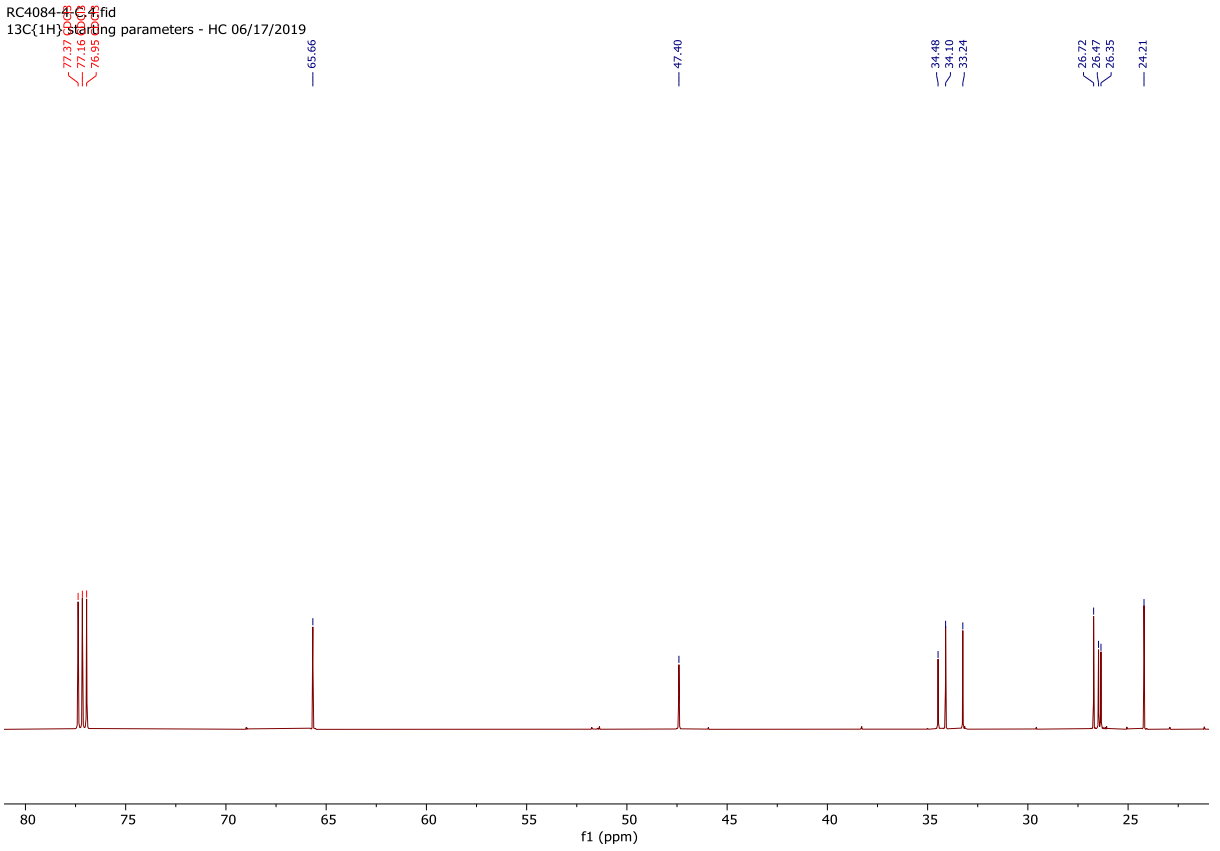
13C{1H} starting parameters - HC 06/17/2019
77.37
77.16
76.95
65.66
47.40
34.48
34.10
33.24
26.72
26.47
26.35
24.21
f1 (ppm)

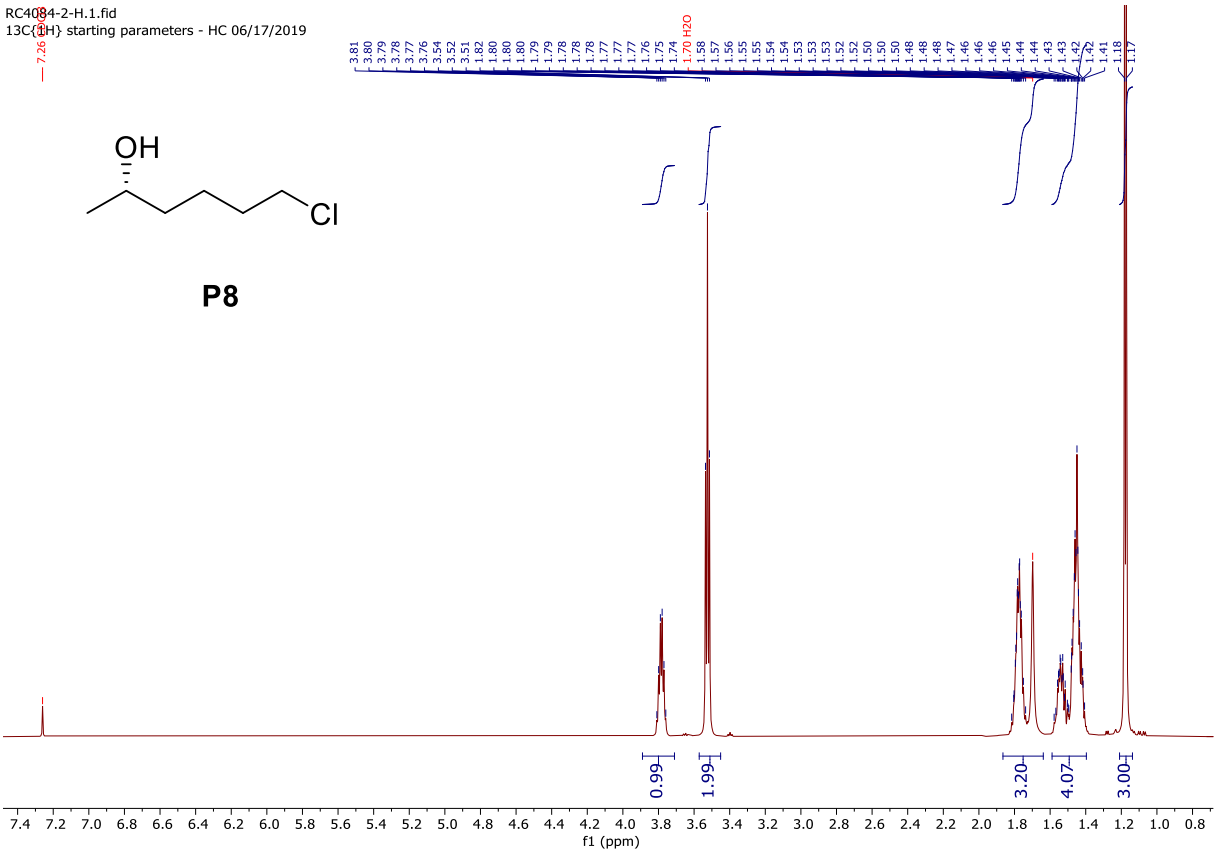
RC4084-2-H.1.fid
13C{1H} starting parameters - HC 06/17/2019
OH
Cl
P8
f1 (ppm)

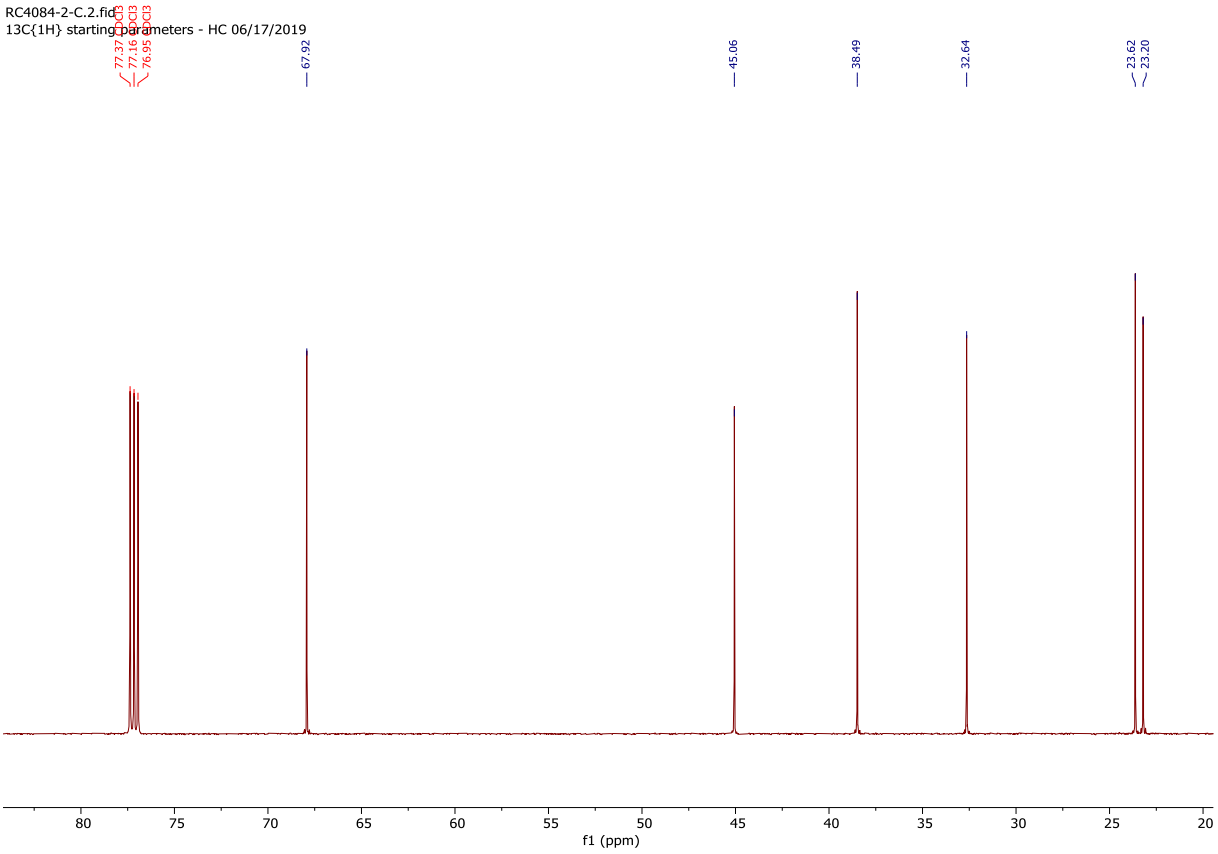
RC4084-2-C.2.fid
13C{1H} starting parameters - HC 06/17/2019
f1 (ppm)

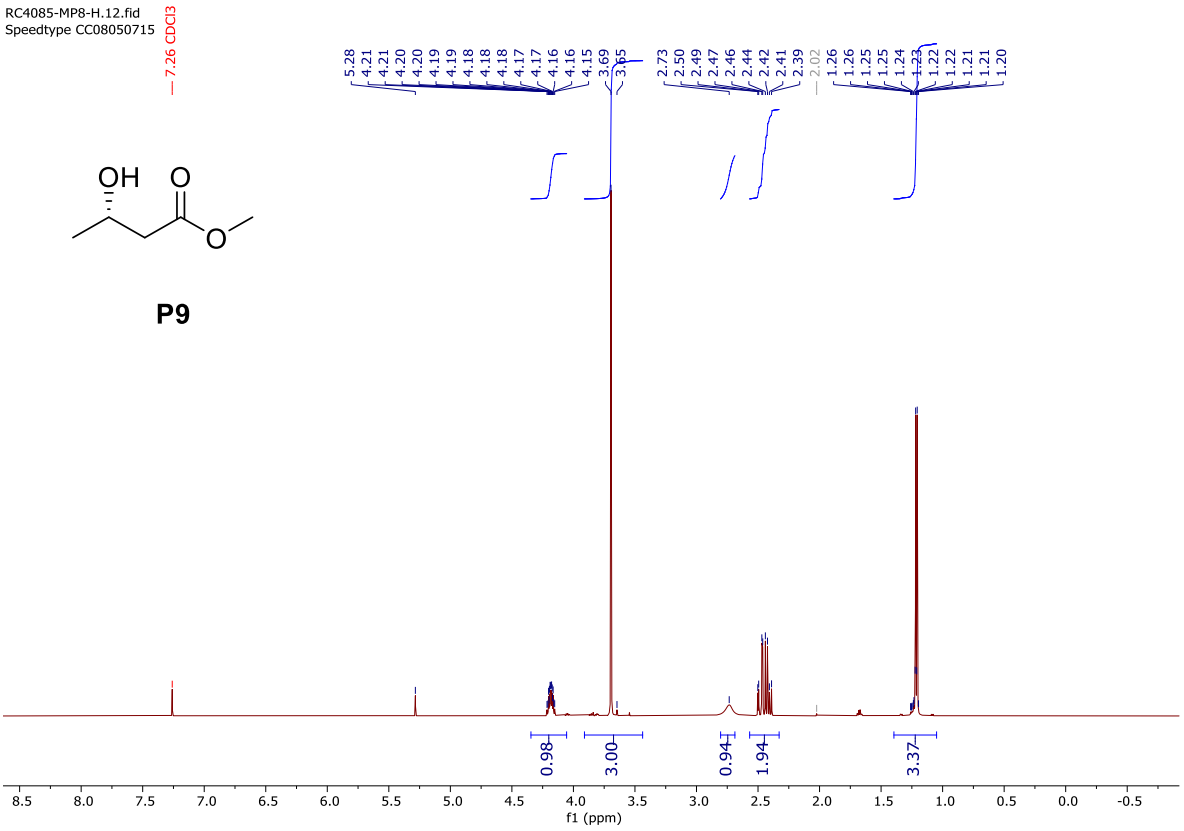
RC4085-MP8-H.12.fid
Speedtype CC08050715
7.26 CDCl3
OH
O
O
P9
5.28
4.21
4.21
4.20
4.20
4.19
4.19
4.18
4.18
4.18
4.17
4.17
4.16
4.16
4.15
3.69
3.65
2.73
2.50
2.49
2.47
2.46
2.44
2.42
2.41
2.39
2.02
1.26
1.26
1.25
1.25
1.24
1.23
1.22
1.22
1.21
1.21
1.20
0.98
3.00
0.94
1.94
3.37
8.5
8.0
7.5
7.0
6.5
6.0
5.5
5.0
4.5
4.0
3.5
3.0
2.5
2.0
1.5
1.0
0.5
0.0
-0.5
f1 (ppm)

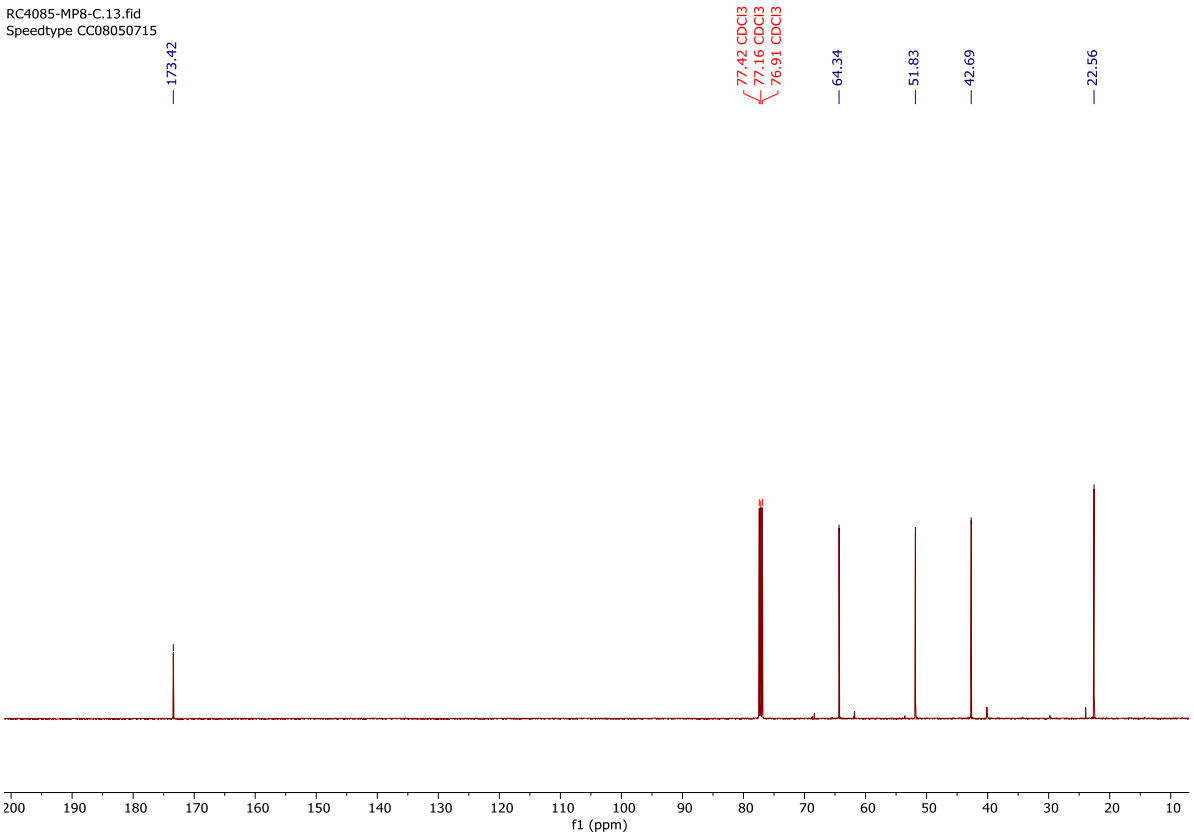
RC4085-MP8-C.13.fid
Speedtype CC08050715
173.42
77.42 CDCl3
77.16 CDCl3
76.91 CDCl3
64.34
51.83
42.69
22.56
200
190
180
170
160
150
140
130
120
110
100
90
80
70
60
50
40
30
20
10
f1 (ppm)

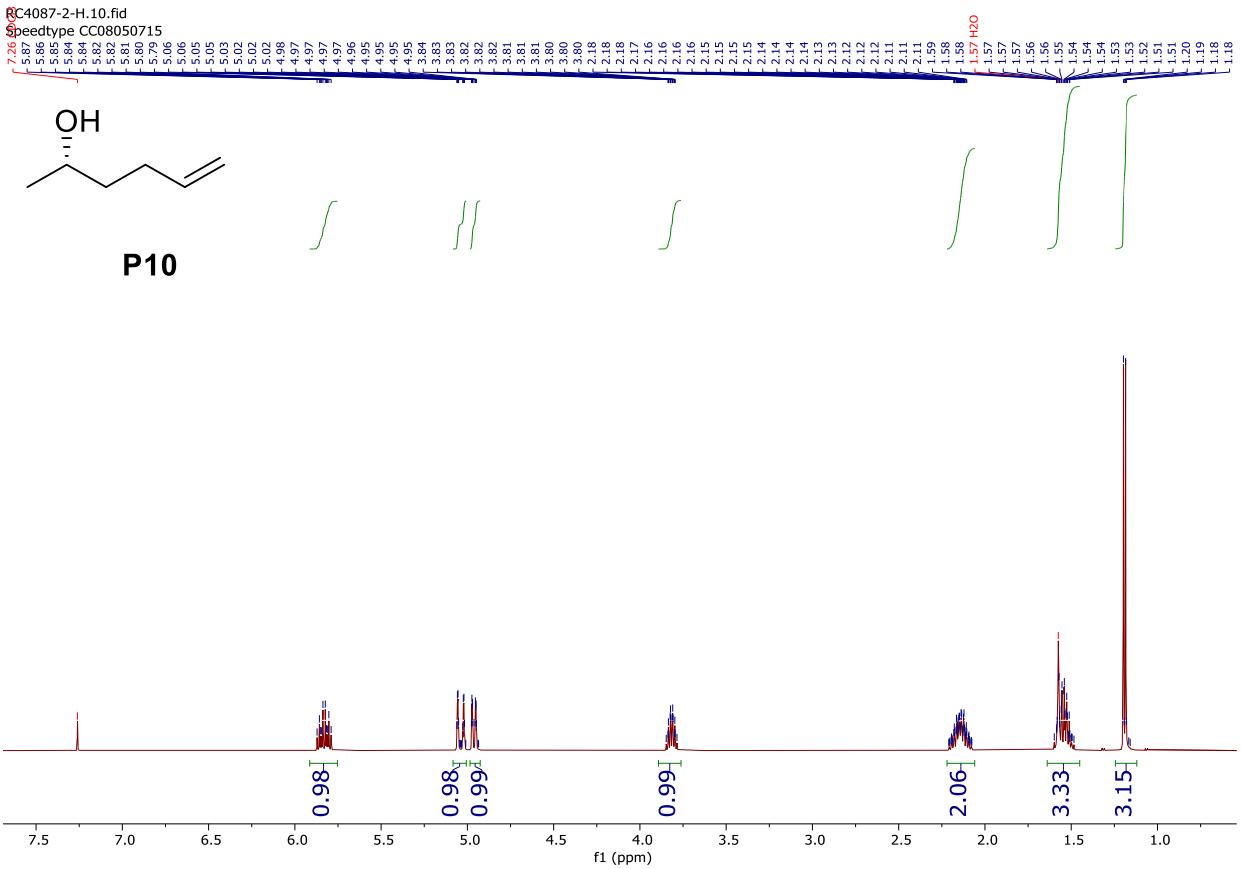
RC4087-2-H.10.fid
Speedtype CC08050715
OH
P10
0.98
0.98
0.99
0.99
2.06
3.33
3.15
f1 (ppm)

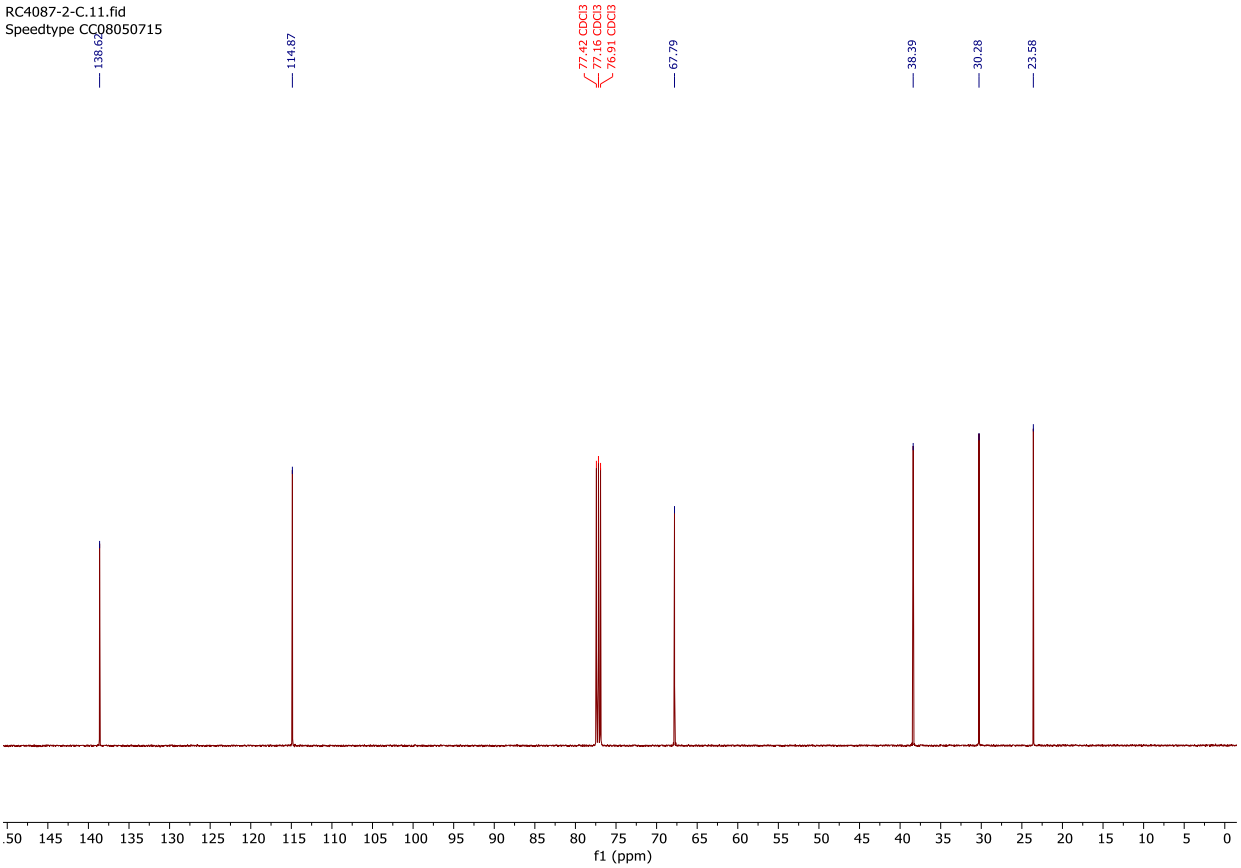
RC4087-2-C.11.fid
Speedtype CC08050715
138.62
114.87
77.42 CDCl3
77.16 CDCl3
76.91 CDCl3
67.79
38.39
30.28
23.58
f1 (ppm)

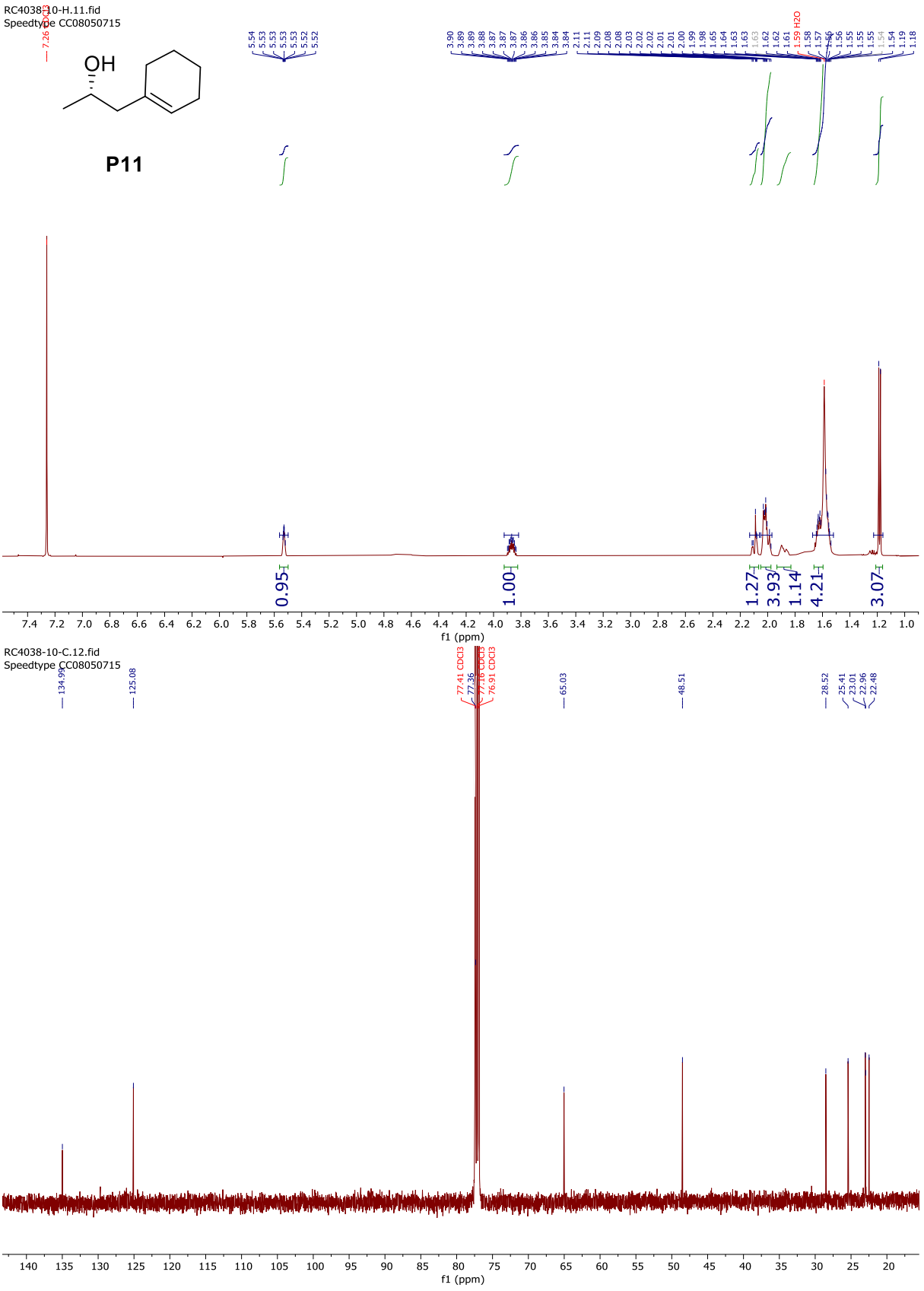
RC4038-10-H.11.fid
Speedtype CC08050715
OH
P11
7.26 CDCl3
1.59 H2O
0.95
1.00
1.27
3.93
1.14
4.21
3.07
f1 (ppm)
RC4038-10-C.12.fid
Speedtype CC08050715
134.99
125.08
77.41 CDCl3
77.36
77.16 CDCl3
76.91 CDCl3
65.03
48.51
28.52
25.41
23.01
22.96
22.48
f1 (ppm)

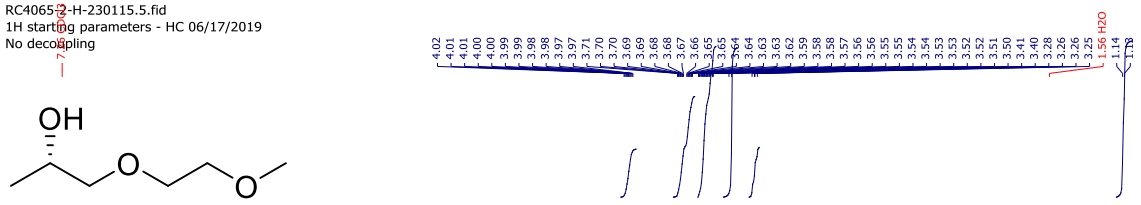
RC4065-2-H-230115.5.fid
1H starting parameters - HC 06/17/2019
No decoupling
OH
O
O

P12

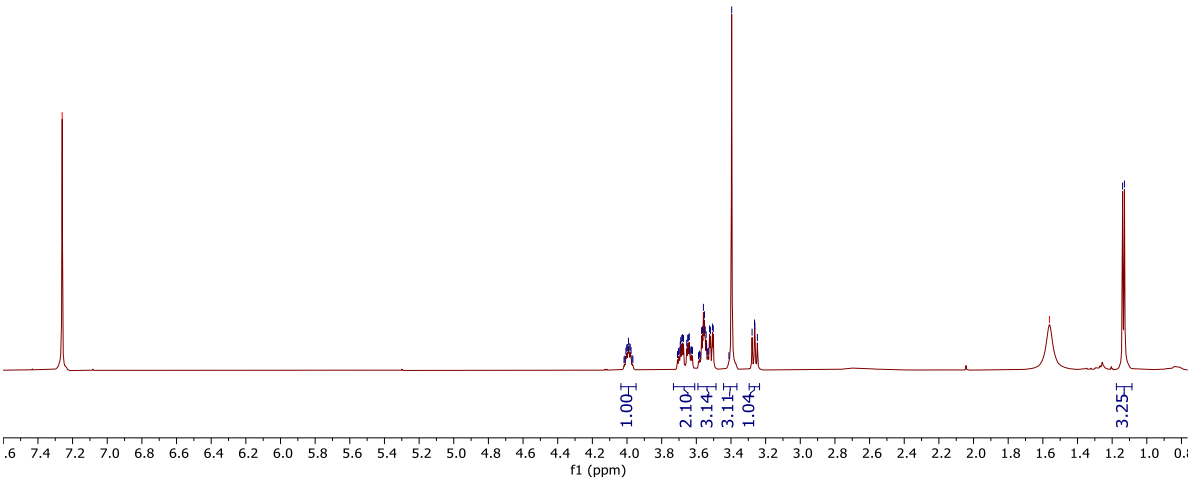
1.00
2.10
3.14
3.11
1.04
3.25
f1 (ppm)

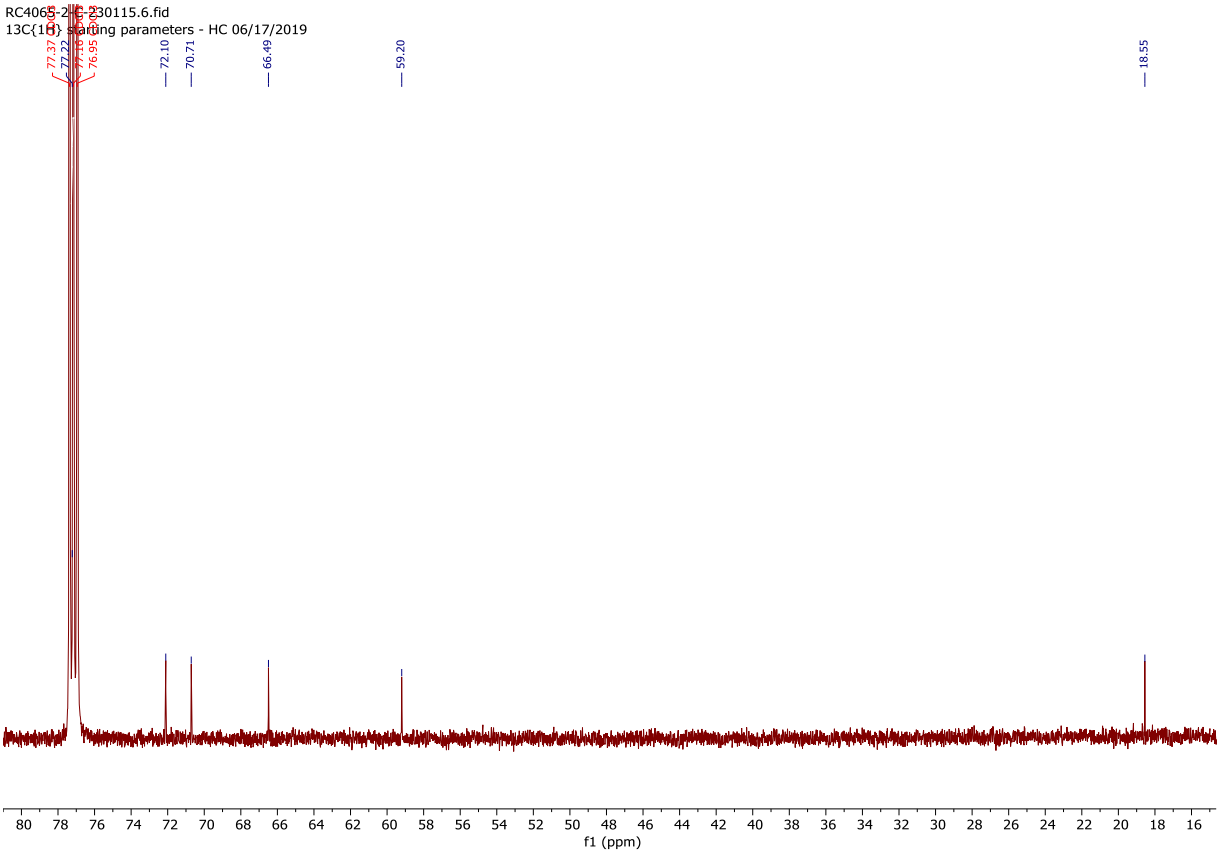
RC4065-2-C-230115.6.fid
13C{1H} starting parameters - HC 06/17/2019
77.37
77.22
77.16
76.95
72.10
70.71
66.49
59.20
18.55
f1 (ppm)

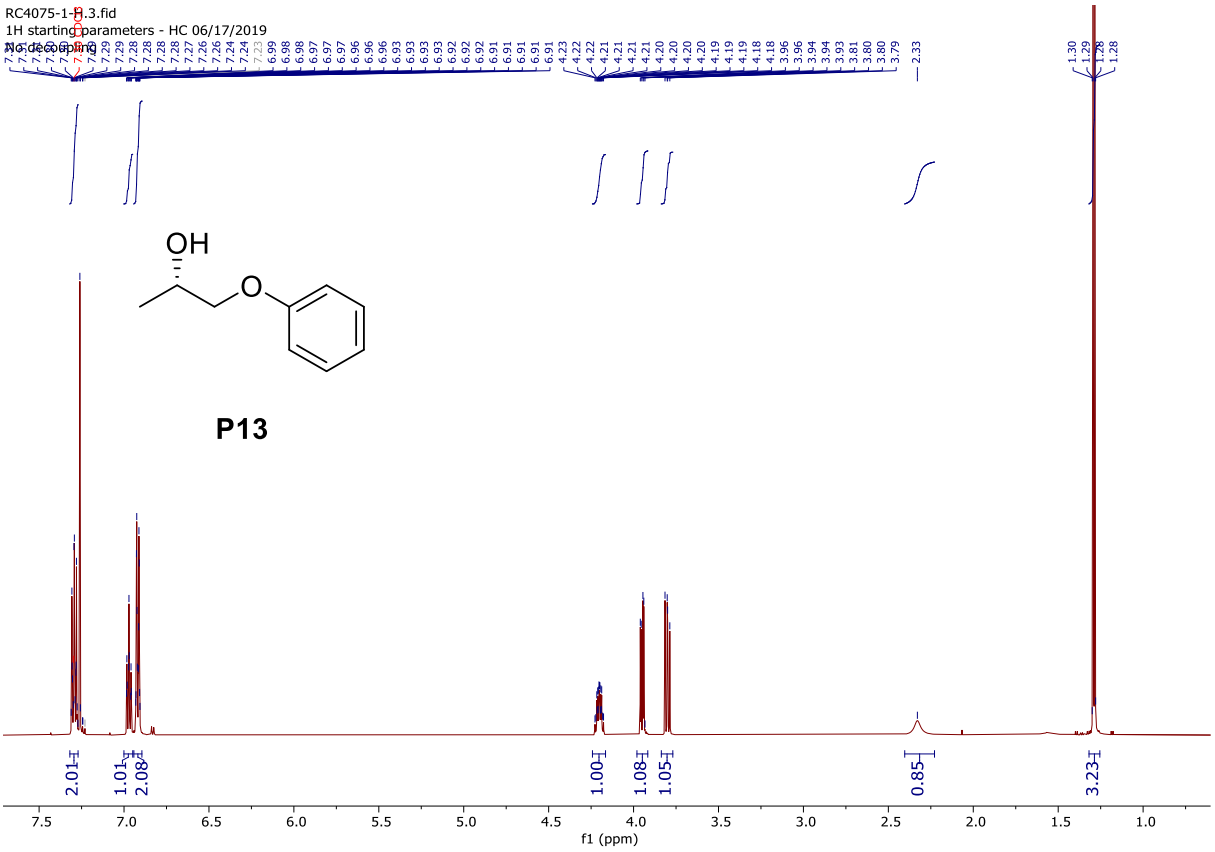
RC4075-1-H.3.fid
1H starting parameters - HC 06/17/2019
No deconvolution
OH
O
P13
2.01
1.01
2.08
1.00
1.08
1.05
0.85
3.23
f1 (ppm)

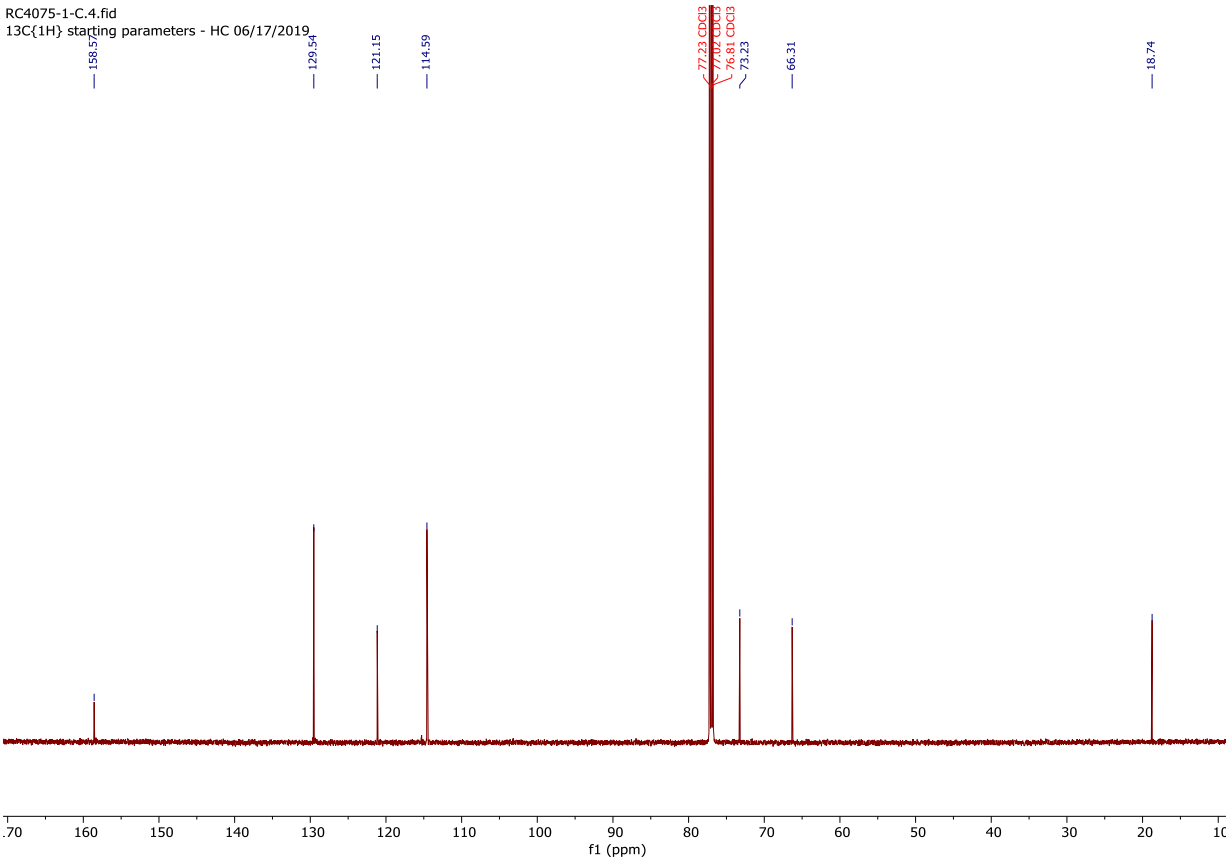
RC4075-1-C.4.fid
13C{1H} starting parameters - HC 06/17/2019
158.57
129.54
121.15
114.59
77.23 CDCl3
77.02 CDCl3
76.81 CDCl3
73.23
66.31
18.74
f1 (ppm)

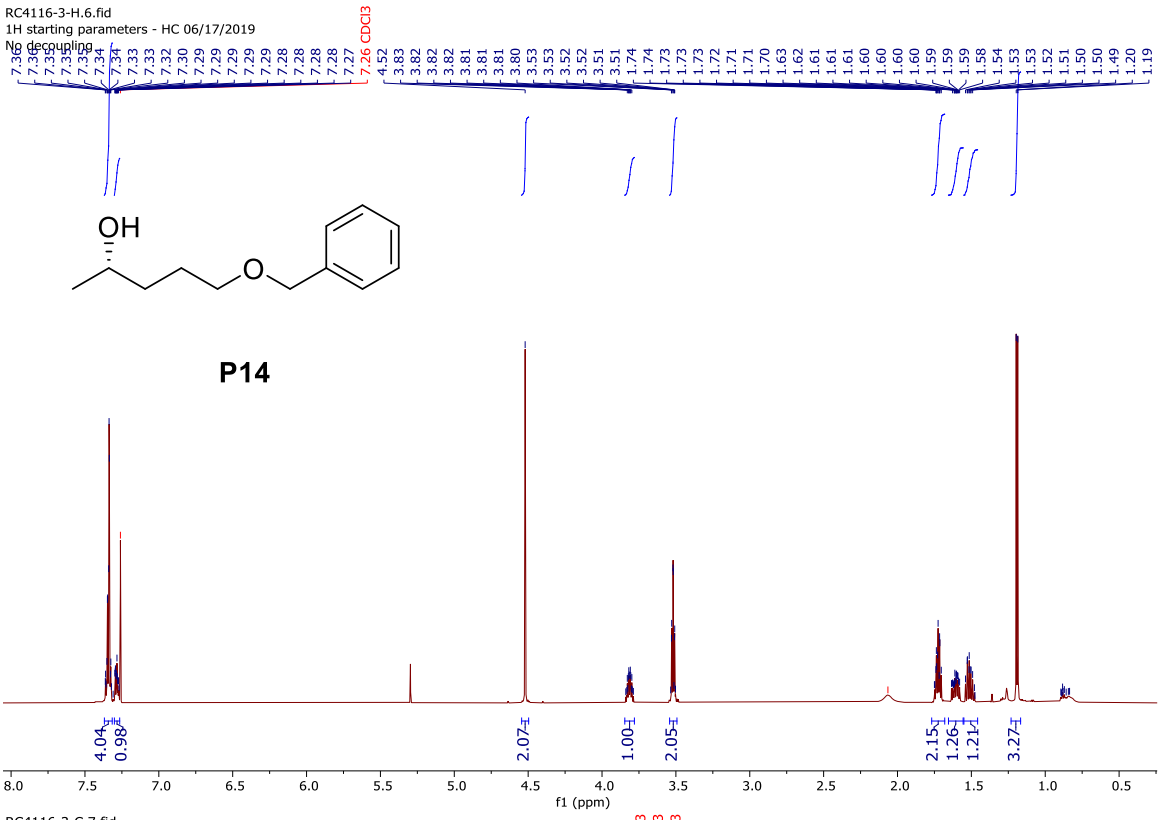
RC4116-3-H.6.fid
1H starting parameters - HC 06/17/2019
Ng decoupling
OH
O
P14
4.04
0.98
2.07
1.00
2.05
2.15
1.26
1.21
3.27
f1 (ppm)

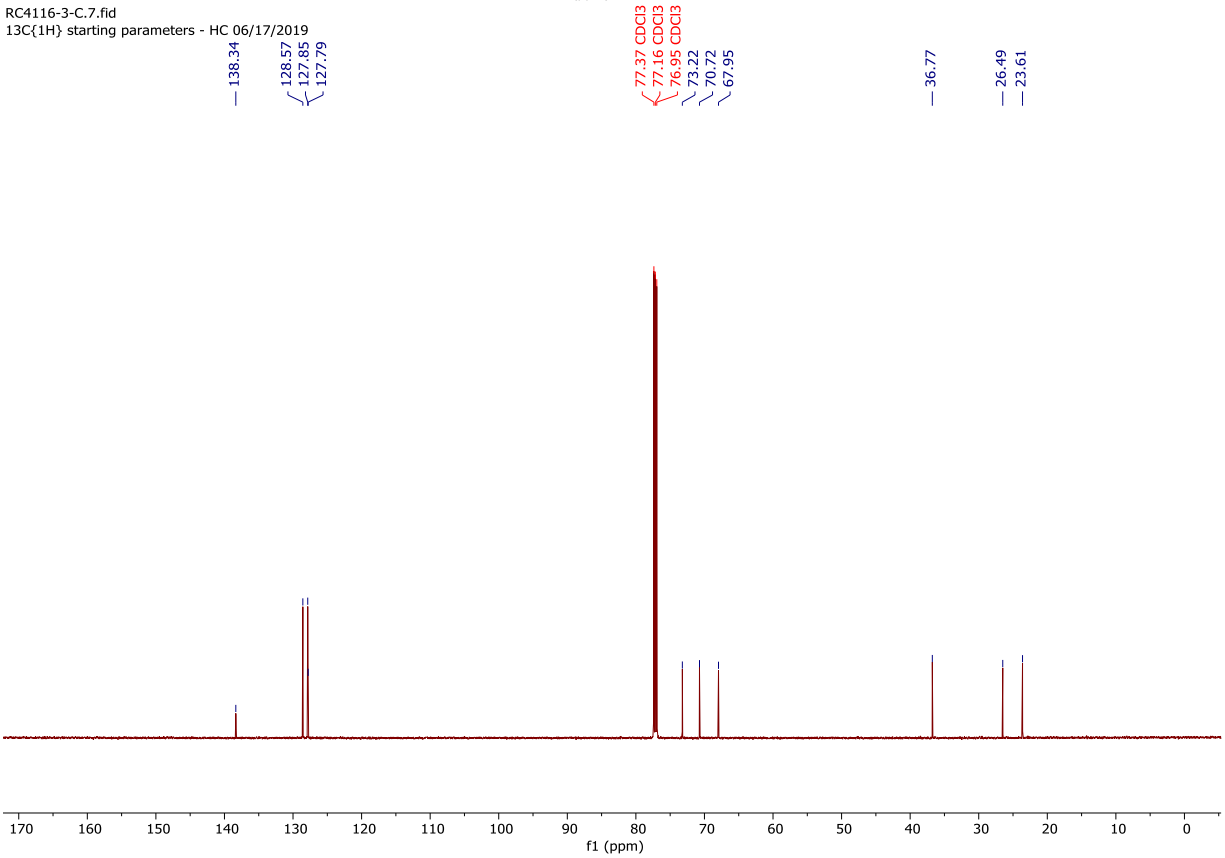
RC4116-3-C.7.fid
13C{1H} starting parameters - HC 06/17/2019
138.34
128.57
127.85
127.79
77.37 CDCl3
77.16 CDCl3
76.95 CDCl3
73.22
70.72
67.95
36.77
26.49
23.61
f1 (ppm)

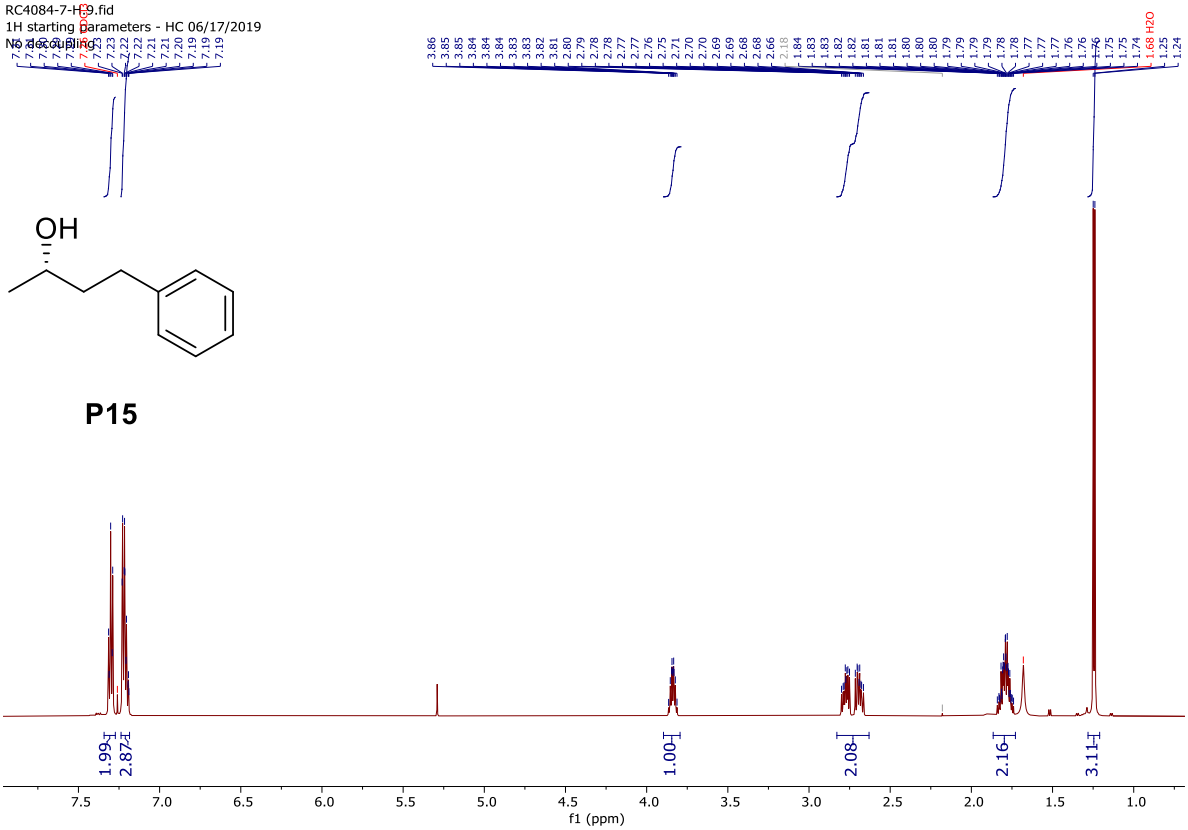
RC4084-7-H-9.fid
1H starting parameters - HC 06/17/2019
OH
P15
1.99
2.87
1.00
2.08
2.16
3.11
f1 (ppm)

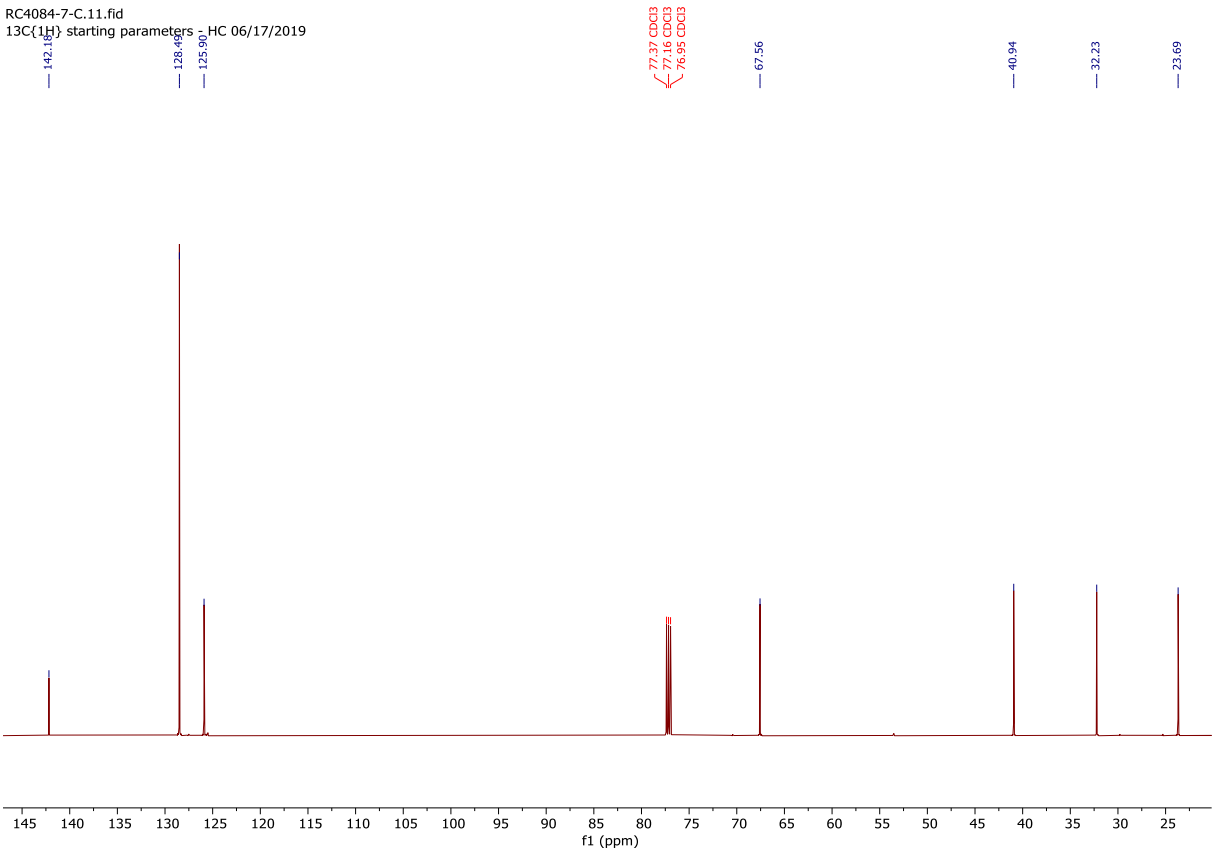
RC4084-7-C.11.fid
13C{1H} starting parameters - HC 06/17/2019
142.16
128.49
125.90
77.37 CDCl3
77.16 CDCl3
76.95 CDCl3
67.56
40.94
32.23
23.69
f1 (ppm)

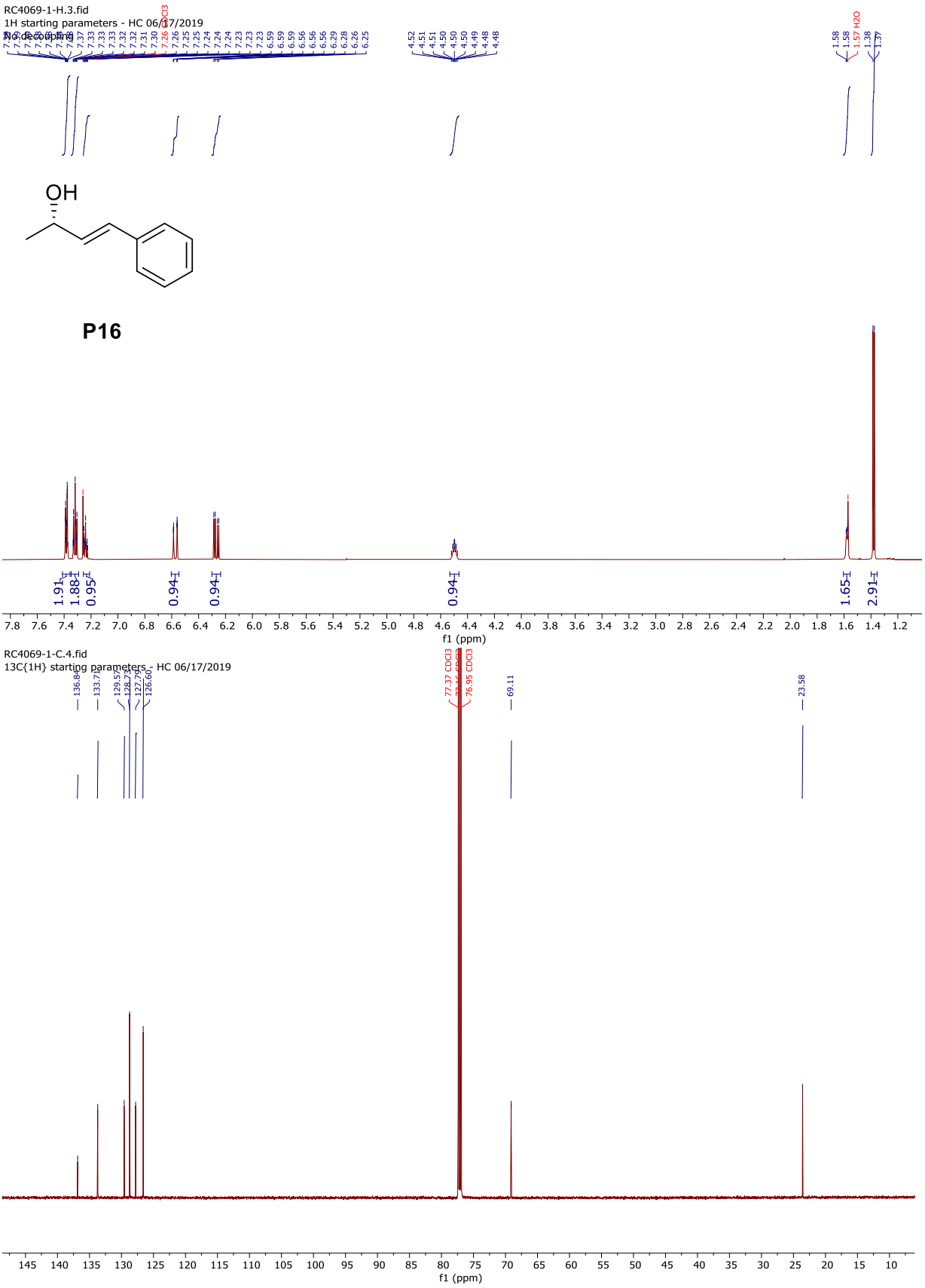
RC4069-1-H.3.fid
1H starting parameters - HC 06/17/2019
No decoupling
OH
P16
1.91
1.88
0.95
0.94
0.94
0.94
1.65
2.91
f1 (ppm)
RC4069-1-C.4.fid
13C{1H} starting parameters - HC 06/17/2019
136.84
133.71
129.57
128.73
127.79
126.60
77.37 CDCl3
76.95 CDCl3
69.11
23.58
f1 (ppm)

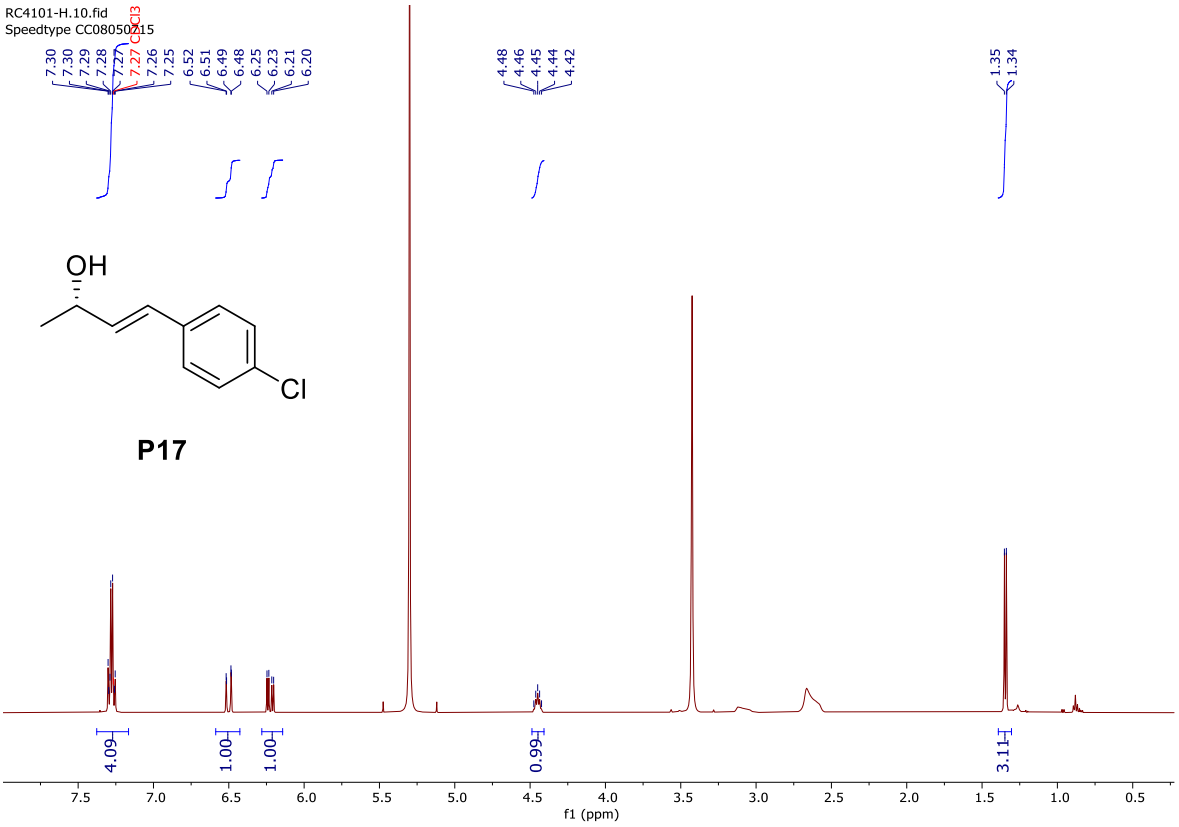
RC4101-H.10.fid
Speedtype CC08050715
7.30
7.30
7.29
7.28
7.27
7.27 CDCl3
7.26
7.25
6.52
6.51
6.49
6.48
6.25
6.23
6.21
6.20
4.48
4.46
4.45
4.44
4.42
1.35
1.34
OH
Cl
P17
4.09
1.00
1.00
0.99
3.11
7.5
7.0
6.5
6.0
5.5
5.0
4.5
4.0
3.5
3.0
2.5
2.0
1.5
1.0
0.5
f1 (ppm)

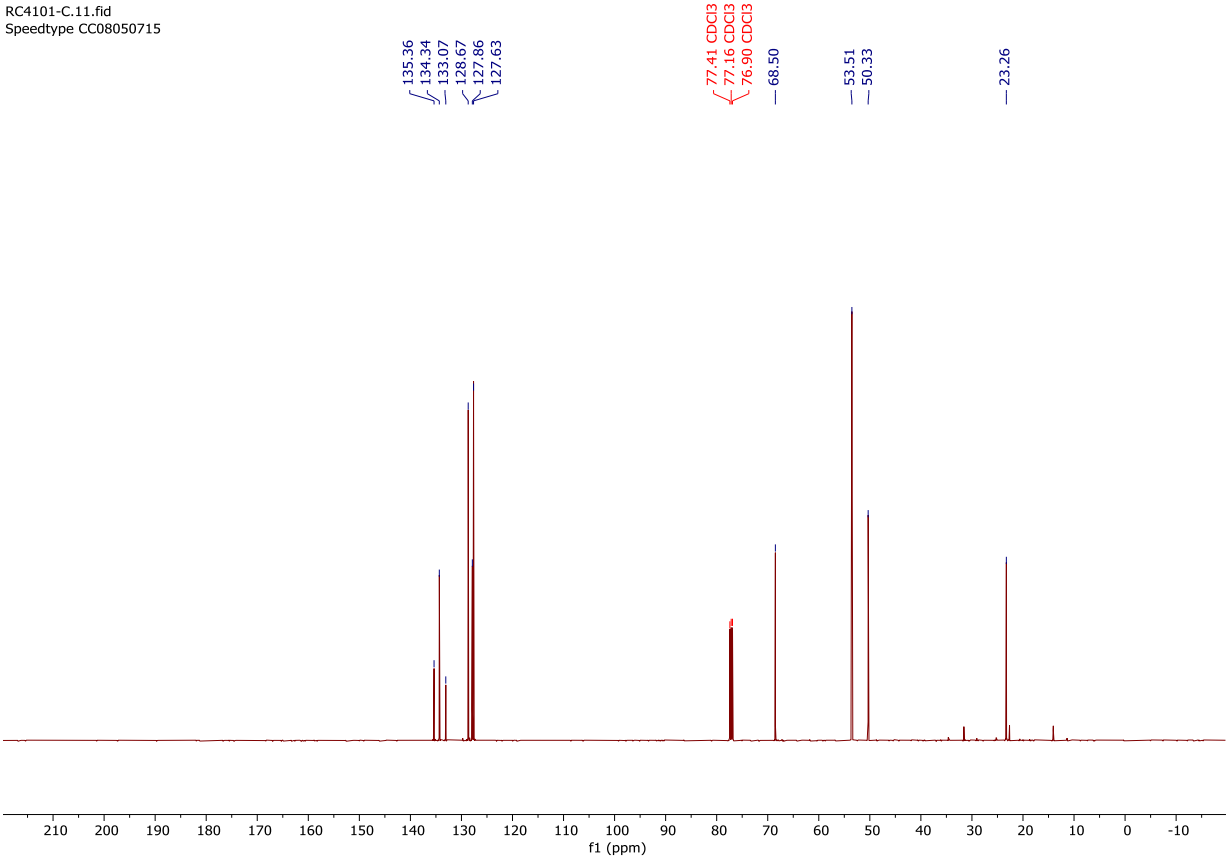
RC4101-C.11.fid
Speedtype CC08050715
135.36
134.34
133.07
128.67
127.86
127.63
77.41 CDCl3
77.16 CDCl3
76.90 CDCl3
68.50
53.51
50.33
23.26
210
200
190
180
170
160
150
140
130
120
110
100
90
80
70
60
50
40
30
20
10
0
-10
f1 (ppm)

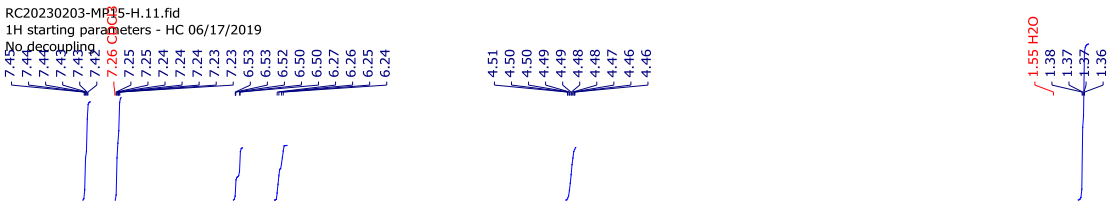
RC20230203-MP15-H.11.fid
1H starting parameters - HC 06/17/2019
No decoupling
7.45
7.44
7.44
7.43
7.43
7.42
7.26 CDCl3
7.25
7.25
7.24
7.24
7.24
7.23
7.23
6.53
6.53
6.52
6.50
6.50
6.27
6.26
6.25
6.24
4.51
4.50
4.50
4.49
4.49
4.48
4.48
4.47
4.46
4.46
1.55 H2O
1.38
1.37
1.37
1.36

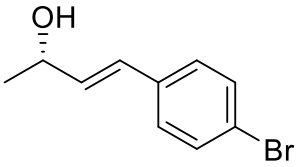
OH
Br

P18

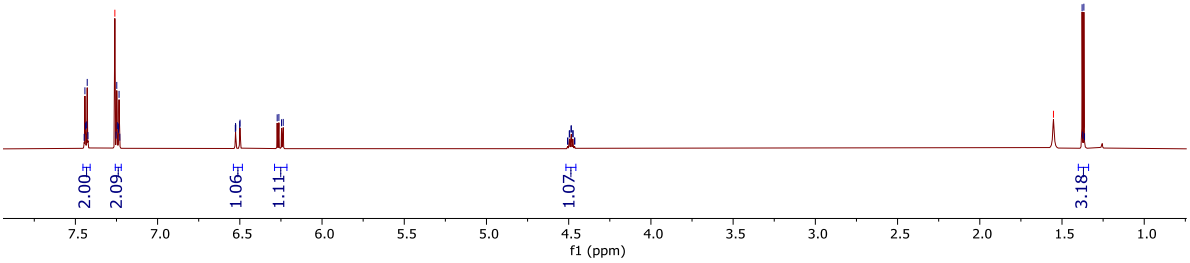
2.00
2.09
1.06
1.11
1.07
3.18
7.5
7.0
6.5
6.0
5.5
5.0
4.5
4.0
3.5
3.0
2.5
2.0
1.5
1.0
f1 (ppm)

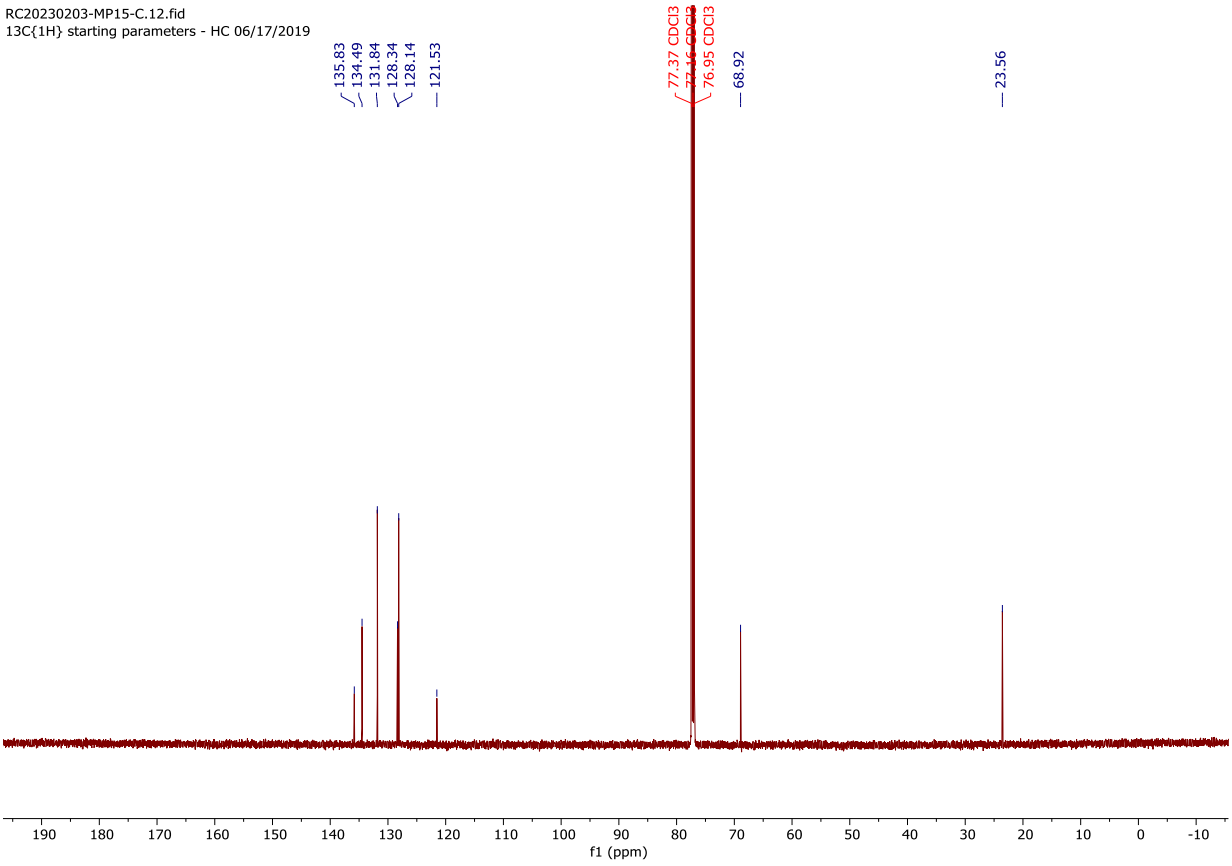
RC20230203-MP15-C.12.fid
13C{1H} starting parameters - HC 06/17/2019
135.83
134.49
131.84
128.34
128.14
121.53
77.37 CDCl3
77.16 CDCl3
76.95 CDCl3
68.92
23.56
190
180
170
160
150
140
130
120
110
100
90
80
70
60
50
40
30
20
10
0
-10
f1 (ppm)

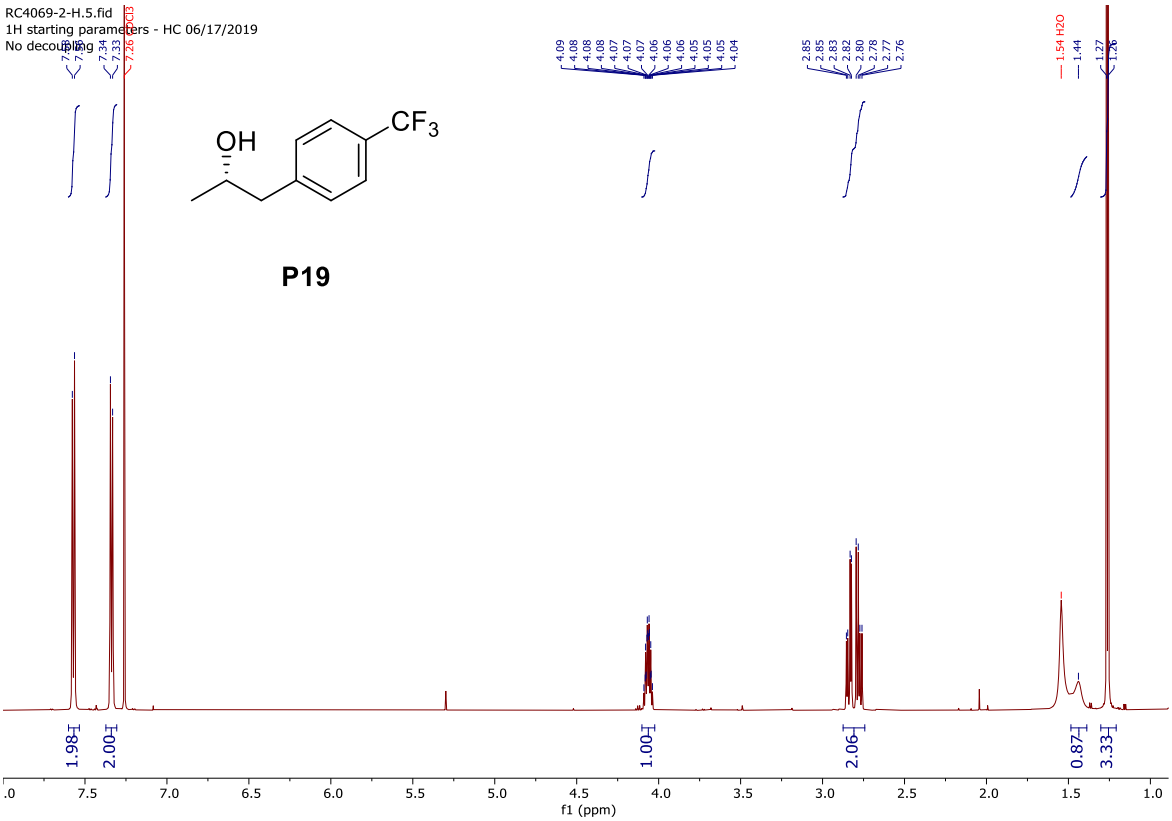
RC4069-2-H.5.fid
1H starting parameters - HC 06/17/2019
No decoupling
OH
CF3
P19
1.98
2.00
1.00
2.06
0.87
3.33
f1 (ppm)

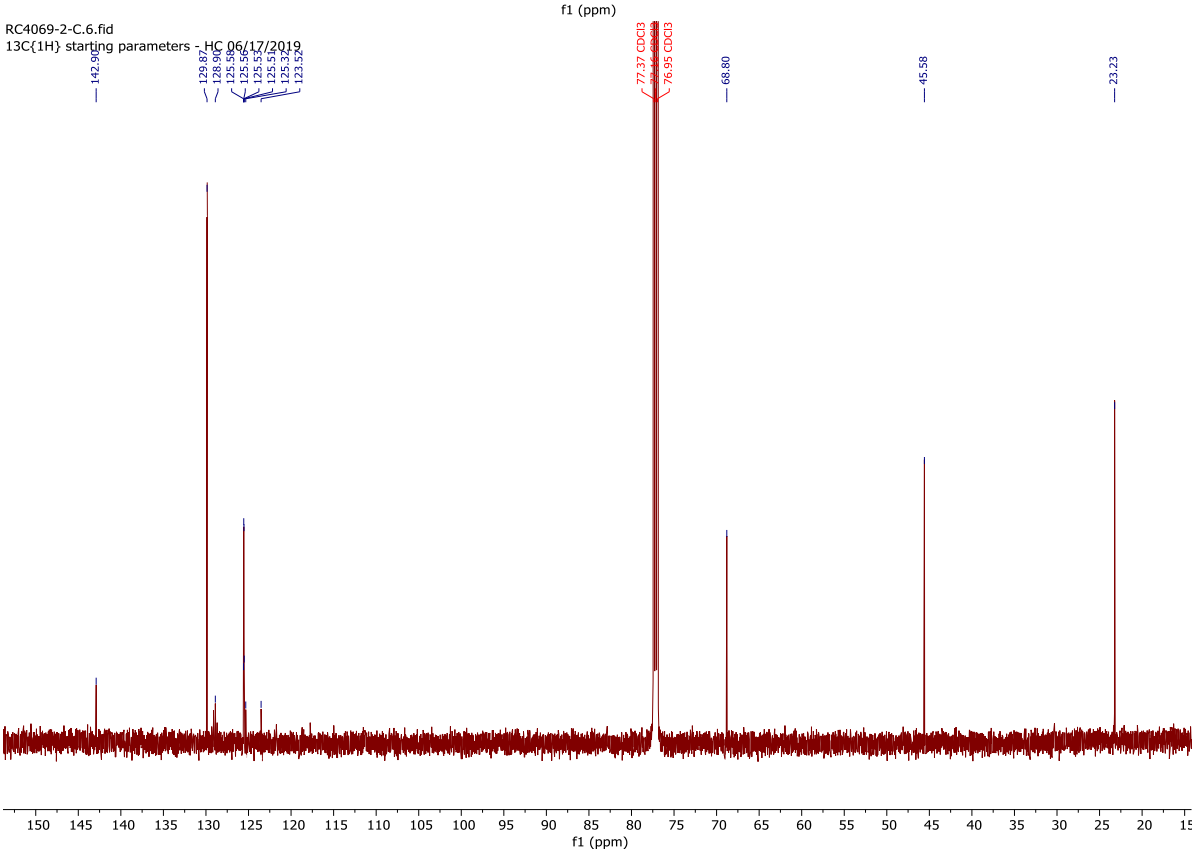
RC4069-2-C.6.fid
13C{1H} starting parameters - HC 06/17/2019
142.90
129.87
128.90
128.58
125.56
125.52
125.51
125.32
123.52
77.37 CDCl3
76.95 CDCl3
68.80
45.58
23.23
f1 (ppm)

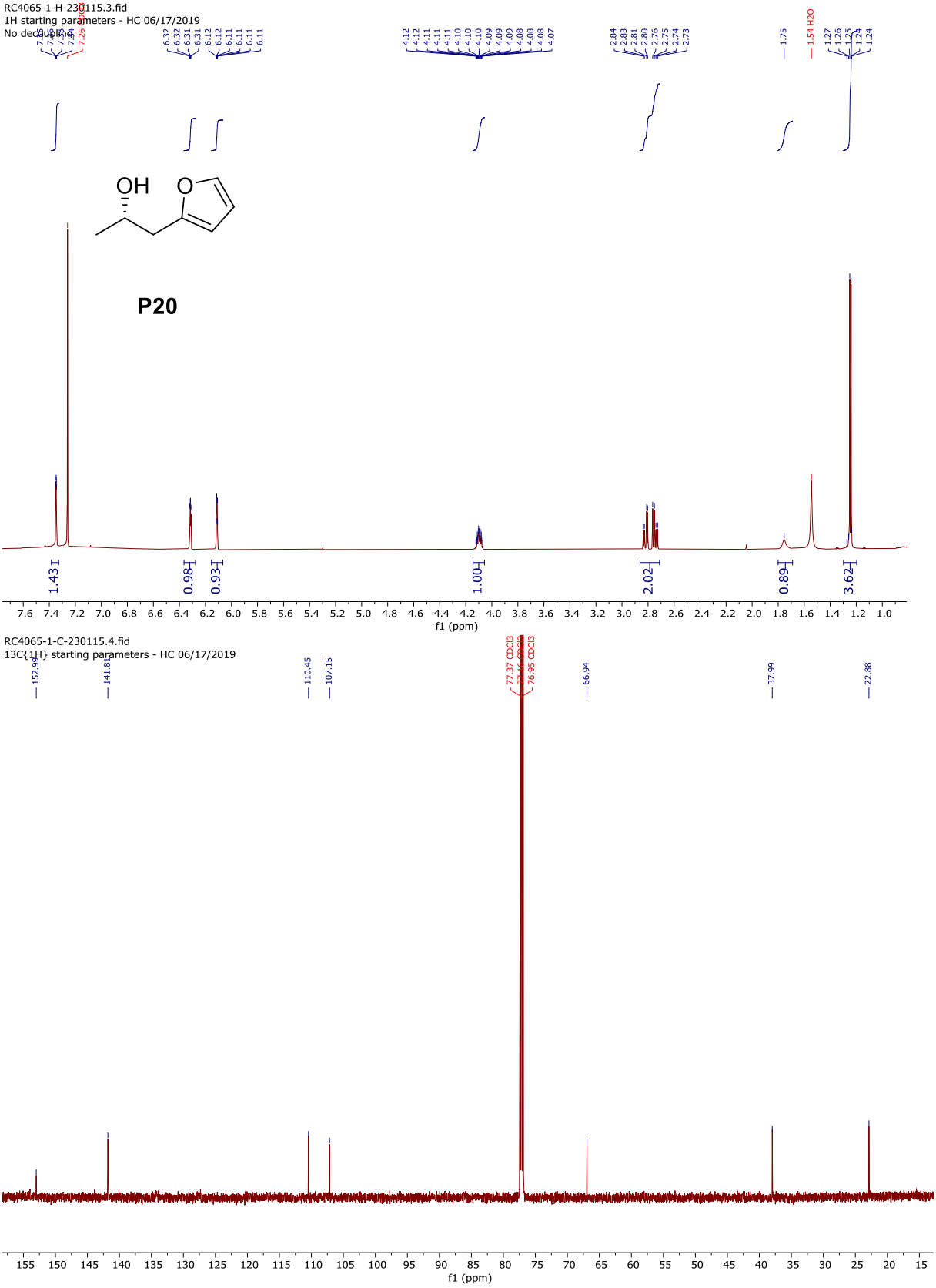
RC4065-1-H-230115.3.fid
1H starting parameters - HC 06/17/2019
No decoupling
OH
O
P20
1.54 H2O
1.43
0.98
0.93
1.00
2.02
0.89
3.62
f1 (ppm)
RC4065-1-C-230115.4.fid
13C{1H} starting parameters - HC 06/17/2019
152.94
141.85
110.45
107.15
77.37 CDCl3
76.95 CDCl3
66.94
37.99
22.88
f1 (ppm)

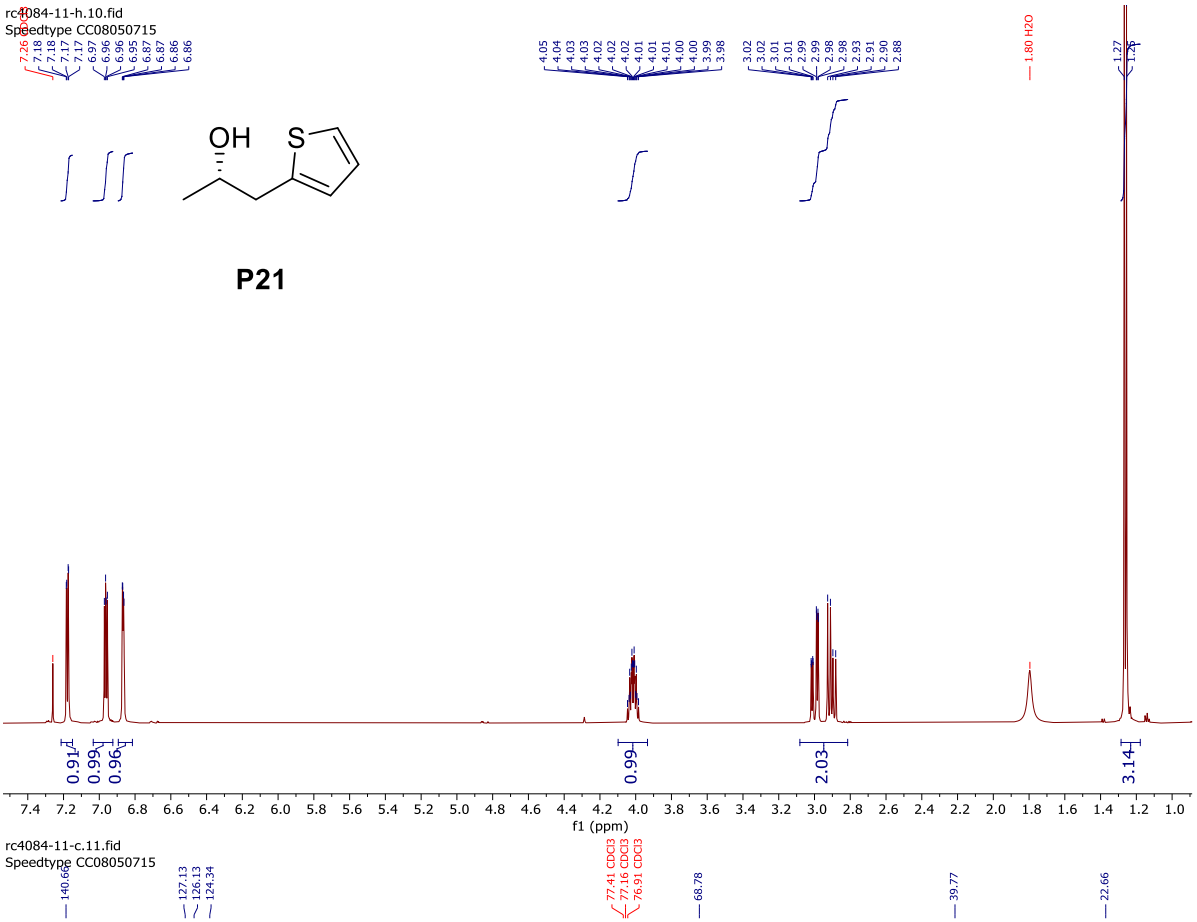
rc4084-11-h.10.fid
Speedtype CC08050715
OH
S
P21
1.80 H2O
0.91
0.99
0.96
0.99
2.03
3.14
f1 (ppm)

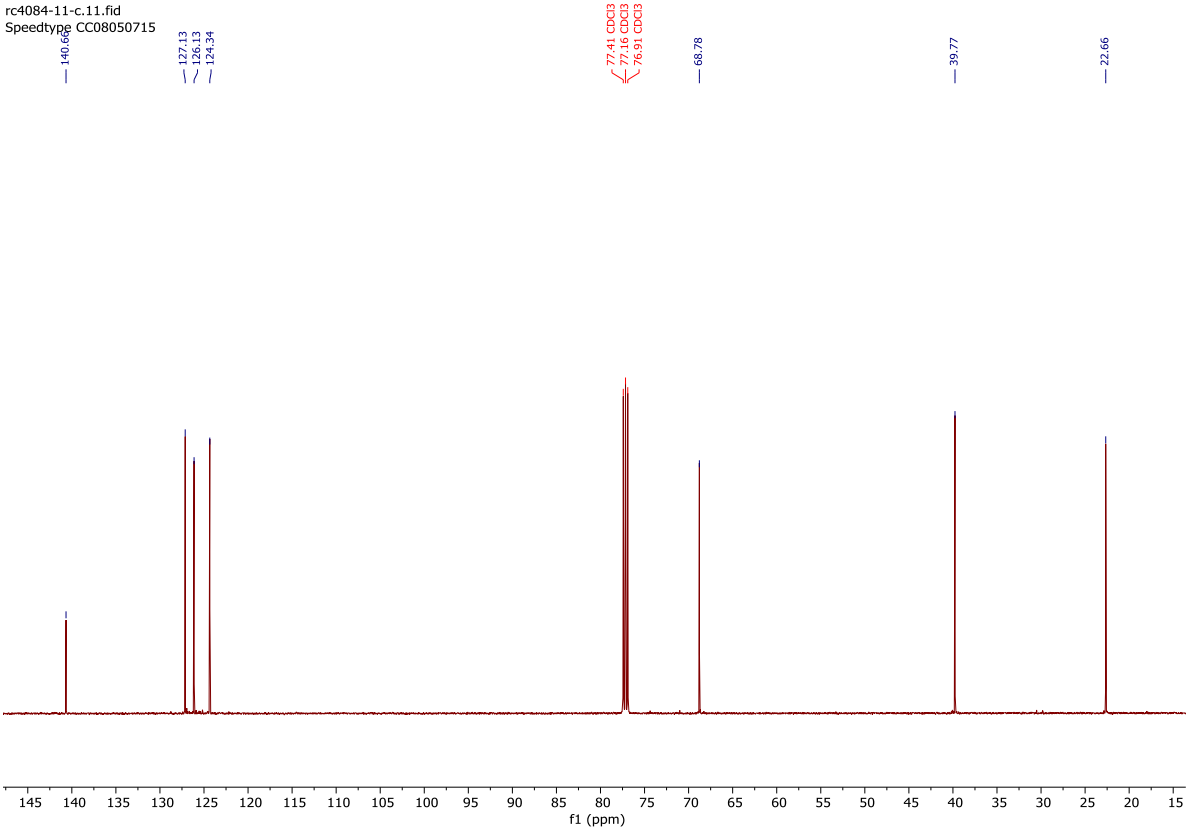
rc4084-11-c.11.fid
Speedtype CC08050715
140.66
127.13
126.13
124.34
77.41 CDCl3
77.16 CDCl3
76.91 CDCl3
68.78
39.77
22.66
f1 (ppm)

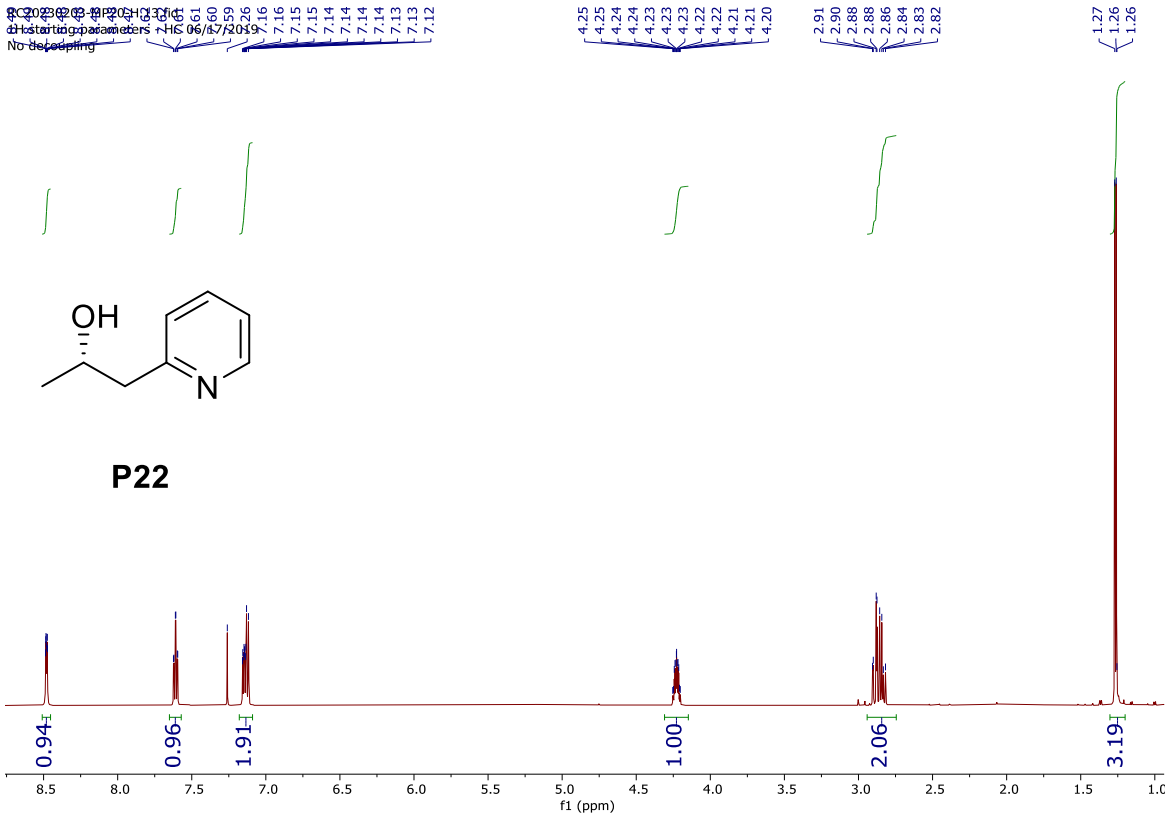
OH
N
P22
0.94
0.96
1.91
1.00
2.06
3.19
f1 (ppm)

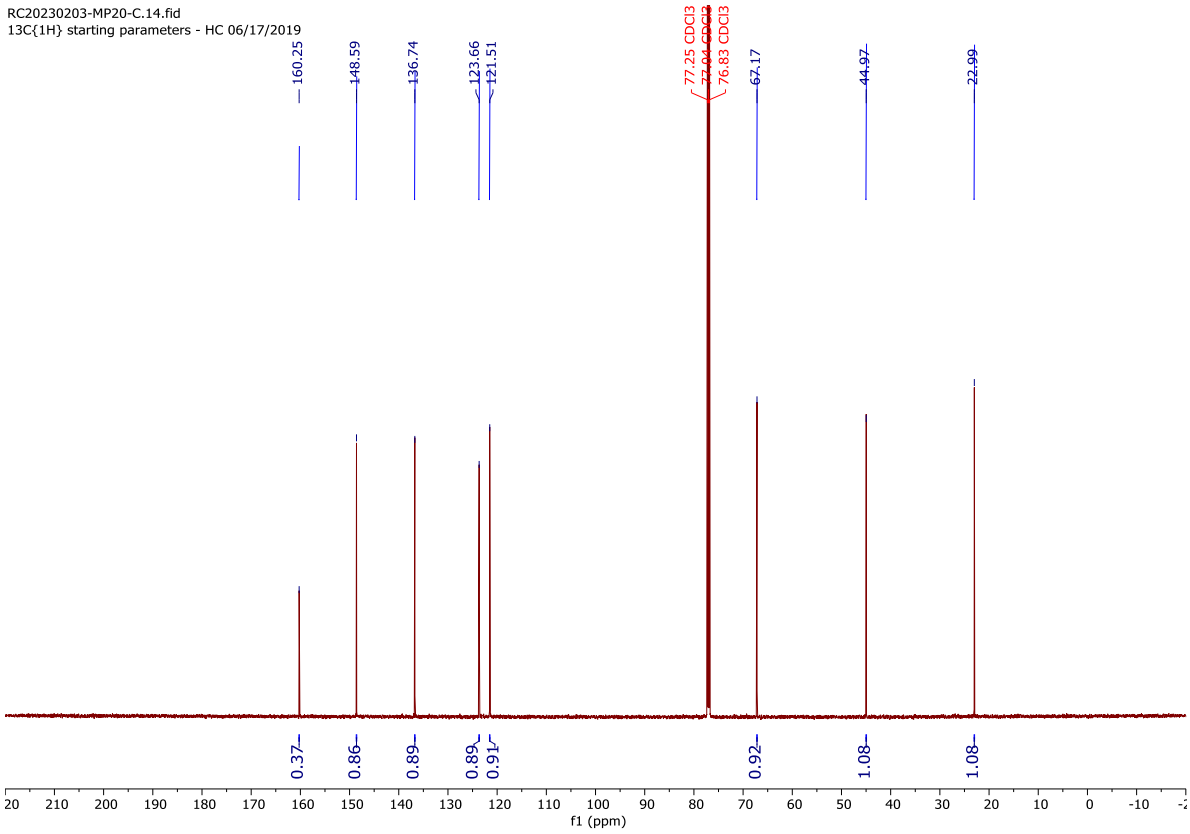
RC20230203-MP20-C.14.fid
13C{1H} starting parameters - HC 06/17/2019
160.25
148.59
136.74
123.66
121.51
77.25 CDCl3
77.04 CDCl3
76.83 CDCl3
67.17
44.97
22.99
0.37
0.86
0.89
0.89
0.91
0.92
1.08
1.08
f1 (ppm)

RC4038-14-H.10.fid
Speedtype CC08050715

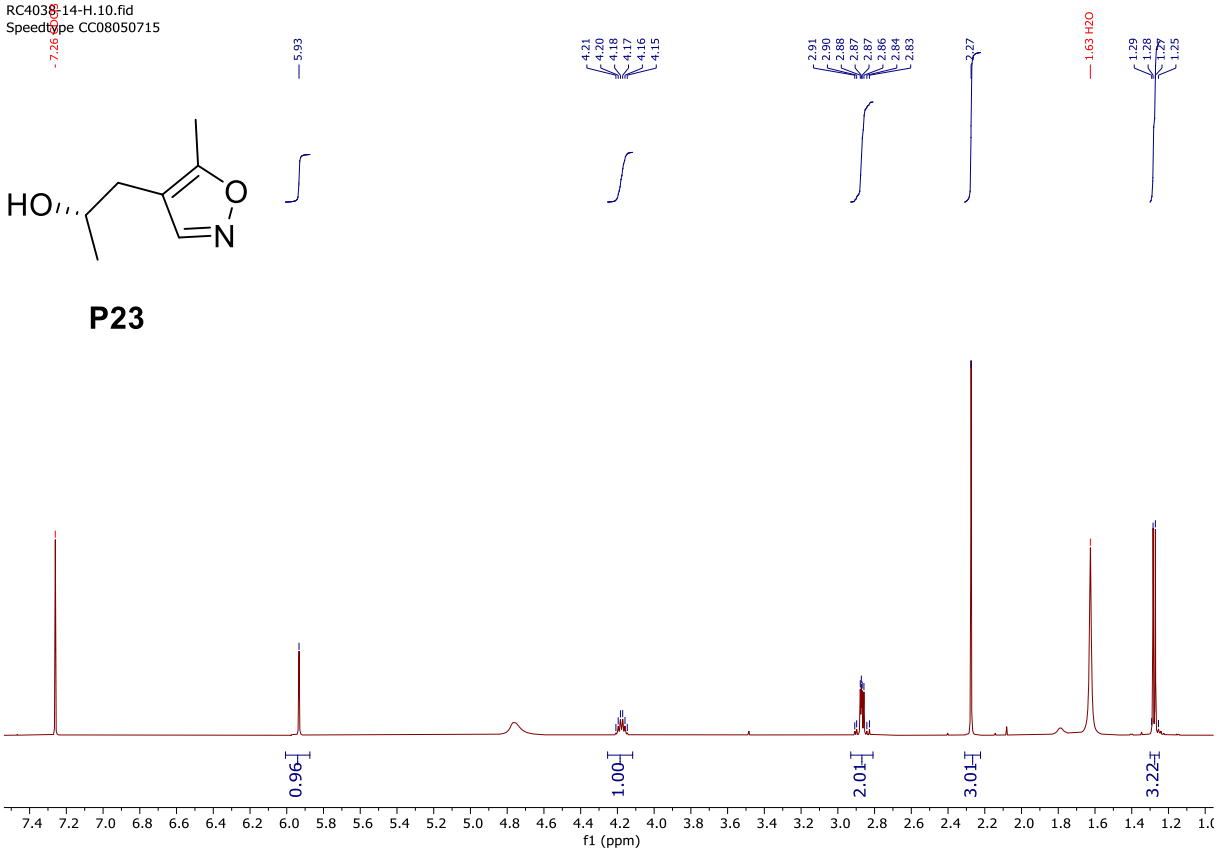

P23

RC4038-14-H.11.fid
Speedtype CC08050715

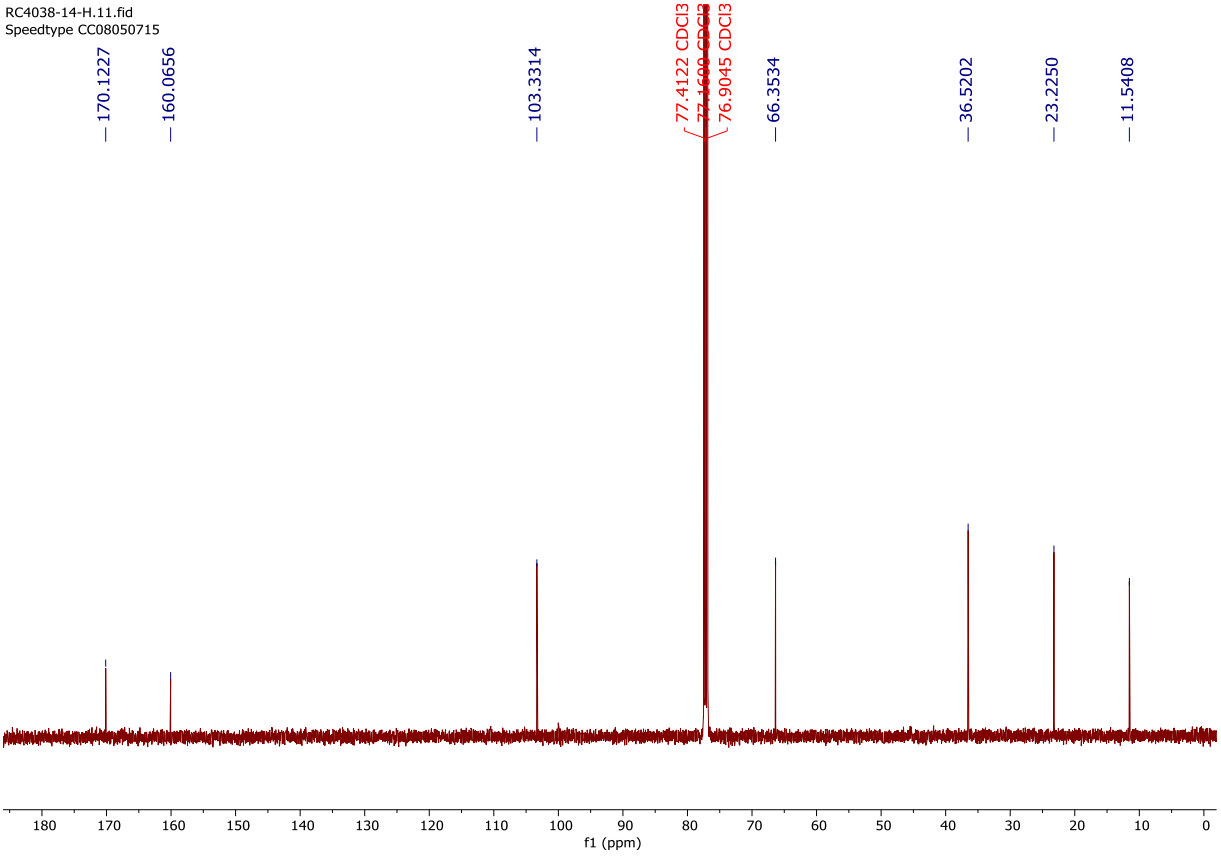

RC4038-12-H.10.fid
Speedtype CC08050715

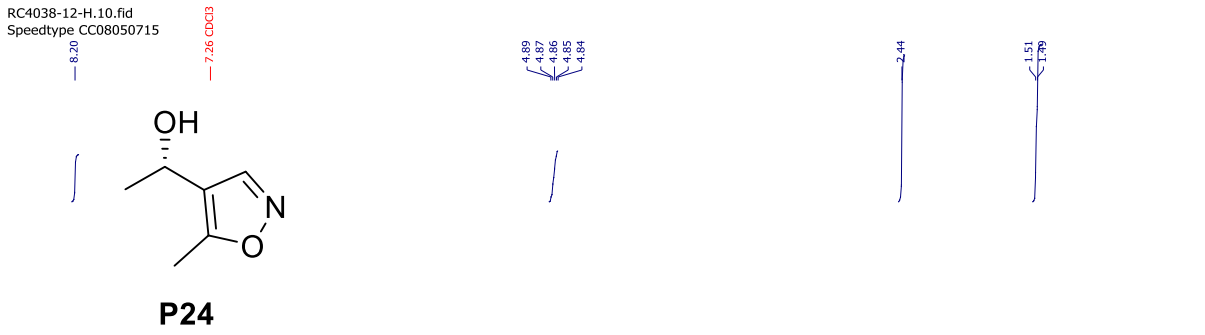

P24

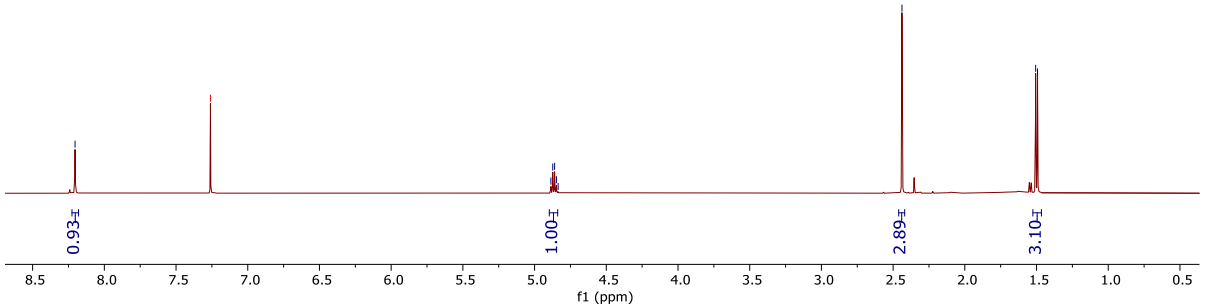

RC4038-12-C.11.fid
Speedtype CC08050715

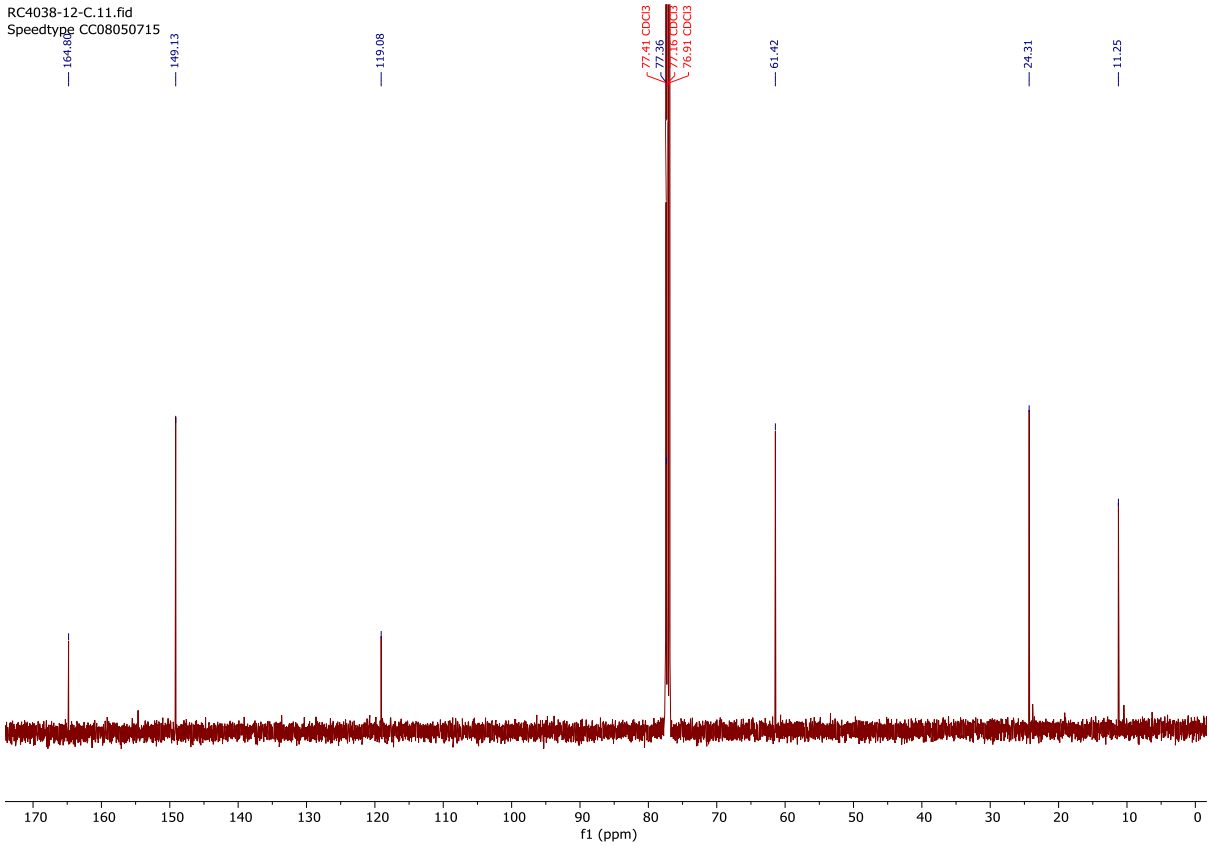

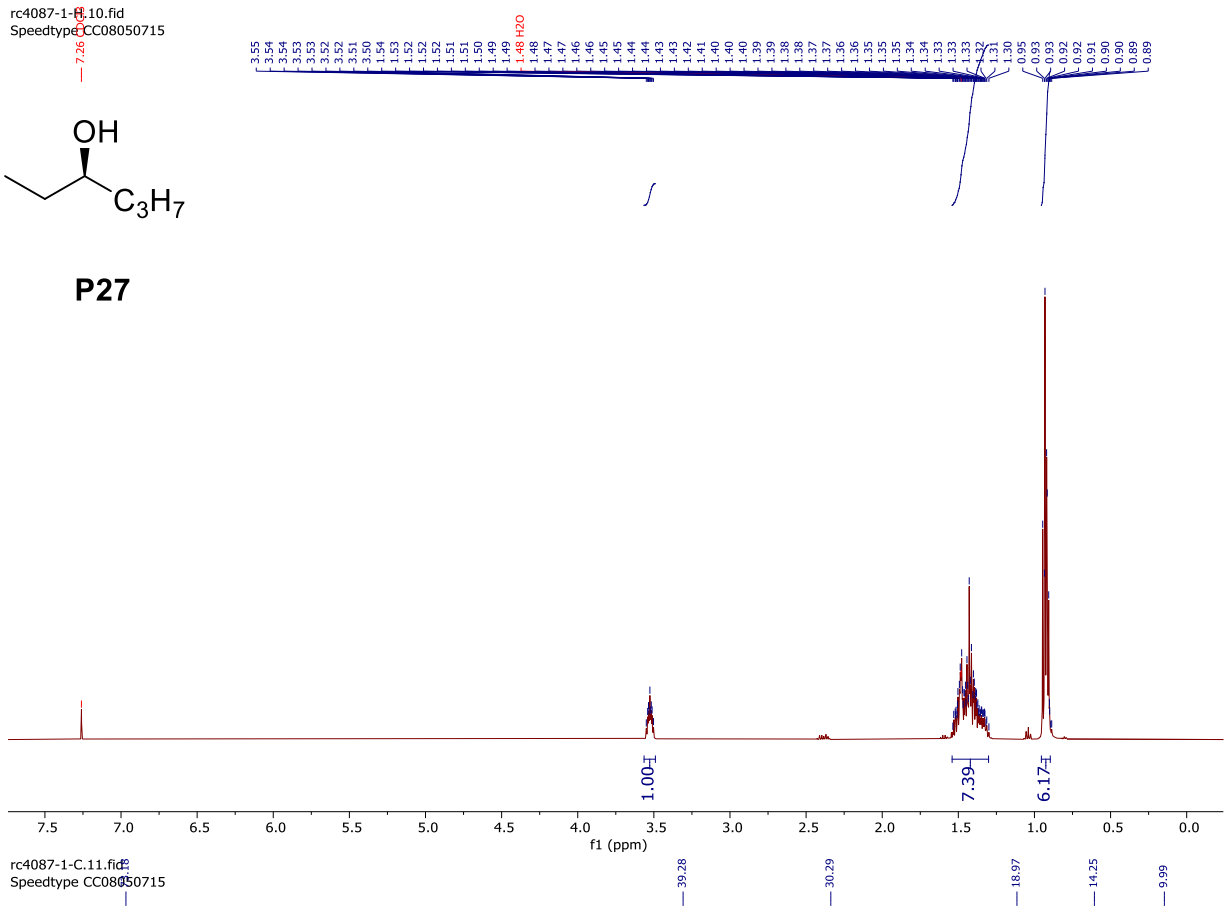
rc4087-1-H.10.fid
Speedtype CC08050715
OH
C_3H_7
P27
1.00
7.39
6.17
f1 (ppm)
rc4087-1-C.11.fid
Speedtype CC08050715
39.28
30.29
18.97
14.25
9.99
f1 (ppm)

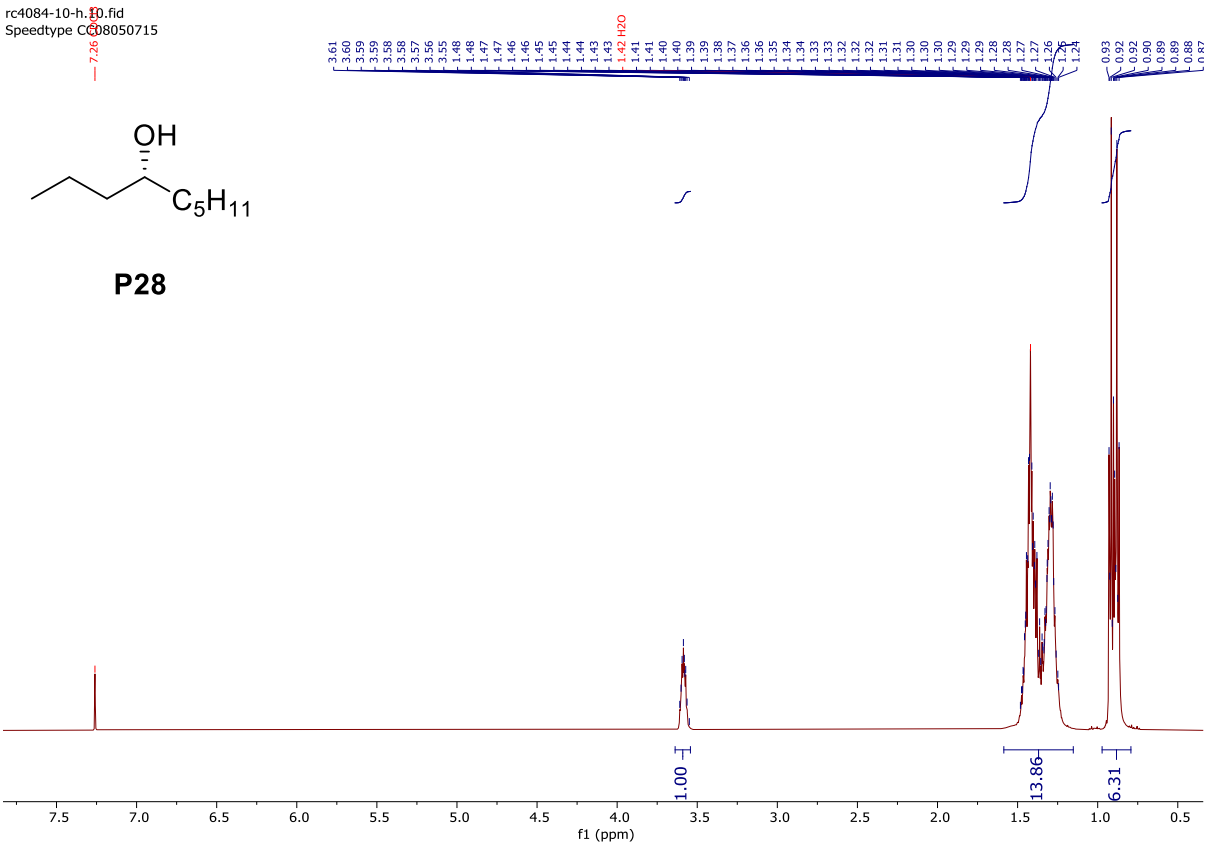
rc4084-10-h.10.fid
Speedtype CC08050715
OH
C_5H_{11}
P28
1.00
13.86
6.31
f1 (ppm)

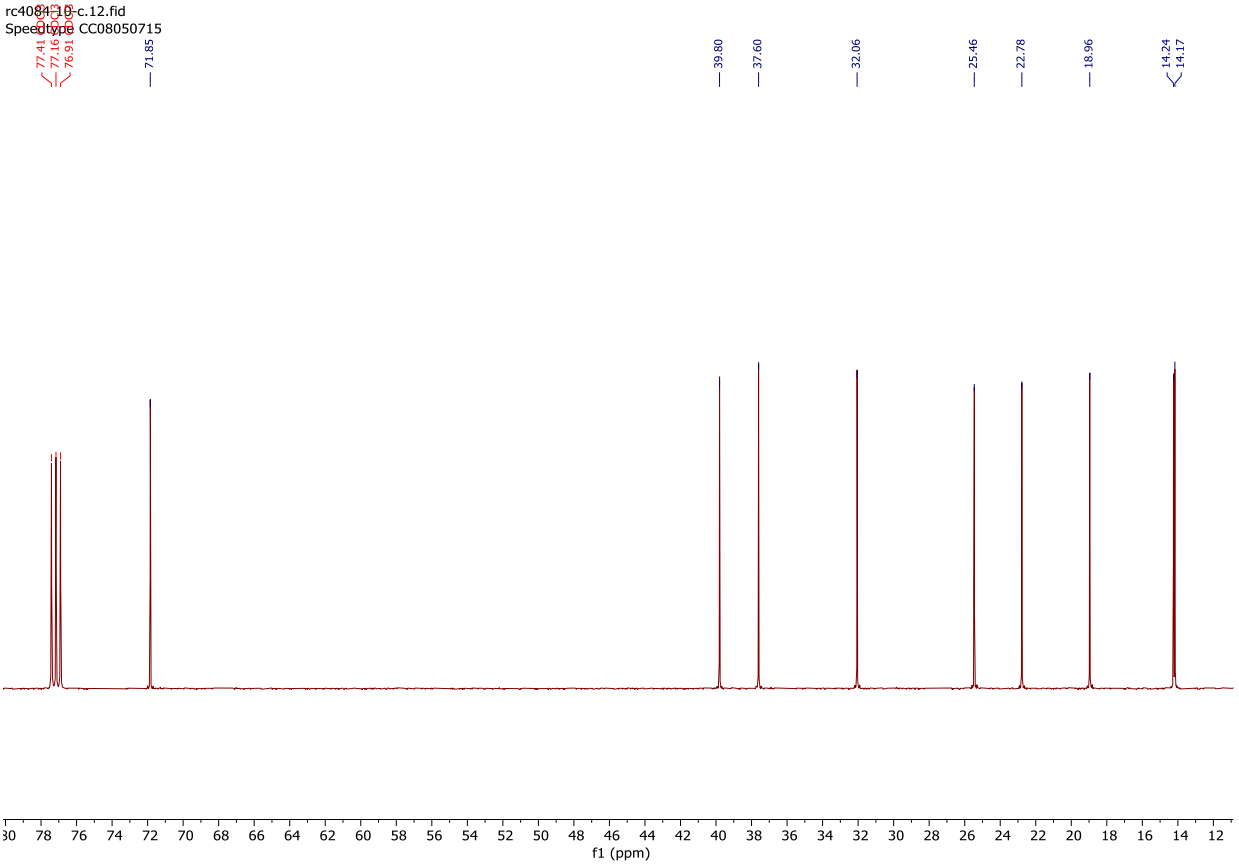
rc4084-10-c.12.fid
Speedtype CC08050715
f1 (ppm)

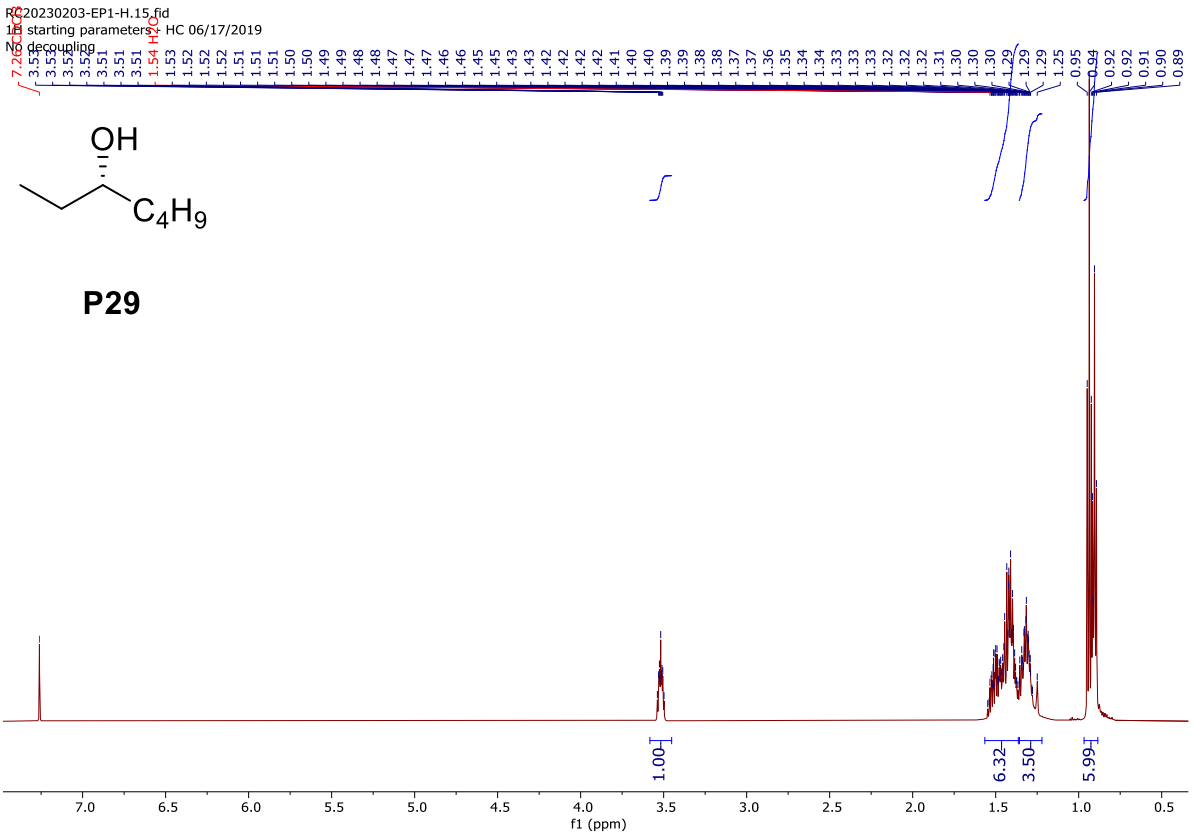
RC20230203-EP1-H.15.fid
1H starting parameters - HC 06/17/2019
No decoupling
OH
C4H9
P29
1.00
6.32
3.50
5.99
f1 (ppm)

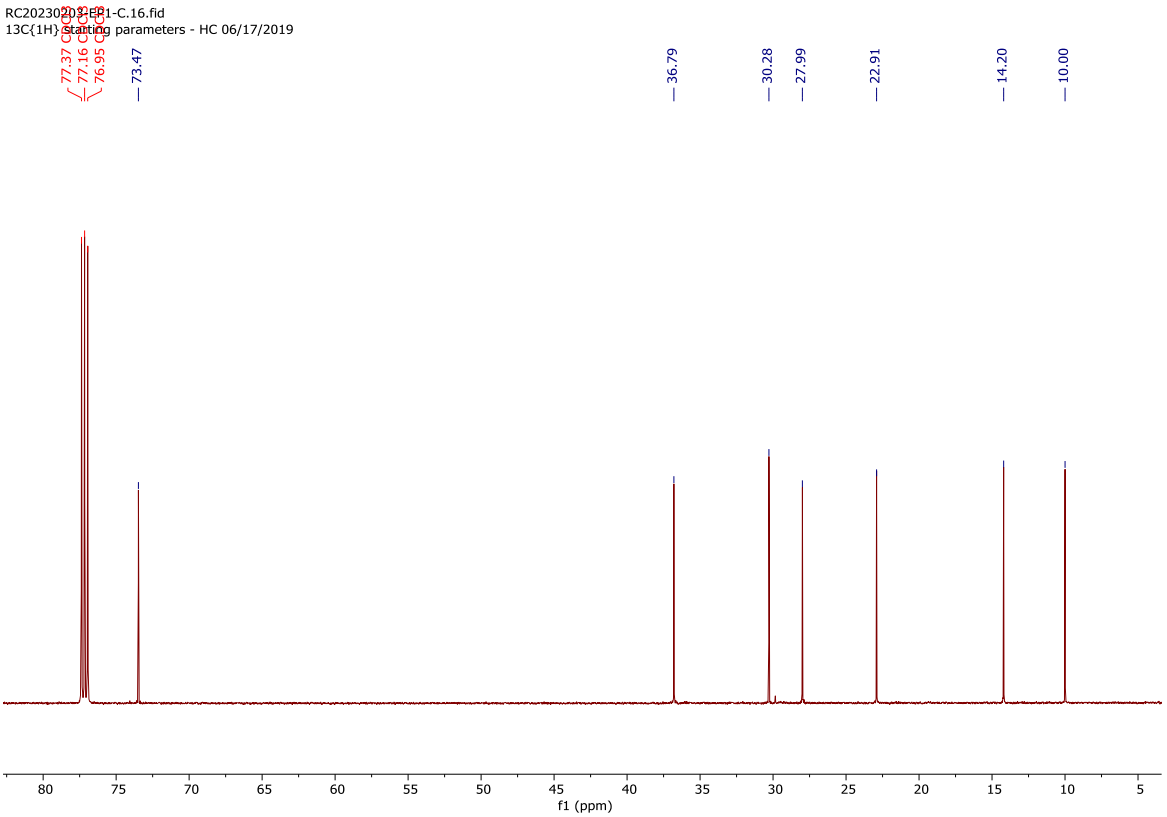
RC20230203-EP1-C.16.fid
13C{1H} starting parameters - HC 06/17/2019
77.37 CDCl3
77.16 CDCl3
76.95 CDCl3
73.47
36.79
30.28
27.99
22.91
14.20
10.00
f1 (ppm)

RC4084-5-H.5.fid
13C{1H} starting parameters - HC 06/17/2019

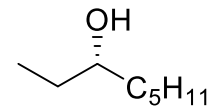

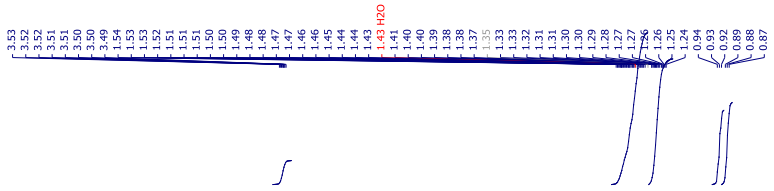

P30

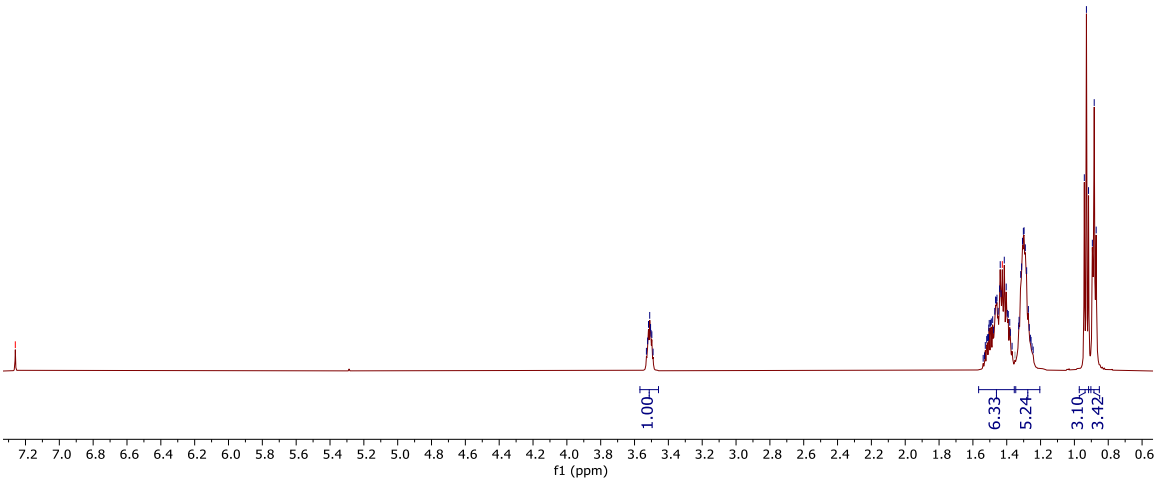

RC4084-5-C.6.fid
1H starting parameters - HC 06/17/2019
No decoupling

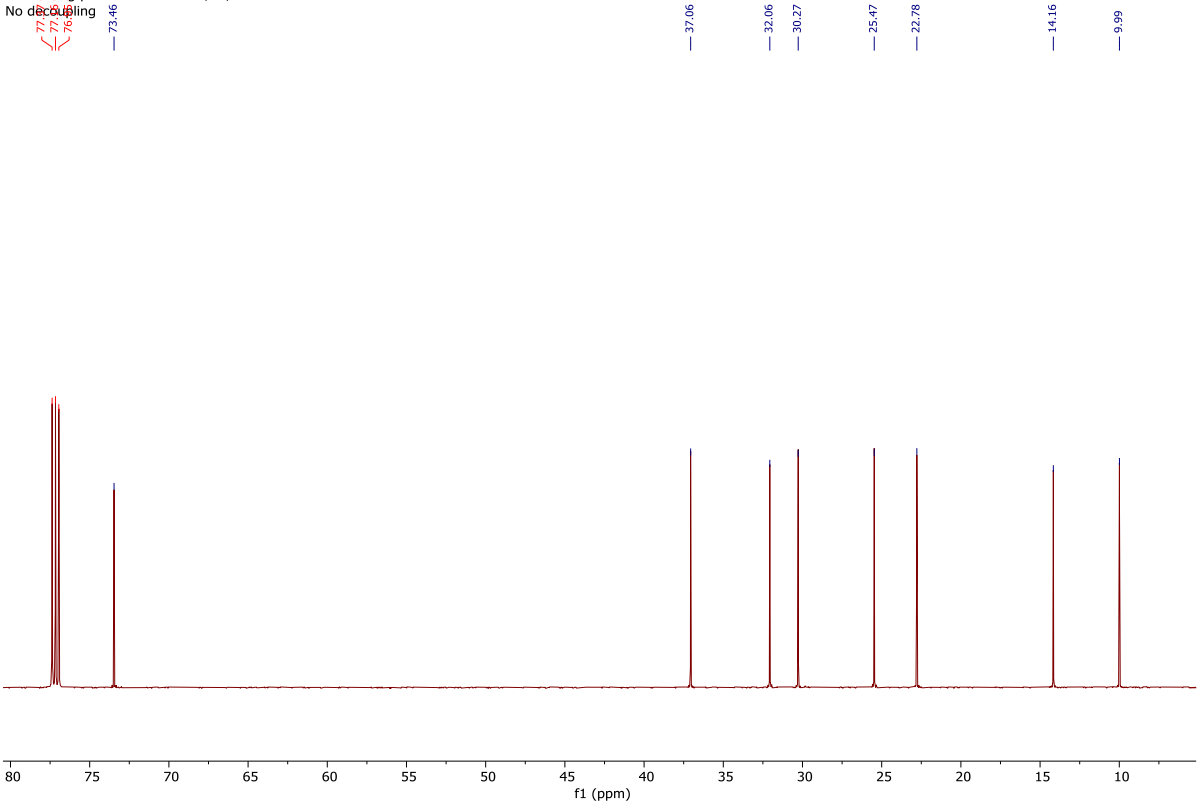

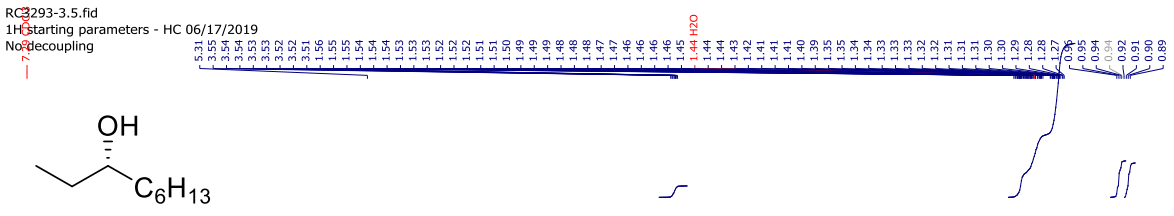
RC3293-3.5.fid
1H starting parameters - HC 06/17/2019
No decoupling
H2O
OH
C6H13

P31

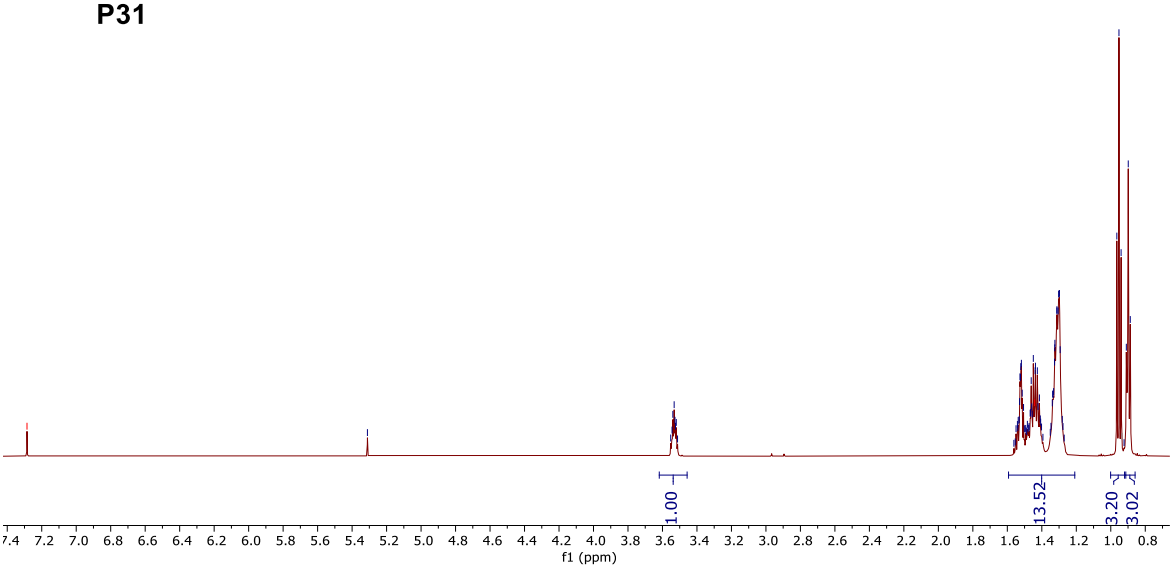
1.00
13.52
3.20
3.02
f1 (ppm)

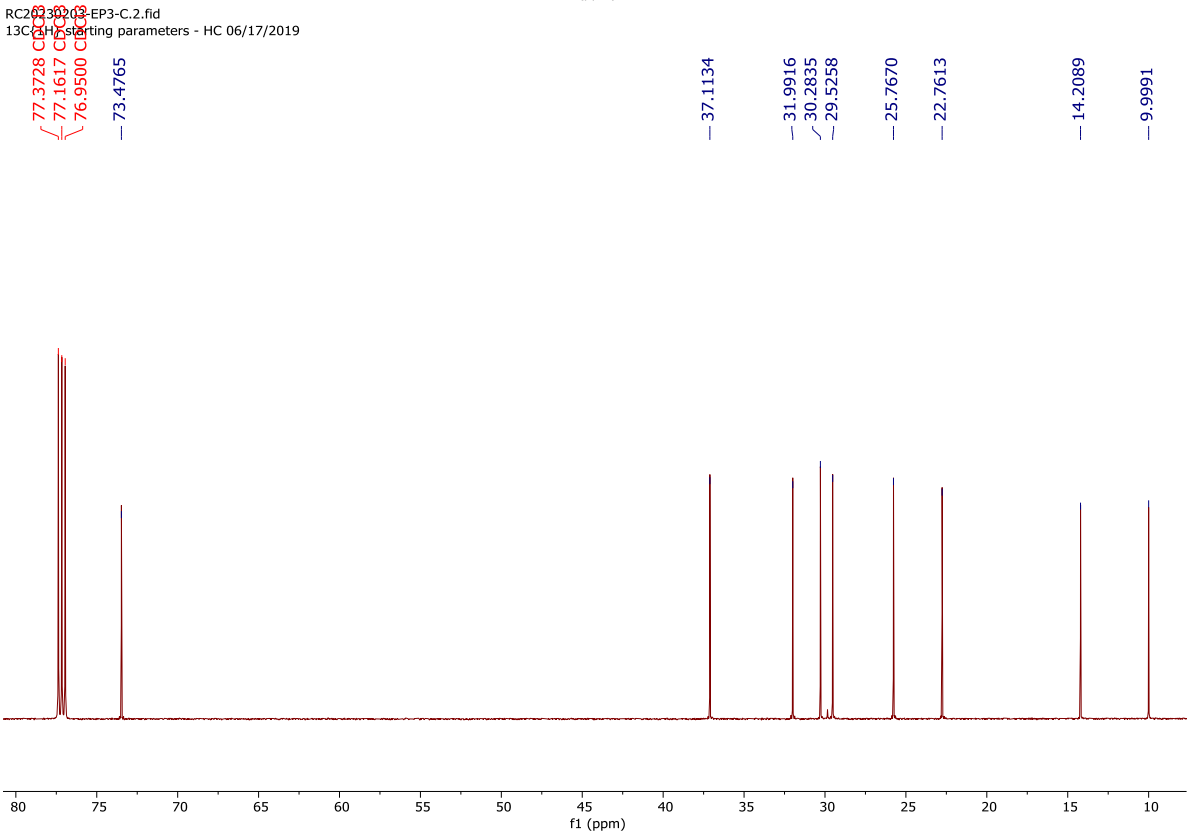
RC2023020C3-EP3-C.2.fid
13C{1H} starting parameters - HC 06/17/2019
77.3728 CDCl3
77.1617 CDCl3
76.9500 CDCl3
73.4765
37.1134
31.9916
30.2835
29.5258
25.7670
22.7613
14.2089
9.9991
f1 (ppm)

RC20230203-EP6-H.7.fid
1H starting parameters - HC 06/17/2019
No decoupling

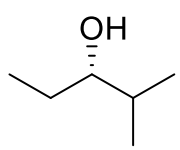

P32

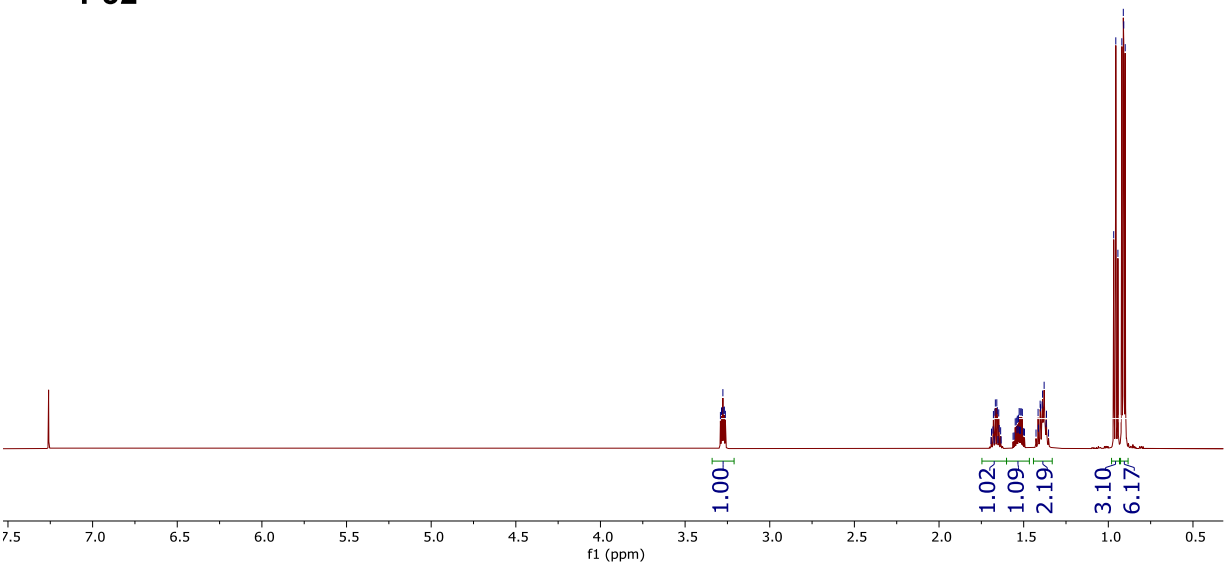

RC20230203-EP6-C.8.fid
13C{1H} starting parameters - HC 06/17/2019

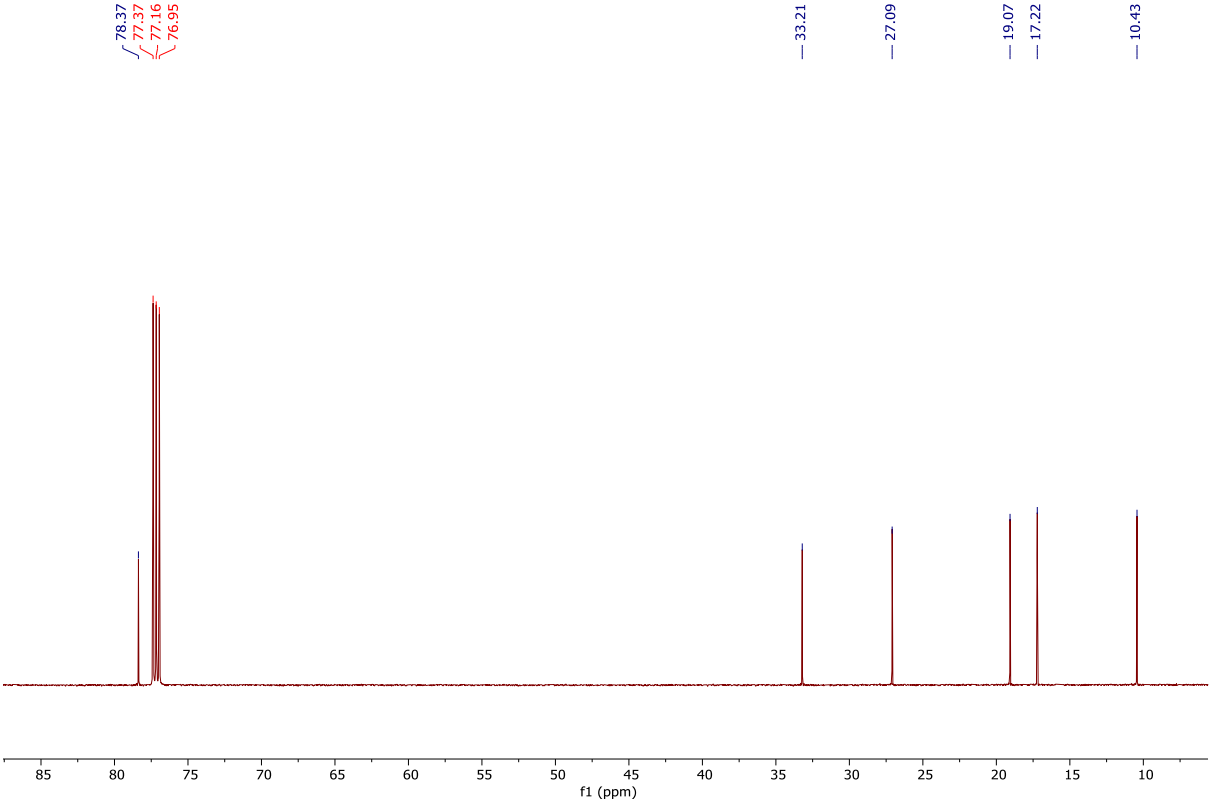

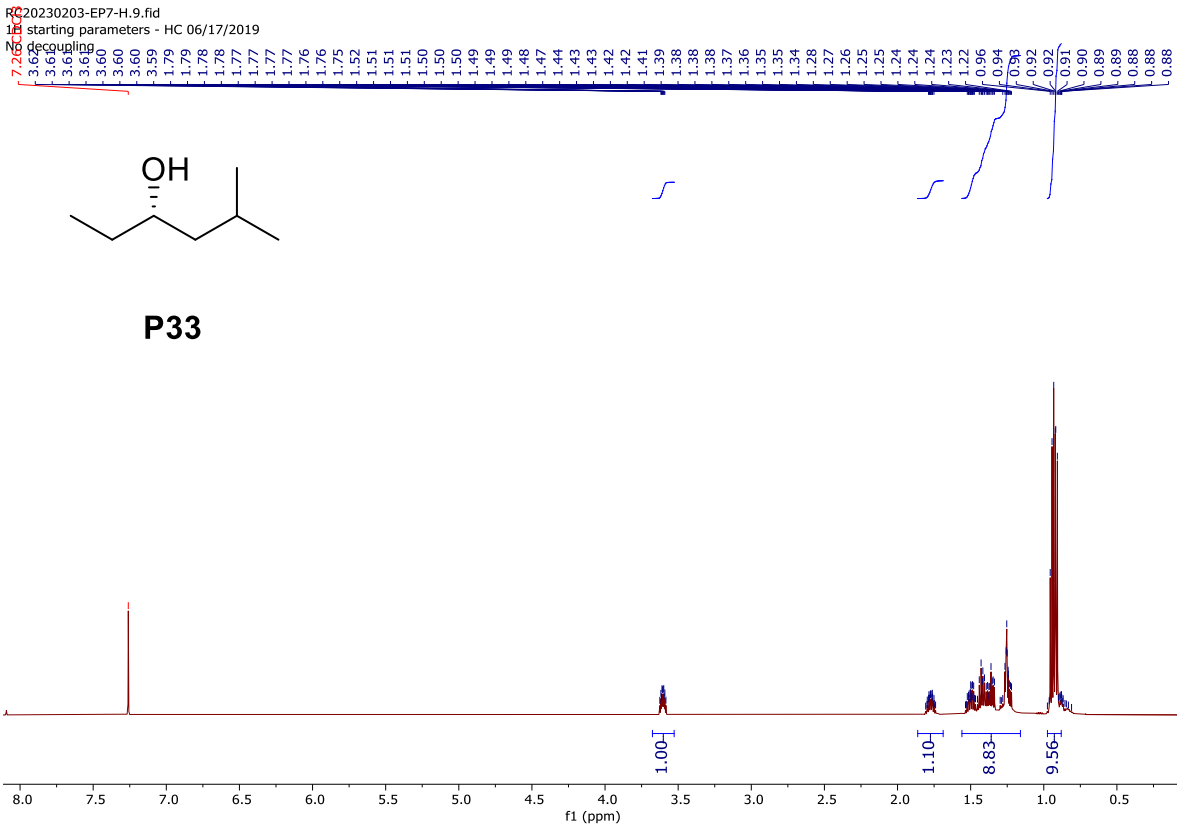
RC20230203-EP7-H.9.fid
1H starting parameters - HC 06/17/2019
No decoupling
OH
P33
1.00
1.10
8.83
9.56
f1 (ppm)

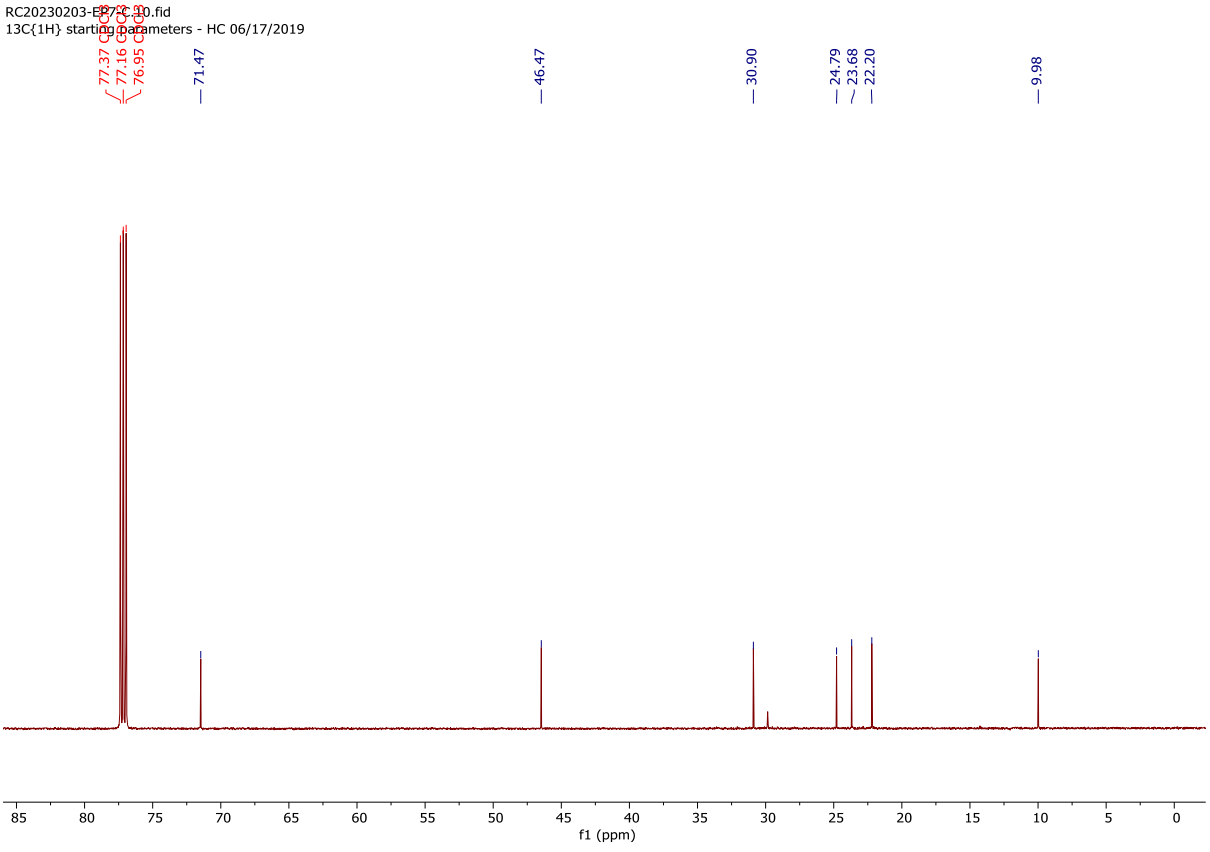
RC20230203-EP7-C.10.fid
13C{1H} starting parameters - HC 06/17/2019
77.37 CDCl3
77.16 CDCl3
76.95 CDCl3
71.47
46.47
30.90
24.79
23.68
22.20
9.98
f1 (ppm)

RC3293-2.4.fid
1H starting parameters - HC 06/17/2019
Acquisition

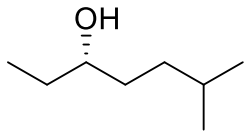

P34

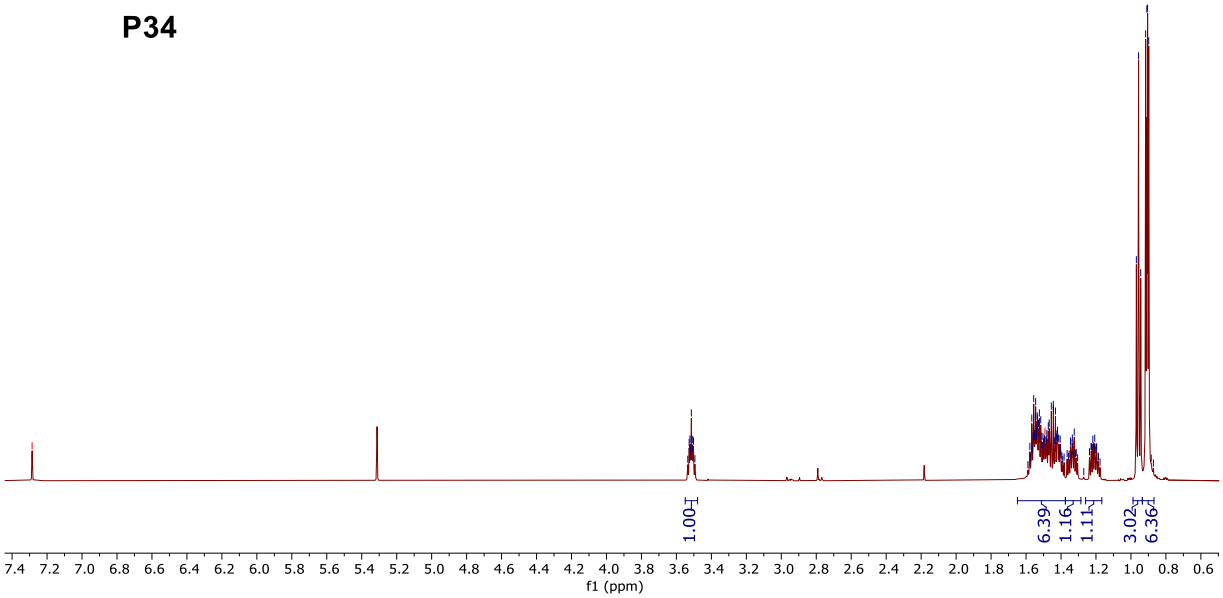

RC4137-new-C.2.fid
13C{1H} starting parameters - HC 06/17/2019

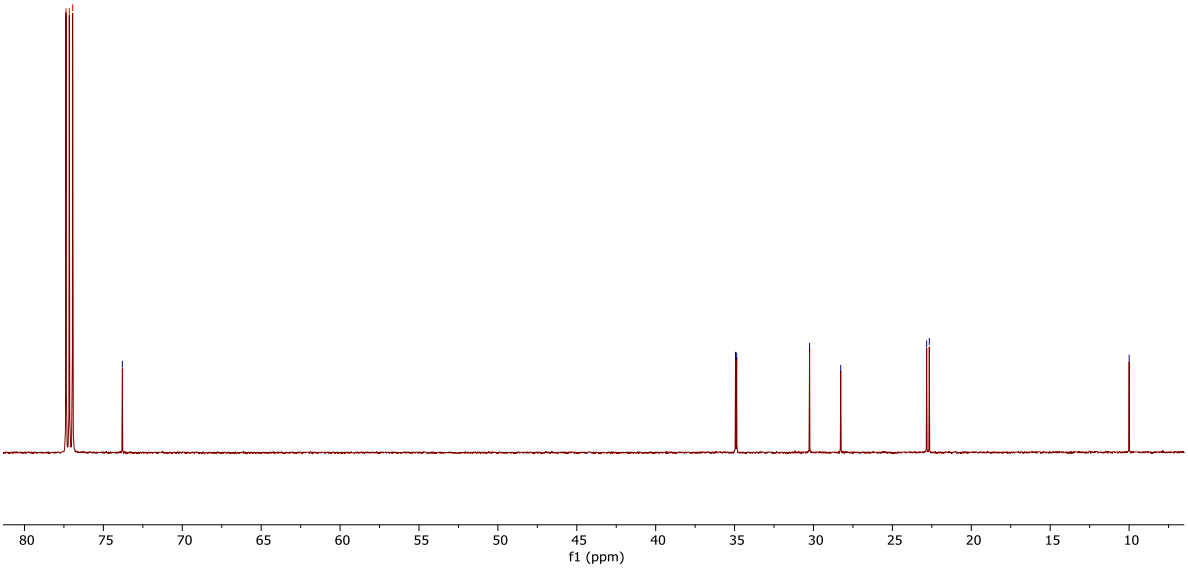

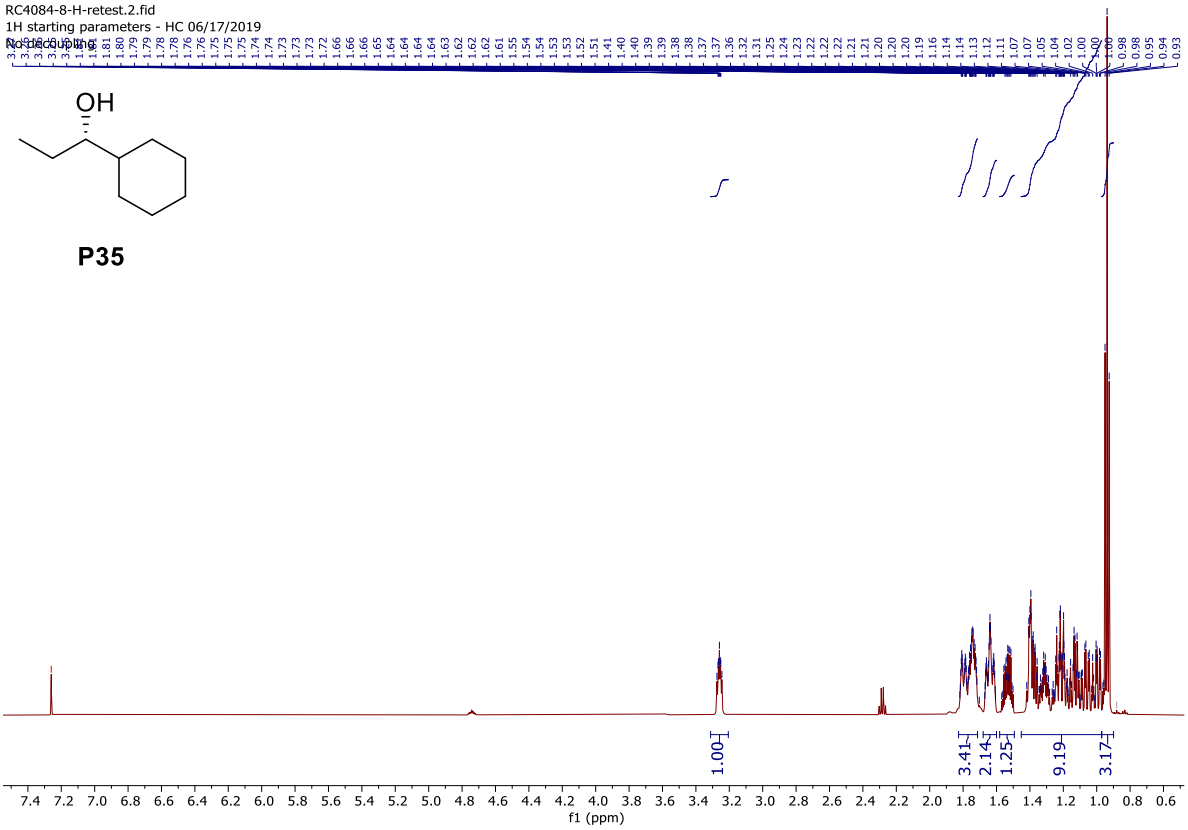
RC4084-8-H-retest.2.fid
1H starting parameters - HC 06/17/2019
OH
P35
1.00
3.41
2.14
1.25
9.19
3.17
f1 (ppm)

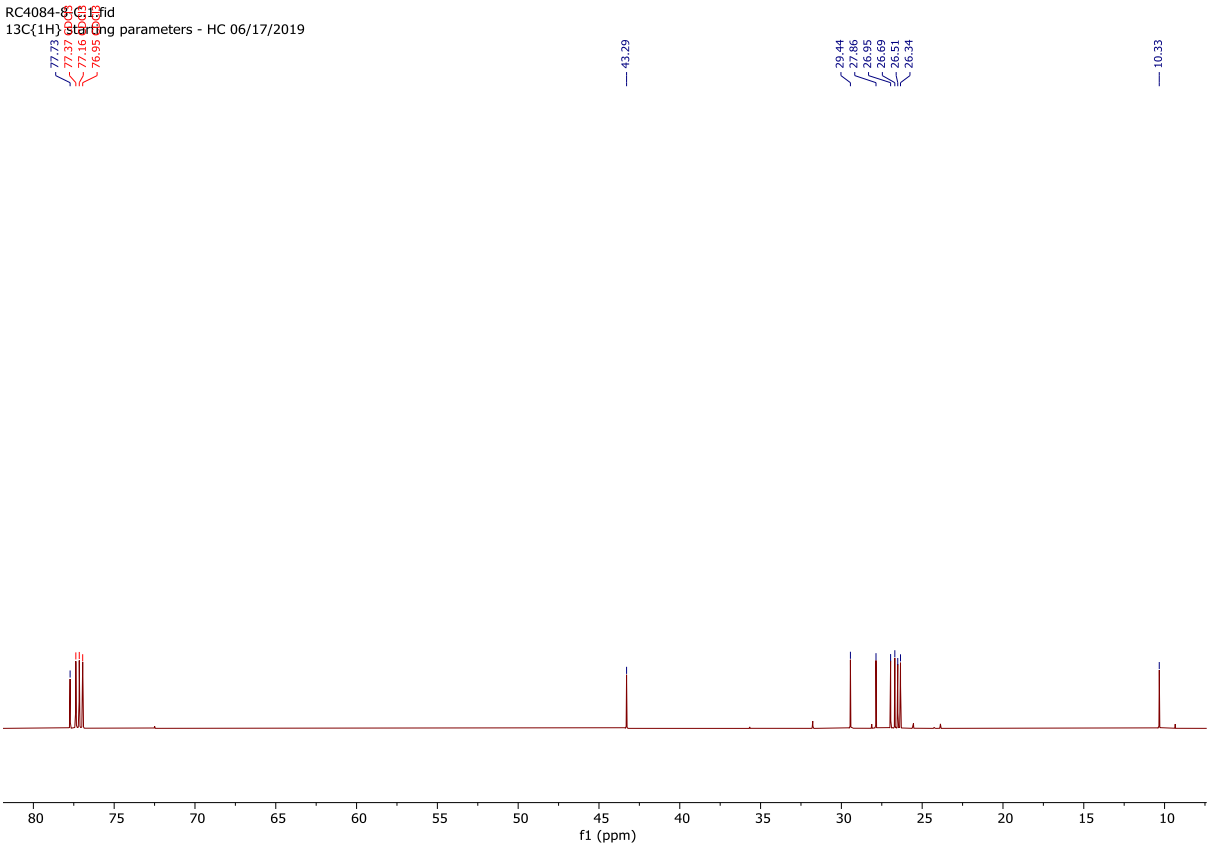
13C{1H} starting parameters - HC 06/17/2019
77.73
77.37
77.16
76.95
43.29
29.44
27.86
26.95
26.69
26.51
26.34
10.33
f1 (ppm)

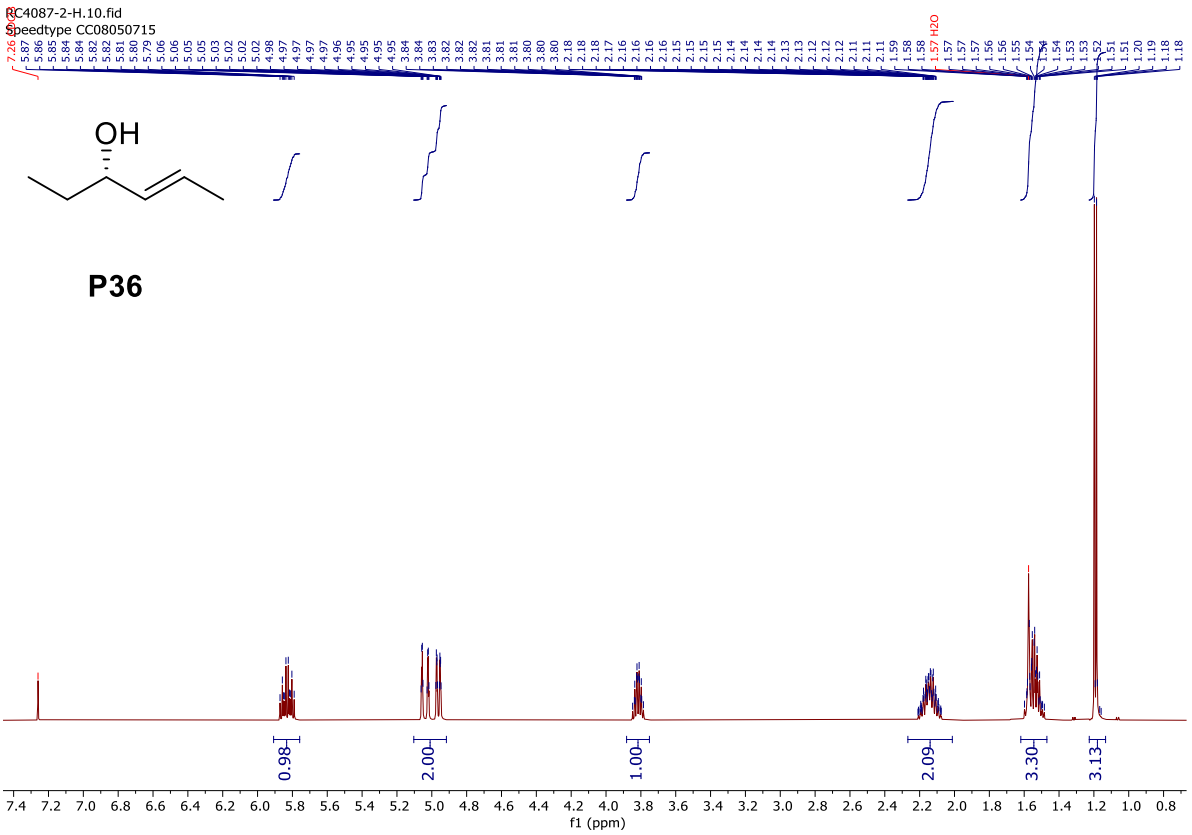
RC4087-2-H.10.fid
Speedtype CC08050715
OH
P36
0.98
2.00
1.00
2.09
3.30
3.13
f1 (ppm)

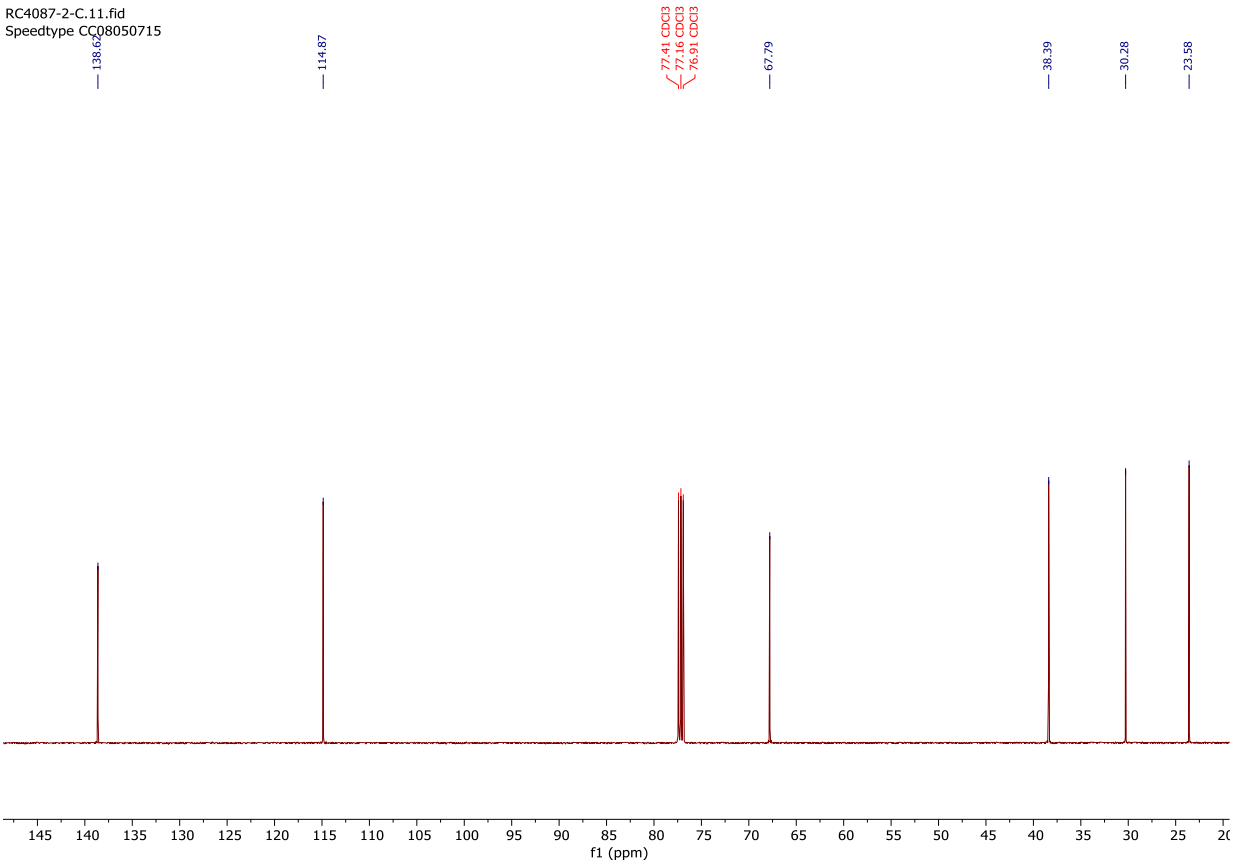
RC4087-2-C.11.fid
Speedtype CC08050715
138.62
114.87
77.41 CDCl3
77.16 CDCl3
76.91 CDCl3
67.79
38.39
30.28
23.58
f1 (ppm)

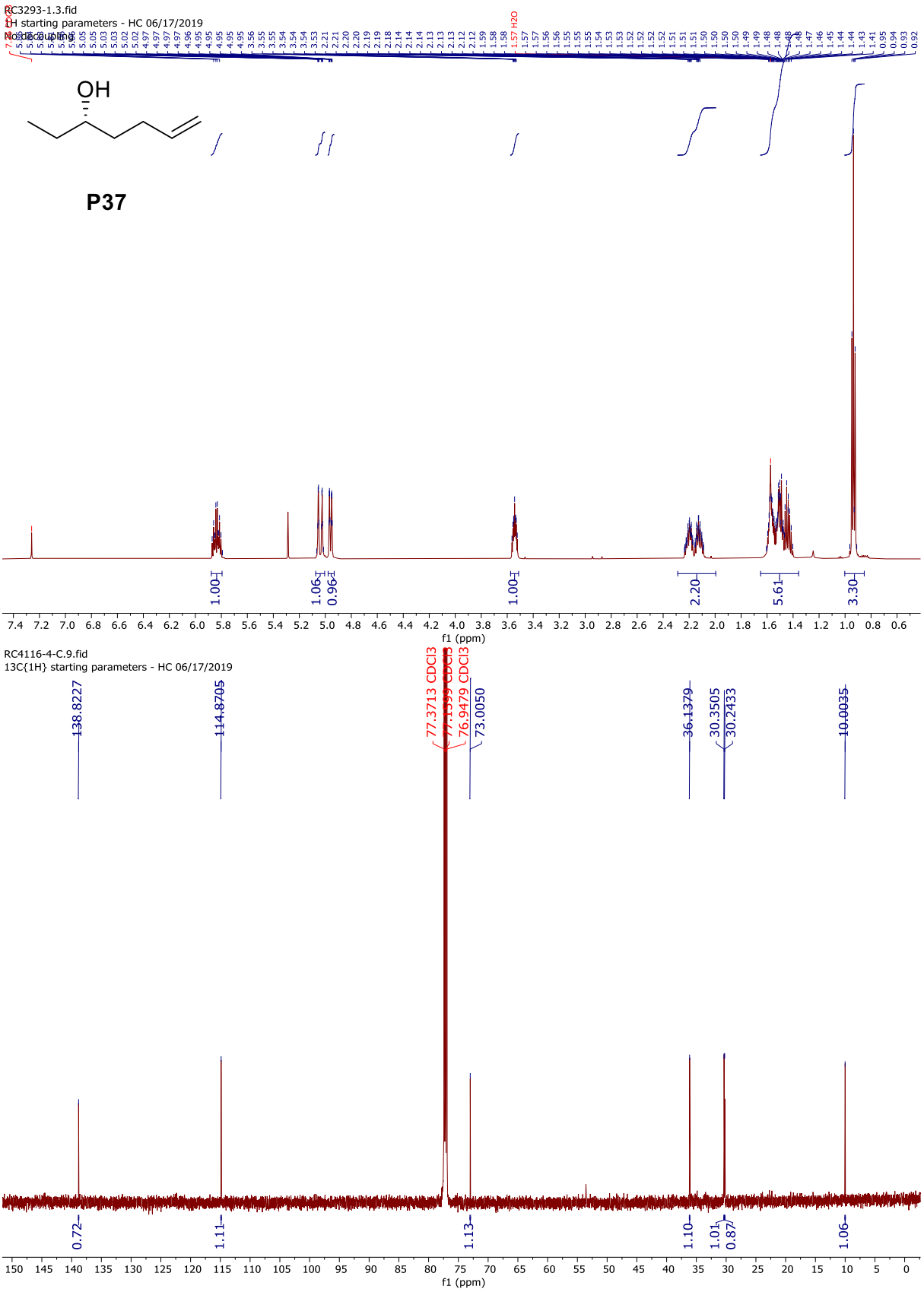
RC3293-1.3.fid
1H starting parameters - HC 06/17/2019
OH
P37
1.57 H2O
1.00
1.06
0.96
1.00
2.20
5.61
3.30
f1 (ppm)
RC4116-4-C.9.fid
13C{1H} starting parameters - HC 06/17/2019
138.8227
114.8705
77.3713 CDCl3
76.9479 CDCl3
73.0050
36.1379
30.3505
30.2433
10.0935
0.72
1.11
1.13
1.10
1.01
0.87
1.06
f1 (ppm)

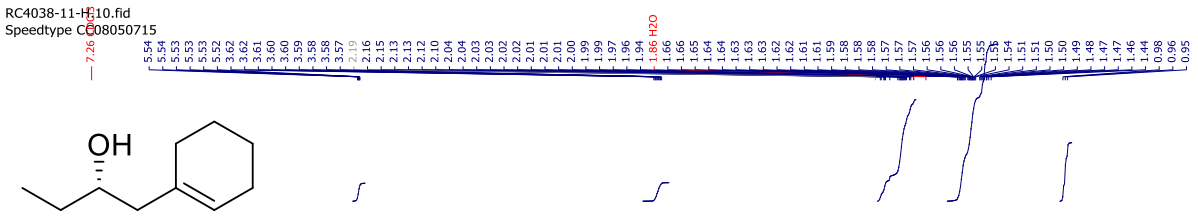
RC4038-11-H.10.fid
Speedtype CC08050715
7.26
1.86 H2O
OH

P38

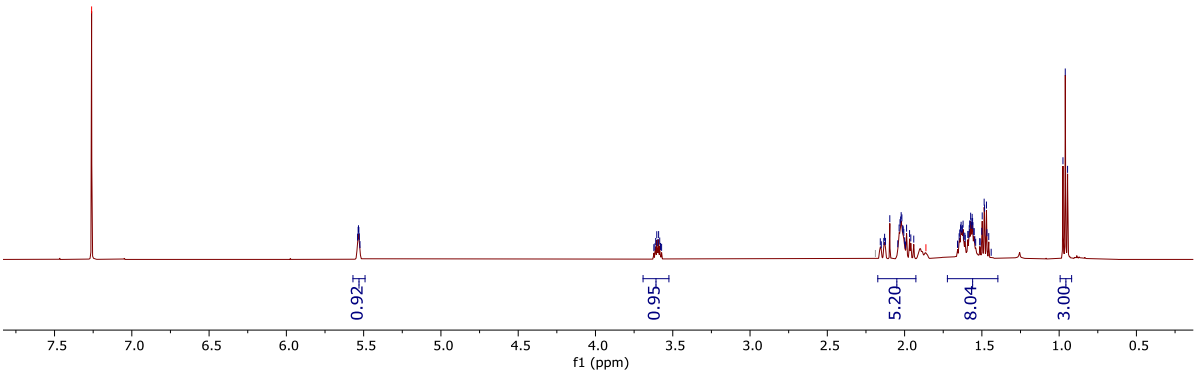
0.92
0.95
5.20
8.04
3.00
f1 (ppm)

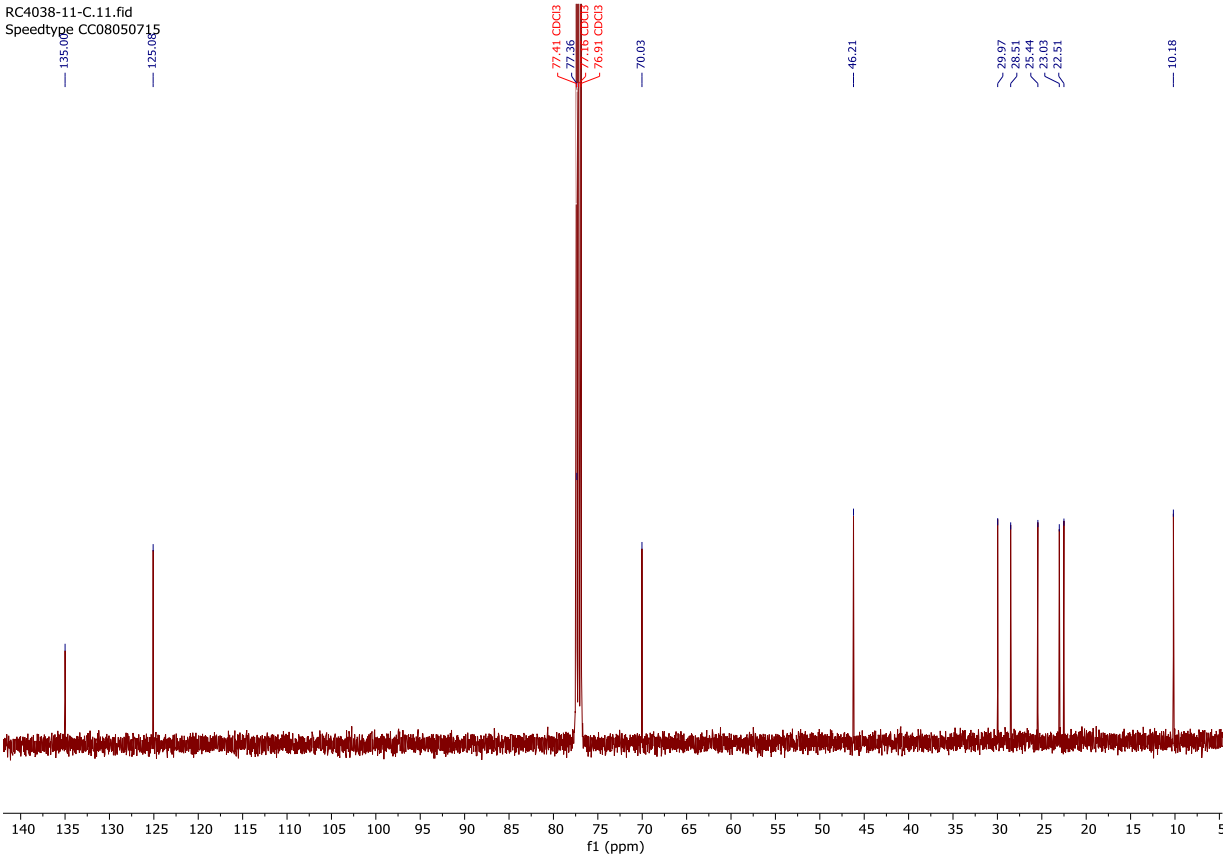
RC4038-11-C.11.fid
Speedtype CC08050715
135.08
125.04
77.41 CDCl3
77.16 CDCl3
76.91 CDCl3
70.03
46.21
29.97
28.51
25.44
23.03
22.51
10.18
f1 (ppm)

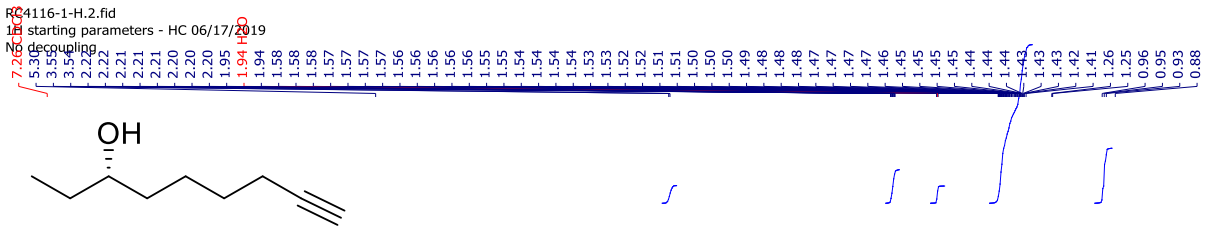
RC4116-1-H.2.fid
1H starting parameters - HC 06/17/2019
No decoupling
OH

P39

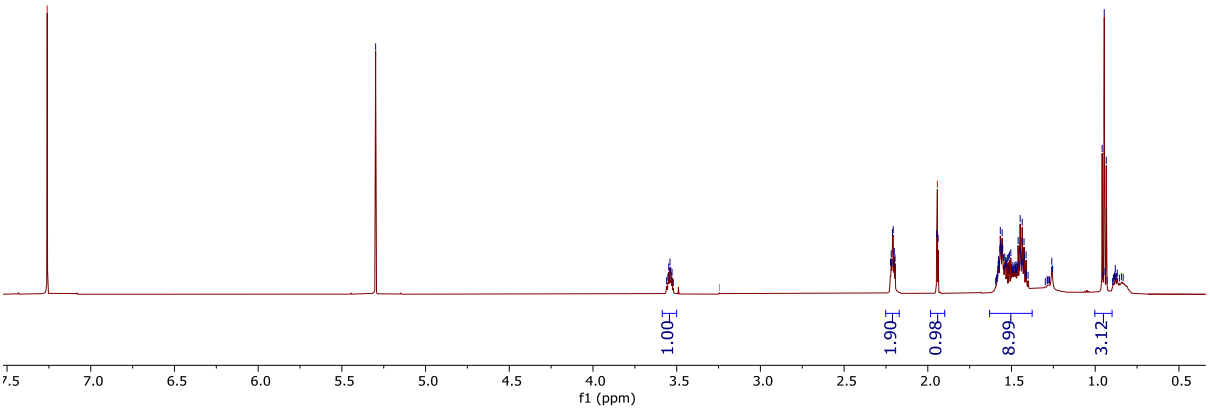
1.00
1.90
0.98
8.99
3.12
f1 (ppm)

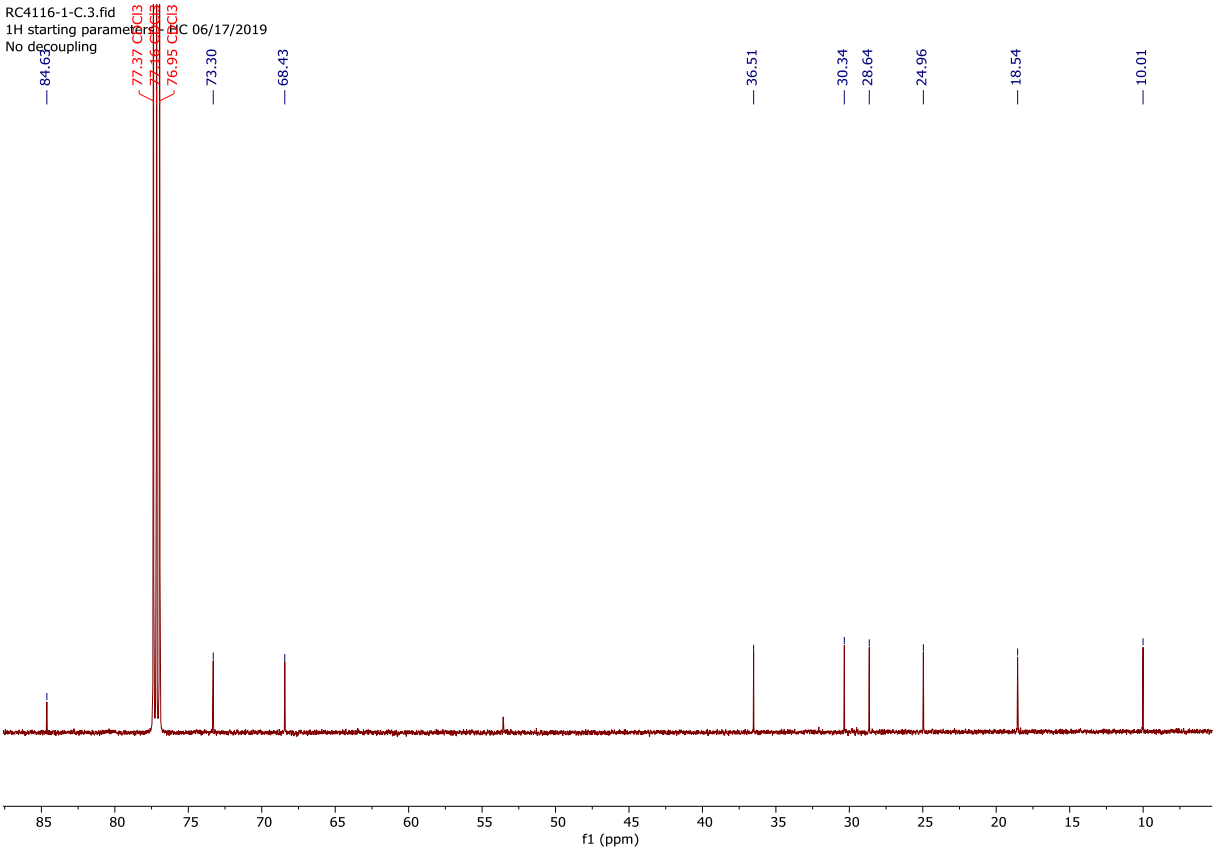
RC4116-1-C.3.fid
1H starting parameters - HC 06/17/2019
No decoupling
84.63
77.37 CDCl3
76.95 CDCl3
73.30
68.43
36.51
30.34
28.64
24.96
18.54
10.01
f1 (ppm)

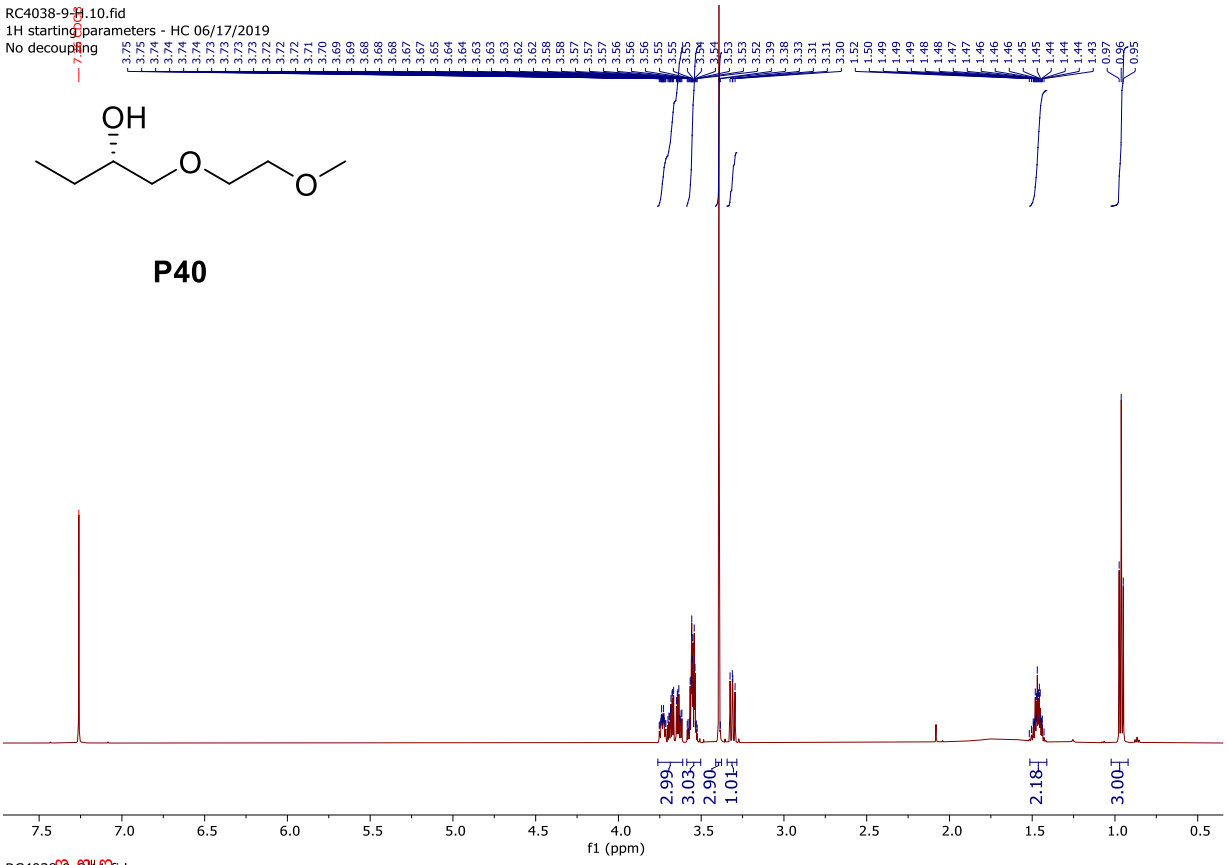
RC4038-9-H.10.fid
1H starting parameters - HC 06/17/2019
No decoupling
OH
O
O
P40
2.99
3.03
2.90
1.01
2.18
3.00
f1 (ppm)

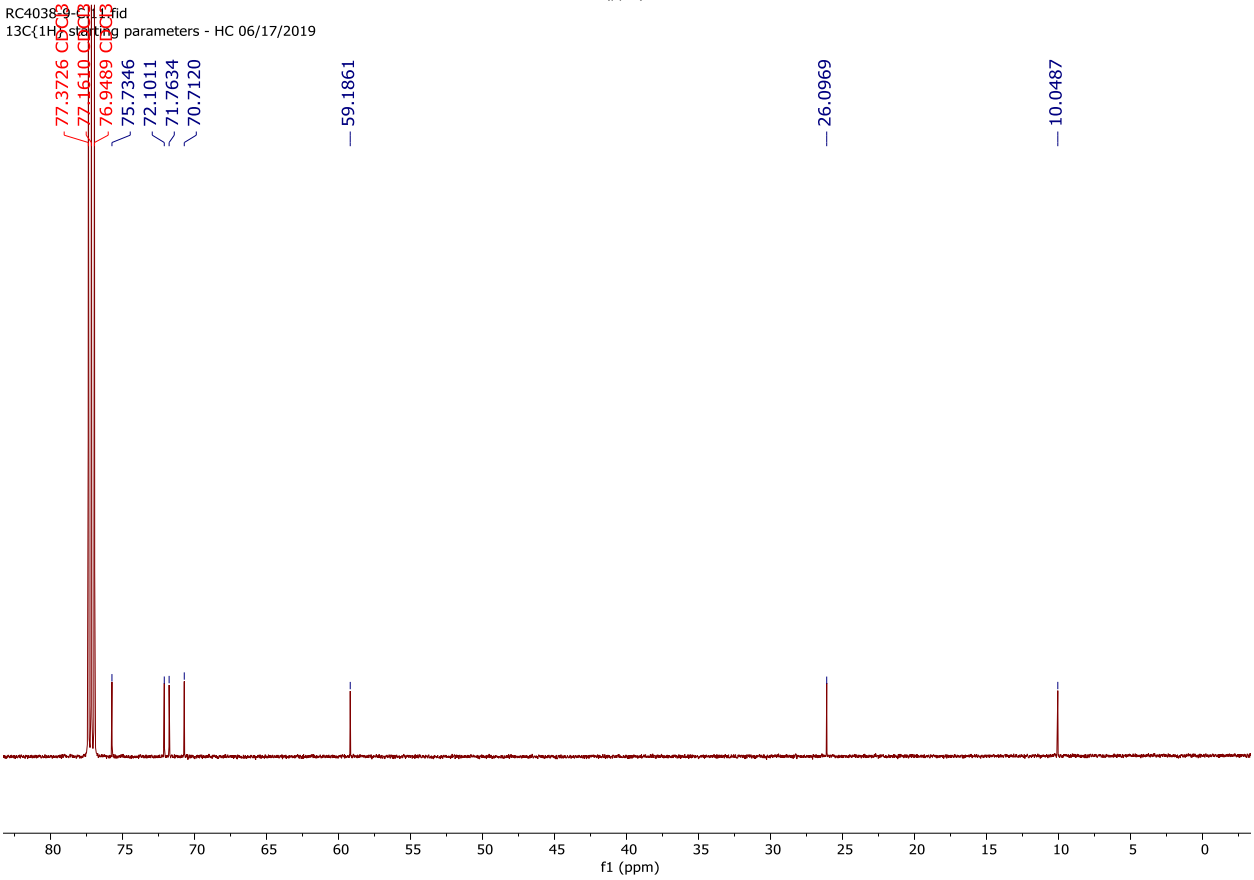
RC4038-9-C13.fid
13C{1H} starting parameters - HC 06/17/2019
77.3726 CDCl3
77.1610 CDCl3
76.9489 CDCl3
75.7346
72.1011
71.7634
70.7120
59.1861
26.0969
10.0487
f1 (ppm)

RC4075-5-H.10.fid
1H starting parameters - HC 06/17/2019
No decoupling

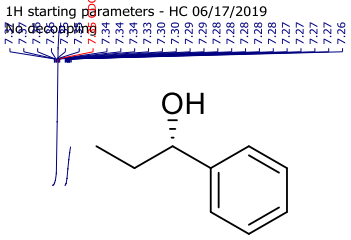

P41

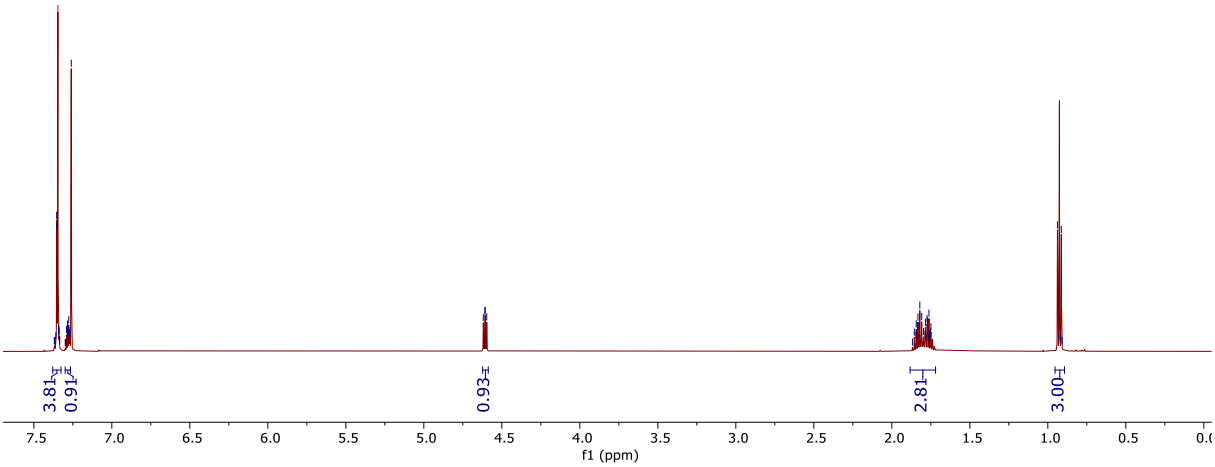

RC4075-5-C.11.fid
13C{1H} starting parameters - HC 06/17/2019

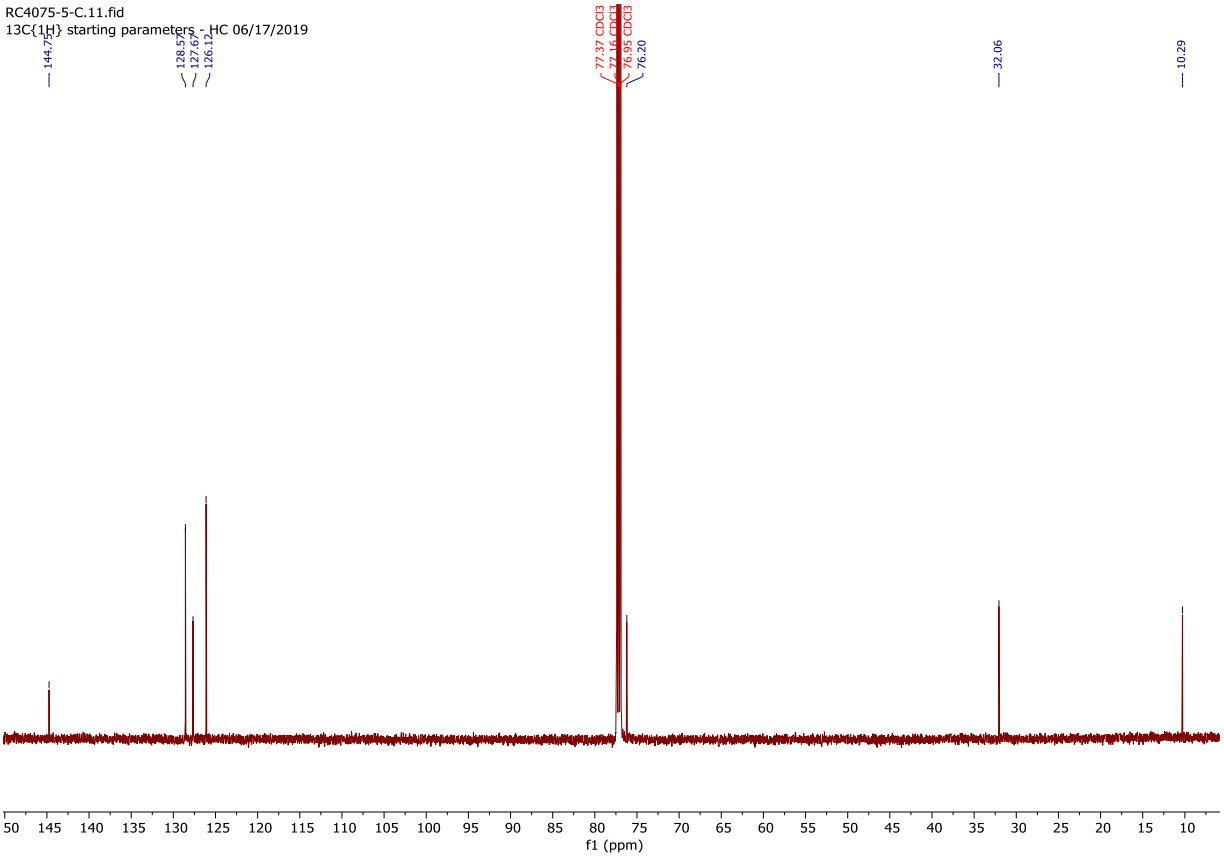

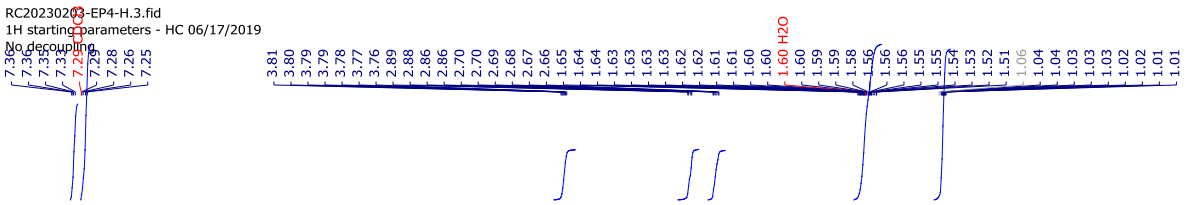
RC20230203-EP4-H.3.fid
1H starting parameters - HC 06/17/2019
No decoupling
7.36 7.36 7.35 7.33 7.29 CDCl3 7.28 7.26 7.25
3.81 3.80 3.79 3.79 3.78 3.77 3.76 2.89 2.88 2.86 2.86 2.70 2.70 2.69 2.68 2.67 2.66 1.65 1.64 1.64 1.63 1.63 1.63 1.62 1.62 1.61 1.61 1.60 1.60 1.60 H2O 1.60 1.59 1.59 1.58 1.56 1.56 1.56 1.55 1.55 1.54 1.53 1.52 1.51 1.06 1.04 1.04 1.03 1.03 1.02 1.02 1.01 1.01

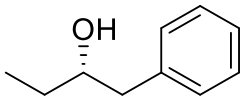
OH

P42

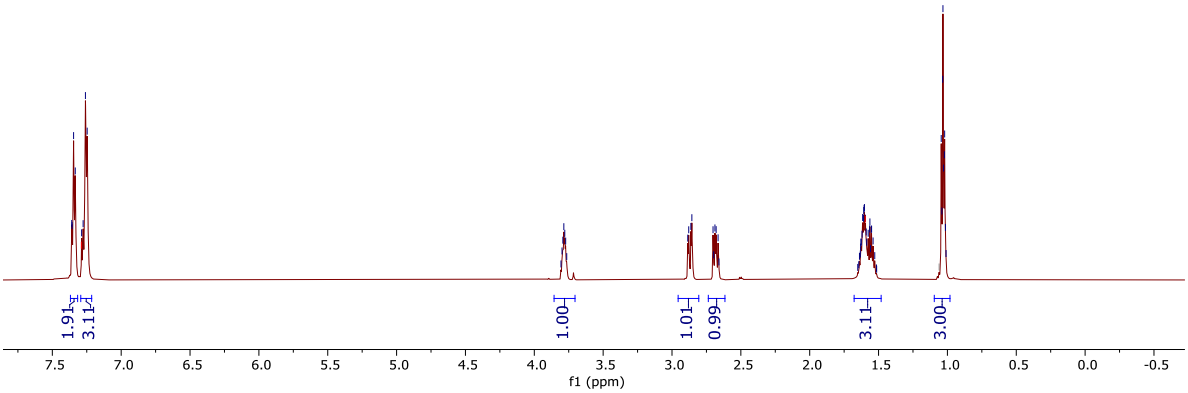
1.91
3.11
1.00
1.01
0.99
3.11
3.00
7.5 7.0 6.5 6.0 5.5 5.0 4.5 4.0 3.5 3.0 2.5 2.0 1.5 1.0 0.5 0.0 -0.5
f1 (ppm)

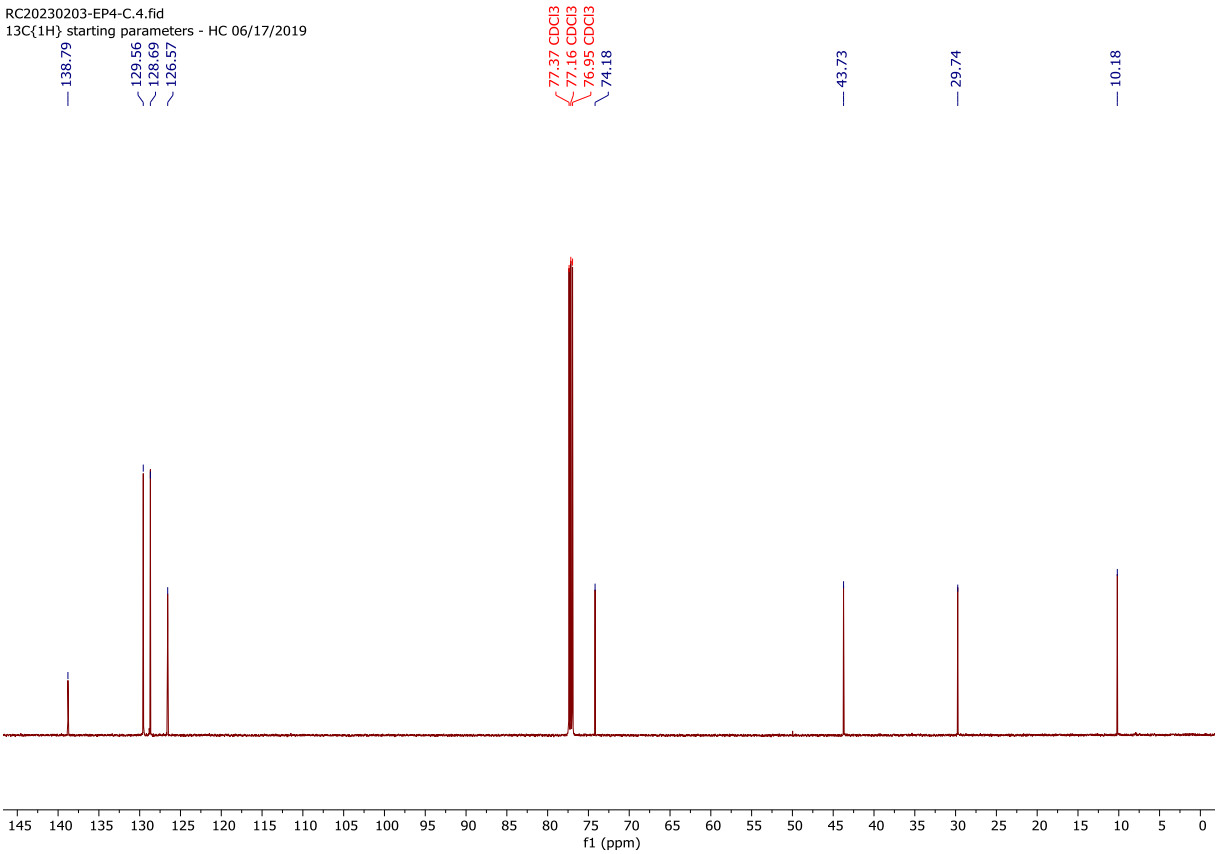
RC20230203-EP4-C.4.fid
13C{1H} starting parameters - HC 06/17/2019
138.79
129.56
128.69
126.57
77.37 CDCl3
77.16 CDCl3
76.95 CDCl3
74.18
43.73
29.74
10.18
145 140 135 130 125 120 115 110 105 100 95 90 85 80 75 70 65 60 55 50 45 40 35 30 25 20 15 10 5 0
f1 (ppm)

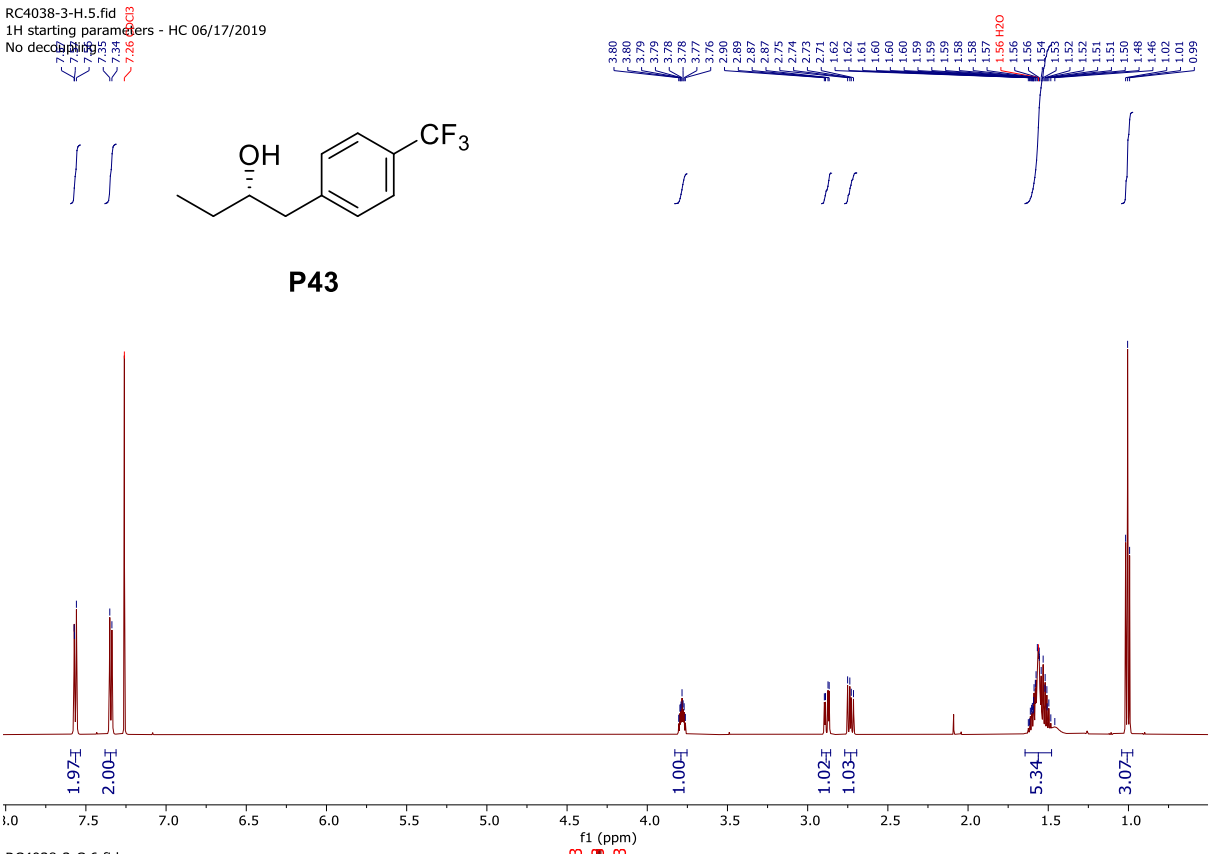
RC4038-3-H.5.fid
1H starting parameters - HC 06/17/2019
No decoupling
OH
CF3
P43
1.97
2.00
1.00
1.02
1.03
5.34
3.07
f1 (ppm)

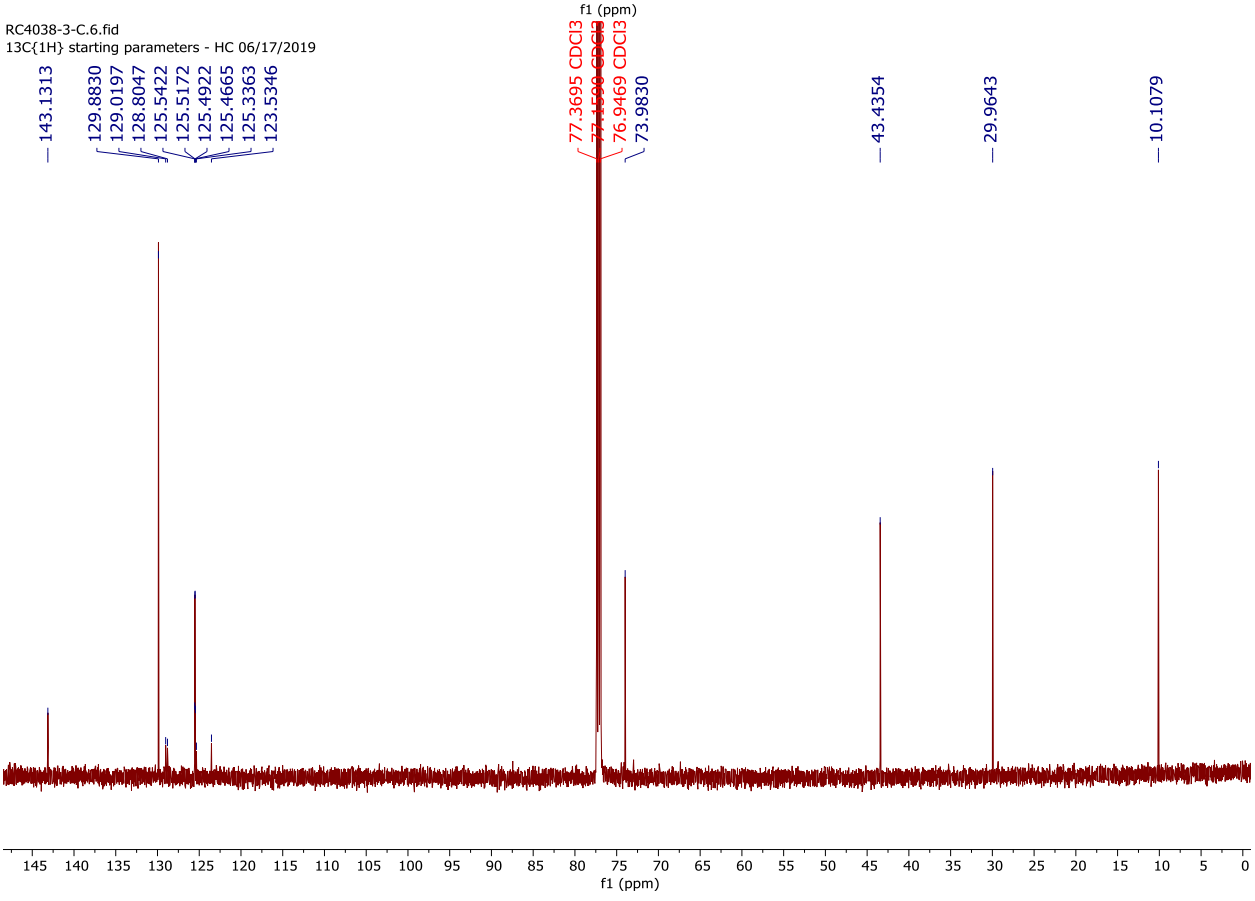
RC4038-3-C.6.fid
13C{1H} starting parameters - HC 06/17/2019
143.1313
129.8830
129.0197
128.8047
125.5422
125.5172
125.4922
125.4665
125.3363
123.5346
77.3695 CDCl3
76.9469 CDCl3
73.9830
43.4354
29.9643
10.1079
f1 (ppm)

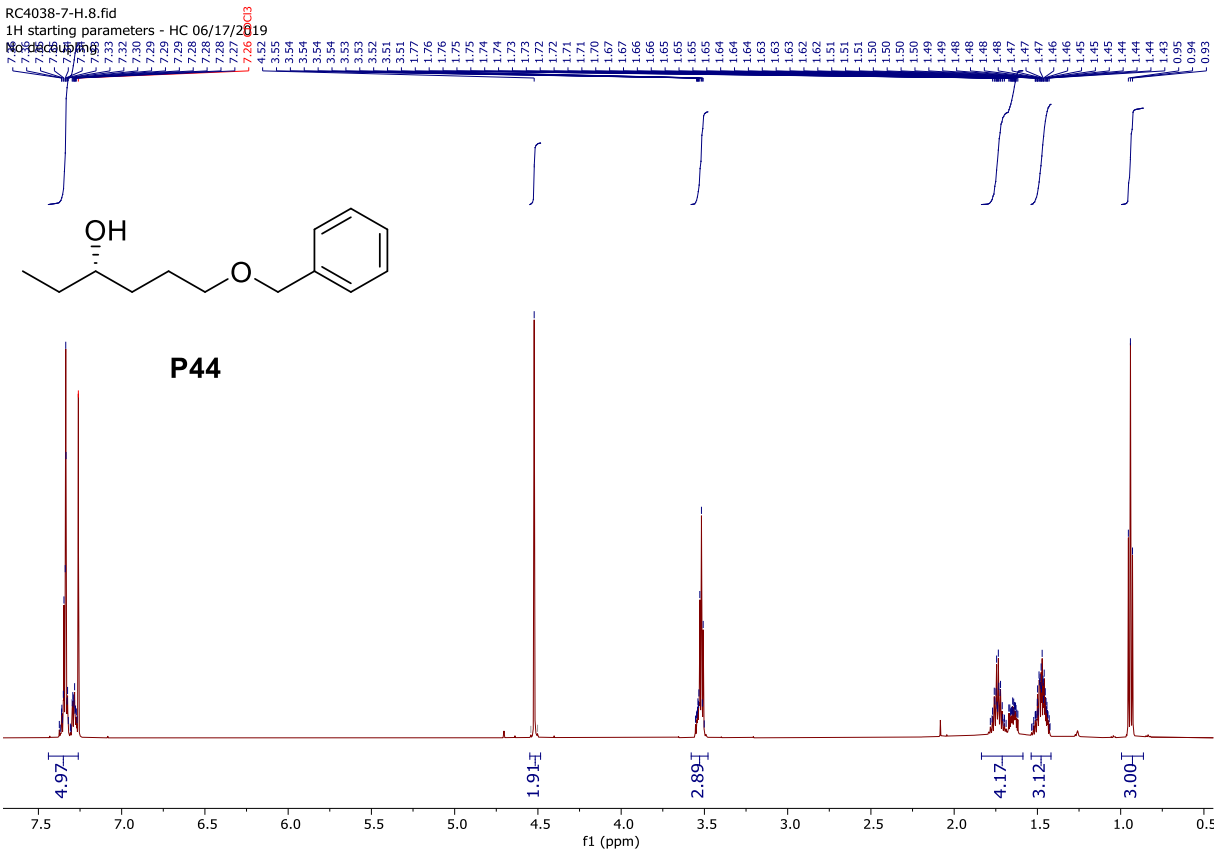
RC4038-7-H.8.fid
1H starting parameters - HC 06/17/2019
OH
O
P44
4.97
1.91
2.89
4.17
3.12
3.00
f1 (ppm)

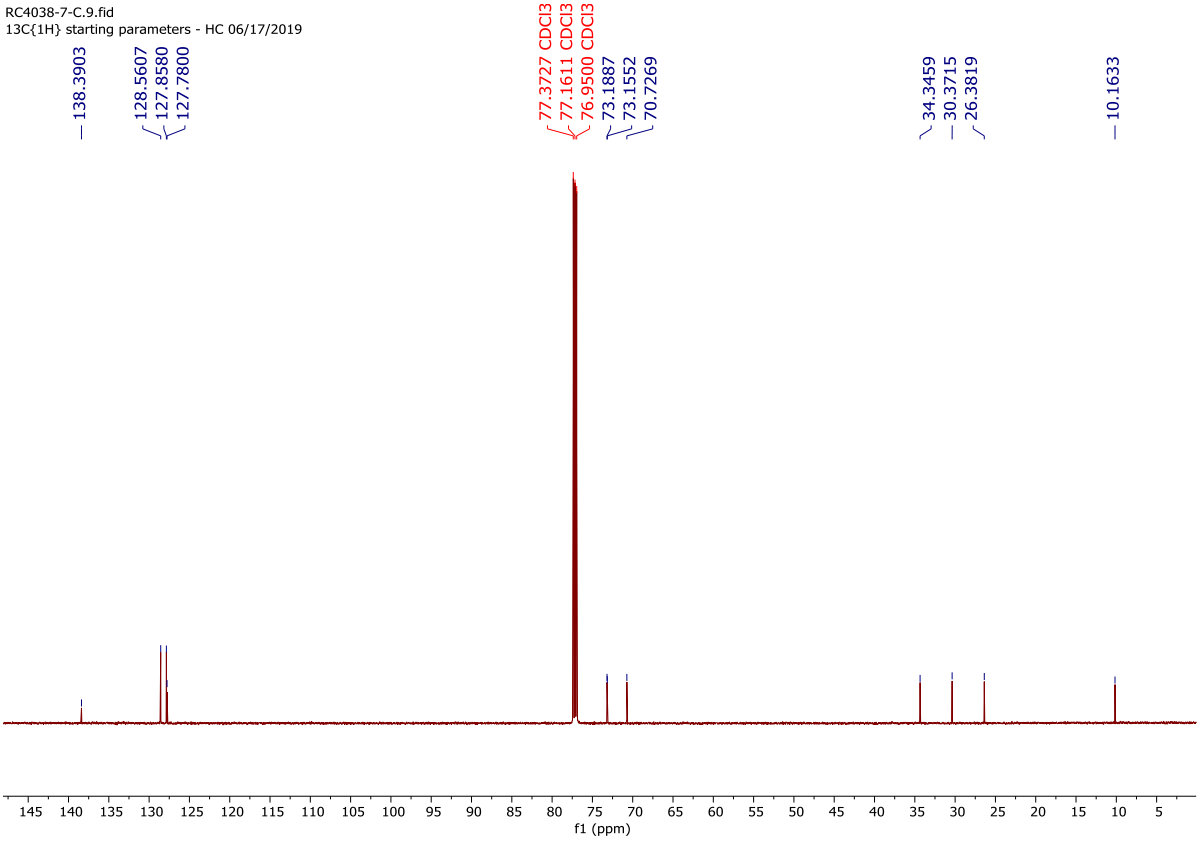
RC4038-7-C.9.fid
13C{1H} starting parameters - HC 06/17/2019
138.3903
128.5607
127.8580
127.7800
77.3727 CDCl3
77.1611 CDCl3
76.9500 CDCl3
73.1887
73.1552
70.7269
34.3459
30.3715
26.3819
10.1633
f1 (ppm)

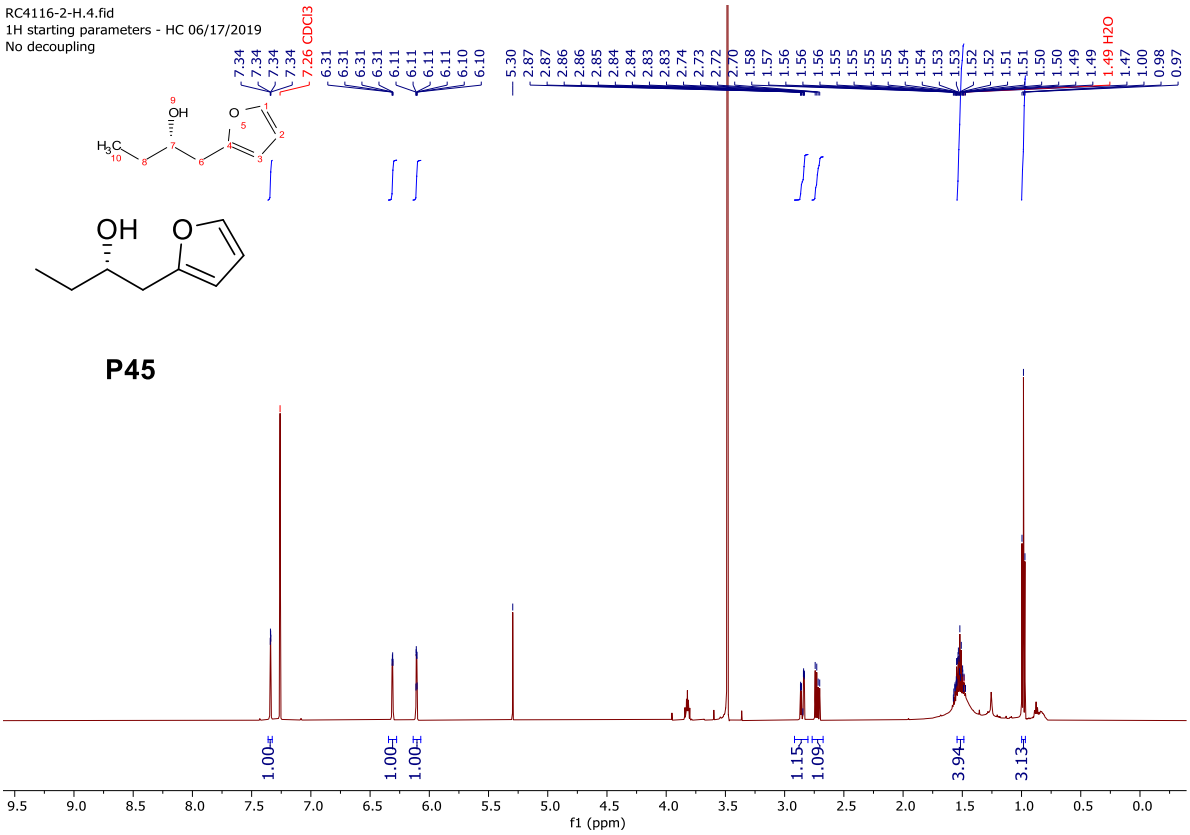
RC4116-2-H.4.fid
1H starting parameters - HC 06/17/2019
No decoupling
OH
O
P45
f1 (ppm)

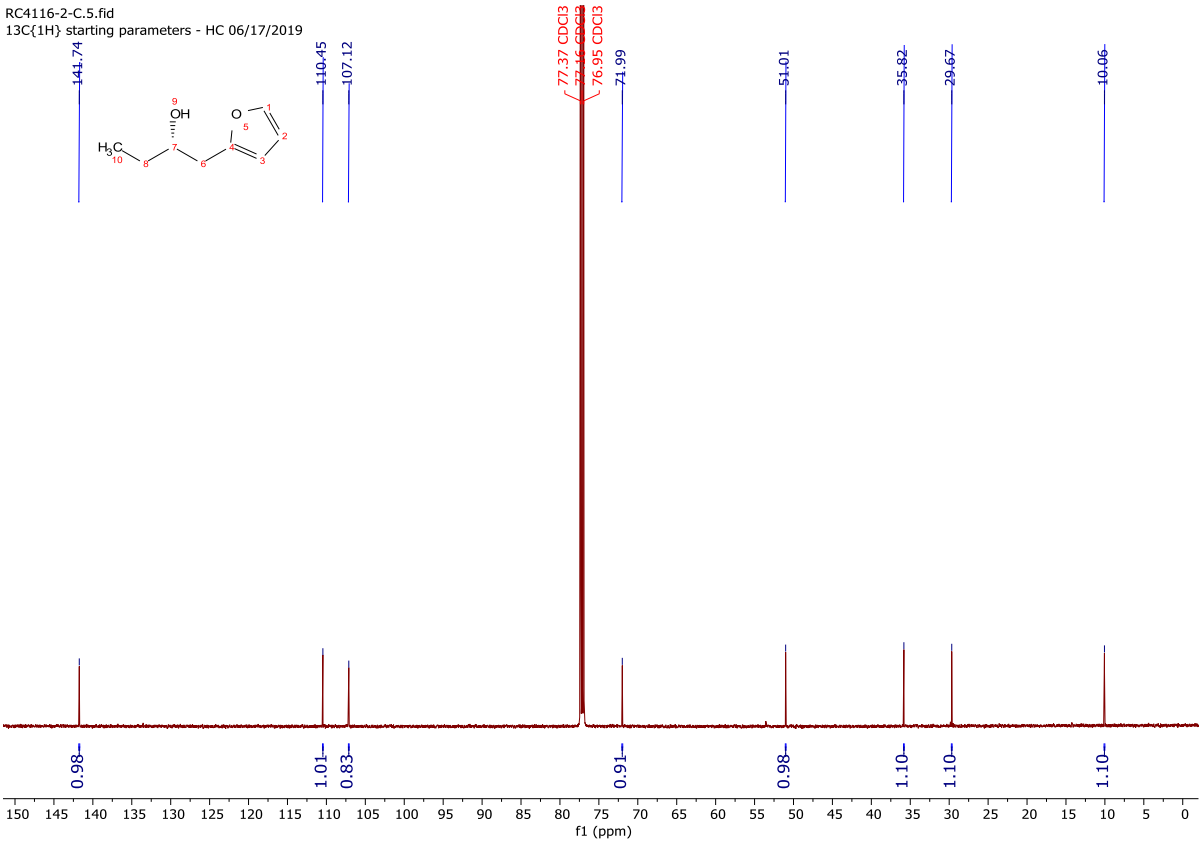
RC4116-2-C.5.fid
13C{1H} starting parameters - HC 06/17/2019
f1 (ppm)

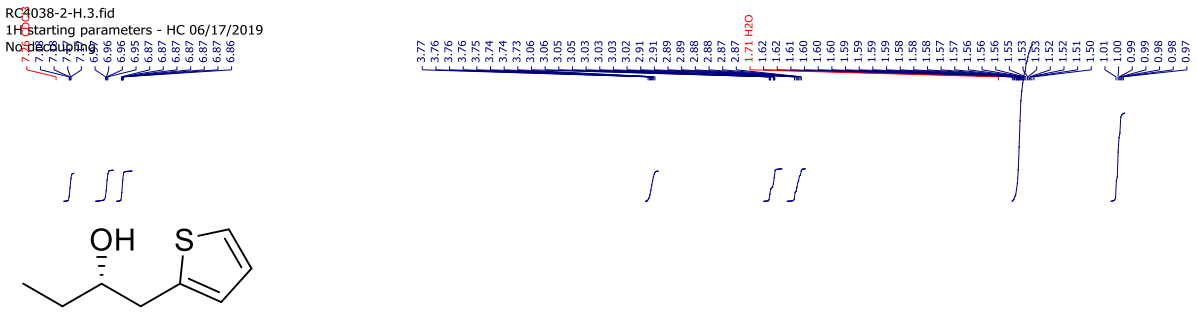
RC4038-2-H.3.fid
1H starting parameters - HC 06/17/2019
OH
S
H2O

P46

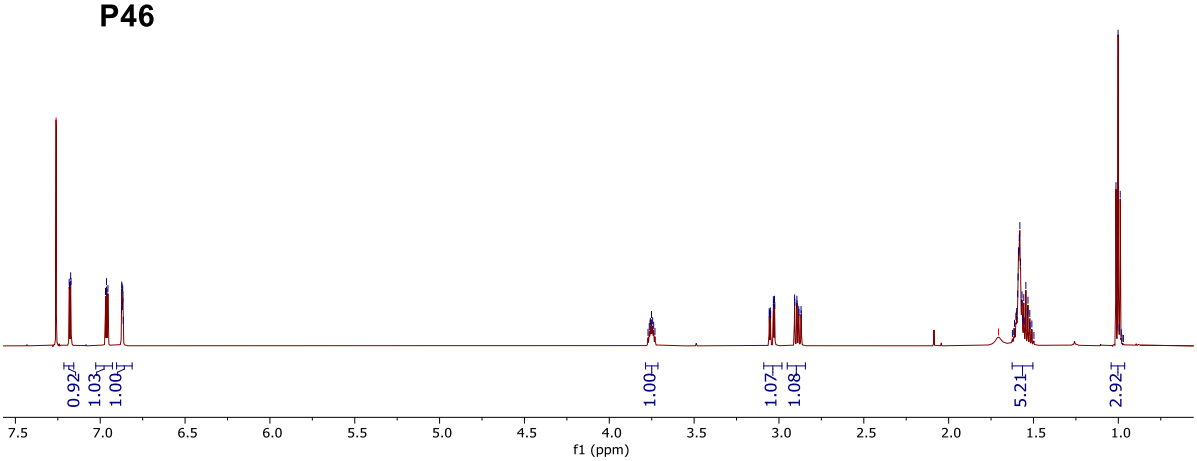
0.92
1.03
1.00
1.00
1.07
1.08
5.21
2.92
f1 (ppm)

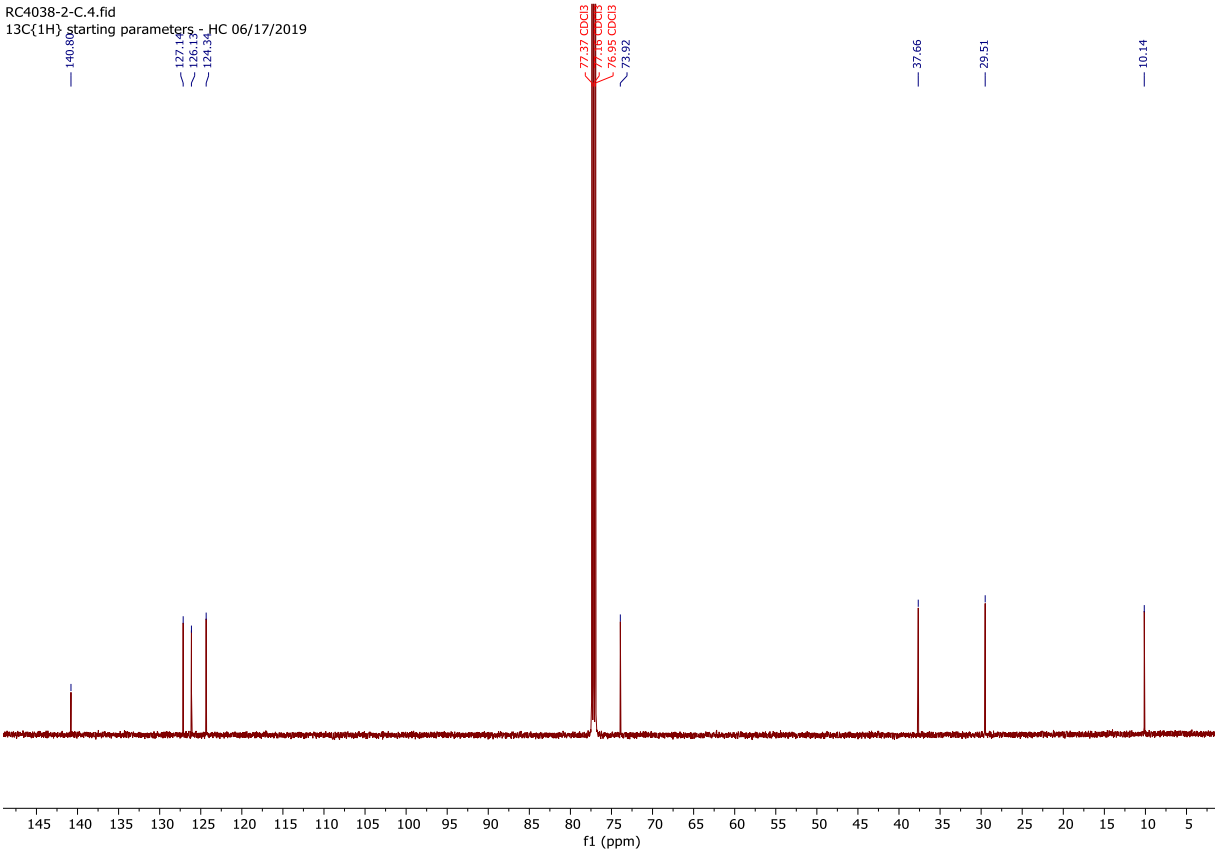
RC4038-2-C.4.fid
13C{1H} starting parameters - HC 06/17/2019
140.80
127.14
126.13
124.34
77.37 CDCl3
77.16 CDCl3
76.95 CDCl3
73.92
37.66
29.51
10.14
f1 (ppm)

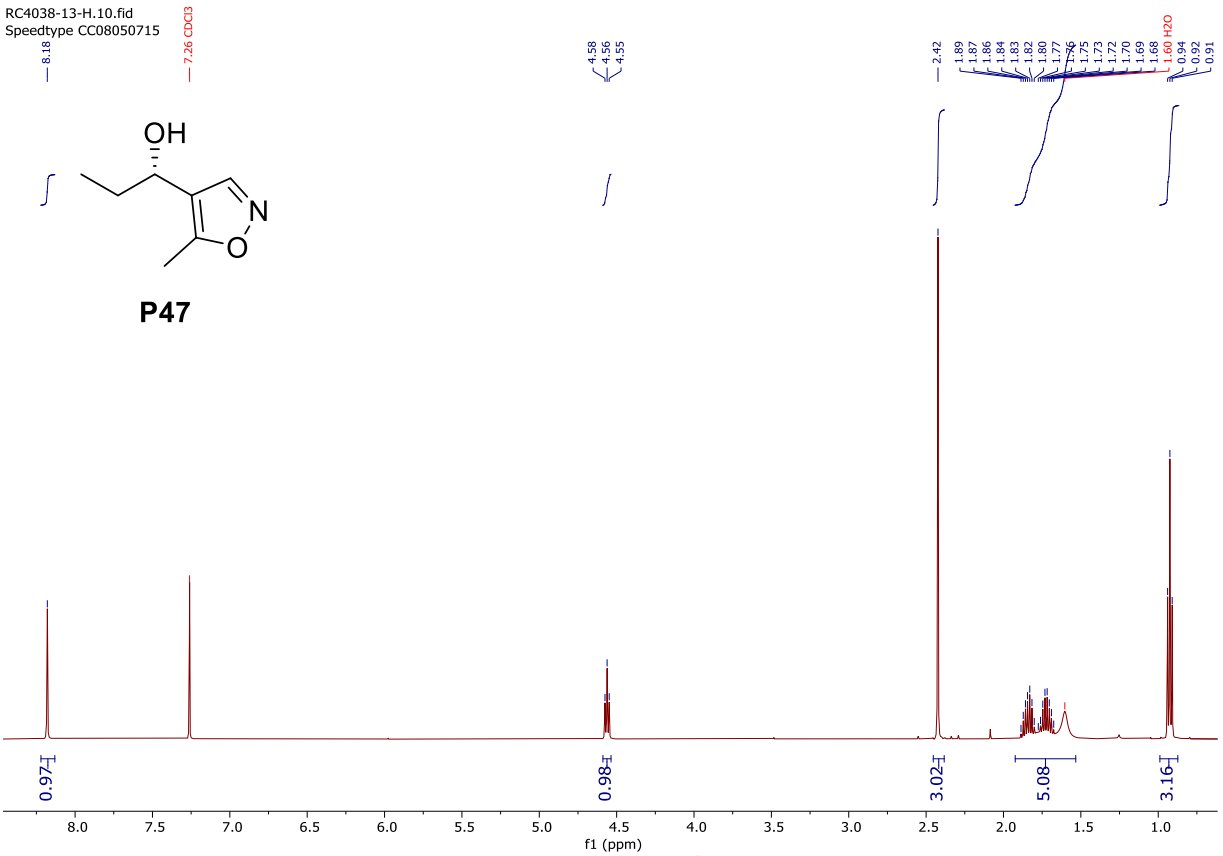
RC4038-13-H.10.fid
Speedtype CC08050715
8.18
7.26 CDCl3
4.58
4.56
4.55
2.42
1.89
1.87
1.86
1.84
1.83
1.82
1.80
1.77
1.76
1.75
1.73
1.72
1.70
1.69
1.68
1.60 H2O
0.94
0.92
0.91
OH
N
O
P47
0.97
0.98
3.02
5.08
3.16
8.0
7.5
7.0
6.5
6.0
5.5
5.0
4.5
4.0
3.5
3.0
2.5
2.0
1.5
1.0
f1 (ppm)

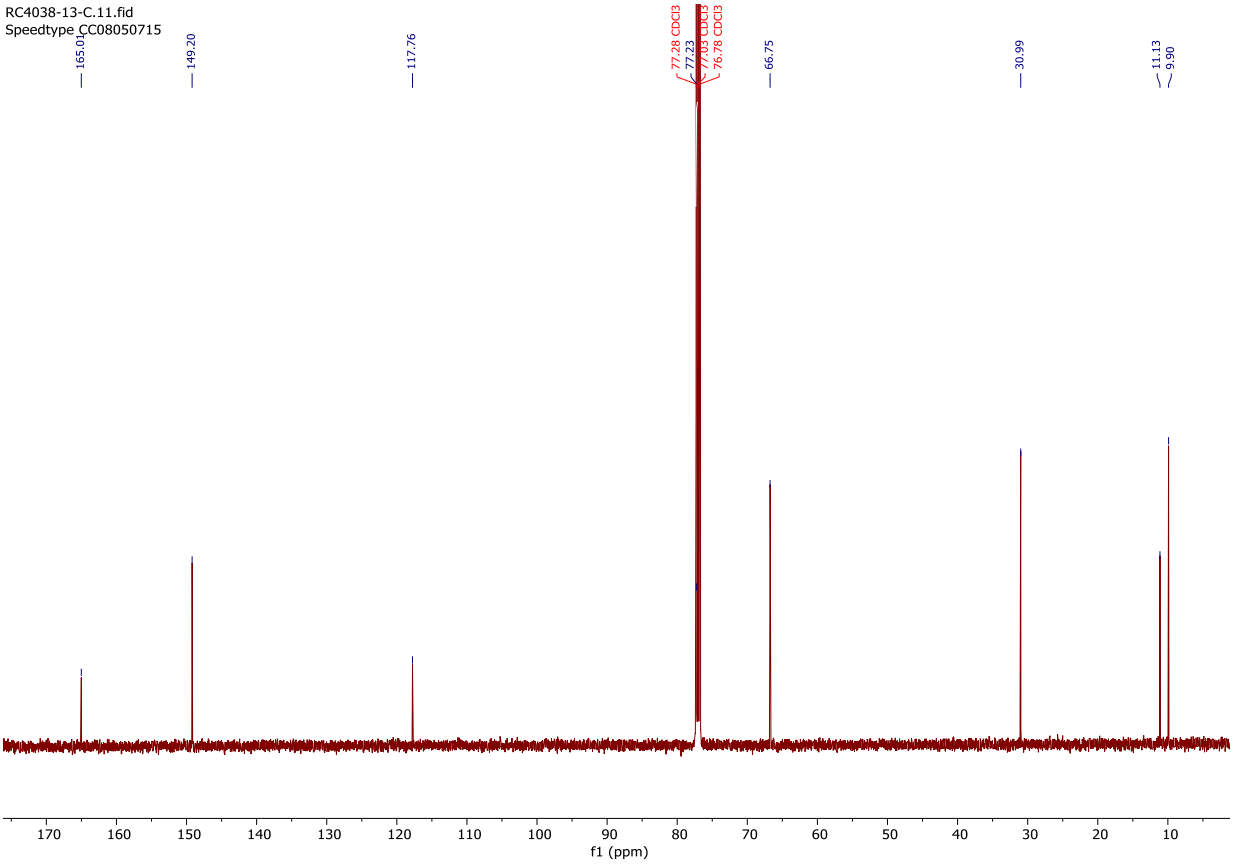
RC4038-13-C.11.fid
Speedtype CC08050715
165.01
149.20
117.76
77.28 CDCl3
77.23
77.05 CDCl3
76.78 CDCl3
66.75
30.99
11.13
9.90
170
160
150
140
130
120
110
100
90
80
70
60
50
40
30
20
10
f1 (ppm)

2.5 References

(1) Schwizer, F.; Okamoto, Y.; Heinisch, T.; Gu, Y.; Pellizzoni, M. M.; Lebrun, V.; Reuter, R.; Köhler, V.; Lewis, J. C.; Ward, T. R. Artificial Metalloenzymes: Reaction Scope and Optimization Strategies. *Chem. Rev.* **2018**, *118* (1), 142–231.

(2) Rosati, F.; Roelfes, G. Artificial Metalloenzymes. *ChemCatChem* **2010**, *2* (8), 916–927.

(3) Davis, H. J.; Ward, T. R. Artificial Metalloenzymes: Challenges and Opportunities. *ACS Cent. Sci.* **2019**, *5* (7), 1120–1136. (4) Adamson, C.; Kanai, M. Integrating Abiotic Chemical Catalysis and Enzymatic Catalysis in Living Cells. *Org. Biomol. Chem.* **2021**, *19* (1), 37–45.

(5) Ji, P.; Park, J.; Gu, Y.; Clark, D. S.; Hartwig, J. F. Abiotic Reduction of Ketones with Silanes Catalysed by Carbonic Anhydrase through an Enzymatic Zinc Hydride. *Nat. Chem.* **2021**, *13* (4), 312–318.

(6) Schilter, D.; Camara, J. M.; Huynh, M. T.; Hammes-Schiffer, S.; Rauchfuss, T. B. Hydrogenase Enzymes and Their Synthetic Models: The Role of Metal Hydrides. *Chem. Rev.* **2016**, *116* (15), 8693–8749.

(7) Gloaguen, F.; Rauchfuss, T. B. Small Molecule Mimics of Hydrogenases: Hydrides and Redox. *Chem Soc Rev* **2009**, *38* (1), 100–108.

(8) Sly, W. S.; Hu, P. Y. Human Carbonic Anhydrases and Carbonic Anhydrase Deficiencies. *Annu. Rev. Biochem.* **1995**, *64* (1), 375–401.

(9) Håkansson, K.; Carlsson, M.; Svensson, L. A.; Liljas, A. Structure of Native and Apo Carbonic Anhydrase II and Structure of Some of Its Anion-Ligand Complexes. *J. Mol. Biol.* **1992**, *227* (4), 1192–1204.

(10) Patel, R. N. Biocatalytic Synthesis of Chiral Alcohols and Amino Acids for Development of Pharmaceuticals. *Biomolecules* **2013**, *3* (4), 741–777.

(11) Truppo, M. D.; Pollard, D.; Devine, P. Enzyme-Catalyzed Enantioselective Diaryl Ketone Reductions. *Org. Lett.* **2007**, *9* (2), 335–338.

(12) Huisman, G. W.; Liang, J.; Krebber, A. Practical Chiral Alcohol Manufacture Using Ketoreductases. *Curr. Opin. Chem. Biol.* **2010**, *14* (2), 122–129.

(13) Jiang, Q.; Jiang, Y.; Xiao, D.; Cao, P.; Zhang, X. Highly Enantioselective Hydrogenation of Simple Ketones Catalyzed by a Rh–PennPhos Complex. *Angew. Chem. Int. Ed.* **1998**, *37* (8), 1100–1103.

(14) Ohkuma, T.; Sandoval, C. A.; Srinivasan, R.; Lin, Q.; Wei, Y.; Muñiz, K.; Noyori, R. Asymmetric Hydrogenation of *Tert* -Alkyl Ketones. *J. Am. Chem. Soc.* **2005**, *127* (23), 8288–8289.

(15) Garbe, M.; Junge, K.; Walker, S.; Wei, Z.; Jiao, H.; Spannenberg, A.; Bachmann, S.; Scalone, M.; Beller, M. Manganese(I)-Catalyzed Enantioselective Hydrogenation of Ketones Using a Defined Chiral PNP Pincer Ligand. *Angew. Chem. Int. Ed.* **2017**, *56* (37), 11237–11241.

(16) Corey, E. J.; Helal, C. J. Reduction of Carbonyl Compounds with Chiral Oxazaborolidine Catalysts: A New Paradigm for Enantioselective Catalysis and a Powerful New Synthetic Method. *Angew. Chem. Int. Ed.* **1998**, *37* (15), 1986–2012.

(17) Zhang, F.-H.; Zhang, F.-J.; Li, M.-L.; Xie, J.-H.; Zhou, Q.-L. Enantioselective Hydrogenation of Dialkyl Ketones. *Nat. Catal.* **2020**, *3* (8), 621–627.

(18) Moore, J. C.; Pollard, D. J.; Kosjek, B.; Devine, P. N. Advances in the Enzymatic Reduction of Ketones. *Acc. Chem. Res.* **2007**, *40* (12), 1412–1419.

(19) Koesoema, A. A.; Sugiyama, Y.; Xu, Z.; Standley, D. M.; Senda, M.; Senda, T.; Matsuda, T. Structural Basis for a Highly (S)-Enantioselective Reductase towards Aliphatic Ketones with

Only One Carbon Difference between Side Chain. *Appl. Microbiol. Biotechnol.* **2019**, *103* (23–24), 9543–9553.
(20) T.sriwong, K.; Koesoema, A. A.; Matsuda, T. Organic–Inorganic Nanocrystal Reductase to Promote Green Asymmetric Synthesis. *RSC Adv.* **2020**, *10* (51), 30953–30960.
(21) Matsuda, T.; Nakajima, Y.; Harada, T.; Nakamura, K. Asymmetric Reduction of Simple Aliphatic Ketones with Dried Cells of Geotrichum Candidum. *Tetrahedron Asymmetry* **2002**, *13* (9), 971–974.
(22) De Miranda, A. S.; Milagre, C. D. F.; Hollmann, F. Alcohol Dehydrogenases as Catalysts in Organic Synthesis. *Front. Catal.* **2022**, *2*, 900554.
(23) Nealon, C. M.; Musa, M. M.; Patel, J. M.; Phillips, R. S. Controlling Substrate Specificity and Stereospecificity of Alcohol Dehydrogenases. *ACS Catal.* **2015**, *5* (4), 2100–2114.
(24) Wu, S.; Snajdrova, R.; Moore, J. C.; Baldenius, K.; Bornscheuer, U. T. Biocatalysis: Enzymatic Synthesis for Industrial Applications. *Angew. Chem. Int. Ed.* **2021**, *60* (1), 88–119.
(25) Sun, Z.; Wikmark, Y.; Bäckvall, J.-E.; Reetz, M. T. New Concepts for Increasing the Efficiency in Directed Evolution of Stereoselective Enzymes. *Chem. – Eur. J.* **2016**, *22* (15), 5046–5054.
(26) Zeymer, C.; Hilvert, D. Directed Evolution of Protein Catalysts. *Annu. Rev. Biochem.* **2018**, *87* (1), 131–157.
(27) Arnold, F. H. Directed Evolution: Bringing New Chemistry to Life. *Angew. Chem. Int. Ed.* **2018**, *57* (16), 4143–4148.
(28) Voss, M.; Küng, R.; Hayashi, T.; Jonczyk, M.; Niklaus, M.; Iding, H.; Wetzl, D.; Buller, R. Multi-Faceted Set-up of a Diverse Ketoreductase Library Enables the Synthesis of Pharmaceutically-Relevant Secondary Alcohols. *ChemCatChem* **2021**, *13* (6), 1538–1545.
(29) Acevedo-Rocha, C. G.; Reetz, M. T.; Nov, Y. Economical Analysis of Saturation Mutagenesis Experiments. *Sci. Rep.* **2015**, *5* (1), 10654.
(30) Siloto, R. M. P.; Weselake, R. J. Site Saturation Mutagenesis: Methods and Applications in Protein Engineering. *Biocatal. Agric. Biotechnol.* **2012**, *1* (3), 181–189.
(31) Wang, Y.; Xue, P.; Cao, M.; Yu, T.; Lane, S. T.; Zhao, H. Directed Evolution: Methodologies and Applications. *Chem. Rev.* **2021**, *121* (20), 12384–12444.
(32) Key, H. M.; Clark, D. S.; Hartwig, J. F. Generation, Characterization, and Tunable Reactivity of Organometallic Fragments Bound to a Protein Ligand. *J. Am. Chem. Soc.* **2015**, *137* (25), 8261–8268.
(33) Hjelmgaard, T.; Gardette, D.; Tanner, D.; Aitken, D. J. Synthesis of (+)-Coniceine via Reductive Photocyclization of Dienamides: An Entry to Indolizidines. *Tetrahedron Asymmetry* **2007**, *18* (5), 671–678.
(34) He, C.; Guo, S.; Huang, L.; Lei, A. Copper Catalyzed Arylation/C−C Bond Activation: An Approach toward α-Aryl Ketones. *J. Am. Chem. Soc.* **2010**, *132* (24), 8273–8275.
(35) Chang, M.-Y.; Lin, C.-H.; Tai, H.-Y. Palladium-Catalyzed Synthesis of Substituted Nitroolefins. *Tetrahedron Lett.* **2013**, *54* (24), 3194–3198.
(36) Guernon, J.; Marcin, L.; Higgins, M.; Yang, F.; Shi, J.; Snyder, L.; Thompson, L. A.; Wu, Y.-J. Synthesis of β-Disubstituted β-Amino Isoxazolyl Ketones by Addition of Ketimines with Isoxazolyl Methyl Ketone Enolates. *Tetrahedron Lett.* **2014**, *55* (13), 2134–2137.
(37) Jin, T.; Yamamoto, Y. Gold-Catalyzed Synthesis of Polycyclic Enones from Carbon Tethered 1,3-Enynyl Carbonyls via Tandem Heteroenyne Metathesis and Nazarov Reaction. *Org. Lett.* **2008**, *10* (14), 3137–3139.

(38) Miura, T.; Fujioka, S.; Takemura, N.; Iwasaki, H.; Ozeki, M.; Kojima, N.; Yamashita, M. Synthesis of 6-Substituted 3-(Alkoxycarbonyl)-5-Aryl-α-Pyrones. *Synthesis* **2014**, *46*(04), 496-502
(39) Morandi, B.; Wickens, Z. K.; Grubbs, R. H. Regioselective Wacker Oxidation of Internal Alkenes: Rapid Access to Functionalized Ketones Facilitated by Cross-Metathesis. *Angew. Chem. Int. Ed.* **2013**, *52* (37), 9751–9754.
(40) Li, J.-L.; Yue, C.-Z.; Chen, P.-Q.; Xiao, Y.-C.; Chen, Y.-C. Remote Enantioselective Friedel–Crafts Alkylations of Furans through HOMO Activation. *Angew. Chem. Int. Ed.* **2014**, *53* (21), 5449–5452.
(41) Zhang, X.-R.; Zhou, S.-L.; Yuan, Y.; Du, W.; Chen, Y.-C. Chemo- and Regioselective Asymmetric Friedel–Crafts Reaction of Furans and Thiophenes with α,β-Unsaturated Aldehydes through Dual Activation. *Synlett* **2017**, *28* (14), 1771–1774.
(42) Patel, R. N.; Banerjee, A.; Nanduri, V.; Goswami, A.; Comezoglu, F. T. Enzymatic Resolution of Racemic Secondary Alcohols by Lipase B from Candida Antarctica. *J. Am. Oil Chem. Soc.* **2000**, *77* (10), 1015–1019.
(43) Li, J.; Tang, Y.; Wang, Q.; Li, X.; Cun, L.; Zhang, X.; Zhu, J.; Li, L.; Deng, J. Chiral Surfactant-Type Catalyst for Asymmetric Reduction of Aliphatic Ketones in Water. *J. Am. Chem. Soc.* **2012**, *134* (45), 18522–18525.
(44) Matsuo, J.; Hattori, Y.; Hashizume, M.; Ishibashi, H. Asymmetric Reduction of Aliphatic Ketones and Acyl Silanes Using Chiral Anti-Pentane-2,4-Diol and a Catalytic Amount of 2,4-Dinitrobenzenesulfonic Acid. *Tetrahedron* **2010**, *66* (32), 6062–6069.
(45) Schlatter, A.; Kundu, M. K.; Woggon, W.-D. Enantioselective Reduction of Aromatic and Aliphatic Ketones Catalyzed by Ruthenium Complexes Attached to β-Cyclodextrin. *Angew. Chem. Int. Ed.* **2004**, *43* (48), 6731–6734
(46) Kitamura, M.; Tokunaga, M.; Ohkuma, T.; Noyon, R. Convenient Preparation of BINAP-Ruthenium Complexes Catalyzing Asymmetric Hydrogenation of Functionalized Ketones *Tetrahedron Letters* **1991**, *32*(33), 4163-4166
(47) Fuchs, M.; Toesch, M.; Schober, M.; Wuensch, C.; Faber, K. Chemoenzymatic Asymmetric Total Synthesis of (R)-Lasiodiplodin Methyl Ether through a Sulfatase-Based Deracemization Process. *Eur. J. Org. Chem.* **2013**, *2013* (2), 356–361.
(48) Snider, B. B.; Rodini, D. J.; Kirk, T. C.; Cordova, R. Dimethylaluminum Chloride Catalyzed Ene Reactions of Aldehydes. *J. Am. Chem. Soc.* **1982**, *104* (2), 555–563.
(49) El'perina, E. A.; Struchkova, M. L.; Serkebaev, M. L.; Serebryakov, E. P. Enhanced Reactivity of Secondary Hydroxyl Groups in the O-Aikylation of Carbohydrate-Related Primary-Secondary Vic-Glycols. Regioselective 2-O-Benzylation of 1,3:2,4-Di-O-Ethylidene-D-Glucitol.*Russian Chemical Bulletin* **1993,** *42*(4), 744-750
(50) Musa; Ziegelmann-Fjeld, K. I.; Vieille, C.; Zeikus, J. G.; Phillips, R. S. Asymmetric Reduction and Oxidation of Aromatic Ketones and Alcohols Using W110A Secondary Alcohol Dehydrogenase from *Thermoanaerobacter Ethanolicus*. *J. Org. Chem.* **2007**, *72* (1), 30–34.
(51) Jones, G. B.; Heaton, S. B. Catalytic Asymmetric Induction Part 2. Chiral Tricarbonyl (η6 arene) Chromium (0) Complexes as Enantioselective Catalysts *Tetrahedron: Asymmetry* **1993**, *4*(2), 261-272
(52) Liu, Y.-C.; Wu, Z.-L. Switchable Asymmetric Bio-Epoxidation of α,β-Unsaturated Ketones. *Chem. Commun.* **2016**, *52* (6), 1158–1161.

(53) Hu, X.; Zhang, G.; Bu, F.; Lei, A. Visible-Light-Mediated Anti-Markovnikov Hydration of Olefins. *ACS Catal.* **2017**, *7* (2), 1432–1437.
(54) Fogagnolo, M.; Giovannini, P. P.; Guerrini, A.; Medici, A.; Pedrini, P.; Colombi, N. Homochiral (R)- and (S)-1-Heteroaryl- and 1-Aryl-2-Propanols via Microbial Redox. *Tetrahedron Asymmetry* **1998**, *9* (13), 2317–2327.
(55) Albarrán-Velo, J.; Gotor-Fernández, V.; Lavandera, I. Markovnikov Wacker-Tsuji Oxidation of Allyl(Hetero)Arenes and Application in a One-Pot Photo-Metal-Biocatalytic Approach to Enantioenriched Amines and Alcohols. *Adv. Synth. Catal.* **2021**, *363* (16), 4096–4108.
(56) Rendler, S.; Auer, G.; Oestreich, M. Kinetic Resolution of Chiral Secondary Alcohols by Dehydrogenative Coupling with Recyclable Silicon-Stereogenic Silanes. *Angew. Chem. Int. Ed.* **2005**, *44* (46), 7620–7624.
(57) Bandeira, P. T.; Alnoch, R. C.; De Oliveira, A. R. M.; De Souza, E. M.; De O. Pedrosa, F.; Krieger, N.; Piovan, L. Enzymatic Kinetic Resolution of Aliphatic Sec -Alcohols by LipG9, a Metagenomic Lipase. *J. Mol. Catal. B Enzym.* **2016**, *125*, 58–63.
(58) Gansäuer, A.; Fan, C.-A.; Keller, F.; Keil, J. Titanocene-Catalyzed Regiodivergent Epoxide Openings. *J. Am. Chem. Soc.* **2007**, *129* (12), 3484–3485
(59) Rawson, D.; Meyers, A. I. The Asymmetric Reduction of Prochiral Ketones Using (S)-2,2′-Dihydroxy-4,5,6,4′,5′,6′-Hexamethoxybiphenyl. *J Chem Soc Chem Commun* **1992**, *6*, 494–496.
(60) Zhang, A.; Yang, L.; Yang, N.; Liu, Y. The Synthesis of Chiral Amino Diol Tridentate Ligands and Their Enantioselective Induction during the Addition of Diethylzinc to Aldehydes. *Tetrahedron Asymmetry* **2014**, *25* (4), 289–297.
(61) Kitamura, Masato.; Suga, Seiji.; Kawai, Koji.; Noyori, Ryoji. Catalytic Asymmetric Induction. Highly Enantioselective Addition of Dialkylzincs to Aldehydes. *J. Am. Chem. Soc.* **1986**, *108* (19), 6071–6072.
(62) Gök, Y.; Kiliçarslan, S.; Gök, H. Z.; Karayiğit, İ. Ü. Enantioselective Ethylation of Various Aldehydes Catalyzed by Readily Accessible Chiral Diols. *Chirality* **2016**, *28* (8), 593–598.
(63) Li, F.; Huang, H.; Zong, H.; Bian, G.; Song, L. Investigation on the Asymmetric Addition Reactions between Varied Nonaromatic Aldehydes and Diethylzinc Catalyzed by Chiral Phosphoramide and Thiophosphorodiamide Ligands. *Tetrahedron Lett.* **2015**, *56* (16), 2071–2076.
(64) Davies, J.; Jones, J. B. Enzymes in Organic Synthesis. 16. Heterocyclic Ketones as Substrates of Horse Liver Alcohol Dehydrogenase. Stereospecific Reductions of 2-Substituted Tetrahydrothiopyran-4-Ones. *J. Am. Chem. Soc.* **1979**, *101* (18), 5405–5410.
(65) Parr, B. T.; Davies, H. M. L. Highly Stereoselective Synthesis of Cyclopentanes Bearing Four Stereocentres by a Rhodium Carbene-Initiated Domino Sequence. *Nat. Commun.* **2014**, *5* (1), 4455.
(66) Kuang, J. PAracGticael SnynethreaticlprAocepduprersoach to Terminal Allenols. *N. Y.* **2013**.
(67) Mulzer, J.; Kaselow, U.; Graske, K.-D.; Kühne, H.; Sieg, A.; Martin, H. J. Stereocontrolled Synthesis of All Eight Stereoisomers of the Putative Anti-Androgen Cyoctol. *Tetrahedron* **2004**, *60* (43), 9599–9614.
(68) Ghosh, A. K.; Simpson, H. M.; Veitschegger, A. M. Enantioselective Total Synthesis of Decytospolide A and Decytospolide B Using an Achmatowicz Reaction. *Org. Biomol. Chem.* **2018**, *16* (33), 5979–5986.

Chapter 3

Preparation of Artificial Metalloenzymes with Myoglobin and Carbonic Anhydrase

3.1 Introduction

Organometallic catalysts have contributed greatly to the advancement of synthetic chemistry, and in recent years the integration of organometallic complexes into protein scaffolds has given rise to the promising field of artificial metalloenzymes. This emerging field offers a novel approach to transition metal catalysis by providing a chiral environment for reactions, thus overcoming the selectivity limitations of traditional transition metal catalysts. Several strategies have been employed for the preparation of artificial metalloenzymes, including covalent anchoring, supramolecular anchoring, dative anchoring, and metal substitution. In this chapter, I present the engineering of two distinct artificial metalloenzymes using myoglobin and carbonic anhydrase as the protein backbone. For myoglobin, we employed both covalent anchoring and metal substitution strategies to create a variant crosslinked with the hemin cofactor. In addition, we utilized a dative anchoring strategy to prepare a copper-substituted carbonic anhydrase. The preparation and activity of both artificial metalloenzymes were demonstrated, highlighting their potential for exploring abiotic reactions catalyzed by artificial metalloenzymes.

3.2 Incorporation of Artificial Metallocofactor through the Covalent Anchoring Strategy

Post-translational modification of proteins plays a crucial role in determining the structure and function of enzymes.[1,2] Several hemoproteins have been discovered to undergo post-translational modifications by the formation of covalent bonds between the heme cofactor and specific residues such as Cys-heme,[3] Met-heme,[4] His-heme,[5] Tyr-heme,[6,7] and Lys-heme[8] cross-linkages. These modifications, particularly the cross-linking of proteins with metallocofactors, have been shown to enhance catalytic activity and enantioselectivity over that of unmodified proteins. For instance, Tan and coworkers discovered that introducing the F43Y mutation in myoglobin promoted a novel tyrosine-heme covalent linkage between the hydroxyl group on tyrosine and the vinyl group on the heme cofactor.[6] The catalytic activity of this crosslinked myoglobin was higher for the activation of H_2O_2 than in the absence of the crosslink. Similarly, Lu and coworkers reported the crosslinking of a Mn-salen cofactor with myoglobin, which increased the enantioselectivity of sulfoxidation reactions.[9] In our group, we have developed artificial metalloenzymes by incorporating Ir(Me)mPIX into CYP119 to catalyze carbene transfer reactions.[10,11] However, we observed lower affinity between the Ir cofactor than the natural heme cofactor and CYP119, due to the absence of the axial histidine, which binds to the iron center in the native heme cofactor. To address this issue, we proposed that the introduction of a covalent anchor between Ir(Me)mPIX and the hemoprotein would enhance protein stability and prevent cofactor dissociation from the active site. Through this crosslinking strategy, we anticipated that the catalytic selectivity and turnover numbers of the engineered enzyme would exceed those in the absence of the crosslink.

3.2.1 Synthesis and Characterization of Heme-Myo crosslinking enzyme

Our initial objective was to develop a method to crosslink the cofactor in myoglobin, inspired by a previous report that the F43Y mutation facilitates bioconjugation between F43Y and the vinyl group on the heme. The myoglobin containing the F43Y mutation was expressed using TB media without the addition of hemin, and the extent of crosslinking was monitored using protein LCMS, revealing a 15% crosslinking efficiency (Figure 1). It is worth noting that LCMS is an ideal

analytical technique because the protein was denatured on the column. Consequently, the protein without covalent linking to the cofactor was detected as the mass corresponding to the apo form, while the protein with crosslinking exhibits a mass that includes both the cofactor and the protein.

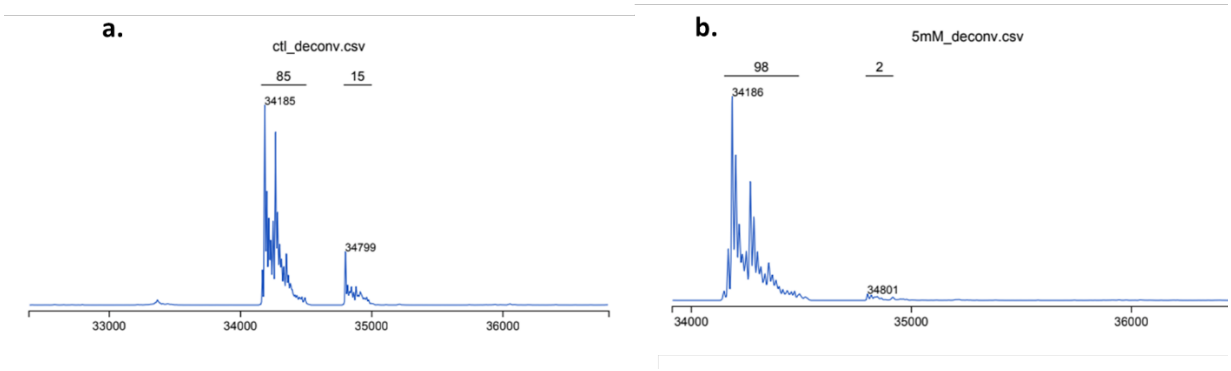

Figure 1. The crosslinking of hemin and myoglobin under different expression conditions. a. TB expression. b. LB expression

However, we sought to increase the level of crosslinking above the 15% observed. Inspired by Watanabe and coworkers who reconstituted the metalloenzyme by adding the metallocofactor during the disruption stage of *E. coli* cells,[12] we refined the protocol with an addition of hemin (1 mL of 3 mM in DMSO) to the resuspension of the cell pellet in lysis buffer (1 L culture of pellet in 30 mL lysis buffer) to improve the cofactor reconstitution and formation of covalent bond. Subsequent LCMS analysis demonstrated a remarkable increase in the crosslinking efficiency between myoglobin and heme, reaching 82% (Figure 2).

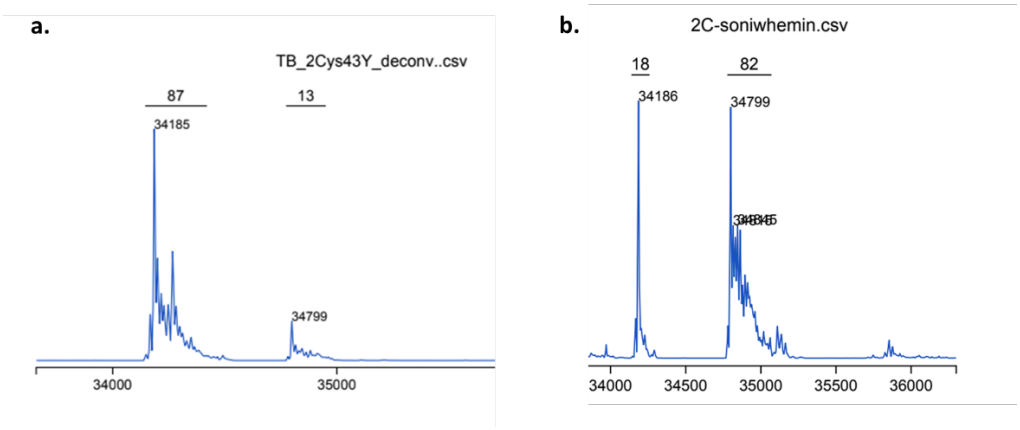

Figure 2. The crosslinking efficiency of hemin and myoglobin with addition of hemin during sonication. a. no additional hemin in cell pellet during sonication step b. addition of 1 mL of 3 mM hemin solution in DMSO to cell pellets during sonication improved the crosslinking percentage.

With a reliable protocol to crosslink the heme to myoglobin, we investigated whether the mutation of the protein affects the crosslinking efficiency. We first mutated the distal ligand from histidine to leucine, which creates a binding pocket for binding of substrates. (H64L) We discovered a decrease in the percentage of crosslinking to 36%. (Figure 3a) We also introduced a mutation of

the axial ligand from histidine to glycine (H93G), which would create a binding pocket for the methyl moiety for the introduction of Ir(Me)mPIX as the cofactor. With the introduction of the second mutant in the active site, the crosslinking was further diminished to 3%. (Figure 3b) Therefore, the result indicated that the modification of the active site decreased the efficiency of the crosslinking due to the change of the structure of the protein which effect the distance and orientation between the cofactor and critical residue for the formation of crosslinking.

Furthermore, our recent crystal structure of Ir(Me)mPIX bound to CYP119 revealed that the iridium cofactor was observed to initially bind in an inactive form, with the methyl group occupying the active site. However, the cofactor exhibited a dynamic behavior, flipping to its active conformation and catalyzed the carbene transfer reaction. This observation implies that crosslinking of the cofactor and protein in the most stable form would likely reduce the activity of the artificial metalloenzyme, rather than enhance it.[13]

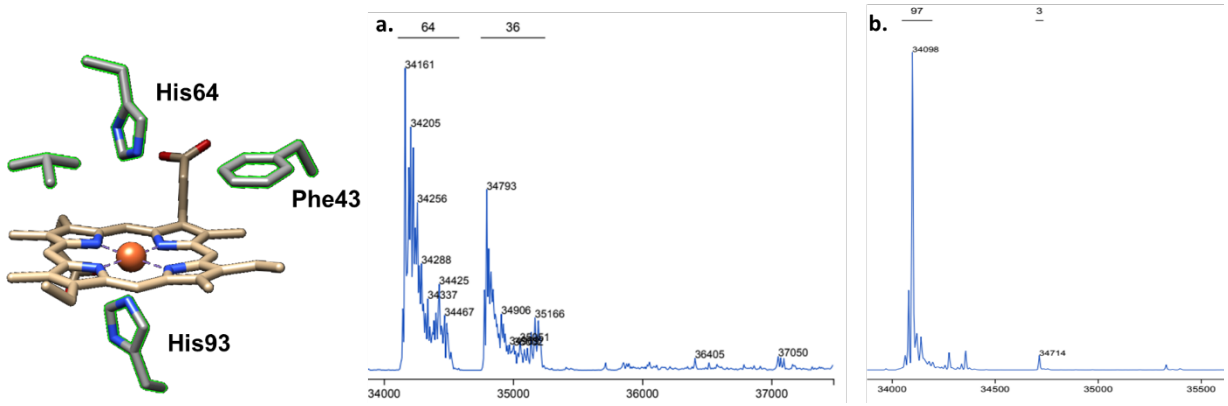

Figure 3. (Left) the active site in myoglobin and the critical residue affecting crosslinking between cofactor and protein skeleton. (Right) Crosslinking percentage with myoglobin variants. a. the variant with mutation at the distal ligand in the active site (H64L) b. the variant with a mutation at both axial ligand and distal ligand (H93G, H64I)

3.2.2 Conclusion

In our study, we focused on the crosslinking between hemin and myoglobin and explored different conditions for protein expression to improve crosslinking efficiency. Through optimization of the purification step, we enhanced the percentage of crosslinked material. Interestingly, we also found that mutations within the active site of the protein influenced the efficiency of crosslinking. This finding suggests that the orientation and distance between the vinyl group on hemin and the tyrosine residue are crucial for successful crosslinking. Additionally, the successful crosslinking of hemin to myoglobin opens opportunities for extending this approach to crosslink porphyrin-containing transition metals with myoglobin, thus expanding the potential applications of artificial metalloenzymes.

3.2.3 Experimental Information

3.2.3.1 General Methods

Unless otherwise noted, all chemicals, salts and solvents were obtained from commercial suppliers (Sigma-Aldrich, Acros, etc.) and used without further purification. All expression media and buffer were prepared using ddH2O (MilliQ A10 Advantage purification system, Millipore). Expression media was sterilized either by autoclave (20 min, 121 °C) or a sterile syringe filter (0.22 μm). To maintain sterile conditions, sterile materials and *E.coli* cells were manipulated near a lit Bunsen burner.

3.2.3.2 Instrumentation

a. UV-Vis Spectroscopy

Protein concentrations were determined by NanoDrop 2000 UV-Vis Spectrophotometer (Thermo Scientific) at 280/260 nm.

b. Mass spectrometry

The percentage of crosslinking between hemin and myoglobin was analyzed an Agilent 1200 series liquid chromatograph (Agilent Technologies) connected in-line with an Agilent 6224 Time-of-Flight (TOF) LC/MS system equipped with a Turbospray ion source. Protein samples were run with a Proswift RP-4H column (Dionex, USA). Protein mass reconstruction was performed on the charge ladder with Mass Hunter software (Agilent, USA).

3.2.4.3 Protein construct and sequence

The myoglobin variants are purified using His-tag affinity purification methods with a Ni-NTA column. A mOCR tag was added in front of the C terminus of the protein of interest.

The highlight letters indicate the residues that were mutated compared to the sequence of the mother myoglobin.

Sequence for the mother myoglobin

VLSEGEWQLVLHVWAKVEADVAGHGQDILIRLFKSHPETLEKFDRFKHLKTEAEMKAS
EDLKKHGVTVLTALGAILKKKGHHEAELKPLAQSHATKHKIPIKYLEFICEAIIHVLHSRH
PGDFGADAQGAMNKALELFRKDIAAKYKELGYQG*

F43Y

VLSEGEWQLVLHVWAKVEADVAGHGQDILIRLFKSHPETLEKYDRFKHLKTEAEMKAS
EDLKKHGVTVLTALGAILKKKGHHEAELKPLAQSHATKHKIPIKYLEFICEAIIHVLHSRH
PGDFGADAQGAMNKALELFRKDIAAKYKELGYQG*

F43Y/H64L

VLSEGEWQLVLHVWAKVEADVAGHGQDILIRLFKSHPETLEKYDRFKHLKTEAEMKAS
EDLKKLGVTVLTALGAILKKKGHHEAELKPLAQSHATKHKIPIKYLEFICEAIIHVLHSRH
PGDFGADAQGAMNKALELFRKDIAAKYKELGYQG*

F43Y/H64L/H93

VLSEGEWQLVLHVWAKVEADVAGHGQDILIRLFKSHPETLEKYDRFKHLKTEAEMKAS
EDLKKLGVTVLTALGAILKKKGHHEAELKPLAQSIATKHKIPIKYLEFICEAIIHVLHSRH
PGDFGADAQGAMNKALELFRKDIAAKYKELGYQG*

3.2.4.4 Protein Expression, Purification, and Reconstitution

a. Protein Expression

Myoglobin was overexpressed in chemically competent Rosetta2 (DE3) pLysS *E. coli.* cells (obtained from the UC Berkeley Macro Lab) with Terrific Broth (TB) Media. Freshly transformed cells were plated on ampicillin/LB (100 mg/L) media and grown overnight at 37 °C in the oven. Single colonies were used to grow the starting culture in 5 mL LB/amp media, which were shaken at 37 °C overnight. This culture from overnight growth was added to 4 × 1 L of LB/amp media and shaken at 37 °C/ 250 rpm for 8 h. After the optical density (OD) of cell culture was measured to be 1.0 to 1.2, the temperature was reduced to 25 °C. The cell culture was induced with IPTG (1 mM/L) and shaken for an additional 16 h. After this time, the cells were collected by centrifugation (5000 rpm, 15 minutes, 4 °C). Cell pellets were resuspended in Ni-NTA lysis buffer (50 mM NaPi, 300 mM NaCl, 10 mM imidazole, pH 8.0) and frozen at -80 °C.

b. Protein Purification and Reconstitution

Cell suspensions were thawed in a room-temperature water bath and transferred to a glass beaker. The hemin solution (1 mL, 3 mM) was added to the cell suspensions. The cell suspensions were lysed on ice by sonication (5 × 10 min on, 5 × 10 min off, 60% amplitude). The cell debris was removed by centrifugation (10,000 rpm, 30 min, 4 °C), and Ni-NTA was added to the cell lysate. The lysate was mixed in Ni-NTA for 30 min at 4 °C, and the resulting material poured onto a glass frit. The resin was washed with Ni-NTA lysis buffer twice and eluted with Ni-NTA elution buffer (50 mM NaPi, 250 mM NaCl, 250 mM Imidazole, pH = 8.0). The eluted protein was dialyzed against tris buffer twice (50 mM, pH = 8.0, 12 h/ 2h, 4 °C). The protein concentration was determined by measuring the absorption at 280 nm with a NanoDrop UV-vis spectrophotometer.

3.2.4 References

(1) Ramazi, S.; Zahiri, J. Post-Translational Modifications in Proteins: Resources, Tools and Prediction Methods. *Database* **2021**, *2021*, baab012.

(2) Lin, Y.-W. The Broad Diversity of Heme-Protein Cross-Links: An Overview. *Biochim. Biophys. Acta BBA - Proteins Proteomics* **2015**, *1854* (8), 844–859.

(3) Barker, P. D.; Nerou, E. P.; Freund, S. M. V.; Fearnley, I. M. Conversion of Cytochrome B562 to C-Type Cytochromes. *Biochemistry* **1995**, *34* (46), 15191–15203.

(4) Kooter, I. M.; Moguilevsky, N.; Bollen, A.; Van Der Veen, L. A.; Otto, C.; Dekker, H. L.; Wever, R. The Sulfonium Ion Linkage in Myeloperoxidase. *J. Biol. Chem.* **1999**, *274* (38), 26794–26802.

(5) Preimesberger, M. R.; Wenke, B. B.; Gilevicius, L.; Pond, M. P.; Lecomte, J. T. J. Facile Heme Vinyl Posttranslational Modification in a Hemoglobin. *Biochemistry* **2013**, *52* (20), 3478–3488.

(6) Yan, D.-J.; Li, W.; Xiang, Y.; Wen, G.-B.; Lin, Y.-W.; Tan, X. A Novel Tyrosine–Heme C□O Covalent Linkage in F43Y Myoglobin: A New Post-Translational Modification of Heme Proteins. *ChemBioChem* **2015**, *16* (1), 47–50.

(7) Liao, F.; Xu, J.-K.; Luo, J.; Gao, S.-Q.; Wang, X.-J.; Lin, Y.-W. Bioinspired Design of an Artificial Peroxidase: Introducing Key Residues of Native Peroxidases into F43Y Myoglobin with a Tyr-Heme Cross-Link. *Dalton Trans.* **2020**, *49* (16), 5029–5033.

(8) Arciero, D. M.; Hooper, A. B. Evidence for a Crosslink between *c* -Heme and a Lysine Residue in Cytochrome P460 of *Nitrosomonas Europaea*. *FEBS Lett.* **1997**, *410* (2–3), 457–460.

(9) Carey, J. R.; Ma, S. K.; Pfister, T. D.; Garner, D. K.; Kim, H. K.; Abramite, J. A.; Wang, Z.; Guo, Z.; Lu, Y. A Site-Selective Dual Anchoring Strategy for Artificial Metalloprotein Design. *J. Am. Chem. Soc.* **2004**, *126* (35), 10812–10813.

(10) Key, H. M.; Dydio, P.; Clark, D. S.; Hartwig, J. F. Abiological Catalysis by Artificial Haem Proteins Containing Noble Metals in Place of Iron. *Nature* **2016**, *534* (7608), 534–537.

(11) Key, H. M.; Dydio, P.; Liu, Z.; Rha, J. Y.-E.; Nazarenko, A.; Seyedkazemi, V.; Clark, D. S.; Hartwig, J. F. Beyond Iron: Iridium-Containing P450 Enzymes for Selective Cyclopropanations of Structurally Diverse Alkenes. *ACS Cent. Sci.* **2017**, *3* (4), 302–308.

(12) Kawakami, N.; Shoji, O.; Watanabe, Y. Single-Step Reconstitution of Apo-Hemoproteins at the Disruption Stage of Escherichia Coli Cells. *ChemBioChem* **2012**, *13* (14), 2045–2047.

(13) Bloomer, B. J.; Natoli, S. N.; Garcia-Borràs, M.; Pereira, J. H.; Hu, D. B.; Adams, P. D.; Houk, K. N.; Clark, D. S.; Hartwig, J. F. Mechanistic and Structural Characterization of an Iridium-Containing Cytochrome Reveals Kinetically Relevant Cofactor Dynamics. *Nat. Catal.* **2023**, *6* (1), 39–51.

3.3 Incorporation of Copper into Carbonic Anhydrase by a Dative Anchoring Strategy

Human Carbonic anhydrase II (hCAII) is a metalloenzyme that contains a zinc ion in its active site coordinated by three histidine residues. The native function of this enzyme is to catalyze the interconversion of carbon dioxide to carbonic acid. Taking advantage of its distinctive active site, researchers have developed artificial metalloenzymes based on the carbonic anhydrase backbone following a series of strategies. For example, Ward and coworkers introduced an artificial transfer hydrogenase to hCAII by creating a covalent linkage between zinc and a sulfonamide on an Ir cofactor.[1] Kazlauskas and coworkers transformed hCAII to an epoxidase by substituting zinc with manganese in the active site.[2] Leveraging the high stability and promiscuity of human carbonic anhydrase, we envisioned that hCAII-based artificial metalloenzymes could be a promising platform for abiotic catalysis after replacement of Zn with other metals.

The synthesis of copper-substituted carbonic anhydrase (Cu-hCAII) is particularly intriguing due to the wide range of copper-catalyzed reactions, including hydrosilylation,[3,4] Diels-Alder reactions,[5] oxidative cross-coupling,[6] allylation,[7–9] and carbene transfer reactions.[10,11] Despite the existence of artificial carbonic anhydrases, there are currently no reported examples of Cu-substituted carbonic anhydrases that catalyze C—C bond formation. In this work, we developed a protocol to synthesize Cu-hCAII. While the preparation of metal-substituted artificial hCAII proteins have been previously reported,[12] the original method for synthesizing metal-substituted hCAII was time-consuming and resulted in low yields, due to the lengthy protocol involved. Therefore, we improved the original protocol to increase the final yield of the enzyme. In addition, we obtained preliminary results demonstrating the capability of the prepared Cu-hCAII to catalyze a carbene transfer reaction.

3.3.1 Synthesis and Characterization of Cu-hCAII

To prepare the Cu-hCAII from purified protein, the process includes three steps: cleavage of the His tag, removal of zinc, and metalation. (Figure 1.)

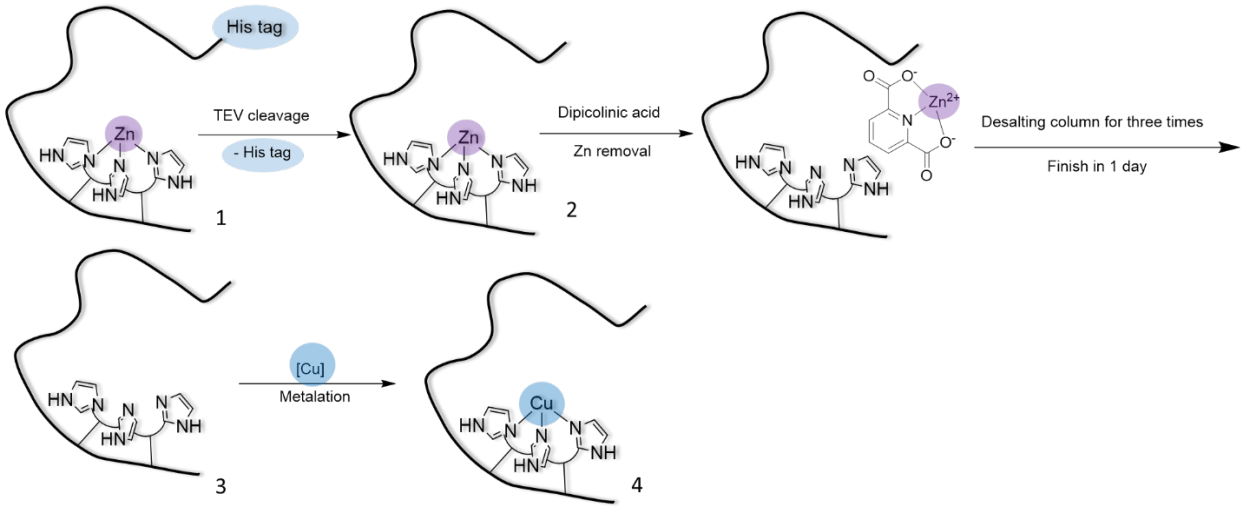

Figure 1. A flow chart of depicting the preparation of Cu-hCAII. 1. hCAII with His-tag, 2.

hCAII after removeal of the His tag, followed by demetallation of zinc by dipicolinic acid, 3. Apo hCAII, 4. Cu-hCAII formed by addition of $Cu(MeCN)_4PF_6$.

The wild-type hCAII was purified by His-Tag affinity chromatography following the reported protocol (Figure S1).[13] However, the presence of the polyhistidine (His-tag) sequence complicates metalation because of the high affinity of the the His tag for copper. Therefore, cleavage of the His-tag is essential for the preparation of Cu-hCAII. Following cleavage of the His-tag, the protein was treated with dipicolinic acid to remove the zinc ion from the active site, resulting in the formation of apo hCAII. The progress of demetallation was monitored by Inductively Coupled Plasma Optical Emission spectroscopy (ICP-OES) and by assessing the decrease in reactivity for the enantioselective reduction of ketones. The ICP-OES measurement showed that the zinc concentration was observed in the protein treated with the dipicolinic acid solution was much lower than the protein that is not treated with dipicolinic acid solution, showing the success of demetallation. (Table S1) Furthermore, the apo protein displayed no activity for the reduction of acetyl pyridine, and this result further verifies the absence of zinc in the active site. (Table S2)

Subsequently, the apo protein was metalated with $Cu(MeCN)_4PF_6$. Following removal of excess metal salt by a desalting column, a light blue protein was obtained, indicating the rapid oxidation of Cu(I) to Cu(II) during the metalation process with a Cu(I) ion source. The efficiency of metalation was determined by ICP-OES analysis, and the percent occupancy of the protein by copper was found to be 80-90%. (Table S3)

3.3.2 Expression of hCAII variants for metal substitution

To investigate the effects of altering the metal coordination residues in Cu-hCAII, we performed mutations at His94 and His96. (Figure 2a.) Specifically, we generated four mutants: H94A, H94C, H96A, and H96C. The substitution of alanine for histidine at positions 94 and 96 was aimed at introducing a non-coordinating residue, whereas the substitution of cysteine was intended to introduce a residue commonly involved in metal coordination.

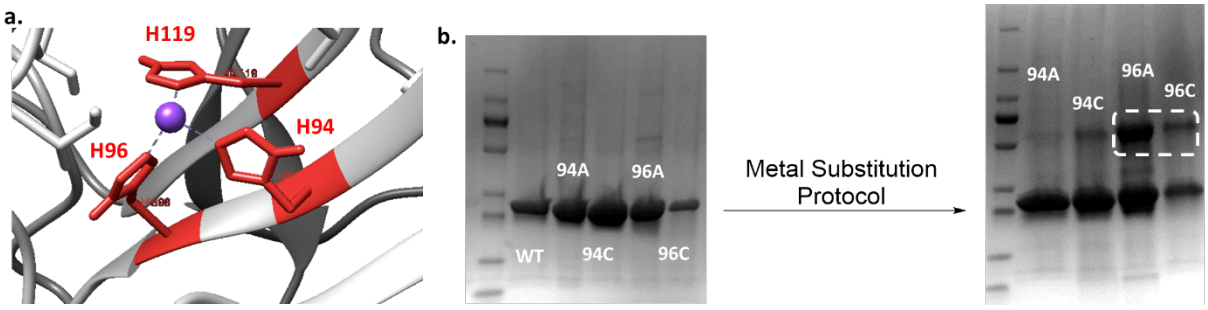

Figure 2. The variants expressed for metalation and the dimerization observed on SDS-PAGE. a. the histidine residue coordinated to zinc in the active site of hCAII. b. the SDS-PAGE with variants before and after the metal substitution protocol.

After implementing the metal substitution protocol on the variants with mutations in the coordinating residues, we observed by SDS-PAGE (Figure 2b) and LCMS (Figure S3) significant dimerization of the protein, particularly of the H96A and H96C variants. We hypothesized that

this dimerization resulted from strong binding between Cu(I) and bipyridine, leading to two proteins chelating a single metal center.[14] We were able to separate the dimers and monomers by SEC-FPLC. (Figure S4)

Efforts were made to minimize the extent of dimerization by optimizing the amount of copper salt added during metalation. However, even with the addition of 2 equivalents of $Cu(MeCN)_4PF_6$, the dimerization caused by the Cu(I) ion was observed, as shown by SDS-PAGE. (Figure 3a) Therefore, we explored an alternative copper salt for the metalation process. We discovered that substituting the Cu(I) complex $Cu(MeCN)_4PF_6$ with the Cu(II) species $Cu(SO_4)•5H_2O$ prevented dimerization (Figure 3b). Moreover, the percentage of the metallated Cu-hCAII remained consistently high at 80-90% when using $Cu(SO_4)•5H_2O$ as the metal source (Table S4).

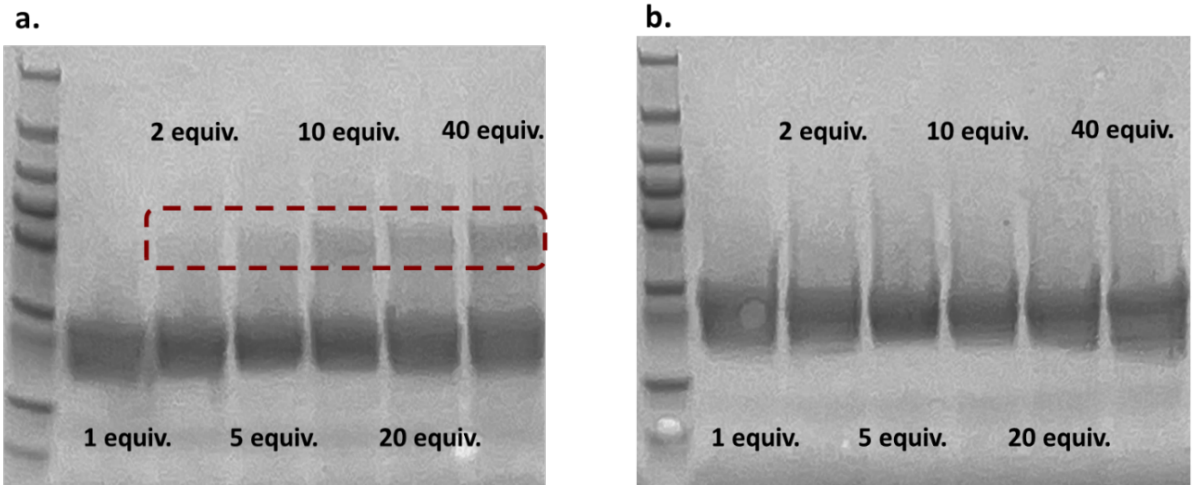

Figure 3. The SDS-PAGE of H94A metalated with Cu(I) and a Cu(II) salts. a. H94A metalated with $Cu(MeCN)_4PF_6$ showing dimerization after addition of 2 equiv of the copper complex. b. H94A metalated with $Cu(SO_4)•5H_2O$, which showed no observable dimer after addition of 40 equiv. of the copper complex.

3.3.3 Development of a Reaction Catalyzed by Cu-hCAII

Note: In the following section, "hCAII" refers to the wild-type (wt) hCAII.

With the wt Cu-hCAII in hand, we first attempted allylation of ketones through copper allyl intermediate (Scheme 1.)

Table 1. Reaction conditions for attempted allylation of 2-pentanone catalyzed by Cu-hCAII

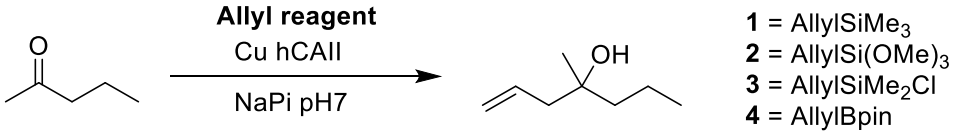

Entry	Cu source	hCAII	Allylation Reagent	Reductant	Conversion

1	Cu(I)	V	**1**	X	0%
2	Cu(II)	V	**1**	X	0%
3	Cu(I)	V	**1**	Sodium ascorbate	0%
4	Cu(II)	V	**1**	Sodium ascorbate	0%
5	Cu(I)	V	**2**	Sodium ascorbate	0%
6	Cu(II)	V	**2**	Sodium ascorbate	0%
7	Cu(I)	V	**3***	Sodium ascorbate	0%
8	Cu(II)	V	**3***	Sodium ascorbate	0%
9	Cu(I)	V	**4**	Sodium ascorbate	0%
10	Cu(II)	V	**4**	Sodium ascorbate	0%

* AllylSiMeCl predissolved in NaPi pH 7.0 buffer before addition to the reaction

Initially, allyltrimethylsilane was tested as an allyl transfer agent (entry 1, 2), and sodium ascorbate was added as reductant to reduce Cu(II) in the metalloenzyme to Cu(I) (entry 3, 4). However, in both cases, no homoallylic alcohol product was observed. During these experiments, we noted the insolubility of allyltrimethylsilane in the aqueous buffer, resulting in the formation of oil drops during the reaction. To overcome this issue, we opted for a more water-soluble allyl reagent (entry 5 to entry 8) with the addition of sodium ascorbate. Nevertheless, no homoallylic alcohol product was detected in these reactions.

While there is no allyl alcohol observed for the allylation reaction of ketone, due to limited reactivity of the allyl silane or steric hindrance between the residues surrounding the copper center in the active site and the substituent on silyl group limiting the allyl transfer from silane to copper, we turned our attention to more reactive allyl transfer reagents, such as allyl boronates. Unfortunately, no product was observed with allylboronic acid pinacol ester (AllylBpin) as an allyl source (entry 9, 10). Moreover, a small amount of allyl alcohol was observed in the reaction, indicating a possible oxidation of the allyl acid pinacol ester.

Given this lack of allyl transfer reactions, we tested carbene transfer reactions catalyzed by Cu-hCAII. The active site of hCAII contains three histidines that bind to copper. Thus, this structure shares similarities with copper-tris(pyrazolyl)borates, which are known to catalyze carbene transfer reactions,[15] and we proposed that the Cu-trihistidine actie site in Cu-hCAII could catalyze carbene transfer reactions. (Scheme 2.)

Table 2. Carbene insertion to N-methyl indole catalyzed by Cu-hCAII and control experiments.

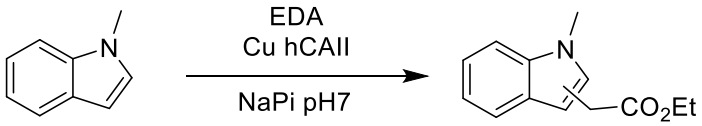

Entry	Cu Source	hCAII	Cu Concentration	Reductant	Conversion
1	Cu(I)	V	0.02 ppm	X	0%
2	Cu(II)	V	0.02 ppm	X	0%
3	Cu(I)	V	0.02 ppm	Sodium ascorbate	14%
4	Cu(II)	V	0.02 ppm	Sodium ascorbate	11%
5	X	V	0 ppm	Sodium ascorbate	0%
6	X	X	0 ppm	Sodium ascorbate	0%
7	Cu(I)	X	0.02 ppm	Sodium ascorbate	2%
8	Cu(I)	X	5 ppm	Sodium ascorbate	5%

We discovered that Cu-hCAII catalyzes the transfer of the carbene from ethyl diazoacetate to *N*-methyl indole. (entry 3, 4) The reaction did not occur without addition of sodium ascorbate as reductant, and this result indicates that the reaction is catalyzed by Cu(I), most likely the Cu(I) in Cu-hCAII (entry 1, 2) The control reaction with addition of Zn-hCAII showed the reaction was not catalyzed by the protein scaffold and the existence of copper ion is essential. (entry 5)

While carbene insertion reaction was also catalyzed by $Cu(MeCN)_4PF_6$ salt without the presence of protein (entry 7), the presence of the enzyme led to 14% conversion of *N*-methyl indole to the carbene insertion product. This conversion is higher after 16 h than the 2% product from the reaction catalyzed by $Cu(MeCN)_4PF_6$ alone at the same concentration of metal in the reaction (0.02 ppm). In addition, increasing the concentration of additional copper salt (5 ppm) did not improve the conversion of the product (entry 8). These preliminary results highlight the improved carbene transfer reactivity achieved by Cu-hCAII as a catalyst, suggesting its potential for enantioselective carbene transfer reactions.

3.3.3 Conclusion

This study presents an advancement in the preparation of Cu-hCAII by offering a more efficient approach that reduces preparation time and improves enzyme yield. Element analysis confirmed the binding of copper to hCAII, validating the formation of Cu-hCAII. Moreover, this study reports, the catalytic reactivity of Cu-hCAII in carbene transfer reactions. The demonstrated catalytic activity of Cu-hCAII opens new possibilities for exploring its potential in other abiotic reactions. With the optimized protocol established for Cu-hCAII preparation, we anticipate that the system can be further expanded to introduce additional abiotic reactivity.

3.3.4 Experimental Information

3.3.4.1 General Methods

Unless otherwise noted, all chemicals, salts and solvents were obtained from commercial suppliers (Sigma-Aldrich, Acros, etc.) and used without further purification. All expression media and buffer were prepared using ddH_2O (MilliQ A10 Advantage purification system, Millipore). Expression media was sterilized either by autoclave (20 min, 121 °C) or a sterile syringe filter (0.22 μm). All sterile materials and *E.coli* cells were manipulated near a lit Bunsen burner. TEV protease was obtained from the UC Berkeley Macrolab.

3.3.4.2 Instrumentations:

a. Gel Electrophoresis

The purity of the protein was determined by sodium dodecyl sulfate-polyacrylamine gel electrophoresis (SDS-PAGE) using precast gels (polyacrylamide, 4-20% linear gradient, Biorad) with tris-glycine as the running buffer.

b. Mass Spectrometry

ESI-MS was used to monitor the status of the His-tag cleavage process and dimerization of the protein. Mass spectra were obtained with an Agilent 1200 series liquid chromatograph (Agilent Technologies) connected in-line with an Agilent 6224 Time-of-Flight (TOF) LC/MS system equipped with a Turbospray ion source. Protein samples were run with a Proswift RP-4H column (Dionex, USA). Protein mass reconstruction was performed on the charge ladder with Mass Hunter software (Agilent, USA).

c. Inductively Coupled Plasma Optical Emission Spectroscopy (ICP-OES)

The concentrations of zinc and copper were determined by ICP-OES (Microanalytical Facility, College of Chemistry, UC Berkeley). The protein sample was digested overnight at room temperature with conc. HNO_3 to make a final concentration of 4 v/v% with 1 ppm yttrium added as internal standard. The samples were analyzed by ICP-OES.

Zinc

A calibration curve of zinc concentration was generated with five samples of varying protein concentrations, (0.2 ppm, 0.4 ppm, 0.8 ppm, 1.6 ppm, 2.4 ppm) with addition of 1 ppm yttrium as internal standard.

Copper

A calibration curve of copper concentration was generated with five samples of varying protein concentrations, (0.05 ppm, 0.1 ppm, 0.2 ppm, 0.5 ppm, 1.0 ppm) with addition of 1 ppm yttrium as internal standard.

f. UV-Vis Spectroscopy

The protein concentration was determined with a NanoDrop 2000 UV-Vis spectrophotometer (Thermo Scientific) measuring at 280/260 nm.

3.3.4.3 Protein sequences

The highlight letters indicate the residues that were mutated compared to the wt hCAII sequence.

WT hCAII

MSHHWGYGKHNGPEHWHKDFPIAKGERQSPVDIDTHTAKYDPSLKPLSVSYDQATSLR
ILNNGHAFNVEFDDSQDKAVLKGGPLDGTYRLIQFHFHWGSLDGQGSEHTVDKKKYAA
ELHLVHWNTKYGDFGKAVQQPDGLAVLGIFLKVGSAKPGLQKVVDVLDSIKTKGKSA
DFTNFDPRGLLPESLDYWTYPGSLTTPPLLECVTWIVLKEPISVSSEQVLKFRKLNFNGEG
EPEELMVDNWRPAQPLKNRQIKASFK*

H94A

MSHHWGYGKHNGPEHWHKDFPIAKGERQSPVDIDTHTAKYDPSLKPLSVSYDQATSLR
ILNNGHAFNVEFDDSQDKAVLKGGPLDGTYRLIQF**A**FHWGSLDGQGSEHTVDKKKYAA
ELHLVHWNTKYGDFGKAVQQPDGLAVLGIFLKVGSAKPGLQKVVDVLDSIKTKGKSA
DFTNFDPRGLLPESLDYWTYPGSLTTPPLLECVTWIVLKEPISVSSEQVLKFRKLNFNGEG
EPEELMVDNWRPAQPLKNRQIKASFK*

H94C

MSHHWGYGKHNGPEHWHKDFPIAKGERQSPVDIDTHTAKYDPSLKPLSVSYDQATSLR
ILNNGHAFNVEFDDSQDKAVLKGGPLDGTYRLIQF**C**FHWGSLDGQGSEHTVDKKKYAA
ELHLVHWNTKYGDFGKAVQQPDGLAVLGIFLKVGSAKPGLQKVVDVLDSIKTKGKSA
DFTNFDPRGLLPESLDYWTYPGSLTTPPLLECVTWIVLKEPISVSSEQVLKFRKLNFNGEG
EPEELMVDNWRPAQPLKNRQIKASFK*

H96A

MSHHWGYGKHNGPEHWHKDFPIAKGERQSPVDIDTHTAKYDPSLKPLSVSYDQATSLR
ILNNGHAFNVEFDDSQDKAVLKGGPLDGTYRLIQFHF**A**WGSLDGQGSEHTVDKKKYAA
ELHLVHWNTKYGDFGKAVQQPDGLAVLGIFLKVGSAKPGLQKVVDVLDSIKTKGKSA
DFTNFDPRGLLPESLDYWTYPGSLTTPPLLECVTWIVLKEPISVSSEQVLKFRKLNFNGEG
EPEELMVDNWRPAQPLKNRQIKASFK*

H96C

MSHHWGYGKHNGPEHWHKDFPIAKGERQSPVDIDTHTAKYDPSLKPLSVSYDQATSLR
ILNNGHAFNVEFDDSQDKAVLKGGPLDGTYRLIQFHF**C**WGSLDGQGSEHTVDKKKYAA
ELHLVHWNTKYGDFGKAVQQPDGLAVLGIFLKVGSAKPGLQKVVDVLDSIKTKGKSA
DFTNFDPRGLLPESLDYWTYPGSLTTPPLLECVTWIVLKEPISVSSEQVLKFRKLNFNGEG
EPEELMVDNWRPAQPLKNRQIKASFK*

3.3.4.4 Protein Expression, Purification, and Metalation

a. Protein Expression

hCAII was overexpressed in chemically competent Rosetta2 (DE3) pLysS E. coli. cells (obtained from UC Berkeley Macro Lab) with Luria Broth (LB) Media. Freshly transformed cells were plated on ampicillin/LB (100 mg/L) media and grown overnight at 37 °C in the oven. Single

colonies were used to grow the starting culture in 5 mL LB/amp media, which were shaken at 37 °C overnight. Overnight culture was added to 4 × 1 L of LB/amp media and shaken at 37 °C/ 250 rpm for 8 h. After the optical density (OD) of cell culture was measured at 1.0 to 1.2, the temperature was reduced to 25 °C. The cell culture was induced with IPTG (1 mM/L) and shaken for an additional 16 h. After this time, the cells were collected by centrifugation (5000 rpm, 15 minutes, 4 °C). Cell pellets were resuspended in Ni-NTA lysis buffer (50 mM NaPi, 300 mM NaCl, 10 mM imidazole, pH 8.0) and frozen at -80 °C.

b. Protein Purification

Cell suspensions were thawed in a room-temperature water bath and transferred to a glass beaker. The cell suspensions were lysed on ice by sonication (5 × 10 min on, 5 × 10 min off, 60% amplitude). The cell debris was removed by centrifugation (10,000 rpm, 30 min, 4 °C), and Ni-NTA was added to the cell lysate. The lysate was mixed in Ni-NTA for 30 min at 4 °C, and the resulting material poured onto a glass frit. The resin was washed with Ni-NTA lysis buffer twice and eluted with Ni-NTA elution buffer (50 mM NaPi, 250 mM NaCl, 250 mM Imidazole, pH = 8.0). The eluted protein was dialyzed against tris buffer twice (50 mM, pH = 8.0, 12 h/ 2h, 4 °C). The protein concentration was determined by measuring the absorption at 280 nm with a NanoDrop UV-vis spectrophotometer.

The purified protein with a His-tag was diluted with tris buffer (50 mM, pH = 8.0) to the concentration of 1 mg/ mL, and TEV protease (1:40, w:w, TEV:CA) was added. The reaction was transferred into a dialysis bag and dialyzed against TEV cleavage buffer (50 mM sodium phosphate, 50 mM NaCl, 50 mM Tris, 0.5 mM EDTA) overnight at 4 °C. The reaction was monitored by LC-MS. Ni-NTA resin was added to the crude cleaved protein solution and mixed for 30 min at 4 °C. The resulting material was poured onto a glass frit and eluted with the Ni-NTA lysis buffer and combined with the flow through.

The protein lacking the His-tag was diluted to (0.5 mg/ mL) with tris buffer (50 mM, pH = 8.0). To generate the apo protein, a freshly prepared solution of dipicolinic acid (250 mM in 50 mM sodium phosphate buffer, pH = 7.0) was added to the diluted protein (1:4, v:v), and the solution was incubated overnight without stirring (16 h, 4°C). The protein solution was concentrated with a spin concentrator (Amicon®Ultra-15 Centrifugal Filter Unit, corning, 10k Da MWCO). The dipicolinic acid was removed by passing the solution through a desalting column (Amersham NAP-10), which was twice equilibrated with 50 mM sodium phosphate, 50 mM NaCl, pH = 7.0. The protein purity was determined by SDS-PAGE, and the concentration of zinc was measured by ICP-OES. The purified apo protein was stored at 4 °C for future metalation.

c. Metalation of Apo hCAII

To a room-temperature solution of apo carbonic anhydrase in 50 mM sodium phosphate buffer (50 mM NaCl, pH = 7.0), 20 equiv of the metal salt was added. The reaction was mixed briefly by an end-over-end shaker and incubated without stirring (16 h, 4°C). After incubation, the protein solution was concentrated with an Amicon spin concentrator (Corning, 10k Da MWCO) and passed through a desalting column (Amersham NAP-10) twice equilibrated with 50 mM sodium phosphate, 50 mM NaCl, pH = 7.0. The protein purity was determined by SDS-PAGE, and the concentration of metal was measured by ICP-OES. The protein mixture was purified by size-exclusion chromatography on a Superdex 75 10/300 GL column with SEC buffer (50 mM sodium

phosphate, 50 mM NaCl, pH = 7.0). The metalated protein was stored at 4 °C for up to a week without losing catalytic reactivity.

d. Determination of protein concentration and purity

Protein concentration was determined by measuring the UV-vis spectroscopic absorption at 280 nm using a NanoDrop 2000c. The protein purity was determined by SDS-PAGE, and the protein lacking the His-tag was further confirmed by LC-TOF-MS (Figure S2)

2.3.4.5 Metalation and Demetallation Analysis

a. ICP-OES analysis of the zinc concentration in Apo-hCAII

Table S1. The zinc concentration was measured by ICP-OES. The apo protein is stable when eluting with sodium phosphate buffer with pH values ranging from pH 7.0 to pH 5.6 through the desalting column.

Condition	Protein conc.	Zn conc. (ppm)
wt hCAII in tris pH 8	26.2	1.13
TEV cleavage hCAII in NaPi pH 7	37.2	0.2
TEV cleavage hCAII in NaPi pH 6.4	21.9	0.25
TEV cleavage hCAII in NaPi pH 5.6	15.3	0.2

b. Activity test for residual zinc

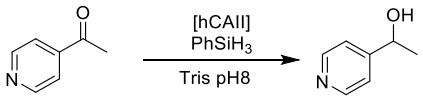

A solution containing 1 µmol hCAII in tris buffer (10 mM, pH 8.0) was thawed to room temperature. To a 4 mL screw-capped glass vial was added the protein solution diluted with the same buffer to 2 mL (final concentration as 0.05 mM solution of hCAII), followed by acetyl pyridine (12 mg, 100 µmol) and phenylsilane (32 mg, 300 µmol, 3.0 equiv). The reaction was conducted on an orbital shaker (20 °C, 300 rpm) for 16 h. After completion, the reaction mixture was extracted with EtOAc, and the conversion was analyzed by gas chromatography (GC).

Table S2. The conversion of acetyl pyridine to (pyridyl)ethanol. Entry 2 shows that the reactivity of hCAII for the reduction is independent of the presence of absence of the His tag. Entry 3 shows a lack of reactivity after demetallation of hCAII, indicating the success of the demetallation process.

Entry	Description	Conversion
1	Zn hCAII	> 99% conversion
2	His tag cleavage Zn hCAII	> 99% conversion
3	Dematalation hCAII	0%

c. ICP-OES for copper concentration in Cu-hCAII metalated by $Cu(MeCN)_4PF_6$

Table S3. The degree of metalation to form Cu-hCAII proteins by metalated of wt hCAII with $Cu(MeCN)_4PF_6$. The table shows that desalting three times leads to a constant level of metalation of hCAII, implying that the remain copper is bound to the active site of protein.

entry	Copper salt	NAP column	Protein conc.	Cu conc.	Theoretical Cu conc.	Metalation percentage
1	$Cu(MeCN)_4PF_6$	2	~15 mg/ mL	0.6 ppm	0.35 ppm	>100 %
2	$Cu(MeCN)_4PF_6$	3	~15 mg/ mL	0.3 ppm	0.35 ppm	86%
3	$Cu(MeCN)_4PF_6$	4	~15 mg/ mL	0.28 ppm	0.35 ppm	80%

d. ICP-OES for copper concentration in Cu-hCAII metalated by $CuSO_4•5H_2O$

Table S4. The degree of metalation of Cu-hCAII proteins by metalated of wt hCAII with $CuSO_4•5H_2O$. The table shows that desalting three times leads to a constant level of metalation of hCAII, implying that the remain copper is bound to the active site of protein.

entry	Copper salt	NAP column	Protein conc.	Cu conc.	Theoretical Cu conc.	Metalation percentage
1	$CuSO_4$	2	~10 mg/ mL	0.44 ppm	0.22 ppm	>100 %
2	$CuSO_4$	3	~10 mg/mL	0.2 ppm	0.22 ppm	90%
3	$CuSO_4$	4	~10 mg/mL	0.2 ppm	0.22 ppm	90%

3.3.4.6 Catalytic reactions

a. Allylation reaction

The solution containing 0.3 µmol Cu-hCAII in NaPi buffer (1 mL, 50 mM NaPi, 50 mM NaCl, pH 7.0) with copper(II) in a final concentration of 0.02 ppm was added to a 4 mL screw-capped glass vial. 2-Pentanone (5.3 µL, 50 µmol) and 33 µL of sodium ascorbate solution (300 mM in 50 mM NaPi) were added to the protein solution, followed by allylboronic acid pinacol ester (150 µmol). The reaction was conducted on an orbital shaker (20 °C, 300 rpm) for 16 h. After completion, the reaction mixture was extracted with 1 mL of ethyl acetate. The reaction was analyzed by gas chromatography.

b. Carbene transfer reaction

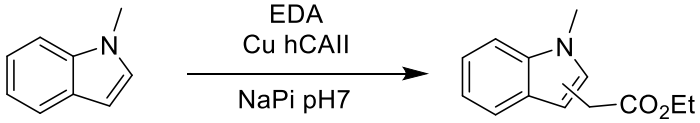

The solution containing 0.3 umol Cu-hCAII in NaPi buffer (1 mL, 50 mM NaPi, 50 mM NaCl, pH 7.0) with copper(II) in a final concentration of 0.02 ppm was added to a 4 mL screw-capped glass vial. 25 µL of *N*-methyl indole (400 mM in DMSO), 33 µL of sodium ascorbate solution (300 mM in 50 mM NaPi), and 25 µL of ethyl diazoacetate were added to the solution. The reaction was conducted on an orbital shaker (20 °C, 300 rpm) for 16 h. After completion, the reaction mixture was extracted with 1 mL of ethyl acetate. The reaction was analyzed by gas chromatography/mass spectrometry (GC/MS). The mass of the resulting product matched the mass of carbene insertion product to *N*-methyl indole.

3.3.4.8 Supplementary figures

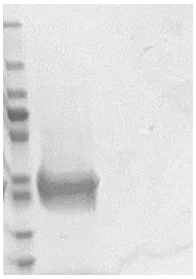

Figure S1. SDS-PAGE of wt-hCAII after His-tag affinity purification

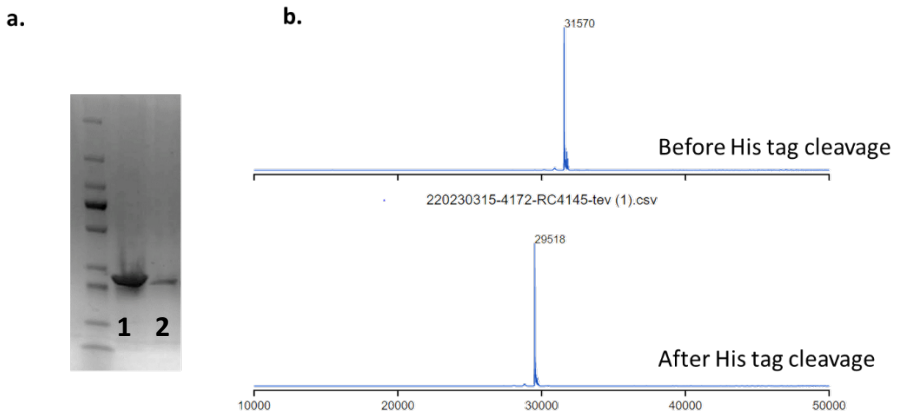

Figure S2. Purification of His-tag cleavage hCAII a. SDS-PAGE before (1) and after (2) the His-tag cleavage of hCAII b. LC-MS before and after His-tag cleavage of hCAII

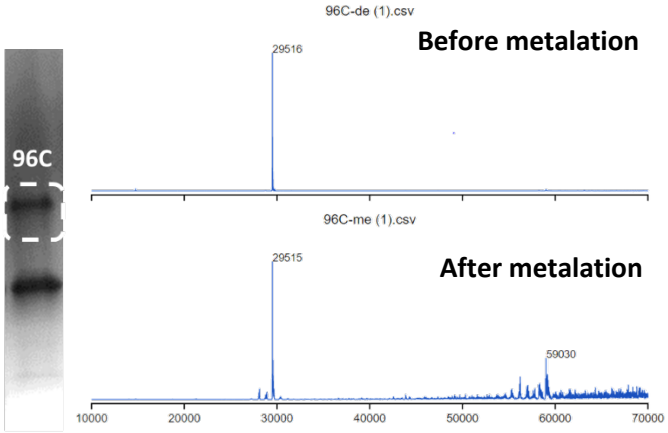

Figure S3. The LC-MS of 96C hCAII before and after the metalation with $Cu(MeCN)_4PF_6$. Dimerization of the protein was observed after the metalation process.

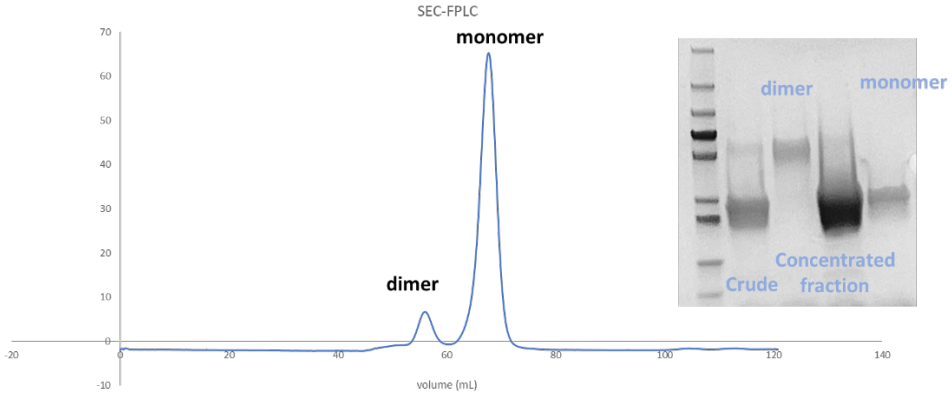

Figure S4. Separation of dimerized Cu-hCAII and monomer Cu-hCAII by SEC-FPLC.

3.3.5. References

(1) Stein, A.; Chen, D.; Igareta, N. V.; Cotelle, Y.; Rebelein, J. G.; Ward, T. R. A Dual Anchoring Strategy for the Directed Evolution of Improved Artificial Transfer Hydrogenases Based on Carbonic Anhydrase. *ACS Cent. Sci.* **2021**, *7* (11), 1874–1884.

(2) Okrasa, K.; Kazlauskas, R. J. Manganese-Substituted Carbonic Anhydrase as a New Peroxidase. *Chem. – Eur. J.* **2006**, *12* (6), 1587–1596.

(3) Gribble, M. W.; Pirnot, M. T.; Bandar, J. S.; Liu, R. Y.; Buchwald, S. L. Asymmetric Copper Hydride-Catalyzed Markovnikov Hydrosilylation of Vinylarenes and Vinyl Heterocycles. *J. Am. Chem. Soc.* **2017**, *139* (6), 2192–2195.

(4) Lee, D.; Yun, J. Copper-Catalyzed Asymmetric Hydrosilylation of Ketones Using Air and Moisture Stable Precatalyst $Cu(OAc)_2 \cdot H_2O$. *Tetrahedron Lett.* **2004**, *45* (28), 5415–5417.

(5) Deuss, P. J.; Popa, G.; Slawin, A. M. Z.; Laan, W.; Kamer, P. C. J. Artificial Copper Enzymes for Asymmetric Diels-Alder Reactions. *ChemCatChem* **2013**, *5* (5), 1184–1191.

(6) Ding, S.; Xu, L.; Li, P. Copper-Catalyzed Boron-Selective $C(Sp^2)$–$C(Sp^3)$ Oxidative Cross-Coupling of Arylboronic Acids and Alkyltrifluoroborates Involving a Single-Electron Transmetalation Process. *ACS Catal.* **2016**, *6* (2), 1329–1333.

(7) Kim, M.; Park, B.; Shin, M.; Kim, S.; Kim, J.; Baik, M.-H.; Cho, S. H. Copper-Catalyzed Enantiotopic-Group-Selective Allylation of *Gem* -Diborylalkanes. *J. Am. Chem. Soc.* **2021**, *143* (2), 1069–1077.

(8) Yamamoto, Yoshinori.; Asao, Naoki. Selective Reactions Using Allylic Metals. *Chem. Rev.* **1993**, *93* (6), 2207–2293.

(9) Yamasaki, S.; Fujii, K.; Wada, R.; Kanai, M.; Shibasaki, M. A General Catalytic Allylation Using Allyltrimethoxysilane. *J. Am. Chem. Soc.* **2002**, *124* (23), 6536–6537.

(10) Rumo, C.; Stein, A.; Klehr, J.; Tachibana, R.; Prescimone, A.; Häussinger, D.; Ward, T. R. An Artificial Metalloenzyme Based on a Copper Heteroscorpionate Enables Sp^3 C–H Functionalization via Intramolecular Carbene Insertion. *J. Am. Chem. Soc.* **2022**, *144* (26), 11676–11684.

(11) Muñoz-Molina, J. M.; Belderrain, T. R.; Pérez, P. J. Trispyrazolylborate Coinage Metals Complexes: Structural Features and Catalytic Transformations. *Coord. Chem. Rev.* **2019**, *390*, 171–189.

(12) Key, H. M.; Clark, D. S.; Hartwig, J. F. Generation, Characterization, and Tunable Reactivity of Organometallic Fragments Bound to a Protein Ligand. *J. Am. Chem. Soc.* **2015**, *137* (25), 8261–8268

(13) Ji, P.; Park, J.; Gu, Y.; Clark, D. S.; Hartwig, J. F. Abiotic Reduction of Ketones with Silanes Catalysed by Carbonic Anhydrase through an Enzymatic Zinc Hydride. *Nat. Chem.* **2021**, *13* (4), 312–318.

(14) Megumu, M.; Susumu, K.; Akio, A.; Hideki, M. Crystal Structure of Bis(2,2′-bipyridine)copper(I) Perchlorate. *BCSJ*, **1987**, *60* (5), 1927-1929

(15) Díaz-Requejo, M. M.; Pérez, P. J. The TpxM Core in Csp3–H Bond Functionalization Reactions: Comparing Carbene, Nitrene, and Oxo Insertion Processes (Tpx = Scorpionate Ligand; M = Cu, Ag). *Eur. J. Inorg. Chem.* **2020**, *2020* (11–12), 879–885.

(16) Delgado-Rebollo, M.; Prieto, A.; Pérez, P. J. Catalytic Functionalization of Indoles by Copper-Mediated Carbene Transfer. *ChemCatChem* **2014**, *6* (7), 2047–2052.